Matthew David Simmons

MChem Chemistry

Being a Thesis submitted for the Degree of Doctor of Philosophy

Synthesis of Fe-Oxide Nanoparticles using Microreactors

The University of Hull

(October 2014)

Declaration

The work described in this Thesis was carried out in the Department of Chemistry, The University of Hull under the supervision of Professor Paul Watts and Dr M. Grazia Francesconi between September 2010 and October 2013. Except where indicated by references this work is original and has not been submitted for any other degree.

Acknowledgements

Firstly I would like to thank the University of Hull for funding, and Chemtix.BV for lending me the microreactor equipment used in this work, I can only apologise for the state it was returned in.

I would particularly like to thank my to supervisors Professor Paul Watts and Dr M. Grazia Francesconi, for pushing me as far as I could go with this, and never losing faith in my abilities even when I had lost faith in myself.

To Dr Charlotte Wiles, Dr Vincent Rocher, and Dr Por Ngyasom, I can't thank you enough for all the help and support you've offered me over the last four years, especially Charlotte for letting me "borrow" so much of your equipment to try and complete some of my strange ideas and listening to me complain so much when nothing seemed to be going my way.

I would also like to thank Dr Ann Lowry, Mr Bob Knight and Professor David Evans, for providing and helping me with TEM, ICP and Mössbauer spectroscopy respectively, and baring with me when I didn't understand anything about these.

Thanks to all the PhD and MChem students of C112 past and present particularly Becky, Mark, Dave, Emma, Connah and Brad) for making the lab a great place to work.

I would like to thank all the friends I've made during my time as a PhD student both in Chemistry and in other departments, there are far too many of you to mention here, but know you have my thanks. First amongst you though are Naomi, Kreshnik, and Chris, for dragging me through the last three years and keep me standing when I wanted to give it all up. Without you guys I would have given up a long time ago.

Finally I would like to thank my family and friends, particularly the three above and Emma, who have convinced me to keep going after I had to resubmit, since my first viva I've seen some of the hardest months of my life and you've all helped me keep going.

So long and thanks for all the fish….

Aims of this Thesis

Throughout this work the aim has been to take a variable focus on the synthesis of biomedical nanoparticles, and improving the properties of these. Iron oxide nanoparticles were chosen for this as they represent a group of nanoparticles in which a variety of synthesis techniques can be used to form these, due to the magnetic properties of the nanoparticles which are manipulated for their use in biomedical applications, these nanoparticles were seen as ideal candidates for study in this work. The aims of this work were therefore to design a synthesis technique that would allow for easy manipulation of the nanoparticles properties, while maintaining a view of the larger picture, in which these nanoparticles would need to be produced on a much larger near industrial scale for use in the biomedical industry.

Abstract

The work described in this thesis focuses upon the development of a novel adaptable continuous flow technique for the synthesis of iron oxide nanoparticles using commercially available microreactor system, to allow for easy scaling up towards a larger industrial scale. The development of the technique focussed around the conversion of commonly used research techniques, which require the use of specifically designed microreactors, for use upon commercially available microreactors in which the design is fixed. A 2D continuous flow focussed technique was developed based upon the attempted conversion of the droplet coalescence and co-axial flow technique which has been previously used for nanoparticle synthesis by other research groups.

The nanoparticles produced using this technique were extensively characterised, in terms of physical and magnetic properties, and seen to be comparable, to those produced by other groups and those currently used as magnetic cores for MRI contrast applications. A critical evaluation of the effect of reaction parameters, e.g. reagent concentration, flow rate, and temperature upon nanoparticle size was made, however little quantifiable conclusions could be drawn. The structure of the nanoparticles was further investigated using a previously developed powder X-ray diffraction calibration technique which relied upon the asymmetry of peaks relating to specific reflections in the γ-Fe_2O_3 and Fe_3O_4 phases present in the nanoparticles. The structures were determined to contain higher quantities of γ-Fe_2O_3 which is more chemically stable but less magnetically favourable of the two phases. Further analysis using Mössbauer and solid state Infra-red analysis confirmed these findings, and as such attempts were made to control the amount of these phases within the nanoparticles. The synthesis technique was therefore adapted to allow for control of the amount of these phases within the nanoparticles by addition of oxidation and reducing agents into the synthesis. By doing this it proved able to synthesise nanoparticles which using the above powder X-ray diffraction technique were seen to be almost completely formed of γ-Fe_2O_3, synthesis of nanoparticles with higher weight percentages of Fe_3O_4, however proved not to be possible.

Further work upon attempting to alter the magnetic properties of the nanoparticles has involved developing cation substitution reactions performed using microreactors. In batch these reactions are common place, however to the best of the author's knowledge however no attempt has yet been made at cation substitution using microreactors. Partial replacement of Fe with another metal cation in the spinel structure was attempted to create a series of $M_xFe_{3-x}O_4$ compounds, this has been seen to alter the cation distribution and magnetic properties of the nanoparticles by other research groups. Several attempts at substituting Co, Mn, Zn, V, and Sn into the structure in batch. Zn substitution appeared the most successful in batch, and the synthesis was adapted to form $Zn_xFe_{3-x}O_4$ nanoparticles, with greater amounts of substitution into the nanoparticles seen when performing the synthesis in microreactors rather than batch.

The 2D continuous flow focussed technique would therefore prove a useful tool for the synthesis of biomedical nanoparticles. Not only those it produce nanoparticles with the correct physical and magnetic properties, but also allows for their adaptation and manipulation of these properties to be tailored for specific applications.

Symbols and Abbreviations

Magnetism and Magnetic Resonance and VSM

M – Sample magnetization

M_z - Longitudinal magnetization

$M_{x,y}$ – Transverse magnetization

C – Curie/ Curie-Weiss Constant M_s – Magnetic saturation

M_A, M_B –Magnetic saturation upon the A and B sublattices in a ferrimagnet

B – Change in magnetic induction or magnetic flux density

B_0 – Initial magnetic induction

μ_0 – Magnetic permeability

H – Magnetic field strength

M_s – Saturation magnetization

M_r – Magnetic remanence

H_c – Magnetic coercivity

μ - Magnetic moment

μ_{sat} – Magnetic saturation

K_b – Boltzmann constant

t – Time pulse of applied radiofrequency

T – Relaxation time

T_1 – Longitudinal relaxation

T_2 – Transverse relaxation

ω_0 – Lamour Frequency

φ – Phase constant

R – Relaxation rate

r – Relaxivity

τ_N – Nèel relaxation time

τ_0 – Pre-exponential factor

K - Anisotropy constant

χ - Magnetic susceptibility

C - Concentration of contrast agent

T – Temperature

V – Particle volume

T_C – Curie temperature

T_N – Nèel temperature

T_f – Ferrimagnetic Curie temperature (temperature at which a ferrimagnets magnetic susceptibility becomes infinite)

ω – Constant relating to the magnetic moments upon the octahedral and tetrahedral holes

ελ – ratio of magnetic moments upon the octahedral and tetrahedral holes

d – Diameter

r_c - Critical radius

Microfluidics

V – Volumetric flow rate

V_{eof} – fluid velocity (electroosmotic flow)

V_{epf} – fluid velocity (electrophoretic flow)

V_{Tot} – Total velocity

U – Fluid velocity

ν – Fluid viscosity

p – Fluid pressure

μ - Fluid viscosity Ca – Capillary number

γ - Interfacial tension

Q_w and Q_O – water and oil fraction of a liquid, respectively

Re – Reynolds number

D – Diffusion coefficient

A – Cross-sectional area

l – Scaling factor

ρ – Fluid density

d – Microchannel diameter

t – Time

E – Electric field

ρ_e – Charge density

Z_e – Charge number

X-ray diffraction

H, k, l – Miller indices

a, b, c – Lattice cell parameters

α, β, γ – Angles between lattice planes

V – Unit cell volume

d – Interplanar spacing

n – Number of lattice planes

λ - X-ray wavelength

θ - Bragg angle

τ - Mean crystalline diameter

K – Shape factor (0.9 for spheres)

β or β_m – Full width at half maximum of PXRD peak

β_s – Contribution to broadening of PXRD peak by instrumentation

Mössbauer

L – Angular momentum quantum number

M_l – Substate of angular momentum quantum number

S – Spin angular quantum number

M_s – Substate of spin angular quantum number

Δ – Difference in energy between substates

Q – Nuclear quadropole moment

V_{zz} – Quantity of charge distribution

B_{eff} – Total effective magnetic field

TEM

h – Planck's constant

m_e – Mass of an electron

v_e – Velocity of an electron

r – Resolution

μ - refractive index of the lens medium

α – semi angle of the aperture

BET

n_m – Capacity of a monolayer

n – Amount of substance

P/P_0 – Relative pressure of absorptive

σ – Average area occupied by each molecule in a monolayer

C – BET constant

a – Surface area

L – Avogadro's constant

f – Packing factor (HCP system = 1.091)

M – Molar mass of an adsorptive

ρ – Density

a – Specific surface area

S – Single point surface area

Φ – Diameter of particle

Contents

1.0. Introduction

The work presented in this thesis focuses upon the synthesis of magnetic iron oxide nanoparticles (IONs) using microreactors, the aim of which was to efficiently produce IONs for use in biomedical applications. Herein the main biomedical applications are discussed, and the different types of magnetism which are crucial to these applications, as well as the crystal structures which lead to these properties. Finally the synthesis of IONs both in batch and through the use of microreactors is described.

1.1. IONs for Biomedical Applications

Iron oxide nanoparticles have multiple uses in technology, but recent research has mainly focussed upon their use in biomedicine as magnetic resonance imaging (MRI) contrast agents, and hyperthermia treatments for arteriosclerosis and cancer.[1] Iron oxide based MRI contrast agents, were first researched in the late 1980's, as a way of providing competition to the traditionally used gadolinium chelate complexes, with several now being upon the market having successfully completed clinical trials.[2] In recent years dual diagnostic/therapy molecules, an area known as theragnostics, has also been developed, where IONs are used as either the diagnostic or treatment part of the molecule.

1.1.1. Magnetic Resonance Imaging (MRI)

Magnetic resonance imaging (MRI) is able to provide high spatial and temporal resolution imaging of the human body. Many traditional methods of tissue imaging rely upon the use of ionizing radiation, MRI avoids this using a combination of radiowaves and

magnetitc fields to provide high contrast images of different tissues, e.g .muscle and bone.[3] MRI relies upon the extremely small magnetic moments of the extremely large number of protons in water molecules present in body tissue. When protons are exposed to a magnetic field their magnetic spins align with the field, producing an equilibrium magnetization in the z-axis (M_z). While aligned the protons resonate at a specific frequency, the Lamour Frequency. A radiofrequency signal is then applied to the protons which cause their spins to be rotated from the z-axis to an angle called the "flip angle", causing a net magnetization in the xy-axis (M_{xy}). When the radiofrequency pulse is removed the protons relax back to their equilibrium position upon the z-axis.[4, 5] The time over which relaxation back to the equilibrium occurs is known as the "relaxation time", and is dependent upon the tissue and any influencing magnetic fields. There are two possible ways in which relaxation can occur; T_1, and T_2. De-phasing of the spins, where the magnetic dipoles randomize through the xy-axis, caused by microscopic variations in the external magnetic field or by interactions with neighbouring molecules, is prominent in T_2 relaxation.[1, 3] The symbol T_2* is used when the time constant is contributed to by both the natural de-phasing of the protons and these outside effects. Spin echo pulse sequence techniques are used to eliminate the external magnetic field effects which contribute to de-phasing; producing purely T_1 or T_2 weighted contrast images. These employ the use of multiple radiofrequency pulses, which induce flip angles of 180 ° and 90 ° to produce spin echoes, followed by a second 180 ° pulse to refocus the spin in the xy-axis.

1.1.1.1. Longitudinal, Spin Lattice Relaxation (T_1)

There are two types of T_1 relaxation short and long, where the magnetization is either fully recovered before further radiofrequency pulses are applied, or not, **eq. 1.1.** The longitudinal relaxation, m_z, is a loss of heat to its surroundings or "lattice", an indirect measure of the dipolar protons coupling to their surroundings.[6]

To measure the T_1 relaxation time a radio frequency pulse is applied to the tissue, causing the protons spins to flip by 180° in the z-axis, **fig. 1.1a.** The proton spins begin to relax back to their equilibrium positions, **fig. 1.1.b.**, before a second radiofrequency pulse is applied causing the spins to flip in a further 90° before equilibrium is reached, the time taken for the spins to relax back to their equilibrium is then measured, **fig. 1.1.c.**, seen as an increase in signal amplitude with time, **fig. 1.1d.**

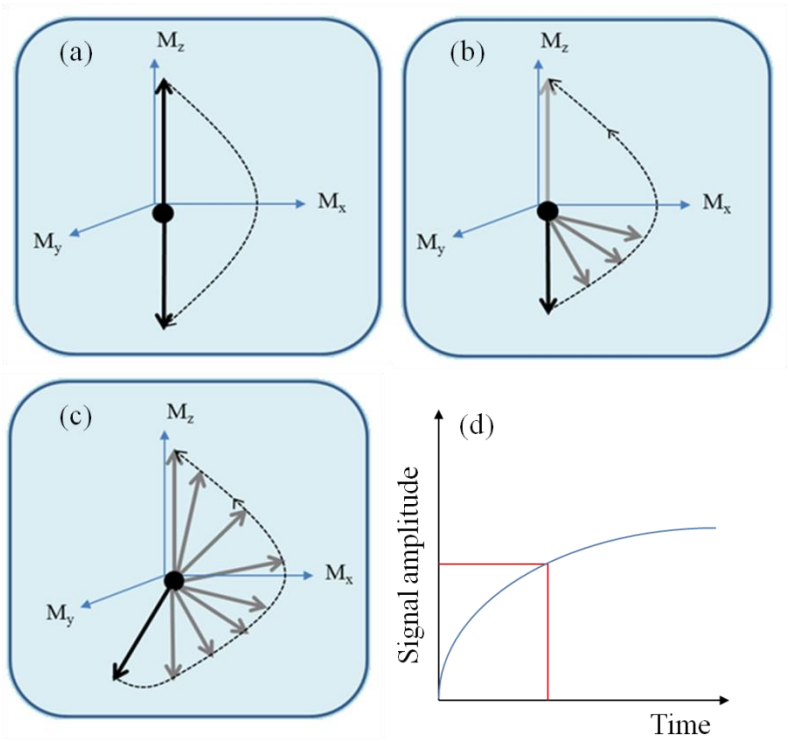

Figure 1.1. T_1 relaxation of magnetic spin of water protons, where a radiofrquency pulse causes the spin to be flipped into the magnetic transverse plain by a radiofrequency pulse applied at 90°. The T_1 relaxation time is the time taken for the magnetization of the sample to recover by 63% after the radio frequency pulse has been applied.

Longitudinal magnetization, is dependent upon the overall sample magnetization, *m*, the relaxation time, T_1, and the time pulse of the radiofrequency, *t*.

Equation 1.1.

$$m_z = m\left(1 - e^{-t/T_1}\right)$$

1.1.1.2. Transverse, Spin-Spin Relaxation, T_2

T_2, is the time constant associated with transverse relaxation, the decay in the magnetization in the xy-axis, M_{xy}, after the application radiofrequency pulse, **eq. 1.2.** It is related to the time taken for the proton spins to align randomly within the xy-axis after the application of the radiofrequency pulse, when fully randomised in alignment no net magnetization is measured.[6]

The T_2 relaxation time is measured by application of a radiofrequency pulse to the tissue which causes the proton spins to be flipped by 90° into the xy-plane, **fig. 1.2.a.** The proton spin will then begin to lose coherence, at which point a second radiofrequency pulse is applied causing a rotation of the spin by 180° from its position in the xy-plane so that the spins are re-focussed, **fig. 1.2.b.** The time taken for the spin to then relax back to its equilibrium position is then measured, the T_2 relaxation time, resulting in a decrease in the signal amplitude with time, **fig 1.2.c and d.**

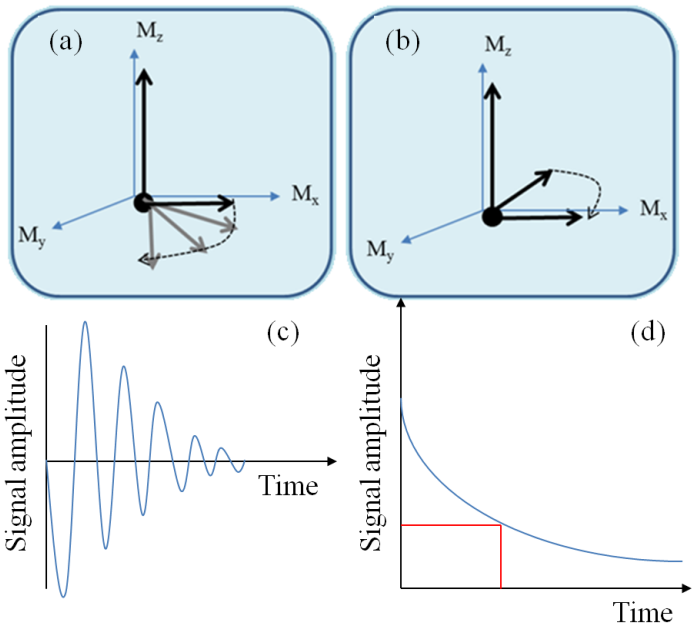

Figure 1.2. T_2 relaxation of proton spin. Where an applied radiofrequency pulse causes the magnetization direction to flip into the transverse plane. The T_1 relaxation time is the time it takes for the magnetic resonance signal to decay below 37% of its initial value after the flipping has occurred.

Transverse magnetization, m_{xy}, is dependent upon the sample magnetization, m, the time pulse of the radio frequency, t, Lamour frequency, ω_0, and a phase constant, φ.

Equation 1.2.

$$m_{xy} = m\sin(\omega_0 t + \varphi)\, e^{-t/T_2}$$

The effectiveness of different imaging agents can be compared by comparing their relaxivity, r, determined by the relaxtion rate, R, the inverse of its relaxation time, T, at a specific concentration, C, **eq. 1.3. and 1.4.**

Equation 1.3.

$$R = \frac{1}{T}$$

Equation 1.4.

$$r = R/C$$

The greater the relaxivity the greater the effectiveness as a contrast agent, as less needs to be injected into the patient.[7] The classification of a contrast agent as a T_1 or T_2 depends upon the ratio of the relaxivity for the T_1 and T_2 times to each other. T_1 weighted images are preferred for anatomical studies, increasing signal intensity, positive contrast, where T_2 weighted images are preferred for pathological studies, decreasing contrast.[6]

1.1.1.3. IONs as Contrast Agents

Iron oxide nanoparticles are used as T_2 contrast agents due to the large magnetic moment possessed by each nanoparticle, in comparison to those of the water protons, the direction of which can be flipped when the particle is placed in a magnetic field. Water protons which diffuse into the localised magnetic field of the nanoparticles, caused by their magnetic moment, experience greater magnetization and therefore have shorter relaxation times, **fig. 1.3.** The size of the nanoparticles also allows for targeting toward specific organs, small IONs (SPIONs), e.g. hydrodynamic radii > 40 nm, are used for liver spleen and lymph node imaging as they are taken up by Kupffer cells.[4, 6, 7] Nanoparticles with hydrodynamic radii below 40 nm are considered to be Ultra small superparamagnetic IONS (USPIONs).

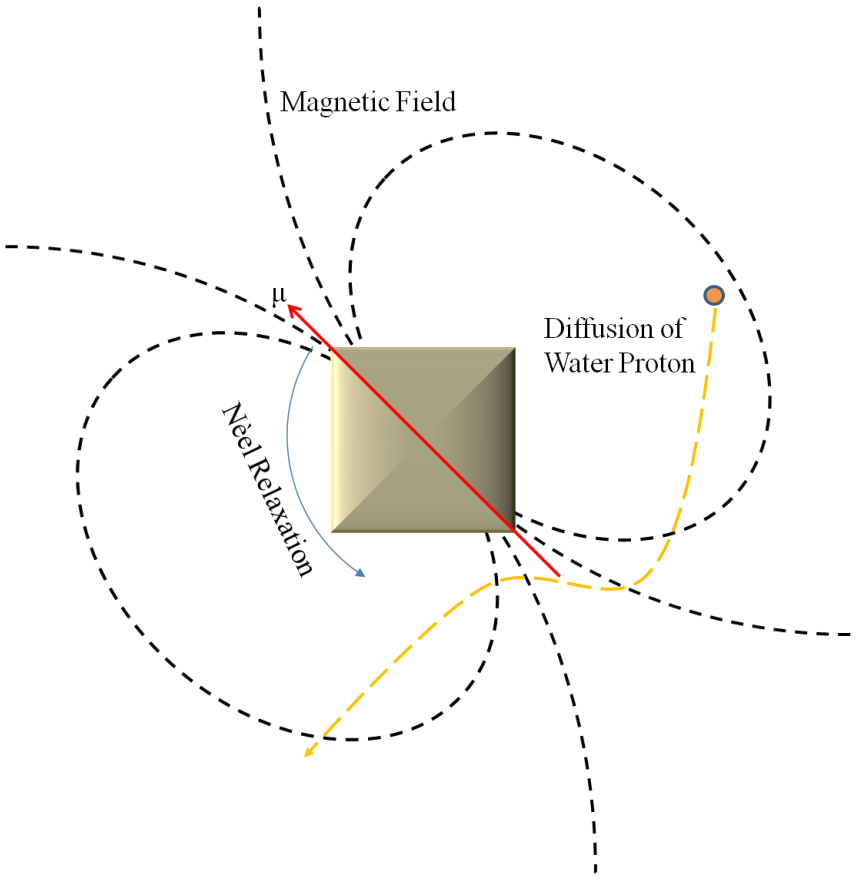

Figure 1.3. A magnetic contrast agents strong magnetic fields affect the diffusion of water protons as they pass through the particles magnetic fields, causing the relaxation times to be altered.

The strength of the applied magnetic field can have a large effect upon a particles magnetic moment, μ, and the relaxivity of the water protons, **eq. 1.5.** The higher the applied field the greater the magnetic moment, and the larger the effect upon the protons relaxation time, up until the point of magnetic saturation, μ_{sat}, which follows a Langevin function, L,

Equation 1.5.

$$\mu = \mu_{sat} L\left(\frac{\mu_{sat} B}{kT}\right)$$

k is the Boltzmann constant, T the temperature of the particle, and B the magnetic flux density.[7]

There are several factors, which can affect the nanoparticles magnetic properties and be used to alter the relaxation times, particularly the size of the particles which affects the Nèel relaxation time, $\tau_{N,}$ **equation 1.6.**[8]

Equation 1.6.

$$\tau_N = \tau_0 e^{\left(KV/k_b T\right)}$$

Where, k_b is the Boltzmann constant, V the particle volume, K the anisotropy constant, and τ_0 the pre-exponential factor. The relaxation time of the nanoparticle is therefore exponentially dependent upon its volume, for nanoparticles with diameters larger than 20 nm the relaxation time > 1 ms, much longer than the diffusion times of water molecules, so the magnetic moment of larger particles has little effect upon the relaxation these.

1.1.2. Magnetic Hyperthermia Treatments

Magnetic hyperthermia treatments use, magnetic nanoparticles to induce cell death by heating the tissue. As magnetic nanoparticles can be targeted to specific cells, and are activated by external application of a magnetic field they are seen as more favourable, requiring no use of potentially harmful laser light, as is required for similar gold nanoparticle induced hyperthermia, or invasive surgery to remove tumours. There are three main types of medical hyperthermia treatments; local hyperthermia, in which heat is applied to a small area of tissue, such as a tumour. Regional hyperthermia focuses upon the heating of a large area of tissue, such as an organ, while whole body hyperthermia is used to treat metastatic cancers which have spread throughout the body.[9]

Local hyperthermia treatments involve the heating of cancerous tissue, so that natural cell death, apoptosis, occurs. The tumour can either be targeted passively, entering cells due to their biophysiochemical properties or via active targeting, where they are coated in

antibodies. As tumours have a lower thermoresistance, due to their increased metabolic rate, heating the tumour to 41 - 45 °C, causes a change in the cellular function and natural cell death.[1] Heating above 45 °C, causes the less desirable thermoblation, leading to cell necrosis, and the formation of scar tissue.

Magnetic nanoparticles can be heated through the application of an alternating magnetic field. When placed in a magnetic field the spins of the magnetic nanoparticles align parallel to the magnetic field, when this is removed the spins "relax" back to their preferred orientation, when this occurs at a slower rate than the field is switched off the remaining magnetic energy is converted to internal energy, released as heat.[6] There are two mechanisms for the relaxation to occur either through Brownian relaxation, involving the physical rotation of the nanoparticles within a fluid, or through Nèel relaxation involving the rotation of the magnetic moment within the nanoparticles, **fig. 1.4.**[9]

The relaxation times, τ_b and τ_N respectively, depend upon the hydrodynamic properties of the particles in the surrounding fluid, for Brownian relaxation, and the magnetic anisotropy, for Nèel relaxation. These two mechanisms are size dependent, for nanoparticles with sizes > 20 nm Brownian relaxation dominates, and for those with sizes < 20 nm, the Nèel relaxation mechanism dominates.

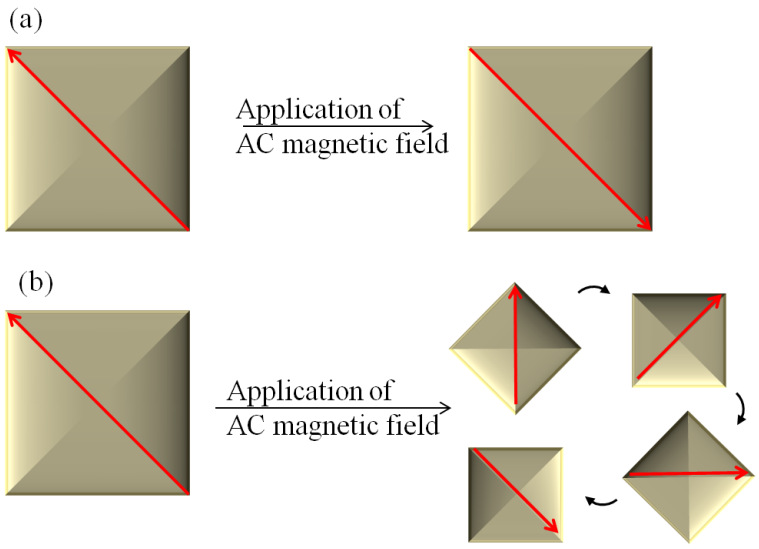

Figure 1.4. Re-direction of magnetic moment (red) when an AC magnetic field is applied through Nèel Relaxation where the direction of the magnetic dipole reverses internally along the magnetic easy axis(a), and Brownian Relaxation where the particle rotates to realign itself with the direction of the alternating magnetic field(b).

The heat generated by the magnetic relaxation is given by the specific absorption rate (SAR), in W g^{-1}.[6]

Current feasibility studies have shown magnetic hyperthermia treatments using magnetic nanoparticles to be useful in the treatment of locally recurrent prostate carcinoma which has previously been treated radioloigcally.[10, 11] The temperatures achieved were found to be in the thermoblative region, ideal for destroying cancerous tissues without the producing scar tissue. Further to this nanoparticle depositions were found to be stable for several weeks, allowing for sequential treatments without the reapplication of nanoparticles. However further work including further phase 1 clinical trials are required to confirm these preliminary findings.

1.2. Magnetism

Magnetism is a material property generally associated with unpaired electrons. Diamagnetism and paramagnetism are associated with no long range ordering of magnetic spins.[12, 13] Ferro, antiferro, and ferrimagnetism are all associated with long range ordering of magnetic moments which give rise to magnetic domains, and are primarily associated with the unpaired electrons in the 3*d* or 4*f* orbitals. A material is classified by its response to an external magnetic field.

1.2.1. Diamagnetism

When a diamagnetic material is placed within a magnetic field the magnetic dipoles, which are usually aligned randomly, cooperatively align so that a magnetic field is generated to oppose the external magnetic field, Lenz's Law. This causes the weakening of the magnetic flux density within the material, and the material is repulsed as a result, **fig. 1.5.** The strength of the repulsion is therefore proportional to the strength of the applied magnetic field.[12,14] Diamagnetism is shown by all materials because of the motion of orbiting electron pairs within their orbitals in the presence of a magnetic field. As the electrons are fully paired there is no spin contribution to the substances magnetism.[12]

Diamagnetism is a weak interaction characterised by a small negative magnetic susceptibility ($\chi < 0$), easily masked by other types of magnetism, and is independent of temperature.

1.2.2. Paramagnetism

Paramagnetism is possessed by materials whose magnetic moments are uncoupled but do not exhibit any long range ordering, most commonly associated with materials containing unpaired electrons (e.g. transition metals with unfilled d-orbitals), as the spins of these electrons give rise to permanent magnetic dipoles.[12] When an external magnetic field is applied these dipoles align with the field, increasing the flux density, **fig. 1.5.**, This aligning of dipoles causes the material to be attracted toward the applied field, and therefore has a small positive magnetic susceptibility, with the degree of attraction proportional to the strength of the magnetic field.

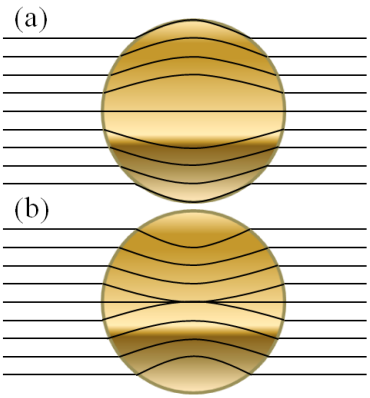

Figure 1.5. Flux density in a diamagnetic material where due to Lenz's law the magnetic flux density within the material is decreased (a) and a paramagnetic material where the magnetic flux density is increased within the material (b).

Although in paramagnetic materials the spins of the electron align within a magnetic field this is highly temperature dependent, as thermal energy seeks to randomize the direction of the magnetic dipoles, **fig. 1.7.a.**, described by the Curie law, **eq. 1.8.**[13]

Equation 1.8.

$$\chi = {}^{C}/_{T}$$

T is the temperature in kelvin, and *C* the Curie constant, a material dependent property. There are two further types of paramagnetism; Pauli paramagnetism, and superparamagnetism which is vital for use of IONs in biomedical applications and described in a later section.

1.2.3. Ferromagnetism

Ferromagnetism occurs in materials containing transition metals with nearly full *3d* orbitals, particularly materials containing iron, cobalt and nickel. The magnetic dipoles of the electrons within a ferromagnetic material cooperatively align, **fig.1.6.a.** As the dipole moments can cooperatively align, a spontaneous magnetization can occur in the absence of a magnetic field. Materials which permanently maintain this magnetization are characterised as being magnetically "hard".[13]

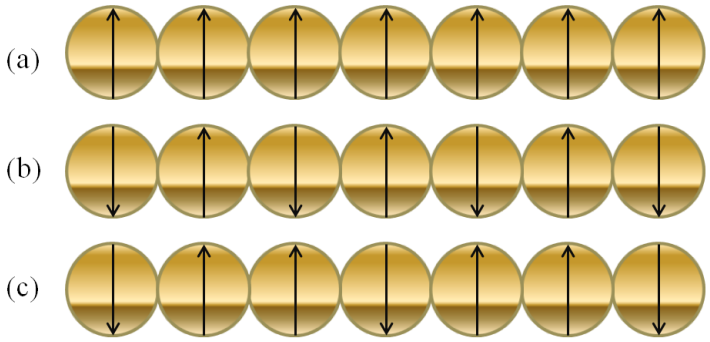

Figure 1.6. Ordering of magnetic dipoles in different types of magnetic behaviour, ferromagnets where short range ordering of the spins occurs aligning the magnetic dipoles (a), antiferromagnets where through the superexchange mechanism the magnetic dipoles of the two (b), and ferrimagnets where due to the crystallographic structure of the material dipoles can align both ferro and antiferromagnetically but in uneven amounts (c).

As the electrons on different ions cooperatively align a temperature dependent switch over from cooperative (ferromagnetic) behaviour to individual (paramagnetic) behaviour

is seen with increasing temperature due to thermal energy causing the spins to align randomly, **fig. 1.7.b.**, as described by the Curie-Weiss law, **eq. 1.9.**, takes on the form of:

Equation 1.9.

$$\chi = {}^{C}/_{(T - T_C)}$$

T_c is the Curie temperature, the temperature at which the switch from cooperative to individual behaviour occurs, χ the magnetic susceptibility, and C the Curie constant.[13]

1.2.4. Antiferromagnetism

Antiferromagnetic materials contain magnetic moments upon neighbouring dipoles which are aligned antiparallel to each other with equal magnitude, **fig 1.6.b.**[12] The magnetic interactions in antiferromagnetic compounds arise most commonly via the superexchange mechanism.[13, 15, 16] In a compound in which a linear orbital arrangement exists between the d_{z^2}orbital of a transition metal and the $2p_z$ of oxygen, the electrons within the d_{z^2} orbital are paired with the electrons within the closed $2p_z$ orbital of the oxygen so that the electrons within the d_{z^2} orbitals have opposite spins.[13] As the antiparallel spins have equal magnitude there is no net magnetization. Antiferromagnets do not act to enhance the magnetic field.

As with ferromagnetic materials the behaviour of antiferromagnetic materials is highly temperature dependent, **fig. 1.7.c.** The temperature dependence of antiferromagnetic materials is described by a modified form of the Curie law, **eq. 1.10.**

Equation 1.10.

$$\chi = {}^{C}/_{(T - T_N)}$$

T_N , is the Nèel temperature.

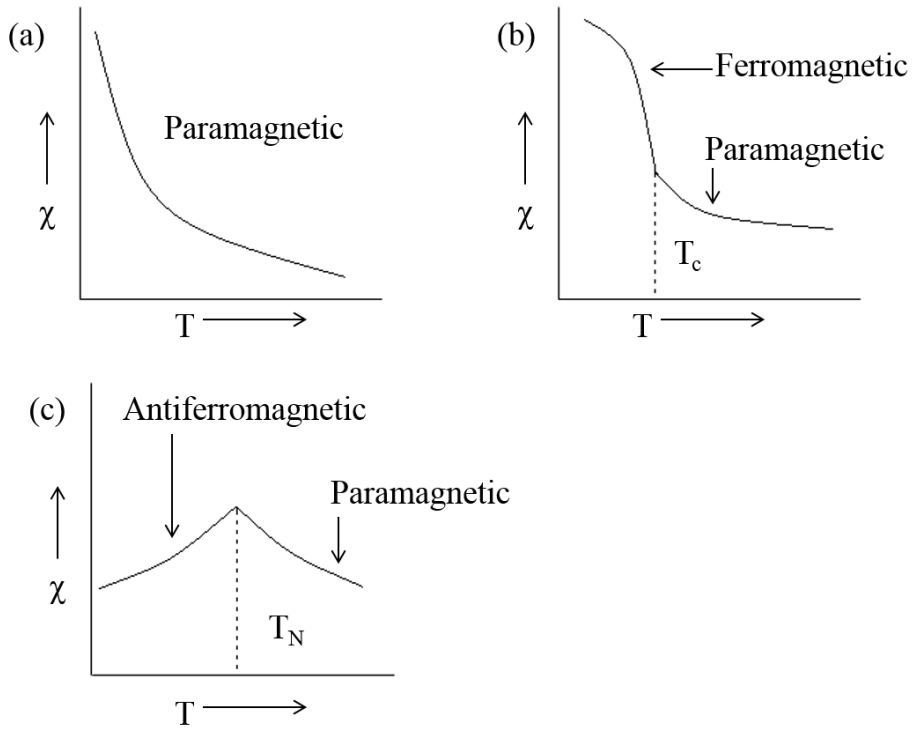

Figure 1.7. Plots of the variation in magnetic susceptibility against temperature for a paramagnet where the magnetic susceptibility of the material decreases with increasing temperature (a), a ferromagnet where the magnetic susceptibility decreases sharply with increasing temperature until the T_C occurs and the sample becomes paramagnetic (b), and antiferromagnetic where the magnetic susceptibility increases with increasing temperature until the T_N is reached where the sample becomes paramagnetic and the susceptibility then decreases (c).

1.2.5. Ferrimagnetism

Ferrimagnetism is a property attributed to materials with an ordered non-parallel crystal structure arrangement, below the Nèel temperature and when no magnetic field is applied.[12] A ferrimagnetic material can be thought of as containing a phase with an uneven number cation sites which couple to each other ferromagnetically, while coupling with others antiferromagnetically through the super exchange mechanism. Most commonly observed in the case of the spinel structure, which has twice the amount of octahedral sites filled as tetrahedral, a cooperative interaction exists between the spins of

the ions upon the octahedral sites aligning parallel, however they interact with the ions upon the tetrahedral sites via the superexchange mechanism, with the spins aligning antiparallel.[13] A net ferromagnetic effect is therefore seen in this case as there are more octahedral sites than tetrahedral, but the overall magnetic moment is more unpredictable than for ferromagnetic compounds.

As the alignment of spins is more complicated within a ferrimagnetic material, so is the temperature dependence of the magnetic properties, **eq. 1.11.**[13]

Equation 1.11.

$$T_f = \sqrt{\omega C(\varepsilon\lambda)}$$

T_f is the temperature at which the magnetic susceptibility of the material becomes infinite, the ferrimagnetic Curie temperature, ω a constant related to the magnetic moments upon the octahedral and tetrahedral sites, and $\xi\lambda$ the ratio of the magnetic moments upon these. Above the Nèel temperature the sample is paramagnetic, however there are different types of interaction which can occur up until this point. These are most easily displayed graphically upon a plot of the magnetic saturation over its magnetic saturation at absolute zero, $M_s(T)/M_s(0)$, against the temperature over Curie temperature of the material, T/T_c, **fig. 1.8.** At absolute zero it is assumed that the moments upon the A and B cation are aligned antiparallel to each other, and the total magnetic saturation, M_s is equal to the difference between the magnetic saturation of the two sublattices, M_B and M_A, **eq. 1.12.**

Equation 1.12.

$$M_s = M_A - M_B$$

There are therefore three types of ferrimagnets depending upon the rate at which each of the magnetic saturations of the octahedral and tetrahedral sites decrease, with increasing temperature.

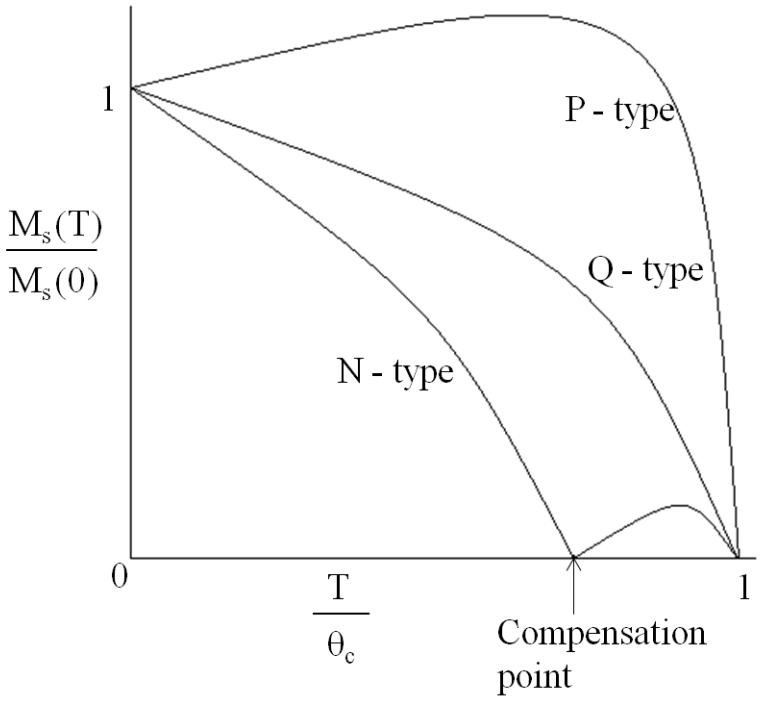

Figure 1.8. Graphical depiction of the P, Q, and N type ferrimagnets, where P-type occur when the magnetic saturation of the tetrahedral sites decreases faster than that of the octahedral sites, in Q-type the magnetic saturation of the octahedral sites decreases at a faster rate than that of the tetrahedral sites, causing a rapid decrease in total magnetic saturation, and N-types which are extreme examples of the Q-type where the octahedral sites magnetic saturation decreases much faster than that of the tetrahedrals.

P-type ferrimagnets, occur when the magnetic saturation of the tetrahedral sites decreases faster than that of the octahedral sites. An initial increase in total magnetic saturation is seen, as M_A decreases, a sharp decrease is then seen once this reaches zero.

Q-type ferrimagnets, occur when the magnetic saturation of the octahedral sites decreases at a faster rate than that of the tetrahedral sites, causing a rapid decrease in total magnetic saturation.

N-type ferrimagnets are extreme examples of the Q-type, where the magnetic saturation of the octahedral sites decrease at a much faster rate than that of the tetrahedral sites. Therefore at a specific value of T/θ_C the magnetic saturation of the two sites will be equal and $M_s = 0$, known as the "compensation point", which is different from the Curie

temperature. Further temperature increases cause M_A to become greater than M_B and M_S, however the magnetic saturation remains positive as it remains parallel to the applied field, **eq. 1.13.**

$$M_s = M_A - M_B$$

The total magnetic saturation will then increase slightly until $M_A = 0$.

1.2.6. Magnetic domains

In ideal ferro/ferrimagnet, magnetic dipoles exhibit long range spin ordering, theoretically in the absence of an applied magnetic field, they will not exhibit any net magnetisation, however, after the removal of the applied field will still exhibit magnetization for a period due to magnetic remanence.[17] For instance when a hard magnet is measured as a function of applied field strength a characteristic hysteresis loop is observed, in which the magnetization of the sample increases linearly with increasing field strength (a), **fig. 1.9.**, until a point of magnetic saturation (b) is reached, **fig. 1.9.**, where a further increase in field strength produces no further increase in magnetization.[13] Decreasing the magnetic field strength causes a gradual loss of magnetisation, however upon complete removal of the magnetic field, the material exhibits a residual magnetization, magnetic remanence (c), **fig.1.9.** As the field strength is reversed the samples magnetization will continue to decrease until it reaches zero, magnetic coercivity (d), **fig. 1.9.** Continuing reversal of the magnetic field produces a decrease in magnetisation until a second point of magnetic saturation (b) is reached. From here increasing the field produces a mirror image of the demagnetisation curve, forming a hysteresis loop.

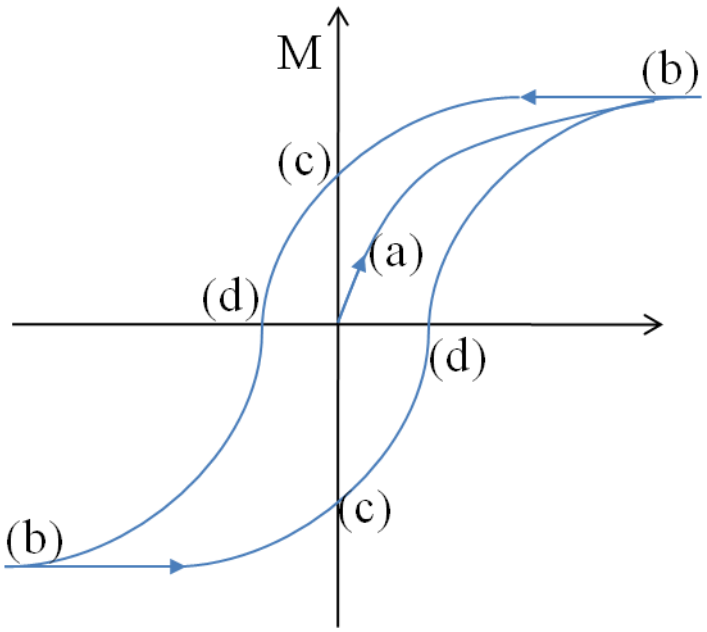

Figure 1.9. Hysteresis loop of a bulk ferromagnet, where the magnetisation of the sample initially increase (a-b) before slowly decreasing when the field strength is reversed to 0, the remaining magnetisation being the magnetic remanence (b-c), the magnetic saturation decreases further with the further reversal of the field until the magnetization reaches 0 (c-d), the magnetic coercivity.

This hysteresis behaviour of ferro/ferrimagnetic materials was explained by Weiss in 1939, in which a bulk magnetic material is separated into domains which seek to minimize the magnetostatic energy of the material.[18] Short range ordering of the magnetic dipoles allows spins to align perfectly, but is opposed by long range magnetic dipole interactions, **fig. 1.10a.** These are stronger than the short range interactions and the dipoles gradually align in such a way as to negate the net magnetization of the material.[17] This results in magnetic domains within which uniform magnetisation occurs, but the magnetic domains throughout the material will align in opposition, so as to negate net magnetisation in the absence of an applied field. These magnetic domains are separated by walls, the energy of which increase proportionally with the surface area, opposed by the magnetostatic energy which is proportional to the materials volume.[17] Application of a weak magnetic field causes domains whose magnetic dipoles are parallel to the external magnetic field

to grow larger, as the domain walls move toward the edges of the particle, shrinking the domains with antiparrallel spins, **fig. 1.10.b.** Application of higher strength magnetic fields causes a second mechanism to occur in which the higher field strengths cause the magnetic dipoles within each domain to rotate, and align to the external field, **fig. 1.10c**.

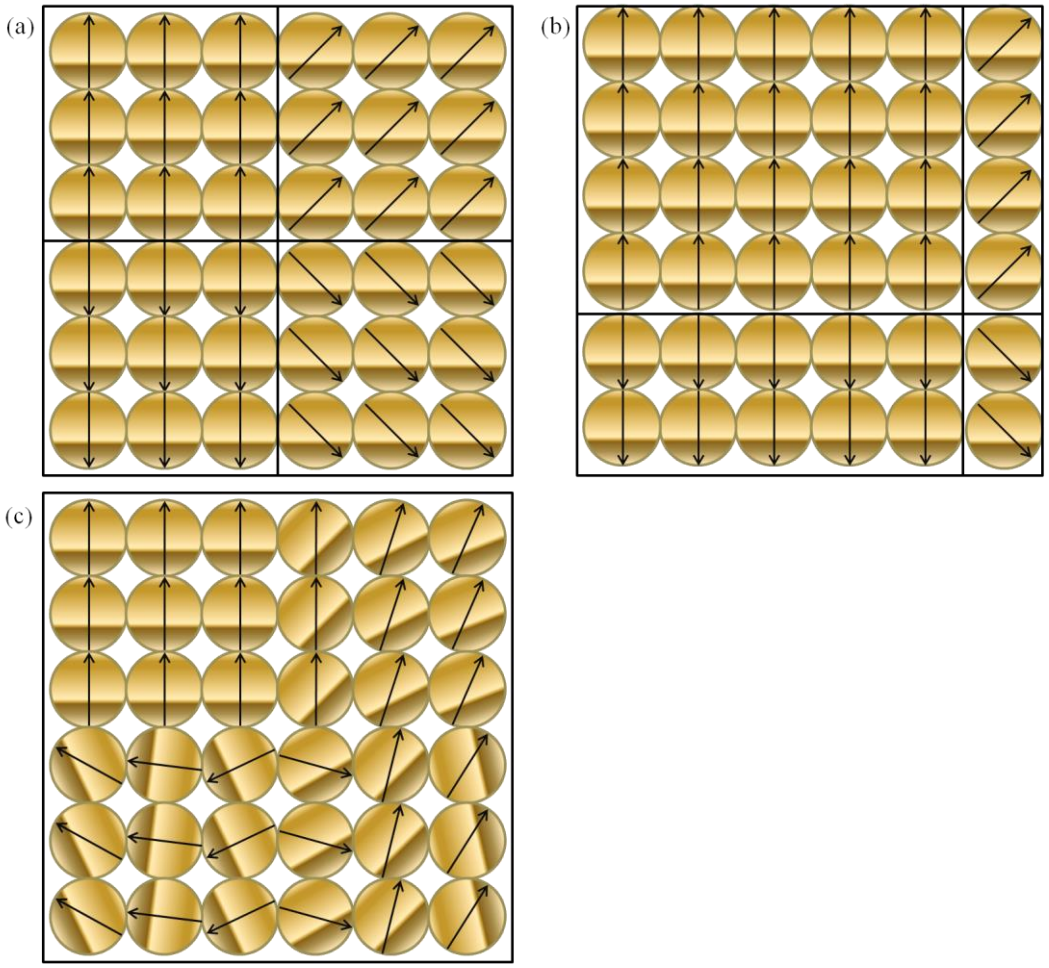

Figure 1.10. Magnetic domains in ideal ferromagnets when, no magnetic field is applied (a), application of a weak magnetic field causes the domains with parallel dipoles to the magnetic field to slowly grow (b), and application of a strong magnetic field where the spins on the individual particles rotate (c).

As the diameter of the nanoparticles decreases the coercivity of the nanoparticles increases, proportionately to $1/d$, until the diameter of the particles reaches a critical point where a single magnetic domain exists.[17] It is energetically less favourable for small particles to contain a closed magnetic flux, and therefore below a critical radius it is more

favourable to have larger magnetic domains, until these are equal to the particle size, **eq. 1.13.** Any further decrease in size leads to the formation of superparamagnetic nanoparticles, in which only a single domain exists.[12]

The critical radius, r_c, below which a particle will exist as a single magnetic domain can be calculated, from its saturation magnetization, M_s.

Equation 1.13.

$$r_c \approx 9\frac{(AK_u)^{1/2}}{\mu_0 M_s^2}$$

A and K_u are the exchange and uniaxial anisotropy constants respectively. For Fe_3O_4 and γ-Fe_2O_3 nanoparticles the critical radius is approximately 30 nm, hence nanoparticles below these sizes are required for biomedical applications.

1.2.7. Superparamagnetism

Superparamagnetism is a property of ferro/ferrimagnetic materials in which only a single magnetic domain is present, and the material exists in a single magnetic state, effectively behaving like an individual paramagnetic atom.[17] Superparamgnetic particles have large magnetic moments which can be easily moved away from the magnetic easy axis by fluctuations in temperature and magnetic field, making them ideal for both MRI and hyperthermia applications.[12] The particles exhibit little in the way of magnetic hysteresis when placed in an applied field, and ideally experience no magnetic coercivity or remanence, effectively allowing the magnetic moments of superparamagnetic particles to rotate rapidly in unison, **fig. 1.11.**

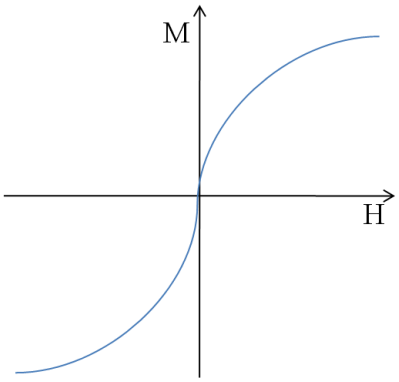

Figure 1.11. Hysteresis loop of an ideal superparamagnet which displays negligible values of magnetic coercivity and remanence.

This magnetic behaviour of superparamagnetic materials is temperature dependent, a blocking temperature (T_b), exists below which the time scale of the rotation of the magnetic dipole, the Nèel relaxation time, becomes longer than that of the measurement time, the time between the radiofrequency pulses used to realign the magnetic dipole. The nanoparticles also possess a Curie point, dependent upon whether the nanoparticles are ferro or ferrimagnetic.

To assess whether a nanoparticle will be useful for biomedical applications requires the measurement of certain parameters. The particle must display superparamagnetism, assessed through the values of magnetic coercivity and remanence, or alternatively this can be determined using Mössbauer spectroscopy, from the presence of a superparamagnetic doublet. Secondly, the particles saturation magnetisation must be analysed, as the samples magnetisation affects the relaxation of the water protons in MRI, and causes the production of heat in magnetic hyperthermia. SQUID magnetometry also proves useful for assessment of temperature dependent qualities of nanoparticles.

1.3. Structure of Magnetic Nanoparticles

There are several polymorphs of iron oxide some of which can be interconverted between via various chemical/physical processes, **fig. 1.12.** The most thermodynamically stable form of iron oxide being that of α-Fe_2O_3, however this only possesses weak antiferromagnetism and is the least useful of the common forms of iron oxide for biomedical applications.[19] The spinel phase iron oxides, Fe_3O_4 and γ-Fe_2O_3, while less thermodynamically stable, possess strong ferrimagnetic properties, and therefore at sizes below the critical diameter, are superparamagnetic.[19] These two phases are therefore the focus of this work.

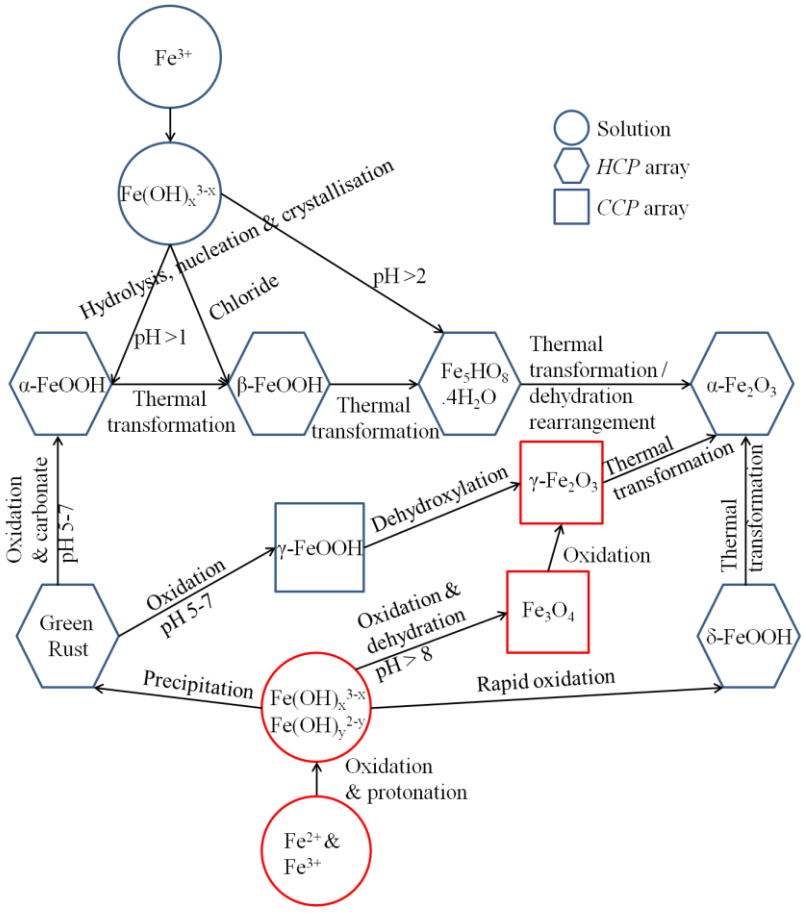

Figure 1.12. The common forms of iron oxides and hydroxides and the transformation routes between these. The phases of iron oxide focussed upon in this work are highlighted in red. Recreated from *The Iron Oxides, R. Cornell and U. Schwetmann.*[19]

1.3.1. The Spinel Phases

The structure of the spinel phases are based upon the parent spinel mineral $MgAl_2O_4$. The "normal" spinel phase consists of a *ccp* array of O^{2-} anions in which, 1/8th of the tetrahedral holes are occupied by divalent cations, A^{2+}, and ½ of the octahedral holes are occupied by the trivalent cation, B^{3+}, giving the general formula as $[A]^{(Tet)}[B]^{(Oct)}{}_2O_4$.[20] The unit cell contains eight formula units in which two sublattices of the divalent and trivalent cations are present, **fig. 1.13.**

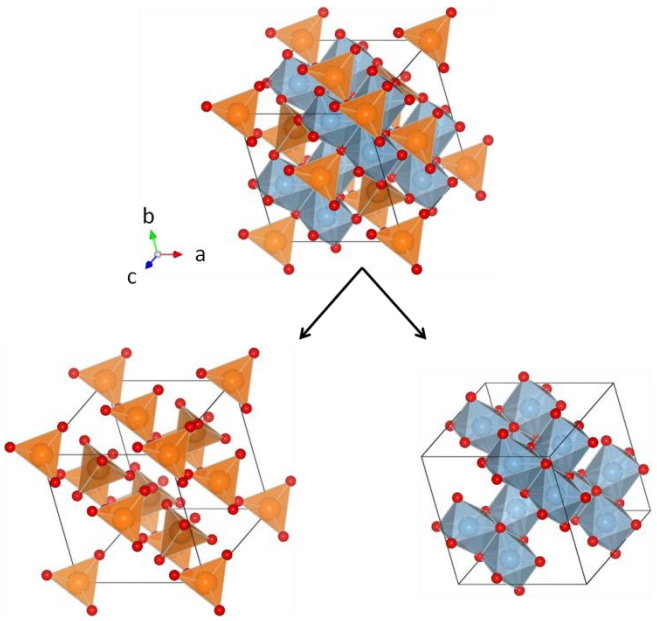

Figure 1.13. The "normal" spinel structure and its two interpenetrating sublattices, where A^{2+} (orange) occupy ½ of the tetrahedral holes, and 1/8 of the octahedral holes are occupied by the B^{3+} (grey) in the O^{2-} *ccp* array.

The A^{2+} sublattice consists of octants of an *fcc* array of O^{2-} anions. The eight tetrahedral sites are located equidistant from both the O^{2-} anions and B^{3+} cations, as cation repulsion does not allow for the occupation of neighbouring tetrahedral and octahedral holes, tetrahedral sites can only be occupied when all of the octahedral holes around it are empty, leading to two different types of octant within the A sublattice, **fig. 1.14.**[19] The B

sublattice comprises of a *ccp* array of O^{2-} anions in which alternating octahedral holes are filled with B^{3+} cations.

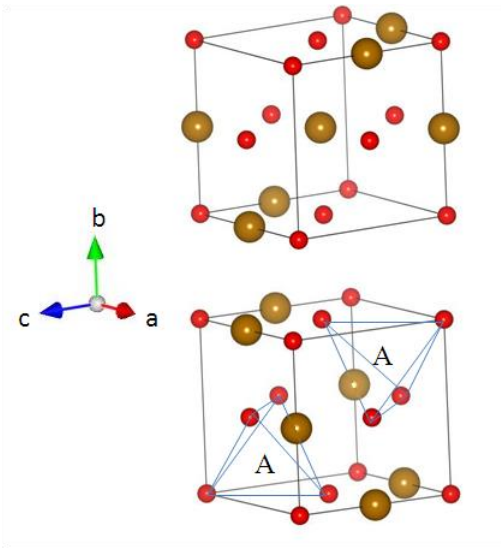

Figure 1.14. Structural representation of the two types of octant present in the A^{2+} sublattice, where the tetrahedral holes created by the *ccp* array of the O^{2-} (red) can only be occupied when its neighbouring octahedral holes are not filled by an Fe^{2+} or Fe^{3+} (brown).

In inverse spinels the A^{2+} cations, and half of the B^{3+} cations occupy ½ of octahedral holes, while $1/8^{th}$ of the tetrahedral holes are filled by the remaining B^{3+} cations, the general formula is often written as $[B^{3+}]^{Tet}[A^{2+}, B^{3+}]^{Oct}O_4$ to enable differentiation between these and the normal spinels. The distribution of the A^{2+} and B^{3+} cations is difficult to determine, and is thought to be completely disordered, **fig. 1.15.**

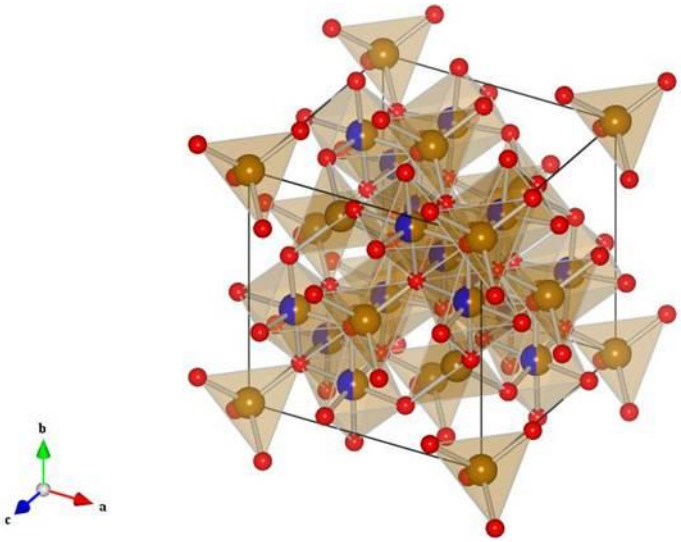

Figure 1.15. Inverse spinel structure in which the tetrahedral sites are completely occupied by B^{3+} (brown), and octahedral sites evenly distributed between the B^{3+} and A^{2+} (blue).

Often the crystal structure will be intermediate between the normal and inverse spinel phases. Where in a normal spinel the A^{2+} and B^{3+} cations exist upon the tetrahedral and octahedral, respectively, and in a an inverse spinel the tetrahedral holes are solely occupied by the B^{3+} cations, in an intermediate spinel the A^{2+} and B^{3+} occupy both the octahedral and tetrahedral holes, respectively, to some extent, for which the degree of inversion, γ, is quoted, **table 1.1.**, e.g. how many of the tetrahedral holes are occupied by the B^{3+} cations in the general formula, $[A^{2+}_{1-x,}\, B^{3+}_{y}]^{Tet}[A^{2+}_{x},\, B^{3+}_{2-y}]^{Oct}O_4$.

Type of Spinel	General Formula	Degree of Inversion, γ
Normal	$[A^{2+}]^{Tet}[B^{3+}]^{Oct}O_4$	0.00
Inverse	$[B^{3+}]^{Tet}[A^{2+},\, B^{3+}]^{Oct}O_4$	1.00
Intermediate	$[A^{2+}_{0.33,}\, B^{3+}_{0.67}]^{Tet}[A^{2+}_{0.67},\, B^{3+}_{1.33}]^{Oct}O_4$	0.67

Table 1.1. Degree of inversion for different types of spinel.

The cation distribution over the sites can be determined using crystal field stabilisation energy. This approach however is limited as it favours the inverse spinel structure and cannot be used for cations with symmetric *d*-orbital occupancy (d^0, d^5, d^{10} cations).[21] Structural sorting maps based upon crystal field theory are useful in the determination of what type of spinel structure a material may exhibit. Crystal field theory (CFT) allows computation of the preference of a transition metal to occupy an octahedral hole, based upon the arrangement of the electrons in the metals *d*-orbital.[22] Using the purely quantum mechanical values of the orbital radii for various transition metal radii in the octahedral and tetrahedral holes Burdett *et.al.*, were able to construct a structure map with a 98% success rate, of which the errors are due to poorly characterised systems, **fig. 1.16.**[22, 23]

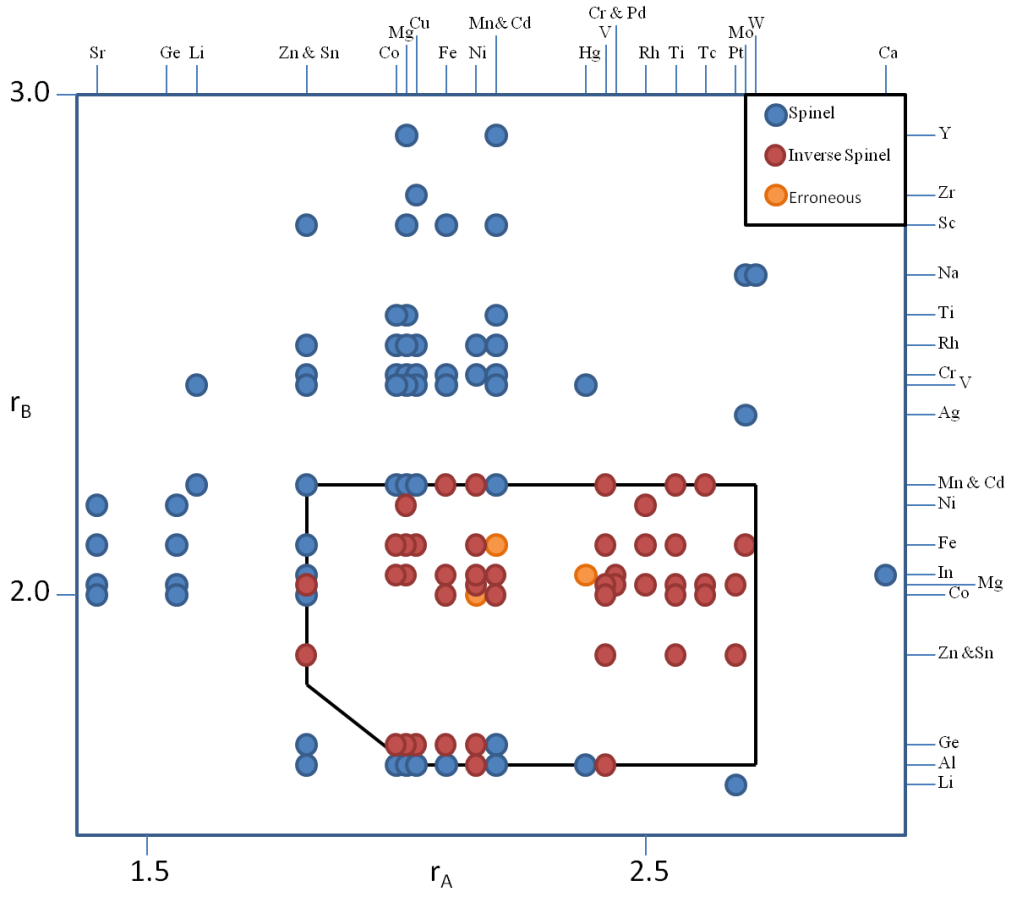

Figure 1.16. Structural map of common spinels using Burdett *et al.* method where only the purely quantum mechanical values of the orbital radii for various transition metal radii in the octahedral and tetrahedral holes are considered.[21]

1.3.2. Structure of Fe_3O_4

Fe_3O_4, magnetite, exhibits the inverse spinel structure, crystallising in the *Fd3-m* space group, with a unit cell parameter of 8.3985(5) Å.[24] The face centred cubic unit cell contains 8 formula units and is based upon a *ccp* array of O^{2-} anions.[19] Fe^{3+} occupy the 8 tetrahedral holes, and half of the octahedral holes, the remaining octahedral holes are occupied by the Fe^{2+}. The unit cell is constructed of alternating layers of edge sharing octahedral, stacked along the (111) axis, and a mixture of corner sharing tetrahedra and octahedra.

An antiferromagnetic interaction exists between the octahedral (B) and tetrahedral (A) sites due to the 127° angle between these, Fe_A-O-Fe_B, the superexchange interaction is stronger than the coupling between the octahedral sites. The spins of the Fe^{3+} upon the octahedral and tetrahedral sites are aligned antiparallel to each other and cancel, effectively leaving an overall magnetic moment of the Fe^{2+} upon the octahedral holes. The magnetic moments align along the chain of octahedral down the (111) axis, the magnetic easy axis.[19]

The interpenetrating sublattices of octahedral and tetrahedral sites within the structure of Fe_3O_4, cause it to displays ferrimagnetism, with a T_c = 850 K. Below this T_c the spins on the octahedral and tetrahedral sites are aligned completely antiparallel to each other.

For particles with diameters below d < 6 nm, superparamagnetism is exhibited at room temperature, the coercivity of which is dependent upon the nanoparticle shape, in which the coercivity increases with the amount of octahedra aligned along the [111] axis (spheres < cube < octahedral), therefore spherical shaped nanoparticles act most closely to ideal superparamagnets.

1.3.3. Structure(s) of γ-Fe_2O_3

γ-Fe_2O_3 is the oxidation product of Fe_3O_4, this oxidation results in the creation of cation vacancies due to charge compensation, maintaining charge neutrality as Fe^{2+} is oxidized to Fe^{3+}.[19] The structure consists of 8 formula units with the formula $Fe_{21⅓}□_{2⅔}O_{32}$ (where □ denotes the vacancies), the structure itself is loosely related to that of lithium ferrite, $LiFe_5O_8$, in which the cation vacancies occupy the "lithium" sites.[25] The ordering of these vacancies can make a difference to the unit cell structure. The three different ways in which the vacancies can be ordered are; (i) randomly distributed vacancies, cubic disordered phase (*Fd3-m*), (ii) partially ordered vacancies ($P4_32$ and/or $P4_12$), (iii) ordered vacancies, in which there is a threefold increase in the unit cell length along the *c*-axis ($P4_32_12$ and/or $P4_12_12$).

In the cubic disordered phase, (in which the material was originally characterised) the vacancies are predicted to be the octahedral sites, due to the preference of Fe^{3+} for the tetrahedral sites.[26] The ordering of the vacancies upon the four octahedral sites within a single unit cell is totally random, of which 2 ⅔ are vacant, e.g. in 3 unit cells there will be 9 vacancies spread over 12 possible sites, **fig.1.17.**

Refinement of neutron diffraction data of γ-Fe_2O_3, showed the presence of superlattice reflections, which suggesting some degree of ordering of the vacancies existed ((ii), partially ordered phase). The neutron diffraction pattern of Greaves showed γ-Fe_2O_3 to have an almost cubic unit cell structure ($P4_32_1$, a = 8.3396(4) Å and c = 8.3221(7) Å).[26] Investigation of the Madelung constants, suggested the vacancy distribution had a marked preference for the octahedral sites and that some long range ordering over several unit cells occurred. However, further investigation of this ordering using ^{57}Fe NMR showed a more complicated vacancy ordering involving four crystallographic sites in the $P4_32_12$ unit cell, in which the vacancies could be upon both the tetrahedral sites as well as the

octahedral. Previous XRD and Mössbauer studies had been insufficient to detect this, hence why this form is referred to as the partially ordered form.[27]

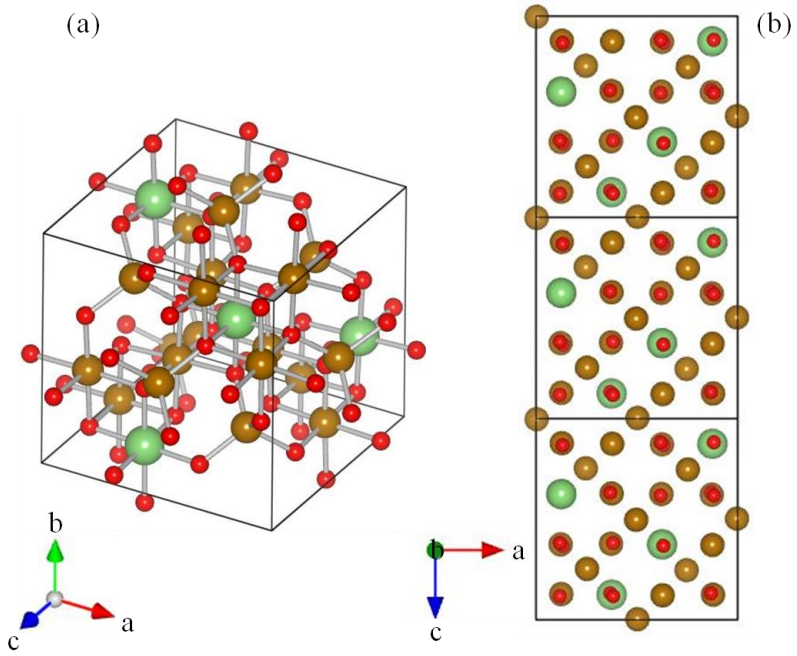

Figure 1.17. Unit cells of the vacancy disordered phase (*Fd3-m*)(a), and the vacancy ordered phase (*$P4_32_12$*), in which 9 of the 12 possible vacancy sites (green) are unoccupied, in the unit cell formed by the Fe^{3+} (brown) and O^{2-} (red).

Theoretical investigations based upon DFT calculations, revealed the most thermodynamically stable form to exist in the *$P4_12_12$* unit cell, an enantiomorphism of the *$P4_32_12$* unit cell, in which the vacancy are ordered. Within the *$P4_12_12$* structure the vacancies never occupy three consecutive possible vacancy sites, e.g. in **fig. 1.18.**, where vacancies exist upon the 1, 4, 7 and 10 layers, minimizing the Coulombic repulsion within the unit cell.[28] The *$P4_12_12$* unit cell has parameters a = 8.332 Å, c = 25.113 Å (c/a ≈ 3).[29] This phase was further detected using in-situ XRD of a hydrothermal reaction, in which the superlattice reflection were noticed, indicating a transformation in the unit cell from the *Fd3-m* unit cell to that of the *$P4_12_12$* unit cell.[28, 29]

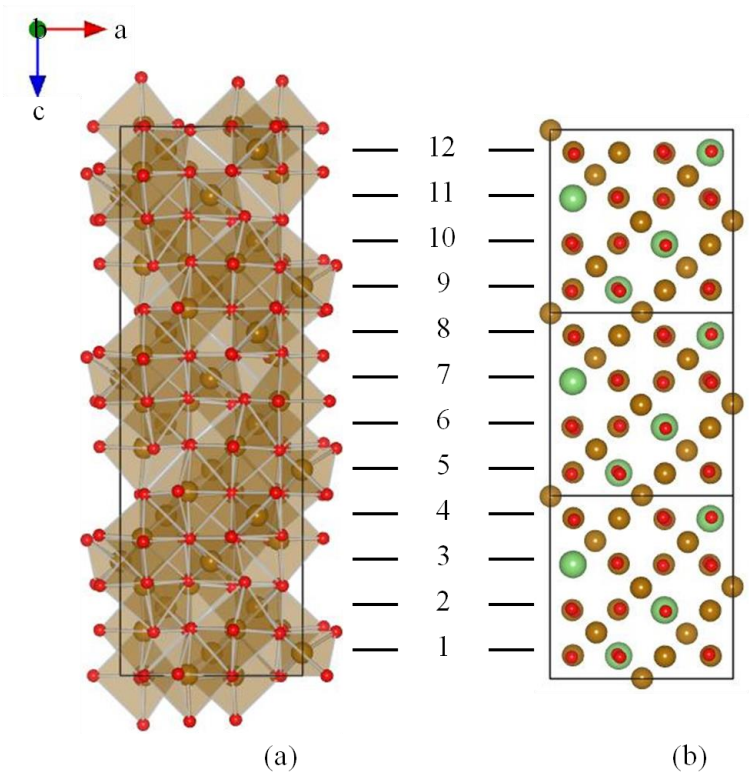

Figure 1.18. Vacancy ordered form of γ-Fe_2O_3 showing the position of the 12 possible vacancy sites (green) (b) in the unit cell formed by the Fe^{3+} (brown) and O^{2-} (red). For the most thermodynamically stable form (*$P4_12_12$*) the vacancies are present at positions 1, 4 ,7 and 10, minimizing the electrostatic repulsion from the Fe^{3+}.

The similarities between the structures of Fe_3O_4 and γ-Fe_2O_3, leads to their similar magnetic properties, making determination of the phase of spinel IONs difficult using traditional X-ray diffraction techniques. γ-Fe_2O_3 displays ferrimagnetism due to superexchange coupling between the octahedral and tetrahedral holes.[28] The Curie temperature of γ-Fe_2O_3 is estimated to be 820-986 K, the thermal instability of γ-Fe_2O_3 makes direct observation of this impossible, due to the thermal transformation between γ-Fe_2O_3 and α-Fe_2O_3.[30] However, a large difference in the saturation magnetisation between Fe_3O_4 and γ-Fe_2O_3 exists, with that of γ-Fe_2O_3 being approximately 20% lower.[19] For particles with d < 10 nm, superparamagnetism occurs at room temperature.

1.3.4. Cation Deficient Magnetite ($Fe_{3-\delta}O_4$)

The issues associated with determination of structure between the iron oxide forms in bulk are further exacerbated upon the nanoscale by cation deficient phases, $Fe_{3-\delta}O_4$. These represent a series of intermediate structures between that of Fe_3O_4 and γ-Fe_2O_3, which occur during the oxidation process. Several studies have been performed upon iron oxide nanoparticles below 20 nm, using various analysis techniques, in an attempt to decipher their structure.[31-34] A general consensuses has been drawn that δ increases in $Fe_{3-\delta}O_4$ with decreasing nanoparticle size, e.g. the amount of γ-Fe_2O_3 present in nanoparticles increases. This is believed to be due to the oxidation of Fe_3O_4 to γ-Fe_2O_3 which occurs at the surface of the nanoparticles, as decreasingly smaller particles have an increased surface area to volume ratio; this oxidation affects a greater volume of each nanoparticle.[31] In nanoparticles with diameters > 20 nm a core shell structure has been shown to be present as the Verwey transition temperature is close to that expected for bulk magnetite.[31] With further measurement of the Verwey transition temperature it was observed that nanoparticles with diameters < 20 nm to have at least 50% of their structure comprising of γ-Fe_2O_3. Further decreases in the particle size result in increasing amounts of γ-Fe_2O_3, nanoparticles smaller than 10 nm have percentages of γ-Fe_2O_3 greater than 85%.

The magnetic properties of $Fe_{3-\delta}O_4$ are dependent upon the amount of γ-Fe_2O_3 and Fe_3O_4 present within the structure. The synthesis parameters can also have a large effect upon the magnetic properties of the IONs, with an increase in base concentration and increase in temperature leading to higher saturation magnetisations.[31]

1.3.5. Structure of Transition Metal Ferrites ($TM_xFe_{3-x}O_4$)

Substitution of various transition metals into the spinel structure can have varying effects upon both the structural and magnetic properties of the material. The site preference of the transition metal will determine whether a material is normal, inverse or intermediate spinel phase, and the magnetic properties will be altered accordingly, due to the change in magnetic dipole moment on the different crystallographic sites.

1.3.5.1. Cobalt Ferrites

Cobalt Ferrite ($CoFe_2O_4$) exhibits the inverse spinel phase, in which the Co^{2+} cations reside upon the octahedral holes.[35] Bulk $CoFe_2O_4$ has a unit cell parameter a = 8.3585(8) Å, with a high blocking temperature (T_B), 267 K and reasonably high magnetic saturation, M_S = 69 emu/g. Intermediate spinels ($[Co_{1-\lambda}Fe_\lambda]_{Tet}[Co_\lambda Fe_{2-\lambda}]_{Oct}O_4$) are also common with the degree of inversion being highly dependent on the synthesis route and the particle size, with an increase in inversion being seen with increasing size. The degree of inversion is primarily measured using EXAFS and XANES spectra. In the bulk state the Co^{2+} predominantly occupies the octahedral holes γ = 80%, so that its structure is closer to that of the inverted state.[36] The degree of inversion decreases to 68 % for nanoparticles with d = 6 nm.

Cobalt substituted ferrites ($Co_xFe_{3-x}O_4$) can be formed by replacing stoichiometric amounts of Fe^{2+} with Co^{2+}. Substitution of Co into the γ-Fe_2O_3 structure leads to an increase in magnetic coercivity and blocking temperature with increasing Co content. Leaching of Co from $CoFe_2O_4$ nanoparticles in solution can also occur altering the amount of Co present leading to the formation of cobalt substituted ferrites.[37] The amount of leaching can be between 50 - 75 % of the Co content; no further leaching is seen to

occur at a Co content of ≈ 16 % ($Co_{0.16}Fe_{2.84}O_4$). The leaching effect has been seen to lead to an increase in the magnetic saturation as well as a 7.2 fold increase in the r_1 relaxation rate and a 1.2 fold increase in the r_2 relaxation rate.[37]

1.3.5.2. Manganese Substituted Ferrites

Bulk manganese ferrite ($MnFe_2O_4$) exhibits an intermediate cubic spinel structure (*Fd3-m*, a = 8.5216(1) Å).[38] A degree of inversion of 20%, $(Mn^{2+}_{0.8}Fe^{2+}_{0.2})_{Tet}(Fe^{2+}_{0.8}, Mn^{2+}_{0.2}, Fe^{3+}_{2})O_4$ is present in bulk. XANES and EXAFS spectra have been used to calculate the degree of inversion, which increases when the particle size is reduced to the nanoscale, up to 80%.[36, 39] The cause as to the degree of inversion has not yet been conclusively proven, with both nanoparticle size and manganese oxidation state thought to have an effect upon the dependence of the degree of inversion.[40, 41] An increase in the M_s is seen with increasing Mn content, while increasing Nèel temperature is noted with increasing particle size.

1.3.5.3. Zinc Substituted Ferrites

Zinc ferrite ($ZnFe_2O_4$) exhibits the normal spinel structure (*Fd3-m*, a = 8.4432(3) Å) in which the Zn^{2+} occupies the tetrahedral sites and the Fe^{3+} the octahedral sites.[42] The cation arrangement within the structure causes the compound to be antiferromagnetic, and therefore would be a poor choice for MRI contrast agents; however, partial substitution of Zn^{2+} into the structure of Fe_3O_4 causes redistribution of cations upon the octahedral and tetrahedral sites, which has been seen to be a more promising candidate for biomedical applications.[43-45]

Zn substituted IONs have been assessed as both MRI contrast agents and hyperthermia treatments. The increased magnetisation with increased zinc content leads to longer T_1 and T_2 relaxation times. [43,46] Substitution of Zn^{2+} into the structure of Fe_3O_4 ($Zn_xFe_{3-x}O_4$) causes an increase in magnetic saturation until x = 0.34, with any further increase in Zn content results in a decrease in magnetic saturation. Their use as hyperthermia agents, when a colloidal dispersion of these was created, showed the intrinsic loss power (ILP), a direct measurement of heating efficiency, to increase until x = 0.37.[47] The ILP for $Zn_{0.3}Fe_{2.7}O_4$ (2.36 nH m^2/kg) is equivalent to those of commercial ferrofluids with similar hydrodynamic diameters.

1.3.5.4. Vanadium Substituted Ferrites

Bulk vanadium ferrite (VFe_2O_4), exhibits the normal spinel type structure (*Fd3-m*, a = 8.421(2) Å).[48] Vanadium substituted Fe_3O_4 is commonly found in nature along with titanium substituted ferrites. In its simplest form vanadium substitution is thought to proceed through substitution of Fe^{3+} for V^{3+}, with the latter occupying the octahedral holes, $(Fe^{2+})_{Tet}(Fe^{3+}_{2-x},V^{3+}_x)_{Oct}O_4$.[49] Infra-red studies have shown that substitution of V^{3+} into the spinel structure of iron oxides can cause partial cation rearrangement within the structure, with V^{3+} occupying the octahedral sites within the spinel phase unit cell, however there is some rearrangement of the unit cell with Fe^{2+} occupying both octahedral and tetrahedral holes, $(Fe^{2+}_{\alpha}, Fe^{3+}_{1-\alpha})_{Tet}(Fe^{2+}_{1-\alpha}, Fe^{3+}_{1-x},V^{3+}_x)_{Oct}O_4$.[50] The insertion of V^{2+} into the structure of spinel phase iron oxide can cause further complications in cation arrangement across the octahedral sites due its oxidation at elevated temperature.[51]

The oxidation of V^{2+} and/or V^{3+} causes more complicated cation arrangements, e.g. $(Fe^{2+}_{\alpha}, Fe^{3+}_{1-\alpha})_{Tet}(Fe^{2+}_{1-\alpha-\beta}, Fe^{3+}_{1-x-\alpha-B},V^{2+}_{\beta}, V^{3+}_{x-\beta})_{Oct}O_4$, until x > 1.5, at which point the

structure reverts to the a more simple 1:1 substitution of V^{3+} for Fe^{3+}, $(Fe^{2+})_{Tet}(V^{3+}, Fe^{3+}_{2-x})O_4$.[50, 51]

1.3.5.5. Tin Substituted Ferrites

Tin substituted ferrites have been investigated for their photoconductivity. Some confusion exists in literature, between $SnFe_2O_4$ and mixtures of SnO and α-Fe_2O_3.[52-54] Substitution of Sn^{2+} into the spinel structure has been proven to be difficult as Sn^{2+} acts as a reducing agent, increasing the Fe^{2+} content within the unit cell, while it readily oxidizes to Sn^{4+}. Sn^{4+} occupies the octahedral holes exclusively due to the large ionic radius of Sn^{4+} cations, and replaces two Fe^{3+} with the resulting charge compensation occurring through the reduction of Fe^{3+} to Fe^{2+} or vacancy formation.[52-54]

1.4. Synthesis of IONs in Batch

The synthesis of iron oxide nanoparticles is one of the most investigated topics in nanoparticle synthesis, second only to that of quantum dots, with many research groups seeking control over the various parameters that affect the nanoparticles size and magnetic properties.[55-57]

The focus of this work involves synthesis of IONs through “wet” chemical bottom up approaches, of which there is much crossover between the general methods, co-precipitation, thermal degradation, and hydrothermal methods.[55]

1.4.1. Co-precipitation

Formation of iron oxide nanoparticles through co-precipitation of iron containing salts is the most common route to the synthesis of iron oxide nanoparticles, due to its simplicity. Generally it involves the precipitation of spinel phase iron oxide from the reaction of mixtures of divalent and trivalent iron salts by altering the pH, typically via the addition of a base (e.g. NaOH or TMAOH).[58, 59] The method proves highly adaptable, surface coating, and functionalisation can be achieved by addition of surface coating agents either *in situ* or after nanoparticle formation, commonly found surface coating agents include citrate, Polyethyleneglycol, dextran, and amino acids, along with other organic coatings.[60-67] Core shell nanoparticles, particularly those with silica shells, can also be formed easily though this method.[68-70]

While spherical nanoparticles are commonly formed through co-precipitation, due to the low surface energy associated with the spherical shape, the morphology of the nanoparticles can be controlled by the addition of salts or ionic surfactants, whose anions prevent the growth of the nanoparticles along specific crystallographic axes, confining their shapes to cubes or octahedra, or allow for more exotic shapes such as "microroses".[71]

1.4.2. Thermal Decomposition

Thermal decomposition reactions involve the decomposition of an iron organic complex at high temperature e.g. $Fe(oleate)_3$, $Fe(acac)_3$ dissolved in an organic solvent.[72, 73] The nanoparticles synthesised using this method are often hydrophobic, due to the organic molecules present upon their surface. The reaction can be tailored by the addition of other molecules to act as surface coating agents, and functionalise them so that they are hydrophilic.[74, 75] The best example of this type of synthesis is that performed by the group

of Qin *et al.* in which $Fe(acac)_3$ is thermally decomposed in the presence of 1-methyl-2-pyrrolidone and oleic acid to form IONs with these groups upon their surface, yielding a functionalized water soluble nanoparticle, **fig.1.19.**[76]

Morphological control is achieved through altering the organic molecules and surface coating agents concentration, and by tailoring the heating method.[77, 78] A high degree of control over cation substitution is also seen when performing these types of reactions.[79-81]

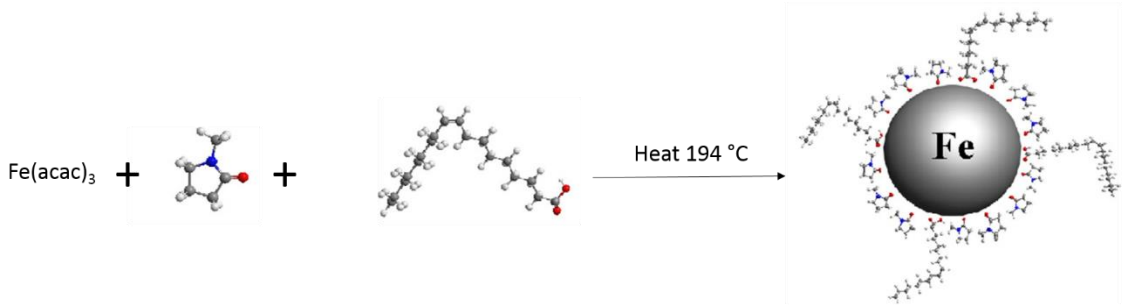

Figure 1.19. Reaction scheme for the thermal decomposition of $Fe(acac)_3$ with pyrrolidone and oleic acid to form iron oxide nanoparticles with surfaces coated in these two organic moieties.

1.4.3. Hydrothermal Synthesis

Hydrothermal syntheses of IONs often involve the reaction of divalent and trivalent salts with oxidizing reagents at high temperatures and pressures within a Teflon lined hydrothermal "bomb". Nearly all inorganic salts are soluble at high temperature and pressure and this method allows for the slow crystallization of the materials from the high temperature fluid, hence the formation of highly crystalline materials is often observed.[55] Reactions usually proceed through the formation of polymeric hydroxides which dehydrate down to the corresponding oxide material; this can lead to production of impurities and unforeseen bi-products.[82, 83, 84] The method can be adapted further so that IONs can be formed from $FeCl_3$ in the presence of reducing agents, or using seeded reactions, in which preformed nanoparticles are used to grow larger ones.[85, 86] As with the

thermal degradation of iron organic complexes hydrothermal methods lead to more precise formation of substituted ferrite nanoparticles.[87]

1.5. Microfluidics

Microfluidics and nanotechnology developed simultaneously through the 1990s, and perhaps it was inevitable that the two research fields became intertwined in the late 1990s and early 2000s. The first microfluidic system was developed in 1975 for miniaturized gas chromatography, however, a further 15 years were required before advances were made in the field enabling utilisation for more applications than just chromotography.[88] Advances were then quickly made for the use of microfluidic systems in separation,[89, 90] pumping, and mixing,[91] before more advanced techniques were adapted for DNA amplification,[92, 93] cytometry,[94] and finally chemical synthesis using microreactors.[95, 96] Micro-total analysis systems (μTAS) or lab-on-a-chip devices were originally inspired integrate two or more of these process into a single microfluidic system allowing for on-line processing and analysis.

The review of the microfluidics field by Whitesides in 2006 highlighted the increased needs of the field to become more than just one of proof of concept techniques, and push forward for more general use especially in industry.[97] Commonly the syntheses of organic and organometallic compounds are performed due as the products are generally liquids or polymers; it was not until the early 2000s that nanoparticles were first produced using microreactors, with the synthesis of quantum dots.[98-100]

1.5.1. Synthesis in Microreactors

Conceptually reactions within microreactors proceed through the controlled diffusion of reagents into each other. Several parameters need to be considered though in how the reagents are pumped through the system, their mixing, and control over the reaction conditions; within the microchannel itself as these can all be seen to have effects upon nanoparticles and their related physical properties.[98, 100, 101]

1.5.2. Pumping Mechanisms

Pumping mechanisms fall into two categories those in which mechanical pumping is utilised, or where electro-osmotic flow (EOF) is employed.

Mechanical pumping is commonly achieved through the use of syringe pumps, which enable the use of stable bidirectional flows. Mechanical pumping is based upon the movement of fluid impermeable membrane, which can be used to "push" the fluid through the microchannel, resulting in a pulsed fluid movement of discrete aliquots.[102] As the fluid is moved mechanically its movement is independent of its nature and any fluid can be pumped in this way. Viscous drag occurs near the surface of the microchannel walls causing the fluid to move at different rates throughout the microchannel, so that the fluid is moving at a higher velocity near the microchannels centre in comparison to at the edge, **fig. 1.20.a.**, which can cause problems in size reproducibility in nanoparticles synthesis. As this method relies on moving parts, it can be susceptible to blocking by particulates depending upon the size of the microchannel, particularly any valves used, and the component wear can be a problem at high flow rates lowering the lifetime of the equipment.

Figure 1.20. Velocity profile of fluids pumped through a microchannel mechanically causing a curved flow profile with fluids flowing faster at the centre of the microchannel due to shear forces near the microchannel walls (a) and electrokinetically which causes a flat fluid velocity profile (b).

Non-mechanical pumping in the form of electrokinetic flow, and its two component effects of electrosmotic and electrophoretic flow, involve the direct energy transfer between an applied potential difference and the fluid, so that no pulsing of the fluid occurs and a flat velocity profile occurs across the microchannel.[102] Electrosmotic flow (EOF) occurs due to the movement of the electric double layer of ionic charges near the surface of the microchannel walls. A negatively charged surface (e.g. glass) is neutralised by positive ions in the solvent, some are adsorbed onto the surface while some remain in the transient fluid layer, **fig. 1.21.** Application of a potential difference parallel to the microchannel causes movement of the positive charges in the transient layer and solvent toward the negative electrode, resulting in a bulk movement of the fluid through the microchannel, with the exception of those charges adsorbed to the microchannel surface.[88]

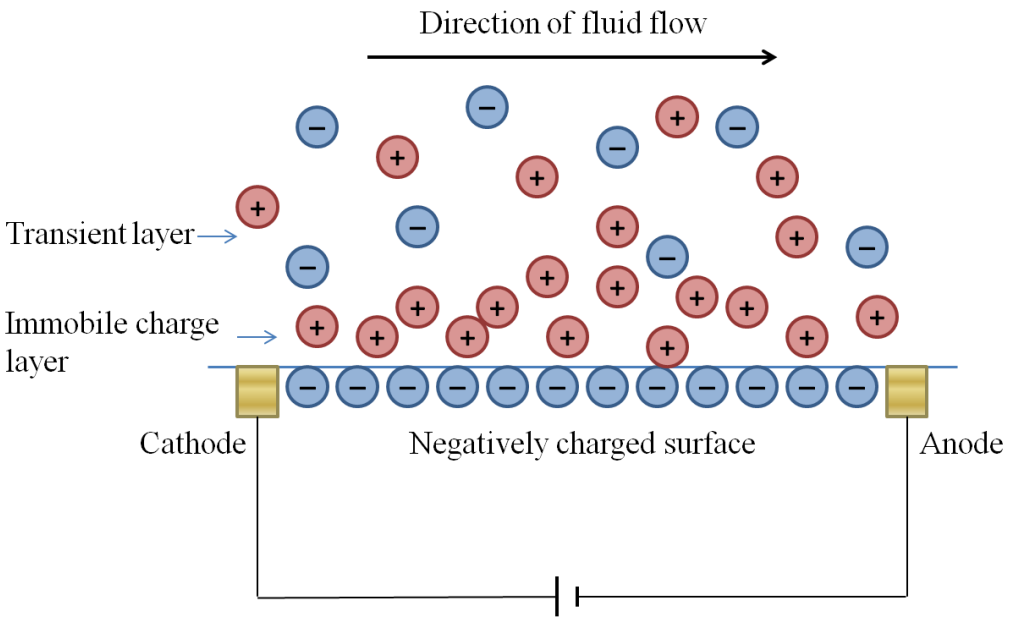

Figure 1.21. Electroosmotic flow in a microchannel, after application of an electric field where negatively charged ions will move toward the cathode and positive toward the anode, and by pulsing the potential difference across several anodes and cathodes, movement of a transient layer of charge can be created.

The electric field, *E*, and fluid velocity, v_{eof}, are proportional, **eq. 1.14.**

Equation 1.14.

$$0 = -\Delta p + \mu \Delta v_{eof} + p_e E$$

Where, *p* is the pressure, μ the fluid viscosity, ρ_e the charge density.

A flat velocity profile is created across the microchannel as the entire fluid volume is exposed to the same voltage, **fig. 1.20b.** While the velocity of the fluid is not dependent upon the cross-sectional area, *A*, of the microchannel the volumetric flow rate, *V*, of the fluid is, **eq. 1.15.**

Equation 1.15.

$$V = v_{eof} \times A$$

The application of an electric field parallel to the microchannel causes the movement of the solvent and all of the molecules within it, however, a second force is applied to the

solution causing further movement of ions within the solution, electrophoretic flow (EPF), which causes cations to be attracted to the anode and anions to the cathode, when an electric field is applied, **fig. 1.22.**

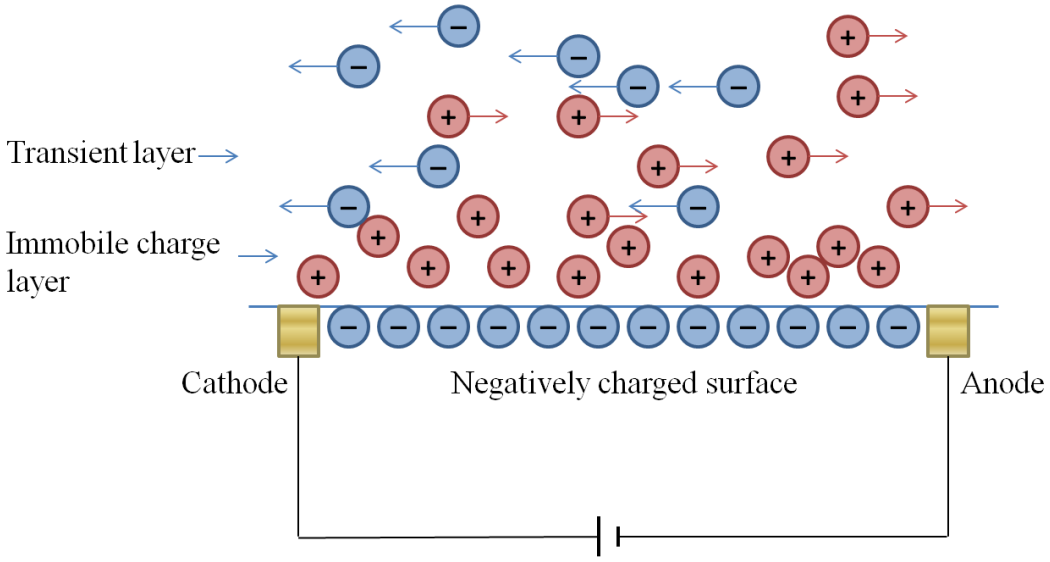

Figure 1.22. Electrophoretic flow in a microchannel, after application of an electric field, where the potential difference is strong enough to cause separation of the positive and negative charges which move toward the anode and cathode respectively.

As the anode is deployed "downstream" cations are accelerated through the microchannel (+ EPF) while anions are retarded (– EPF), the magnitude of this increase in velocity is dependent upon the ions charge to mass ratio, with smaller highly charged ions moving faster than larger weakly charged ones, **eq. 1.16.**

Equation 1.16.

$$v_{epf} = \frac{Z_e E D}{K T}$$

Where, v_{epf} is the velocity of the electrophoretic flow, Z_e the charge number of the ion, D the molecules diffusion coefficient, K the Boltzman constant, and T, temperature.

If the EPF is greater than EOF then the ions will actually move toward the electrodes, which is the basis of separation of molecules in μTAS systems. The total velocity (v_{tot}) of

the flow system is dependent upon both the velocity of the electrosmotic and electrophoretic flows, as well as the strength of the applied field, **eq. 1.17.**

Equation 1.17.

$$v_{tot} = (v_{eof} + v_{epf})E$$

1.5.3. Mixing of Fluids in Microchannels

The mixing of reagents within microchannels is primarily dependent upon the type of flow present within the microchannel, under laminar flow conditions mixing increases with time as it occurs via diffusion, while in turbulent flow conditions mixing of reagents happens over a short time scale as it would in batch. Transport times for mass and heat across a microchannel are short and highly controllable due to the small scale of the systems, with both being dependent upon molecular diffusion.[88] Control of molecular diffusion is achieved by manipulation of scaling phenomena, particularly Laminar flow, in which the viscous forces become predominant on such small scales. Characterization of the type of flow can be made by calculation of the dimensionless Reynolds number, *Re*, **eq. 1.18.**

Equation 1.18.

$$Re = \frac{Ul}{v}$$

Reynolds number, *Re*, characterises the type of flow in terms of its velocity, *U*, and its kinetmatic viscosity, *v*, in a system of scale, *l*.[88] In more practical terms the Reynolds number can be calculated using the fluid density, *ρ*, and the microchannel dimensions, **eq. 1.19.**, in the case of a circular microchannel its diameter, *d*.

Equation 1.19.

$$Re = \frac{\rho Ud}{v}$$

For *Re* > 2000, turbulent flow is present and mixing of reagents occurs chaotically, typical of a batch reaction. Laminar flow is present at *Re* < 10, at which point multiple flows will form lamellae, which slip past each other without areas of turbulence or eddy currents being present, **fig. 1.23.**, mixing of the streams occurs via diffusion across the microchannel, **fig. 1.3.** For 10 < *Re* < 2000 is an area of transient flow in which lamellae are present but also are small areas of transient flow in which lamellae are present but also are small areas of turbulence, with mixing occurring through diffusion and chaotically.

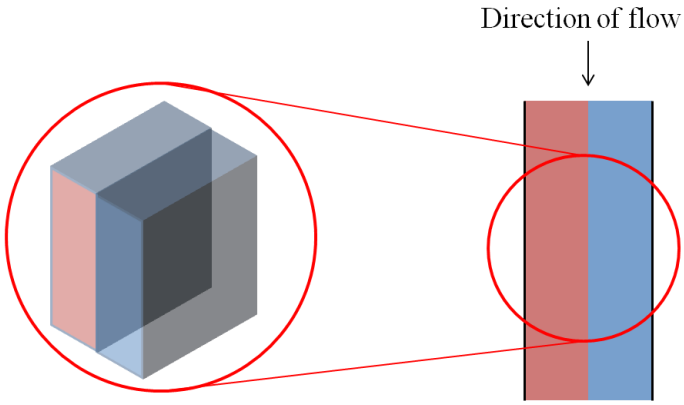

Figure 1.23. Fluid flows moving through a microchannel under laminar flow conditions, where no chaotic mixing of the fluids occur the lamaellae effectively slide past each other.

As diffusion is a predictable phenomenon the time taken for reagents to mix is calculable under laminar flow conditions, **eq. 1.20.**, where the time, *t*, required for an ion to diffuse across a microchannel, calculated from its molecular diffusion coefficient, *D*, and the diameter of the microchannel, *d*.

Equation 1.20.

$$t = \frac{d^2}{2D}$$

The diffusion times of small molecules or ions across microchannels, are usually below a few seconds, for larger molecules such as proteins this can take as long as a few minutes.

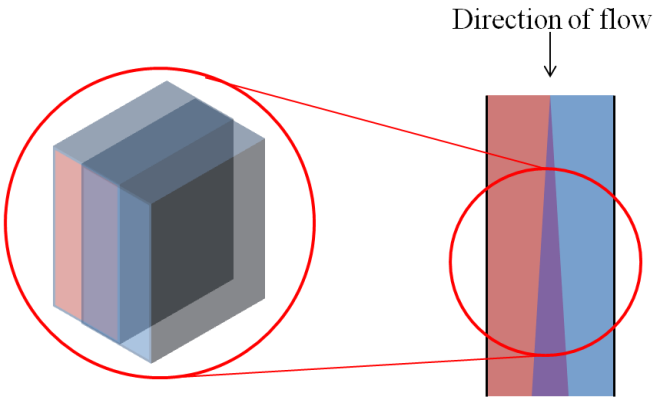

Figure 1.24. Diffusion of reagents under laminar flow conditions within a microchannel, where diffusion occurs slowly across the microchannel over time.

As a general rule exists in which the smaller and more highly charged an ion the quicker it diffuses, nanoparticles which are far larger than charged ions, and the charge upon these is more diffused across the particles volume, the nanoparticles diffuse at a much slower rate.[103]

1.5.4. Droplets in Microchannels

Droplet microfluidics involves the encapsulation of fluid droplets within another fluid, e.g. water in oil. In terms of synthesis it can be used to access much higher temperatures than continuous flow techniques and has been widely utilised for the synthesis of quantum dots, which require higher degrees of crystallinity.[104]

Formation of droplets within a biphasic fluid flow can be very complicated; the interfaces are often affected by the force imposed by the fluid velocity, U, of the liquid, its dynamic viscosity, μ, and the interfacial tension, γ, and capillary number, Ca, of the microchannel, **eq. 3.1.**

Equation 3.1.

$$Ca = \frac{\mu U}{\gamma}$$

For small values of capillary number, capillarity dominates causing spherical droplets of the reagent phase, which can be carried without deformation through the microreactor by the carrier phase, **fig. 1.25.** At larger values of capillary number viscous forces dominate, affecting the droplets morphology, aligning the fluid interfaces along stream lines in the direction of the microchannel, **fig. 1.26.**

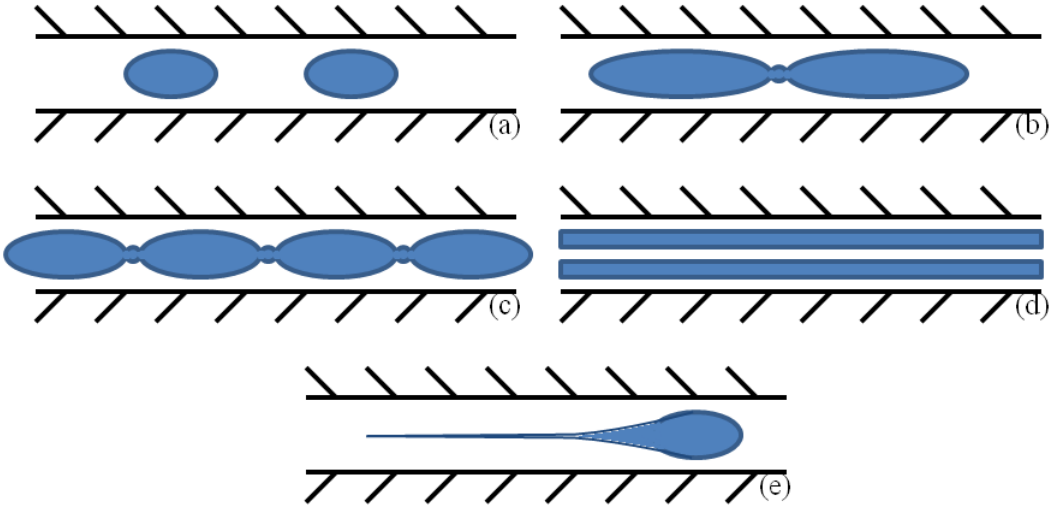

Figure 1.25. Organised flow regimes of two immiscible flows within a microchannel. When the flow rate of the carrier phase is high then the aqueous phase low, isolated droplets occur (a), as the carrier phase flow rate is decreased and the aqueous phase flow rate kept low these droplet coalesce creating pearl necklace (b) and coalesced regimes (c). When both flow rates are high the stratified regime is present (d). If the aqueous phase flow rate is the increased pear shaped droplets occur (e).

The presence of a surfactant lowers the interfacial tension, leading to the formation of well-defined regimes in the shape of droplets, pears (a pear shaped droplet with a long streamlined tail) and various forms of coalesced streams; allowing for droplets to be transported without contacting the microreactor surface. The absence of a surfactant favours less organised regimes, in which partial wetting often occurs.[88]

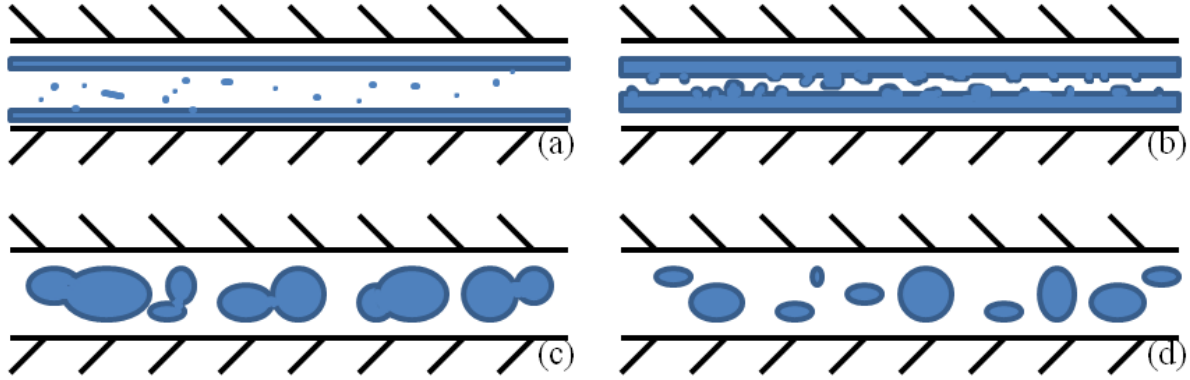

Figure 1.26. Disorganized flow regimes of two flow immiscible flows within a microchannel. As the flow rate of the oil flow is increased stratified regimes such as (a) & (b) are present. If the flow rate of the water phase is increased then the flows become less stratified and more droplet based, although droplet size and coalescence prove difficult to control, (c) & (d).[88]

Depending upon the application oil in water (O/W) or water in oil (W/O) systems can be created by controlling the surface coating of the microchannels, **fig. 1.27.** Hydrophobic surfaces will create W/O systems with the aqueous droplets containing the reagents and the oil acting as the carrier phase, often used for the synthesis of inorganic nanoparticles.

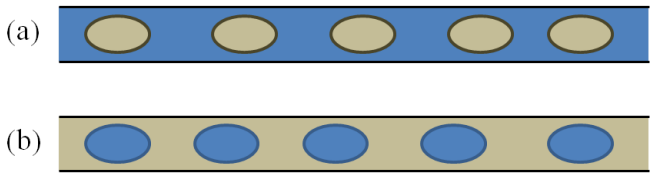

Figure 1.27. Droplets in different microfluidic channels, where (a) is a hydrophilic channel as such the aqueous phase (blue) preferentially wets the microchannel walls, creating oil droplets, and (b) where the hydrophobic microchannel walls create aqueous droplets.

The size of the droplets is controllable through the flow rate of the reagents. In a W/O system the droplet size increases with the "water fraction" which is dependent upon the flow rate, *Q*, of the aqueous reagents, **eq. 1.21.**

Equation 1.21.

$$Water\ Fraction = \frac{Q_w}{Q_w + Q_o}$$

With a larger water fraction the droplet size is seen to increase, **fig. 1.28.**[105] Thus through controlling the flow rate of the reagents, a finite degree of control of the volume and concentration of reagents within a single droplet can be obtained, key to nanoparticle synthesis.

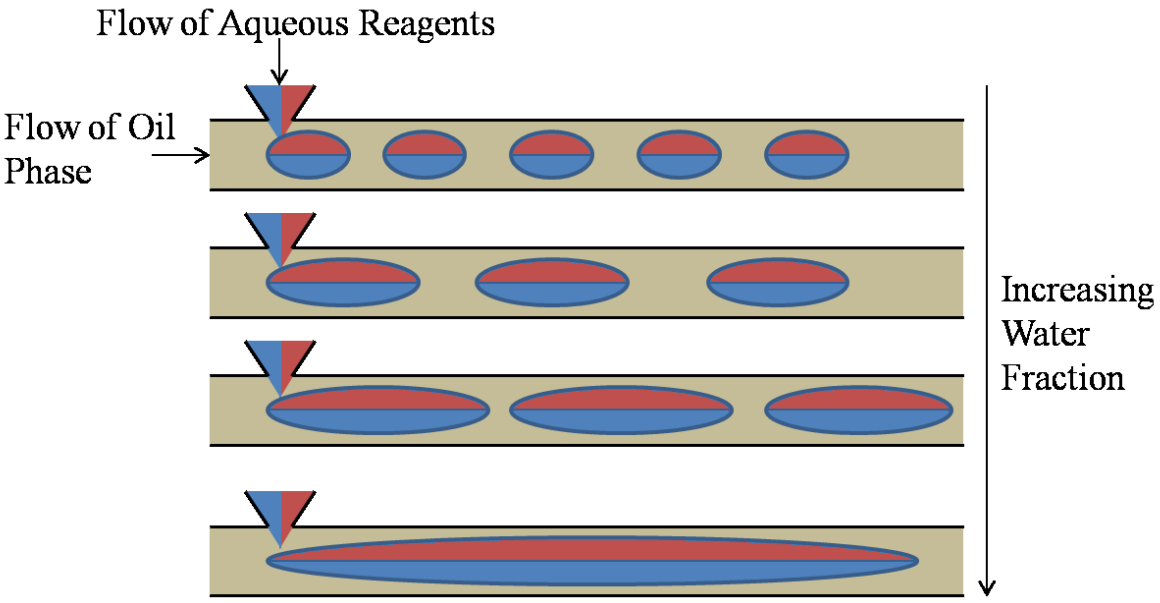

Figure 1.28. Synthesis of larger aqueous droplets occurs with increasing water fraction, as a greater volume of the aqueous phases are introduced into the carrier stream.

For reactions to occur droplets are merged, often with multiple sets of reagents in each. There are two methods for the merging of droplets, relying upon either a tailored microchannel design, in which one droplet is often forced to slow down and merge with the other, by altering the width of the microchannel and therefore the velocity of the droplet, **fig. 1.27a.** The size and frequency of droplet generation are important, as both can affect the flow rate of the oil and water phases, and therefore the droplet velocity.[106] The second method of formation is electrocoalescence, where an electric field is applied

perpendicular to the microchannel causing droplets with opposite charges to be created, which are attracted toward each other, and coalesce upon contact, **fig 1.26b.**[107]

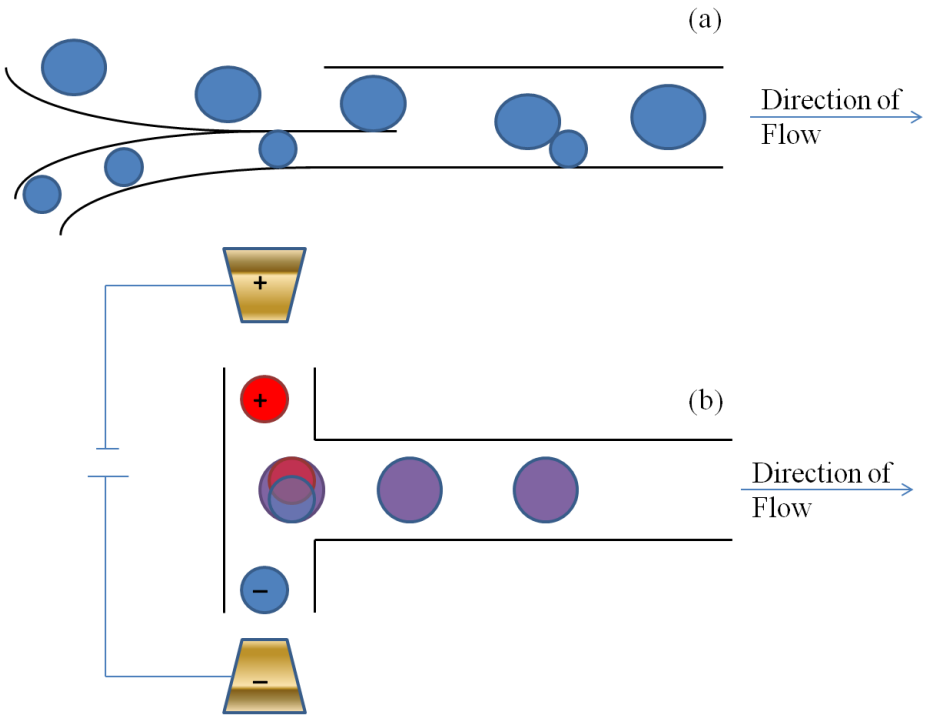

Figure 1.27. Coalescence of droplets in a microchannel, through altering the width of the microchannel, altering the flow rates and causing droplets to collide (a), and through electrocoalescence where positively and negatively charged droplets are created by application of a potential difference, the resulting electrostatic charge cause the droplets to be attracted to each other and collide (b).

Stable droplet formation is often a complicated process, a good example of which is the work of Frenz *et al.* who have used an intricately designed system of hydrodynamically coupled nozzles to produce alternating droplets of an aqueous phase in an oil phase that occur due to the changes in flow rate during droplet detachment. Pairs of aqueous droplets were formed from this process with the volume of each controlled and stabilised by use of a surfactant, limiting uncontrolled coalescence of droplets, so that over 99% of the droplets were paired accurately.[108]

After formation of droplets within the microchannel, mixing of the reagents occurs through diffusion as, recirculation of the fluids within the droplet occurs due to the viscous drag applied upon the area of the droplet closest to the microreactor walls. This recirculation and diffusion of reagents within the droplet leads to mixing in a straight or serpentine microchannel, however, the rate of mixing can be increased by the creation of chaotic advection. To do this droplets are accelerated through tightly winding section of microchannel or "switchbacks", **fig. 1.28.** As a droplet proceeds through a tightly winding section of microchannel, the fluid lamellae within the droplet become stretched and folded back upon themselves. This quickly leads to the production of many smaller lamellae of which diffusion of reagents between these occurs at a greater rate due to the much smaller diffusion distance.[109]

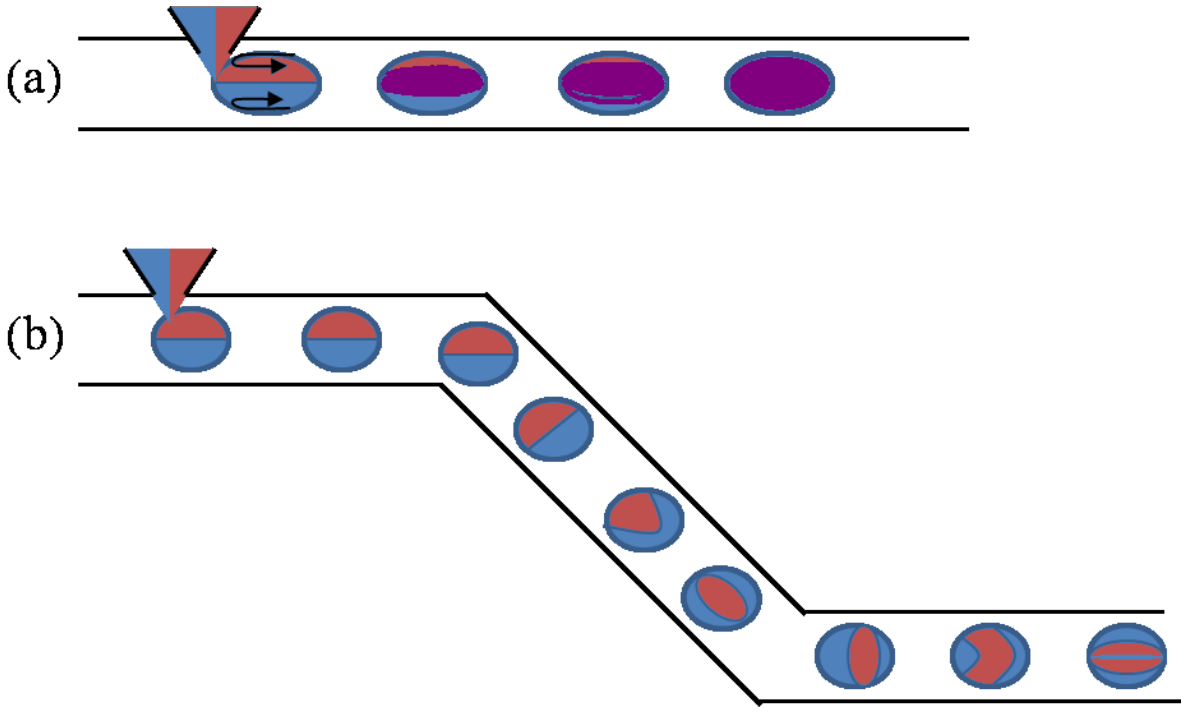

Figure 1.28. Droplet mixing by recirculating current (a), and chaotic advection induced by switchback, where the fluid lamellae within the droplets are constantly folded back upon themselves allowing diffusion to occur over much smaller distances (b).

Micromixers can also be used to accelerate the mixing process, and while common for organic liquid based syntheses, but are less common for nanoparticles syntheses, due to the synthesis of solid particulates.[98, 110, 111] In this work only the use of controlled diffusive mixing under laminar flow conditions and the use of droplets as "small reactors" was considered viable, due to the constraint upon microreactor design.

1.6. Synthesis of Iron Oxide Nanoparticles using Microreactors

In comparison to the vast amount of synthesis techniques for IONs in batch, little research has been performed into their synthesis using microreactors despite the advantages that microfluidics offers in terms of control of size and continuous production.[98, 112]

The earliest reported synthesis of IONs in microreactors involved the synthesis of α-Fe_2O_3 nanoparticles in a flow based tubular reactor, from the thermal degradation of ferric nitrate nonahydrate (1.00 M), in formamide.[113] This was performed using a simple capillary tube design, where a tightly wound glass capillary tube (1.0 m length, internal diameter, *id* = 0.32 mm, reactor volume = 320 ml) was immersed in an oil bath and heated at 150 °C, so as to cause the degradation of the $Fe(NO_3)_3.9H_2O$, as it was fed through the capillary tube using a syringe pump. By altering the internal diameter of the capillary tube (*id* = 0.32 - 0.53 mm, reactor volume = 320 – 530 ml), the nanoparticle size could be altered to give nanoparticles with sizes between 10 - 60 nm. The shape and percentage yield could also be controlled by selection of the capillary tubes surface coating and internal diameter. The morphology and size of nanoparticles could also be controlled, those produced using a glass capillary tube coated in TMS, showed a rod-like morphology (*l* = 20 nm, *id* = 3 nm).

Droplet-based microreactor techniques for the synthesis of IONs were first reported in 2008. Frenz *et.al.* to developed an approach for the synthesis of aqueous droplets of

reagents within an immiscible carrier phase, using two spatially separated but hydrodynamically coupled nozzles.[108] As an aqueous droplet forms at the nozzle of the first channel, an increase in the oil flow is created through the second nozzle. After release of the droplet the oil flow switches to the first channel allowing for an aqueous droplet to form at the second, **fig. 1.29.**

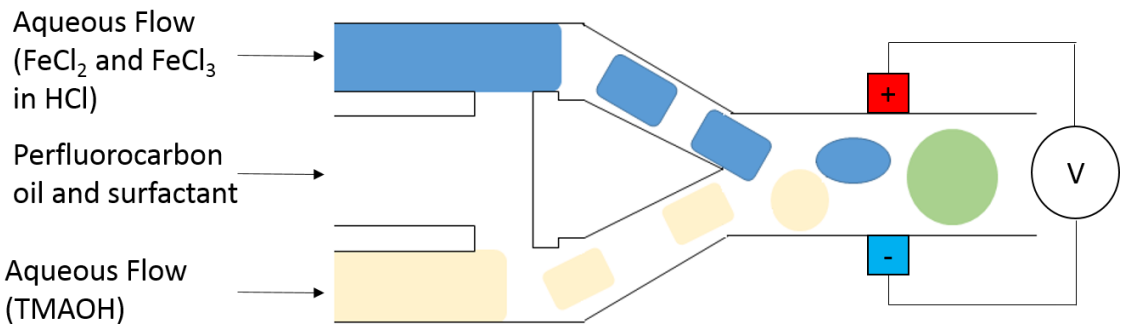

Figure 1.29. Schematic diagram of the hydrodynamically coupled droplet generation module used by Frenz *et al.* to synthesise pairs of droplets containing the aqueous reagents which are then electrocoalesced further down the droplet.

The alternating oil flow between the two nozzles allows for one to one droplet pairing at any flow rate ratio, with 99.99 % accuracy. The droplet pairs are coalesced further into the microreactor using electrocoalescence, with the electrical current provided by two on chip electrodes, the dynamic rupturing of the interface between the two droplets as they coalesce helps to increase the mixing of reagents within the new droplet. The two aqueous droplets contained a mixture of ferric and ferrous chloride (0.48 M and 0.24 M, respectively), and ammonium hydroxide (28 V/V%), stabilised using a surfactant within a perfluorocarbon oil carrier phase. As the reactor has a total volume of the droplet based approach allowed for the production of nanoparticles without the fouling (nanoparticle build up upon the microreactor walls) of the microreactor. The nanoparticles produced using this technique had a spherical morphology with diameters smaller than those

produced using the same reagents in bulk, 4 ± 1 nm and 9 ± 3 nm, respectively. From electron diffraction patterns the phase of the nanoparticles was determined to be spinel phase iron oxide, although no judgement on whether this was Fe_3O_4 or γ-Fe_2O_3 was made, and showed superparamagnetism.

The droplet coalescence method was also adopted by Kumar *et. al.* for the direct synthesis of dextran coated IONs.[114] Unlike the work of Frenz *et. al.* which used a complicated hydrodynamic coupled nozzle design, Kumar *et. al.* used a more passive mode of droplet formation, in which a piece of silicone tubing (*id* = 1 mm) was used along with two glass filament capillaries (*id* = 150 μm) placed at 90˚ to each other, so the outlets of each met at the centre of the silicone tube, **fig. 1.30.**[108, 115]

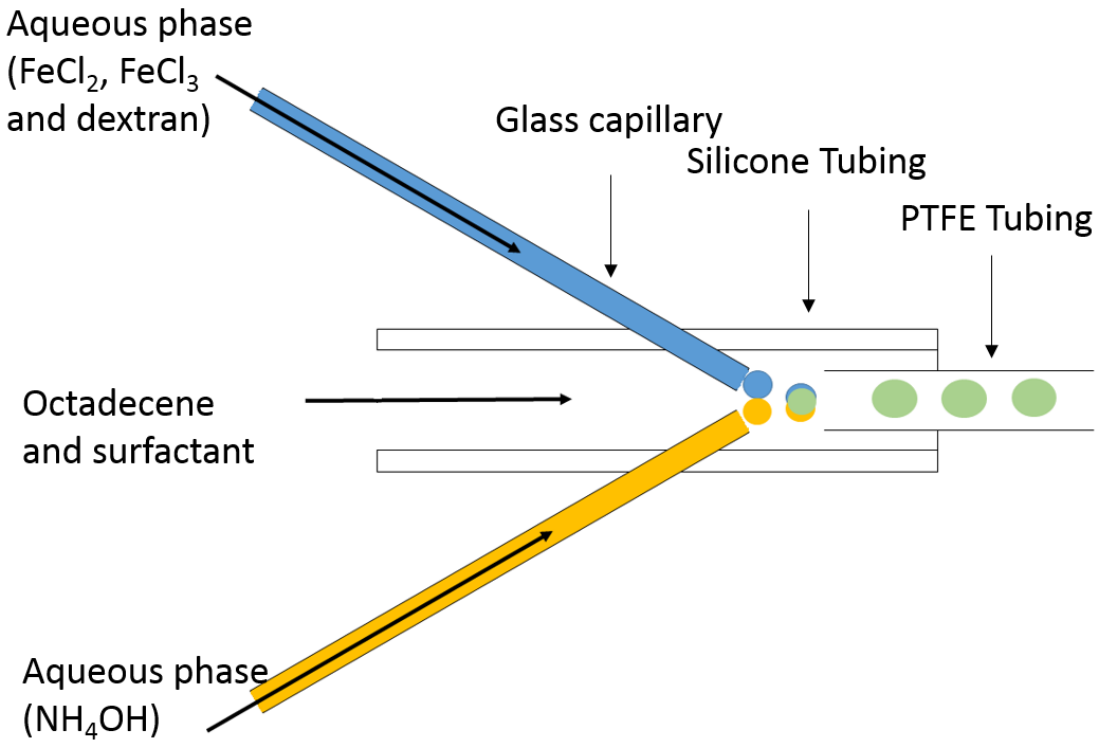

Figure 1.30. Schematic diagram droplet generation module used by Kumar *et al.* where the aqueous droplets are both generated and merged simultaneously in the carrier phase before being carried through a length of tubing in an oil bath to increase nanoparticle crystallinity in the droplets.

The aqueous reagents, ferrous and ferric chloride with dextran (0.02, 0.04, and 0.05 M, respectively) and ammonium hydroxide (28 %V/V) were introduced into the octadecene carrier phase (600 μl min^{-1}) simultaneously using syringe pumps (67 μl min^{-1}, and 133 μl min^{-1}, respectively). A droplet of the merged reagents was formed at the meeting point between the two aqueous inlets, before being stretched and detached by the axial force of the carrier fluid. The detached droplets were then transported through a PTFE capillary (length = 4 m, *id* = 0.82 mm) into a heating stage (60 °C) so as to aid crystallisation. No fouling of the system was noted with the nanoparticles remaining compartmentalised for the length of the reactor (reactor volume 4.14 ml, residence time of 5.18 mins). The nanoparticles produced were roughly spherical in morphology with diameters of 3.6 ± 0.8 nm. A combination of energy dispersive X-ray spectroscopy (EDX) and Selected Area Electron Diffraction (SAED) measurements characterised the nanoparticles as spinel phase iron oxide, unlike in the work of Frenz *et.al.* the group acknowledged that they could not determine which of the two phases of iron oxide were present.[108] FTIR spectroscopy, was used to characterise the dextran coating of the nanoparticles, and it is likely that the next step will be the automation of this synthesis.[116] Further to this the nanoparticles magnetic properties were characterised, finding them to be superaparamagnetic with high magnetic saturation (58 emu/g), and favourable relaxivities 66 ± 1 mm/s.

Simultaneous development of the co-axial flow technique occurred, alongside that of droplet coalescence. Abou -Hassan *et.al.* developed a simple ad-hoc co-axial flow microreactor for the synthesis of IONs in late 2007.[102] Co-axial flow techniques rely upon diffusion of flows of miscible reagents into one another under laminar flow conditions; they overcome the problem of microreactor fouling due to by completely encapsulating one flow of reagents within the other, producing nanoparticles at the interface between the two, **fig. 1.31.**

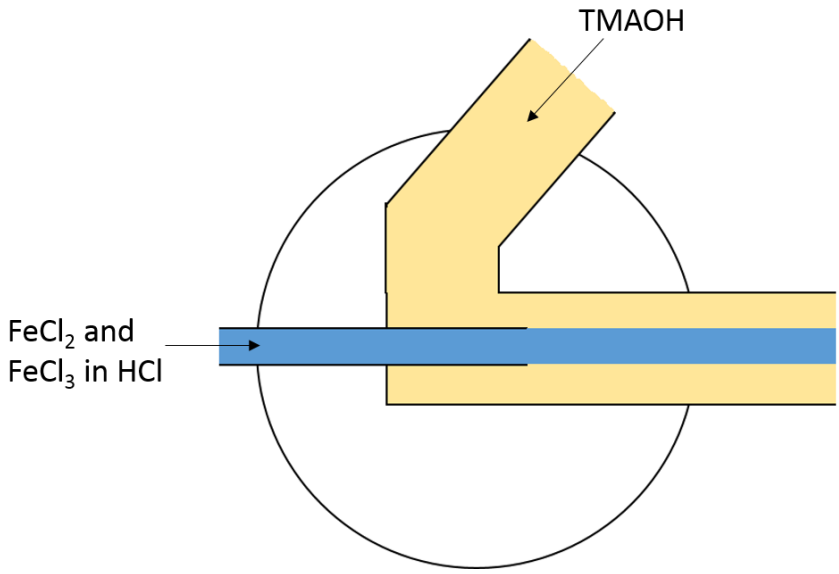

Figure 1.31. Schematic diagram of the co-axial flow module used by Abou-hassan *et al.* where a central flow is directly into the centre of another causing it to be totally encapsulated b the outer flow.

To do this a coaxial flow device was moulded into a Petri dish using polydimethylsiloxane, an outer capillary (*id* = 1.7 mm) was first moulded into the resin, the central capillary (glass, *id* = 150 µm) was then inserted into the outer capillary using a micropipette tip so as to allow for precise centering of one flow within the other (reactor volume = 322.48 µl). A solution of ferrous and ferric chloride (total concentration = 1 x 10^{-2} M) was pumped through the central capillary inlet, simultaneously with a flow of tetramethylammonium hydroxide (TMAOH, 0.172 M). The flow rates of the inner flow was adjusted between 10–100 µl min^{-1}, while the outer flow rate was kept constant at 400 µl min^{-1}, to avoid turbulence at the point of confluence, leading to residence times of between 10 to 48 seconds. Under these conditions both flows were subject to laminar flow as the reaction proceeded by diffusion of the OH^- from the outer flow into the central flow, due to its shorter diffusion time than those of Fe^{2+} or Fe^{3+}.[117] The excess of TMAOH allows for the dispersion of forming nanoparticles without their contacting the microreactor walls, preventing fouling. The reaction was then quenched by fast solvent extraction, into cyclohexane using a cationic surfactant, allowing for the collection of a

colloidal suspension of IONs. The nanoparticles were characterised with dynamic light scattering and TEM to calculate their hydrodynamic and physical diameters, 160 nm and 7 nm, respectively. EDX was again used to confirm the spinel phase of iron oxide, but as with the work of Frenz *et. al.* no assertion as to whether this was γ-Fe_2O_3 or Fe_3O_4 was made.[108] The nanoparticles were shown to be superparamagnetic.

The co-axial flow technique proved to be very adaptable, follow up work saw the use of multiple co-axial flow microreactors used to graft silica shells upon the nanoparticles, performed through several intermediary steps all requiring an individual microreactor.[118] The drawback, however, was the need to first take the stable colloidal solution of nanoparticles previously prepared and dilute it before using this in the multistep synthesis. The nanoparticular suspension was taken and (3-aminopropyl)triethoxysilane (APTES) grafted to the surface citrate groups after activation with *N*-(3-Dimethylaminopropyl)-*N′*-ethylcarbodiimide (EDC) and *N*-Hydroxy succinimide (NHS). The grafted APTES was then reacted with a mixture of tetraethylorthosilicate (TEOS) and rhodamine B labelled APTES, to synthesise a silica shell with embedded fluorescent nanoparticles. The core/shell nanoparticles synthesised were roughly spherical with a diameter of 50 nm. The idea of creating multi-structured nanoparticles has also been taken further in creating a theranostic agent by embedding both the magnetic nanoparticles and gold nanoparticles within a silica shell, to act as the diagnostic and therapeutic parts of the theranostic agent respectively.[119] The system has been further utilised to produce various other mineral forms of iron oxides, e.g. goethite (α-FeOOH) by separating the nucleation and growth of the nanoparticles.[120] As well as the synthesis of cobalt ferrite ($CoFe_2O_4$), which to the best of the authors knowledge the only synthesis of any type of transition metal ferrite, other than Fe_3O_4, synthesised using microreactor technology to date.[121] These nanoparticles were produced with a faceted morphology with a length of 7.4 ± 3.5 nm, and found to be magnetically "hard", displaying large values of coercivity and remanence,

making them more suitable for magnetic data storage than as superparamagnetic contrast agents.

2.0. Experimental

2.1. Synthesis of Nanoparticles in Batch

In order to provide a comparison to microfluidics results, experiments were also conducted in batch reactions. Nanoparticle synthesis was achieved in batch via a co-precipitation reaction of stoichiometric concentrations of divalent and trivalent metal salts with an excess of concentrated base, **eq. 2.1.**

Equation 2.1.

$$Fe^{2+} + 2Fe^{3+} + 8OH^{-} \rightarrow Fe_3O_4 + 4H_2O$$

Equal volumes of $FeCl_2.6H_2O$ (0.01 mol dm^{-3}) in HCl (1.10 mol dm^{-3}) and $FeCl_3$ (0.02 mol dm^{-3}) in HCl (1.10 mol dm^{-3}) were mixed at 500 rpm using a magnetic stirrer, for 30 minutes under a nitrogen atmosphere. Precipitation was induced by addition of twice the volume of NaOH solution (1.00 mol dm^{-3}). Oxidation of Fe^{2+} cations, was inhibited by the presence of HCl.[102] Any atmospheric oxidation was further prevented, by deoxygenating all solutions prior to their use by bubbling nitrogen through them for 1 hour. By preventing oxidation Fe_3O_4 could be formed. If as in later experiments γ-Fe_2O_3 was the target structure Fe_3O_4 must first be formed before oxidation to this occurs. A reflux condenser was attached when temperatures higher than 25°C were used, to prevent solvent evaporation, as solvent evaporation within the microreactor would be impossible, as the system is pressurised. Any magnetic precipitate synthesised was separated from the supernatant via magnetic decantation, where a large neodymium bar magnetic was used to collect any magnetic precipitate upon the bottom of the reaction vessel, so that the supernatant could be decanted off. The collected magnetic material was washed with deionised water and ethanol to facilitate removal of any by-products (e.g. sodium

chloride), which may be present on the nanoparticles surface or are in the remaining supernatant. Collected material was then dried in an inert atmosphere at 100 °C overnight.

2.1.1. Synthesis of Transition Metal Substituted IONs

Substituted nanoparticles were synthesised using a modified version of the above co-precipitation reaction of stoichiometric concentrations of divalent and trivalent metal salts with an excess of concentrated base, **eq. 2.2. and 2.3.**

Stoichiometric volumes of MCl_2 or MCl_3 (0.01 mol dm^{-3}) in HCl (1.10 mol dm^{-3}) replaced the relevant volume of $FeCl_2.6H_2O$ (0.01 mol dm^{-3}) in HCl (1.10 mol dm^{-3}) or $FeCl_3$ (0.02 mol dm^{-3}) in HCl (1.10 mol dm^{-3}) and mixed at 500 rpm for 30 minutes under a nitrogen atmosphere. Precipitation was then induced by addition of twice the volume of NaOH solution (1.00 mol dm^{-3}).

Equation 2.2.

$$xMCl_2 + (1-x)FeCl_2 + 2FeCl_3 \rightarrow M_xFe_{3-x}O_4 + 4H_2O + 8\text{NaCl}$$

or,

Equation 2.3.

$$xMCl_3 + FeCl_2 + (2-x)FeCl_3 + 8NaOH \rightarrow M_xFe_{3-x}O_4 + 4H_2O + 8NaCl$$

Magnetic precipitate was separated from the supernatant via magnetic decantation where a large neodymium bar magnet was used to collect any magnetic precipitate upon the bottom of the beaker, so that the supernatant could be decanted. The collected magnetic material was washed with deionised water and ethanol to facilitate removal of any by-products (e.g. sodium chloride). Collected material was then dried in an inert atmosphere, argon gas, at 100 °C overnight.

2.1.2. Synthesis of Pure γ-Fe_2O_3 or Fe_3O_4 Nanoparticles

Synthesis of nanoparticles of pure γ-Fe_2O_3 or Fe_3O_4 was attempted using a modified version of the above co-precipitation reaction of stoichiometric concentrations of divalent and trivalent metal salts with an excess of concentrated base.

Stoichiometric volumes of $FeCl_2.6H_2O$ (0.01 mol dm^{-3}) in HCl (1.10 mol dm^{-3}) and $FeCl_3$ (0.02 mol dm^{-3}) in HCl (1.10 mol dm^{-3}) and mixed at 500 rpm for 30 minutes under a nitrogen atmosphere. Precipitation was then induced by addition of twice the volume of NaOH solution (1.00 mol dm^{-3}). The reaction was agitated for a further 30 minutes before addition of stoichiometric volume of either hydrogen peroxide or sodium borohydride in ethanol, to form γ-Fe_2O_3 or Fe_3O_4, respectively.

Magnetic precipitate was separated from the supernatant via magnetic decantation where a large neodymium bar magnet was used to collect any magnetic precipitate upon the bottom of a beaker, so that the supernatant could be decanted. The collected magnetic material was washed with deionised water and ethanol to facilitate removal of any by-products (e.g. sodium chloride). Collected material was then dried in an argon atmosphere at 100 °C overnight.

2.2. Synthesis of IONs Using Continuous-Flow Focussing Synthesis

A continuous flow synthesis technique was developed for the synthesis of magnetic nanoparticles in commercially available microreactors, relying upon the flow focussing of aqueous reagent streams in 2D (**see Chapter 3.0. Method Development**).

Continuous flow focussing utilises a co-precipitation reaction of stoichiometrically concentrated divalent and trivalent metal salts with an excess of concentrated base, **eq. 2.1.**

A precursor solution was first prepared, by mixing of stoichiometric volumes of $FeCl_2.4H_2O$ (0.01 mol dm^{-3}) in HCl (1.10 mol dm^{-3}) and $FeCl_3$ (0.02 mol dm^{-3}) in HCl (1.10 mol dm^{-3}), along with a base solution, NaOH (1.00 mol dm^{-3}). The solutions were pumped into the chip simultaneously, the precursor solution pumped into the central microchannel, while the base pumped through the two lateral microchannels, **fig. 2.1.** By "squeezing" the precursor solution between the two flows of base the area upon which nanoparticles can adhere to the microreactor walls was minimised. Total flow rates of 1500 to 6000 μl hr^{-1}can be used, flow rates < 1500 μl hr^{-1} lead to clogging of the microreactor, while flow rates > 6000 μl hr^{-1} lead to back pressure issues. Oxidation of the reagents particularly Fe^{2+} was prevented by acidifying the precursor solution, to further prevent any atmospheric oxidation of either the precursor or the nanoparticles, all solutions were deoxygenated for 1 hour prior to use by bubbling nitrogen through them, and stored under nitrogen when not in use.

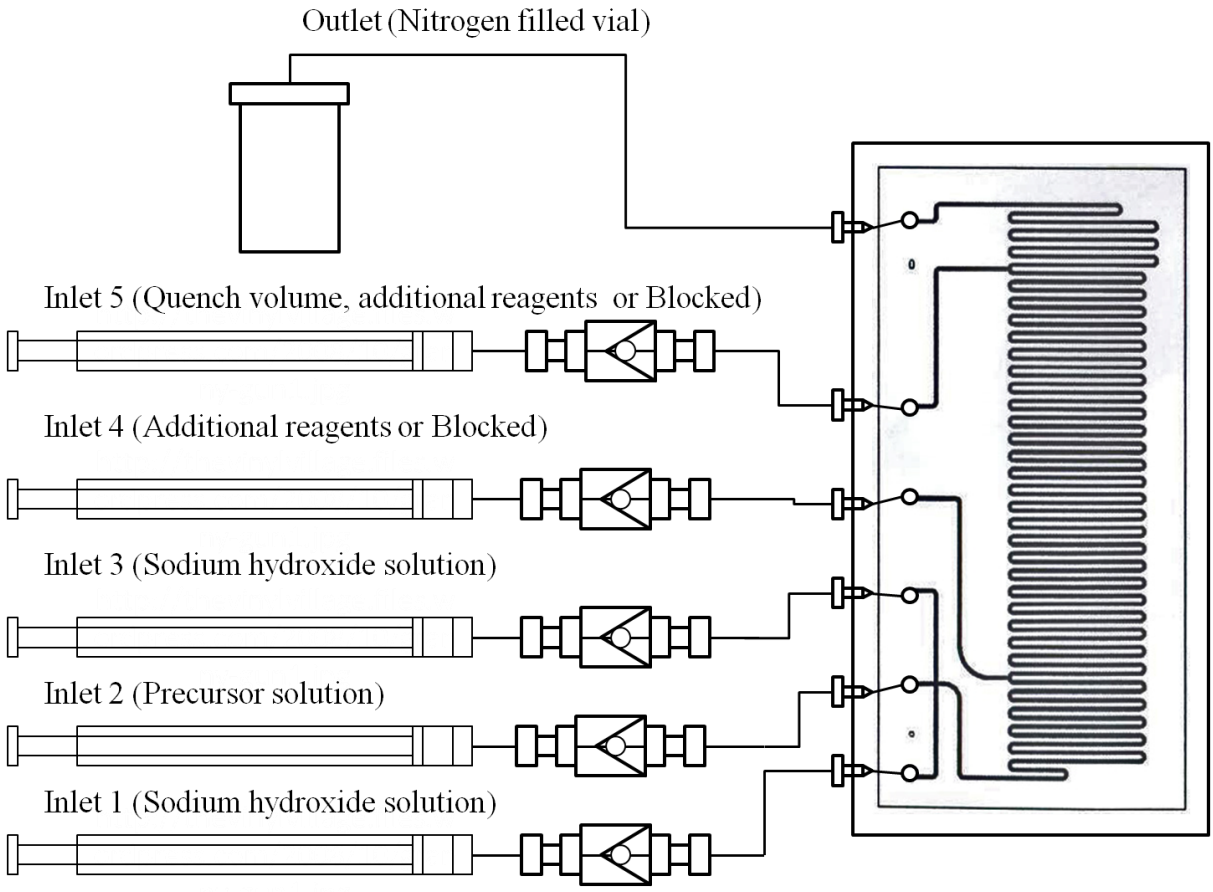

Figure 2.1. Schematic of microreactor set up used to produce continual flow focussing, allowing for continuous synthesis of IONs, where the precursor solution containing a mixture of transition metal iron salts is "squeezed" between two flows of sodium hydroxide, at the cross junction. Further reagents can be added in through a later inlet to oxidize or reduce the nanoparticles accordingly.

Any precipitated nanoparticles were collected from the microreactor, along with any effluent, in a nitrogen filled outlet vial preventing atmospheric oxidation of the nanoparticles. Any magnetic precipitate was then removed from the effluent via magnetic decantation. The collected magnetic precipitate was further washed with deionised water and ethanol to facilitate removal of any by-products (e.g. sodium chloride). Collected material was then dried in an argon atmosphere at 100 °C overnight.

2.2.1. Synthesis of Cation Substituted IONs using Continuous-Flow Focussing Synthesis

The synthesis of transition metal substituted IONs was achieved via a modified version of the above procedure. Stoichiometric volumes of either $FeCl_2$ (0.01 mol dm^{-3}) in HCl (1.10 mol dm^{-3}) or $FeCl_3$ (0.02 mol dm^{-3}) in HCl (1.10 mol dm^{-3}) within the ISPS, were substituted for the relevant volume of transition metal chloride, MCl_2 (0.01 mol dm^{-3}) in HCl (1.10 mol dm^{-3}) or MCl_3 (0.01 mol dm^{-3}) in HCl (1.10 mol dm^{-3}), **eq. 2.2.,** and **2.3.** The solutions were then pumped into the chip simultaneously, the precursor solution pumped into the central microchannel, while the base pumped through the two lateral microchannels, **fig. 2.1.** Flow rates of 2000 μl hr^{-1} per flow (6000 μl hr^{-1} total flow rate) were used. Any magnetic precipitate was collected via magnetic decantation and washed with deionised water and ethanol, before being dried in an inert atmosphere at 100 °C overnight.

2.2.2. Synthesis of Nanoparticles with Higher Weight Percentages of γ-Fe_2O_3 or Fe_3O_4

The formation of IONs with higher weight percentage of γ-Fe_2O_3 or Fe_3O_4 was attempted by modifying the approach outlined in **section 2.2.** IONs were formed using this method; however, a fourth reagent flow was added through inlet 4, **fig. 2.1.** This reagent stream contained either a solution of hydrogen peroxide or a solution of sodium borohydride in ethanol, to oxidize or reduce the formed nanoparticles, respectively. Flow rates of 1500 μl hr^{-1} were used per flow (6000 μl hr^{-1} total flow rate). Any magnetic precipitate was collected via magnetic decantation and washed with deionised water and ethanol, before being dried in an inert atmosphere, argon gas, at 100 °C overnight.

2.3. Structure Determination – Crystallography

X-ray diffraction is a powerful tool for phase identification and structure determination. Powder X-ray diffraction is particularly useful for the determination of polycrystalline samples which contain multiple phases, as each individual chemical compound can be identified. X-rays are diffracted in specific ways related to the internal structure of crystalline solids which are characterised by their high degree of internal order. The internal structure of a crystalline solid is a three dimensional array or lattice of atoms, the order of lattices can be described using symmetry elements and operations.[20, 122, 123]

2.3.1. Symmetry Operations

A symmetry operation is a geometric movement after which the object is left unchanged. Two types of symmetry operation exist; point symmetry in which the lattice point remains stationary and translational symmetry in which the lattice point is moved to a different position along an axis while a point symmetry operation is also performed.

2.3.1.1. Point Symmetry

Point symmetry is a geometric movement in which one point of the molecule remains unaltered.

Rotation axis (n) - the anticlockwise rotation about an axis by $360/n°$. The rotation around this axis is repeated n times to obtain the original configuration. n can have values of 1,

2, 3, 4 or 6 (n = 5 or 7 rotations are never observed as pentagonal and heptagonal symmetries can never be exhibited by a whole crystal system).

Reflection planes (m) - an image is created via reflection through a mirror plane so that a new set of points are created equidistant from the plane.

Centre of Inversion ($\bar{1}$) - each point of the molecule is inverted through its centre creating an equivalent point equidistant from the centre of inversion.

Rotoinversion ($\bar{n}$ or n-) - a combination of a rotation anticlockwise about an axis by 360/n° followed by an inversion through a point upon the axis, limited to integers of $\bar{1}$, $\bar{2}$, $\bar{3}$, $\bar{4}$, and $\bar{6}$.

Rotoreflection ($\tilde{n}$) - is a rarely used combination of a rotation 360/n° followed by a reflection in a mirror plane. The rarity of the symmetry operation is due to the equivalence of many of the rotoreflections with rotoinversions.

2.3.1.2. Translational Symmetry

Translational symmetry operations are geometric movements along an axis.

Rototranslation or screw axis (n_m) - combination of a rotation by $360/n$ followed by a translation parallel to the axis of rotation. The symbol n_m refers to the rotation (n) and the integer (m) of which the molecule is translated by a distance m/n. For example a 4_1 screw

axis involves a rotation 90° anticlockwise (360°/4) followed by a translation of ¼ the length of unit cell.

Reflectotranslation or glide plane (*a, b, c, n* or *d*) - combination of a reflection in a mirror plane followed by a translation of the molecule parallel to the plane. Three possible permutations of glide planes can occur, depending upon the nature of the translation. *a, b* and *c* glide planes involve translations along ½ of the respective axis of the unit cell. *n* glide planes involve translations of ½ along a face or body diagonal, while *d* glide planes involve translations of ¼ along a face or body diagonal.

2.3.2. Unit Cells and Crystal Systems

Unit cells are defined as "the smallest regular repeating units that show the full symmetry of the three dimensional crystalline solids".[20] All unit cells are defined by the length of their edges (*a, b,* and *c*) and the angles at which these intercept (α, β, and γ). The symmetry operations present within the unit cell are often used define it more accurately, as each contains its own distinct set, **table 2.1.**

Type of Unit Cell	Lattice Parameters	Symmetry Operations
Cubic	a=b=c, α=β=γ=90°	4 threefold rotation axes
Tetragonal	a=b≠c, α=β=γ=90°	1 fourfold rotation axis
Orthorhombic	a≠b≠c, α=β=γ=90°	3 twofold axes/mirror planes
Trigonal	a=b≠c, α=β=90°, γ=120° or a=b=c, α=β=γ≠90°	1 threefold rotation axis
Hexagonal	a=b≠c, α=β=90°,γ=120°	1 sixfold rotation axis
Monoclinic	a≠b≠c, α=γ=90° β≠90°	1 twofold axis/mirror plane
Triclinic	a≠b≠c, α≠β≠γ≠90°	none

Table 2.1. The unit cells and their symmetry operations.

Points within unit cells are defined by a set of coordinates, represented as fractions of the unit cell lengths. For example the red "atom" in **fig. 2.2.**, has coordinates of x=1, y=1/2, z=3/4, therefore its relation to the origin of the unit cell is *a***x**1, *b***x**1/2, *c***x**3/4. Vectors are also used to describe lattice points in relation to the origin, **eq. 2.4.** The arrangements of the points within the unit cells are referred to as the lattice.

Equation 2.4.

$$r = xa + yb + zc$$

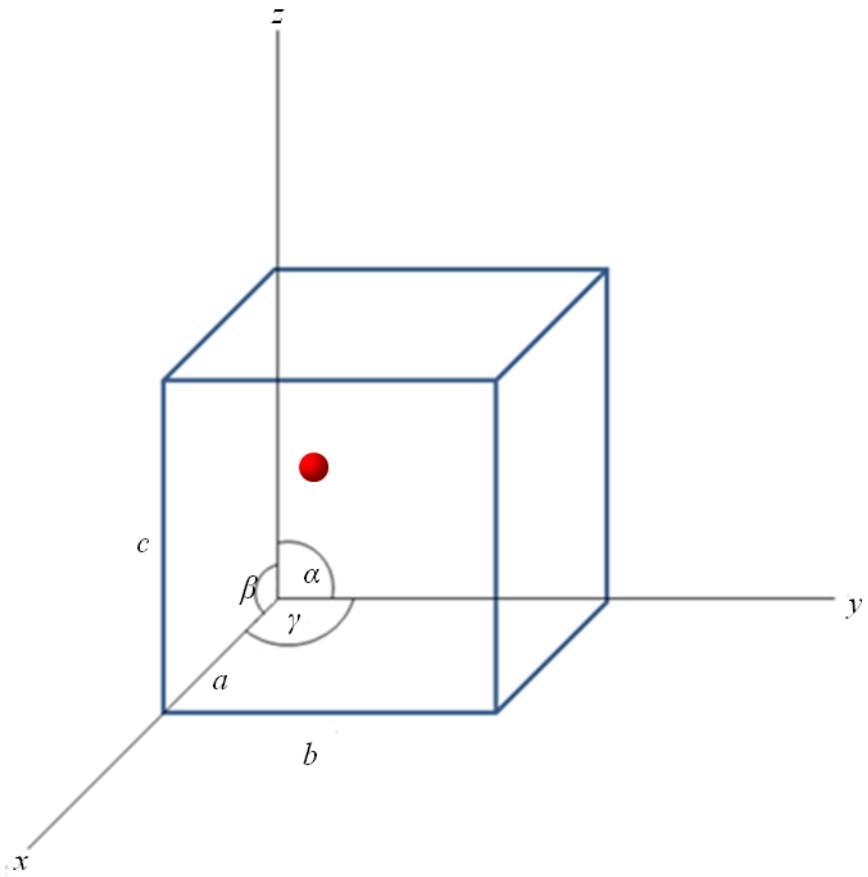

Figure 2.2. Schematic diagram of a unit cell showing the relationship between the axes (a, b, and c) and the angles (α, β, and γ) of the unit cell. An "atom" at lattice coordinates *x*=1, *y*=1/2 *z* =3/4 is also shown.

2.3.3. Lattices

The repeating structure of a 3D crystalline solid can be thought of as a grid lattice of points, in which each point represents a single atom, or molecule, or ion. The type of lattice created by linking the points together depends upon the number and location of lattice points, four types of lattice can exist, primitive, face centred, body centred and side centred, **fig. 2.3.**

Primitive lattices (*P*) - contain a single lattice point within a unit cell, the lattice point is typically represented as having a lattice point at each corner. In a typical cubic unit cell each lattice point situated upon the corners contribute $1/8^{th}$ toward the unit cell.

All of the other unit cells possess translational symmetry within the unit cell body rather than just translational symmetry of the unit cell itself.[124]

Face centred lattices (*F*) - contain four lattice points in total, a single lattice point is contributed from the points upon each corner as in a primitive lattice. Further lattice points are located at the centre of each face, related to an atom at *x*, *y*, *z* by additional translation of (*x*, *y*+1/2, *z*+1/2), (*x*+1/2, *y*, *z*+1/2) or (*x*+1/2, *y*+1/2, *z*+1/2).

Side centred lattices (*A*, *B* or *C*) - contain a primitive lattice with additional lattice points upon only a single pair of parallel faces. Translational symmetry causes a second atom to be generated at (*x*+1/2, *y*+1/2, *z*) in relation to an atom at (*x*, *y*, *z*).

Body centred lattices (*I*) - is a primitive lattice a single lattice point within the body translated by (*x*+1/2, *y*+1/2, *z*+1/2) in relation to an atom at point (*x*, *y*, *z*). The point therefore has coordinates of (1/2, 1/2, 1/2) in relation to the origin.

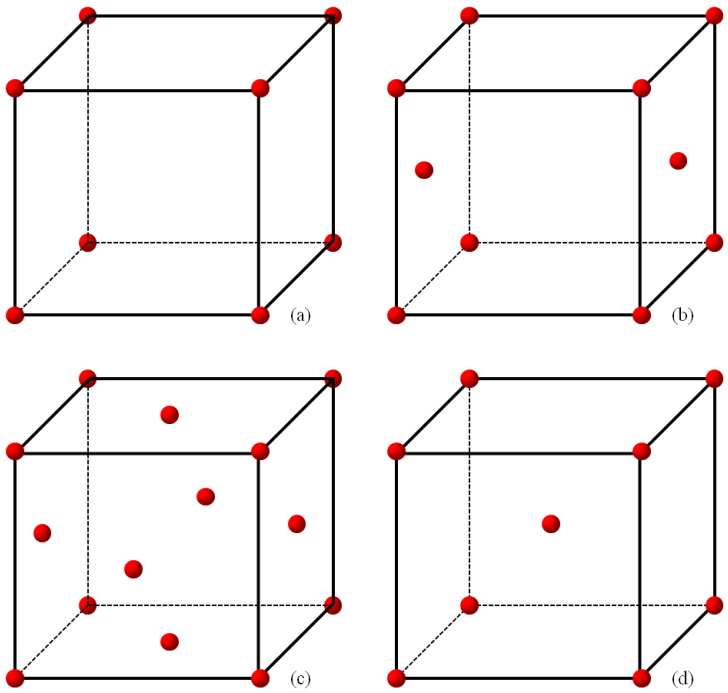

Figure 2.3. The four types of crystal lattice, Primitive where atoms exist only at the corner of the unit cells (a), Side centred where atoms exist upon each corner and a single pair of faces (b), Face centred where atoms exist on both the corners and upon each face (c), and body centred where atoms exist upon each corner and at the centre point of the unit cell (d).

Combining the crystal systems and the lattice types yields the 14 Bravais lattices, **table 2.2.**

Type of Unit Cell	Allowed Lattices
Cubic	Primitive (*P*), Face-centred (*F*), Body centred (*I*)
Tetragonal	Primitive (*P*), Body centred (*I*)
Orthorhombic	Primitive (*P*), Face-centred (*F*), Body centred (*I*), Side centred (*C*)
Trigonal	Primitive (*P*)
Hexagonal	Primitive (*P*)
Monoclinic	Primitive (*P*), Side centred (*C*)
Triclinic	Primitive (*P*)

Table 2.2. The Bravais lattices, and the relationship to unit cells.

The combination of unit cell and lattice that is not noted in **table 2.2.**, either violates the symmetry requirements, or could be represented by a smaller unit cell.

2.3.4. Lattice Planes

Lattice planes are formed by joining sets of lattice points together and are integral to Bragg's law of diffraction. Parallel sets of lattice planes are separated by a distance, *d*, known as the interplanar distance or *d*-spacing. How a lattice plane cuts through a unit cell can be written as a set of Miller indices, these are assigned to each family of parallel lattice planes by their relation to the origin of the unit cell and are written as a reciprocal of the fraction of the unit cells length. For example if a lattice plane intersects a unit cell at ½ the length of edge *a*, at 1/3 of edge *b*, and at the end of edge *c*, 1/1, the Miller indices are therefore (231). The *d*-spacing between a set of parallel lattice planes can be calculated from the Miller indices (*h, k, l*) and the lattice cell parameters (*a, b, c*), **table 2.3.**

2.3.5. Bragg's Law

X-ray diffraction analysis is based upon the interaction of X-rays with matter and is related to Bragg's law, **eq. 2.7.**, of diffraction by assuming that, the angular distribution of diffracted X-ray radiation is partially reflected by lattice planes, e.g. the lattice planes act as semi permeable mirrors. When a lattice plane is hit by a monochromatic beam of X-rays some are reflected. The beam is seen to deviate by 2θ (the sum of the angles of incidence and reflection) from its original path. Some X-rays will also pass through the first plane to be reflected by subsequent parallel planes of the same family. **Fig. 2.4.**, shows the derivation of Bragg's law, where beam A → A' is reflected by the initial lattice plane, and beam B → B' is reflected by a parallel lattice plane. The extra distance travelled by beam B → B'(distance *xyz*) must be equal to an integral number of wavelengths for the beams to be in phase.[125]

Crystal System	Expression for the Interplanar Distance
Cubic	$\frac{1}{d^2} = \frac{h^2 + k^2 + l^2}{a^2}$
Tetragonal	$\frac{1}{d^2} = \frac{h^2}{a^2} + \frac{l^2}{c^2}$
Orthorhombic	$\frac{1}{d^2} = \frac{h^2}{a^2} + \frac{k^2}{b^2} + \frac{l^2}{c^2}$
Hexagonal	$\frac{1}{d^2} = \frac{4}{3}\left(\frac{h^2 + hk + k^2}{a^2}\right) + \frac{l^2}{c^2}$
Monoclinic	$\frac{1}{d^2} = \frac{1}{\sin^2\beta}\left(\frac{h^2}{a^2} + \frac{k^2 \sin^2\beta}{b^2} + \frac{l^2}{c^2} + \frac{2h\cos\beta}{ac}\right)$
Rhombohedral	$\frac{1}{d^2} = \left\{\frac{[(h^2 + k^2 + l^2)\sin^2\alpha + 2(hk + kl + lh)(\cos^2\alpha - \cos\alpha)]}{\alpha^2(1 - 3\cos^2\alpha + 2\cos^3\alpha)}\right\}$
Triclinic*	$\frac{1}{d^2} = \left[1/V^2\right]\{[S_{11}h^2] + [S_{22}h^2] + [S_{33}h^2] + [2S_{12}hk] + [2S_{23}kl] + [2S_{13}hl]\}$

Table 2.3. Calculation of d-spacing from miller indices.

As there are a near infinite amount of lattice planes within a bulk sample only specific angles produce constructive superpositioning of X-rays. In a purely crystalline solid all other reflections cause destructive superpositioning to occur as a deeper plane (p) will reflect the X-ray so that it is out of phase, e.g. $p\Delta = n\lambda$, where Δ is the difference between the planes.[126]

---

* V = unit cell volume
$S_{11} = b^2c^2\sin^2\alpha$
$S_{22} = a^2c^2\sin^2\beta$
$S_{33} = a^2b^2\sin^2\gamma$
$S_{12} = abc^2(\cos\alpha\cos\beta - \cos\gamma)$
$S_{23} = a^2bc(\cos\gamma\cos\beta - \cos\gamma\alpha)$
$S_{13} = ab^2c(\cos\alpha\cos\gamma - \cos\beta)$

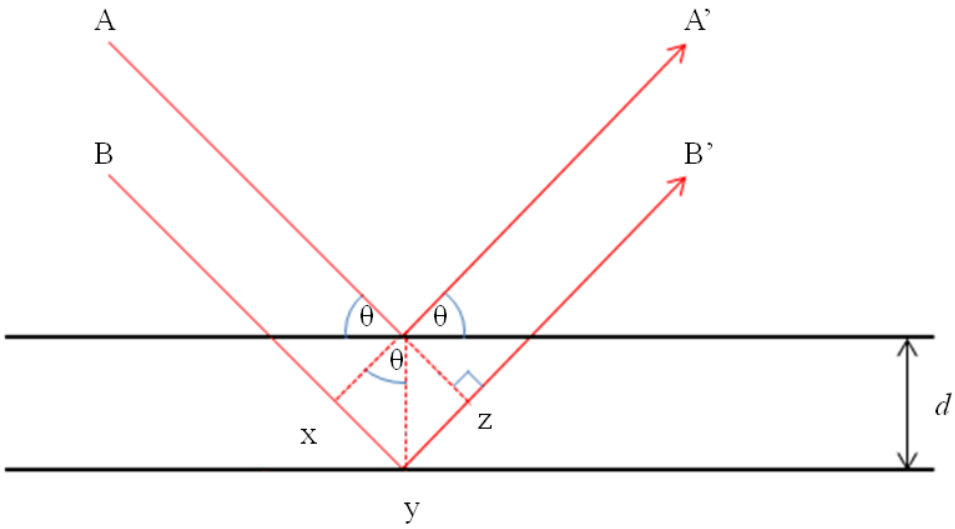

Figure 2.4. Derivation of Bragg's law, where x-rays can only be reflected in phase at specific angles, relating to the interplanar distance between the parallel lattice planes.

The spacing between the lattice planes, *d*, is related to the Bragg angle through the extra distance travelled by the parallel beam:

Equation 2.5.

$$xy = yz = d \sin\theta$$

Thus,

Equation 2.6.

$$xyz = 2d \sin\theta$$

If $xyz = n\lambda$, then,

Equation 2.7.

$$n\lambda = 2d \sin\theta$$

In practice the value of *n* is always taken to be 1.

2.3.6. X-ray Generation

X-rays are electromagnetic waves with wavelengths between 0.1 and 10 Å. The standard procedure for the generation of X-rays is to use an X-ray tube. An X-ray tube contains a short filament, over which an electrical current is placed. The electrons are then accelerated from the filament toward a metal target by application of a large potential difference, **fig. 2.5.** Upon collision with the metal target the vast majority of the energy of the collision is converted to heat and wasted, however, from a small proportion of collisions X-rays are produced.

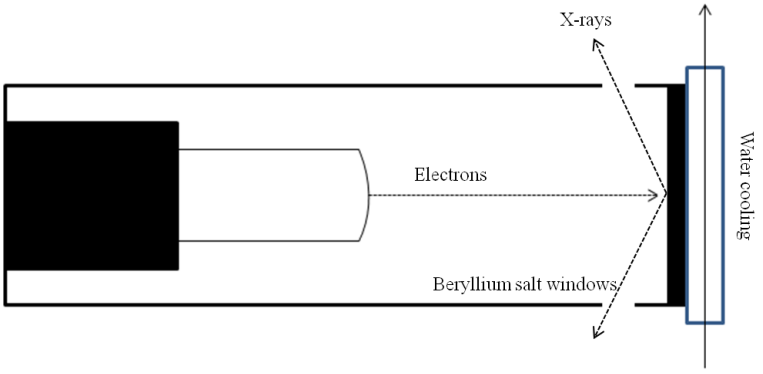

Figure 2.5. A schematic diagram of an X-ray tube, where electrons are accelerated from a filament toward a target by application of a potential difference, upon collision with the target core electrons are removed, and x-rays produced by the decay of electrons from higher orbitals to the lower core orbitals.

Electrons colliding with the target can cause the ejection of a core orbital electron from a metal atom, creating a vacancy within an orbital. Subsequently an electron from a higher energy orbital decays to fill the vacancy, an X-ray of specific frequency is then emitted due to the difference in energy levels.

The filling of vacancies gives rise to radiation emitted at specific wavelengths, $K_{\alpha 1}$ radiation is caused by the decay of an electron from the $2p^1$ to the 1*s* orbital, and $K_{\alpha 2}$ is caused by the decay of an electron from the $2p^3$ to the 1s orbital. Decay from the $3p^1$ and

$3p^3$ to the 1*s* orbital causes $K_{\beta 1}$ and $K_{\beta 2}$ radiation to be emitted, respectively. K_{α} radiation is observed at moderate to high diffraction angles as a doublet; due to the small energy difference between $K_{\alpha 1}$ and $K_{\alpha 2}$. K_{β} radiation is practically never observed. Heavier metal targets (e.g. Ag) can be used to create decays from higher orbitals and X-rays with greater energies (L and M radiation). As several different transitions are possible for each metal the spectrum of X-rays emitted from an X-ray tube consist of several sharp maxima for each quantum transition imposed upon a background of radiation caused by non-quantum processes, e.g. where electrons are diffracted by the metal target, known as Bremmstrahlung radiation **fig. 2.6.**

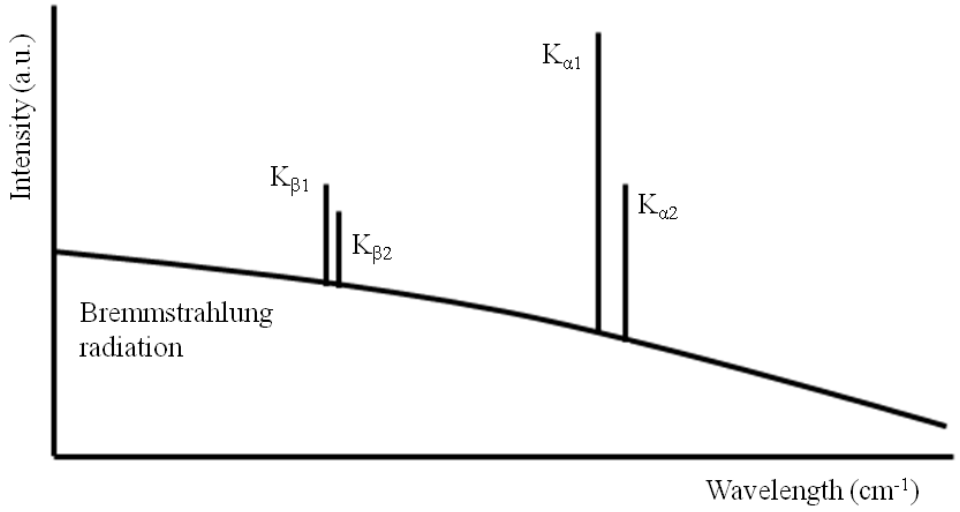

Figure 2.6. Spectrum of radiation produce by an X-ray tube, where the K_{α} and K_{β} wavelengths of X-ray radiation commonly used for crystallography can be seen over the background (Bremmstrahlung) radiation, caused by non-quantum processes.

X-rays produced from copper targets produce X-rays where λ = 1.54184 Å, and molybdenum λ = 0.71073 Å.

2.3.7. Data collection

Data collection using a powder X-ray diffractometer in Bragg-Brentano geometry involves placing a polycrystalline sample with a flat surface within the incident beam of X-rays, and measuring the intensity of the X-rays diffracted at specific angles, **fig. 2.7.**

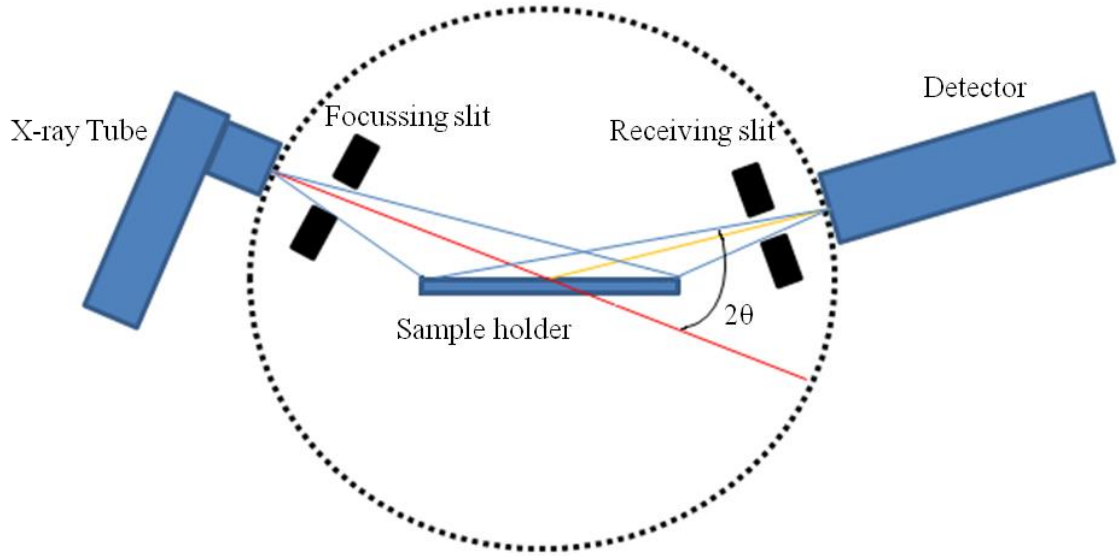

Figure 2.7. A schematic representation of a powder X-ray diffractometer, where both the angle of the source and detector are altered by a goniometer so as to record the intensity of diffracted X-rays at specific angles.

As polycrystalline samples contain large numbers of crystalline particles all of which are randomly orientated, X-rays are scattered in all possible directions at once, with each lattice spacing giving rise to an individual cone of diffracted X-rays, **fig. 2.8.**

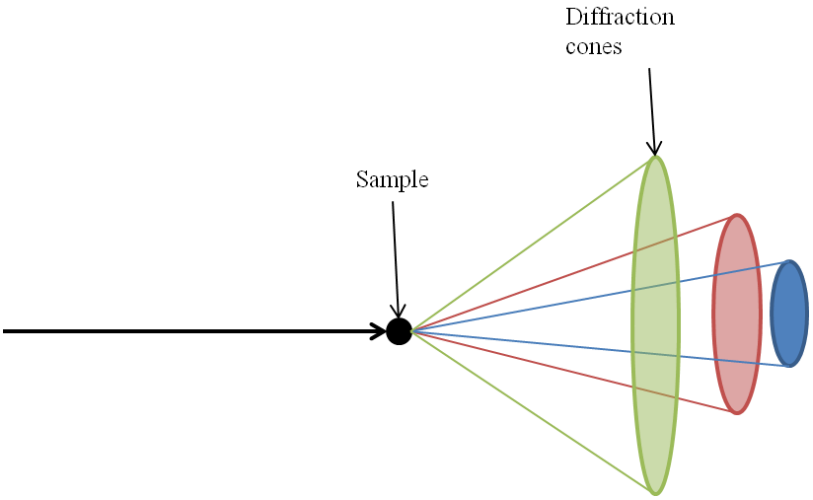

Figure 2.8. Diffraction cones created by bombardment of a polycrystalline sample with a monochromatic X-ray beam.

The detector is moved around the sample in a circle so as to cut through the diffraction cones, which form intensity maxima at angles specific to the lattice planes present. The unit cell parameters can be calculated from the peak positions and the d-spacing.

2.3.8. Phase Determination

Phase determination is performed by comparison of the collected data with previously recorded X-ray diffraction data obtained from either the Joint Committee on Powder Diffraction Standards (JCPDS) or the Inorganic Crystal Structure Database (ICSD). It is also beneficial to use software (e.g. EVA) to compare relative intensities and 2θ positions to collected data and standard patterns. Problems can occur however when dealing with impurities, broadening of diffraction peaks, and peak overlap.

2.3.9. Particle Size Determination Using PXRD

When the extra distance travelled by an X-ray reflected from a lower parallel lattice plane is equal to an integral number of wavelengths, λ, the waves scattered by both the initial and lower planes will be exactly in phase and superposition constructively, and if the extra distance travelled is equal to half a wavelength, 0.5 λ, the waves are perfectly out of phase and superposition destructively. Thus according to Bragg's law only specific angles lead to scattering of X-rays, within a polycrystalline sample as a near infinite number of lattice planes are present, **section 2.3.4.**. The presence of a near infinite number of lattice planes leads to the assumption that at some point within the polycrystalline sample a second lattice plane will exist in a symmetry that will scatter X-rays completely out of phase to the original lattice plane. In nanocrystalline samples however, only a small number of lattice planes are present within each particle, and destructive superpositioning of the out of phase scattered X-rays does not always occur, thus broadening of the reflection peaks is observed due to diffraction at angles close to that of the Bragg angle. For example a crystal 1000 Å in size with lattice planes separated by a distance equal to 1.0001 λ, scattering for the first lattice plane will be perfectly out of phase with the wave scattered by the 5001st lattice plane within the crystal, which will not be present, as only 1000 lattice planes are present within the crystal. Thus no destructive superpostioning will occur and the peak at the Bragg angle will be broader due to some scattering at slightly lower and higher angles.[127, 128] From this broadening a mean crystallite dimension can be used to calculated, **eq. 2.8.** in the case of spherical nanoparticles the mean crystallite diameter, τ, of a nanocrystalline sample.

Equation 2.8.

$$\tau = \frac{k\lambda}{\sqrt{\beta_m^2 - \beta_s^2}\cos\theta}$$

Where, k the "shape factor" is a constant related to the shape of the nanoparticles (0.9 for spheres) and θ the Bragg angle. β_m is the full width at half maximum (FWHM) of the peak at the Bragg angle, and β_s the broadening caused by the instrumentation. The mean crystallite dimensions are taken to be the diameter for spherical nanoparticles but can also be related to cylindrical or sheet like nanoparticles depending upon their orientation.[124, 128] In particles with dimensions of less than 10,000 Å the peak becomes so broad as to render the contribution by the instrumentation negligible, **eq. 2.9.**, therefore;

Equation 2.9.

$$\tau = \frac{k\lambda}{\beta \cos \theta}$$

Where β is the full width at half maximum of the peak.

As non-uniform strain and stresses caused by impurities or vacancies within the crystal lattice can also cause peak broadening, the size obtained from the Scherrer equation is an estimate. In samples in which large amounts of cation or anion doping has been performed the Scherrer equation cannot be used due to both the movement of the reflection caused by uniform strain or due to the broadness caused by non-uniform stress significantly, which will significantly alter the *d*-spacing.

2.3.10. Determination of Percentage Weight of Mixtures of Compounds

Quantification of phases in powder diffraction data in which overlapping is present relies upon the calculation of the contribution each phase makes to the overall intensity of peaks. Commonly, methods fall into two groups; those that rely upon a single or group of peaks, in which it is assumed that the intensity of these peaks are representative of the amount of the individual phases (e.g. the method of standard additions and the more commonly used internal standard method), or the whole pattern methods which rely upon

comparison of experimental data with intensities calculated from either pure phase samples, or from crystal structure data (the adsorption diffraction method).[126-128]

In this work a method devised by Kim *et.al.*, has been adapted and developed for quantification of both γ-Fe_2O_3 and Fe_3O_4 in a binary mixture of the two, adaptation and development is discussed in further detail in **chapter 5**.[129] As seen in **section 1.3.**, the structures of the two compounds and therefore their X-ray diffraction patterns are very similar. The technique relies upon peak asymmetry and calculating the contributing intensities of γ-Fe_2O_3 and Fe_3O_4 in the (511) and (440) reflections to asymmetric peaks present within PXRD patterns containing the two.

Briefly, calibration graphs were constructed by taking multiple stepwise scans between $55 < 2\theta^{\circ} < 65$ to record the intensity of the (511) and (440) reflections of different weight percentage mixtures of γ-Fe_2O_3 (Sigma Aldrich, particle size < 50 nm) and Fe_3O_4 (Sigma Aldrich), see **table 2.4.** A sum of the intensity of multiple scans was then taken and loaded into XFIT software and an asymmetric peak fitted to this around the positions of the (511) and (440) reflections in both Fe_3O_4 (*Fd3-m*) and γ-Fe_2O_3 (*$P4_12_12$*), **fig. 2.9.a**.[24, 26, 130]

Phase	Unit Cell	2θ Position of (511) Reflection (°)	2θ Position of (440) Reflection (°)
Fe_3O_4	*Fd3-m*	56.958	62.545
γ-Fe_2O_3	*$P4_12_12$*	57.369	63.001

Table 2.4. 2θ positions of the (511) and (440) reflections in Fe_3O_4 (*Fd3-m*) and γ-Fe_2O_3 (*$P4_32_12$*).

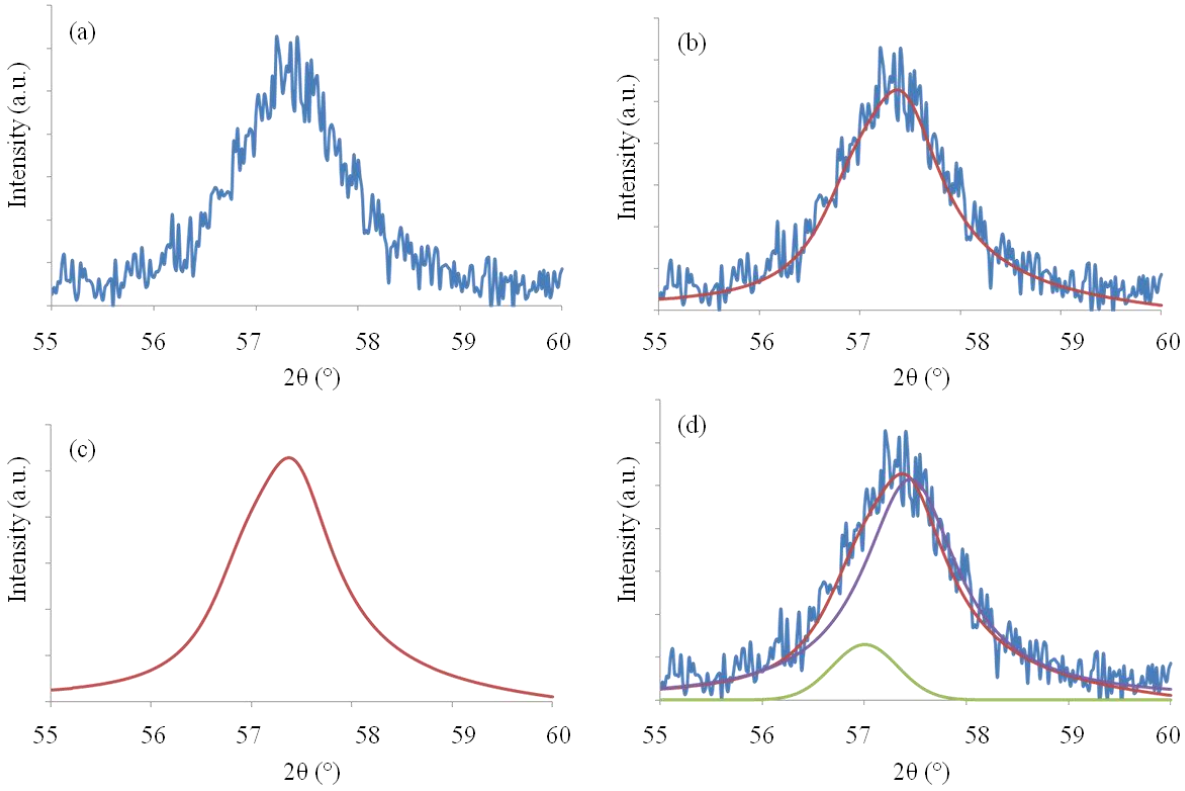

Figure 2.9. Schematic diagram of peak deconvolution, (a) the raw data, (b) the asymmetric curve which is fitted to the raw data using XFIT, (c) the asymmetric curve, (d) the two symmetric peaks which contribute to the asymmetric peak.

The asymmetric peak was then reloaded into XFIT and the positions of the reflections for both γ-Fe_2O_3 and Fe_3O_4 set as the initial positions of the two symmetric peaks. The asymmetric peak is then deconvoluted into its two symmetric components relating to γ-Fe_2O_3 and Fe_3O_4, **fig.2.9.d**. The intensities of these peaks are then taken from the output file and the integrated intensity calculated, **eq. 2.10.**

Equation 2.10.

$$Integrated\ Intensity\ (\%) = \left(\frac{I_{Maghemite}}{I_{Magnetite} + I_{Maghemite}}\right) \times 100$$

The integrated intensity in percent is then plotted against the weight percentage of γ-Fe_2O_3 or Fe_3O_4 within the weight percentage mixture, **fig. 2.10.** Statistical testing using the

Dixon Q test was performed upon the data to remove any grossly erroneous data points, increasing the calibration graphs accuracy, and allowing for the calculation of both the detection limit at various levels of confidence and the error upon the graph, **table 2.5.**.[131]

Detection limit (%)	Factor of Confidence Interval				
Reflection	99.9 %	99.0 %	95.0 %	90.0 %	80.0 %
Fe_3O_4 (440)	23.55	18.47	14.03	11.74	9.23
γ-Fe_2O_3 (440)	21.89	17.17	13.04	10.91	8.58

Table 2.5. Detection limits for percentage weight of γ-Fe_2O_3 at various factors of confidence for the (511) and (440) reflections.

For a confidence interval of 99 %, e.g. the correct answer is obtained 99 times out of 100, γ-Fe_2O_3 can be detected from the (440) reflection if more than 21.89 % of the sample is γ-Fe_2O_3. To calculate the weight percentage of γ-Fe_2O_3 within a sample a sum of multiple scans with an equal step size to that of the calibration graph over a range of $55 < 2\theta° < 65$ are performed. The added data of these scans is then placed back into Xfit and the integrated intensity of the (511) or (440) reflections calculated, and compared to the calibration graph, yielding the weight percentage of Fe_3O_4 and γ-Fe_2O_3 within the sample, **fig. 2.10.**

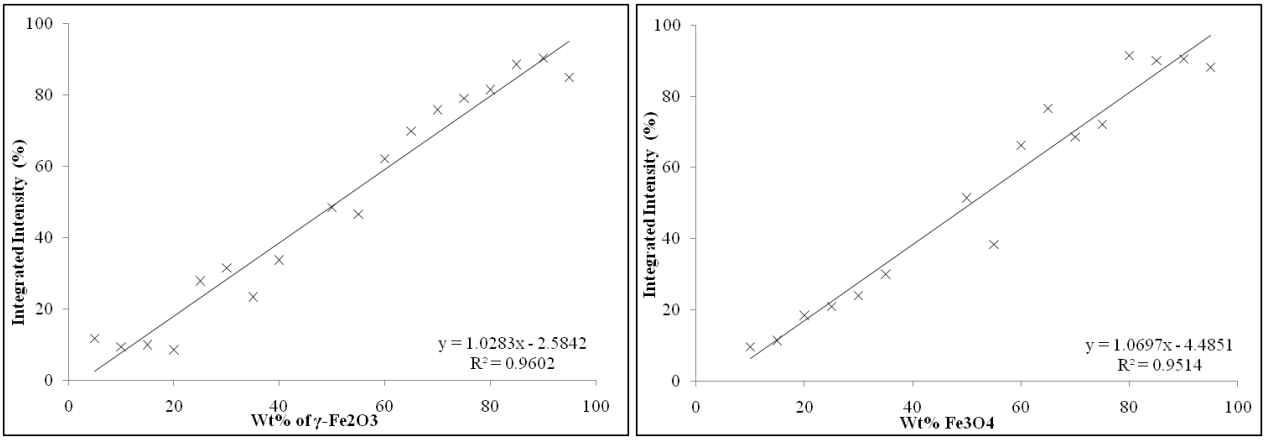

Figure 2.10. Calibration graphs for determining the weight percentage of γ-Fe_2O_3 or Fe_3O_4 the (440) reflections in this work after removal of statistical outliers.

2.4. Structure Determination Using Infrared Spectroscopy

Infrared spectroscopy is a useful tool for qualitative structure determination. A wide array of polynuclear molecules can be analysed using infra-red spectroscopy as nearly all molecules absorb infra-red radiation. Polynuclear molecules absorption of infra-red radiation gives rise to a unique absorption spectrum for the molecule. As radiation in the infra-red region of the electromagnetic spectrum is not energetic enough to cause excitation of orbital electrons, only vibrational or rotational transitions of the molecule are observed. [132-135] Unlike simpler versions of infra-red spectrometers Fourier Transform Infra-red (FTIR) spectrometers use a modulated source code to transmit detect and measure all wavelengths within the wavelength range of the scan simultaneously. To do this a Fourier transform algorithm is used to decode and interpret the measured adsorption at specific wavelengths. The percentage of the light transmitted or adsorbed by the sample is plotted versus the wavelength infra-red light adsorbed.

2.4.1. Potassium Bromide (KBr) Disk Method

To record the spectrum of the nanoparticles the KBr disk method was employed, in which a small mass of sample was intimately ground with a larger quantity of potassium bromide (KBr), usually a concentration of 1:100 (sample : KBr). The intimate mixture was then compressed under 10 tons of pressure for several minutes forming a translucent disk of the nanoparticles held in a KBr matrix. As the thickness and opacity of the disk are difficult to measure this technique is usually used for qualitative rather than quantitative analysis. The infrared absorption spectrum of the disk was plotted over a range of wavenumbers (4000 - 375 cm^{-1}).

2.4.2. Qualitative Structure Determination of Spectra

Bands associated with vibrational transitions occur at specific wavenumbers within a molecules infra-red spectrum. The number of the bands can be calculated for simple molecules within the liquid or gaseous phases through the application of group theory. In the solid phase the vibrational modes used to calculate the number of bands, are often hindered due to the rigid bonding structure within the crystal lattice. For complicated solid structures like γ-Fe_2O_3 and Fe_3O_4, the calculation of the exact number of infra-red active modes requires the use of computational methods. Therefore it is often more advantageous to consider the shape of the bands within the "fingerprint" region (1000 - 375 cm^{-1}) the shapes of the peaks within the fingerprint region of γ-Fe_2O_3 and Fe_3O_4 are shown in **fig. 2.11.**[19]

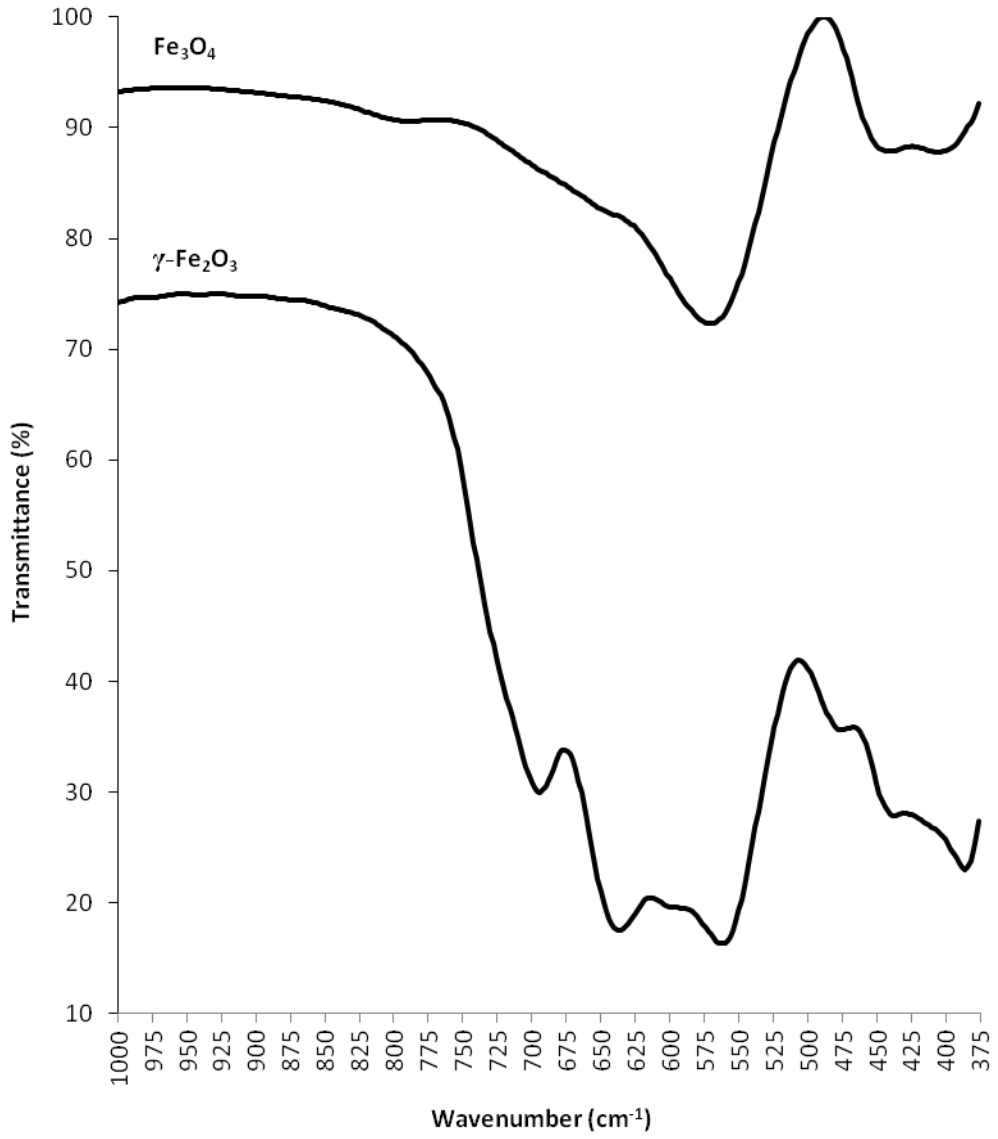

Figure 2.11. Comparison of the fingerprint IR regions of Fe_3O_4 and γ-Fe_2O_3.[19]

As γ-Fe_2O_3 is produced from the oxidization of Fe_3O_4 cation vacancies occur within its structure leading to a more complicated structure, and hence the two broad bands present in the "fingerprint" region of Fe_3O_4 split into multiple bands, **table 2.6.** Identification can be difficult if the resolution is not carefully selected, too high a resolution and additional bands appear within the spectrum due to noise; too low a resolution and bands merge together. This is especially problematic in the case of distinguishing between γ-Fe_2O_3 and Fe_3O_4.

Compound	Peak Positions (cm^{-1})
Fe_3O_4	580, 400
γ-Fe_2O_3	700, 660-640, 620, 580, 560, 460, 430, 390, 305
α-Fe_2O_3	620, 574, 478, 352
γ-FeOOH	600, 450

Table 2.6. Peak positions of Fe-O bonds in selected iron oxides.[19]

2.5. Mössbauer Spectroscopy

Mössbauer spectroscopy is a specialised spectroscopy technique that allows for the accurate determination of the spatial arrangement of bonds, the valency, and the spin state of ions within a solid. It has shown particular use for solving problems in which the atomic oxidation states and coordination numbers of ions within compounds are unclear, helping to also shed light upon the ionicity and covalency of bonds in, inorganic, organometallic and intermetallic systems.[136, 137] It is based upon the "Mössbauer effect" the recoilless absorption and emission of gamma-rays. As with PXRD the simplest use of Mössbauer spectra is to use them as a fingerprinting technique so that a specific compound can be identified, either by direct comparison of spectra, or comparison the values associated with the isomer shift, quadropolar splitting and magnetic splitting. Spectra of ^{57}Fe containing compounds are very common, with ^{57}Fe possessing low gamma-ray energies and a long lived excited state.[136-138]

2.5.1. The Mössbauer effect

When gamma-rays and atomic nuclei interact the nuclei can undergo a variety of energy level transitions which are affected by the environment of the nuclei, e.g. what molecules surround it, and are associated with the resonance fluorescence caused by the absorption or emission of a gamma-ray.[136-138]

The resonance flurorescence that is caused by the interaction of the gamma-ray with the nuclei, and used to detect these energy level transitions however, is easily masked as they are very small in energy, and the energy associated with the recoil of nuclei when a gamma-ray is absorbed or emitted is much larger. Nuclei will recoil when a gamma-ray is absorbed or emitted due to the conversation of momentum, and the energy associated with this, E_R, will cause the emitted gamma-ray to be E_R less than what is required to cause detectable resonance fluorescence.[136-138] Further to this is the gamma-ray will also lose energy due to the Doppler effect as thermal motion of the atoms causes them to move, and so the gamma-rays with the required amount of energy to cause resonance fluorescence is extremely small.[136-138]

To overcome the recoil and Doppler effects the sample is often held in a solid matrix, preventing the movement of the nuclei by holding it in place and the energy is dispersed throughout the matrix, a recoilless event. If this occurs then the absorption and emission of the gamma-rays and the resulting energy level transitions can be observed using a detector.

The tiny hyperfine energy levels can be determined by using a gamma-ray emitting source, the frequency of the gamma-rays is changed using the Doppler effect by resonating the source backward and forward, so that the energy of the gamma-rays and the energy difference between the energy levels match exactly. A spectrum is then recorded of the intensity of the resonance against the speed at which the source is

oscillating. The position of the peak(s) within the spectrum can then be used to draw conclusions about the environment surrounding the nuclei.[136-138]

2.5.2. Isomer Shift

Isomer shift determines the position of the spectrum on the energy/velocity scale, occurring when a monopole interaction alters the nuclear energy levels of the nuclei. The monopole interaction is generally caused due to the nuclei having a non-zero volume and the resulting electron charge density within this.[136-138] The difference in the s-electron environments between the gamma-ray source and the absorbing nuclei cause a shift in the resonance energy transition, depending upon the electron charge density of the s-electrons, altering where the peak is centred. This can only be detected when comparing the spectra to that of a known absorber, in the case of ^{57}Fe spectra this is compared to the spectra of α-Fe, **fig. 2.12.**

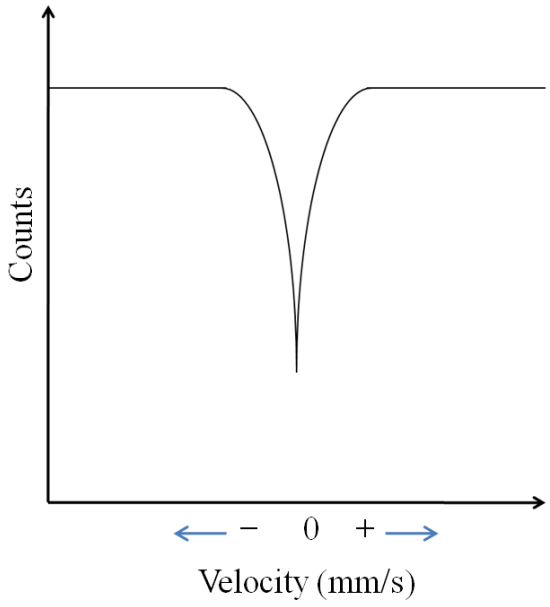

Figure 2.12. Isomer shift in Mössbauer spectra, where the peak may shift to lower or higher velocity (energy), in relation to the spectrum of α-Fe.

The isomer shift is particularly useful in determining the valency state of the absorber, in the case of Fe^{2+} the electron configuration is $(3d)^6$ which has less electrons near the nucleus due to the screening of the *d*-electrons and will have a larger positive shift compared to that of Fe^{3+} which has an electron configuration of $(3d)^5$.[136-138]

2.5.3. Quadropole Splitting

For nuclei with nuclear quadropole moments, e.g. those with an angular momentum quantum number of $I = ½$, are susceptible to quadropole splitting.[136-138] When these nuclei are placed within an asymmetric electric field, such as that created by certain charge distributions or by specific ligands, the nuclear energy levels can be split. In the case of a nuclei which has an $I = 3/2$ excited state this can be split into two substates, $m_I \pm 3/2$ or $m_I \pm ½$, **fig. 2.13.**

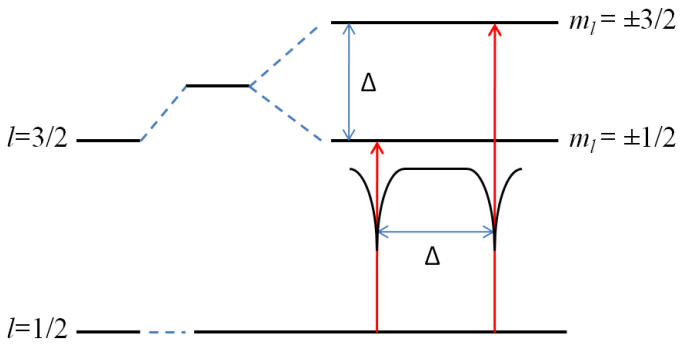

Figure 2.13. Quadrupole splitting where the energy levels of the adsorbing nuclei have split into multiple substates, creating multiple peaks upon the Mössbauer spectrum.

This gives rise to a doublet upon the Mössbauer spectrum of the sample, the difference between the two peaks within the doublet can be used to calculate the difference in energy between the two substates, Δ, **eq. 2.11.**, which is related to the main component of the

electric field gradient, the quantity by which the charge distribution is characterised, V_{zz}, and the nuclear quadropole moment, Q.

Equation 2.11.

$$\Delta = \frac{Q \times V_{zz}}{2}$$

Quadrupole splitting can be affected by the valency of the iron cations, as they may exist in either high or low spin forms. The quadrupole splitting reflects the number and arrangement of the *d*-electrons, in some low and high spin forms the contributions to this from the bonding and non-bonding electrons partially cancel each other. High spin Fe^{2+} has a high isomer shift and large quadrupole splitting, while high spin Fe^{3+} has a lower isomer shift and a smaller quadrupole splitting.[136-138]

2.5.4. Magnetic Splitting

Magnetic spitting is most often encountered in the spectra of ferromagnetic samples containing ^{57}Fe due to their magnetic ordering. Splitting of nuclear levels can be performed by inducing a dipolar interaction in the sample due to the interaction of the nuclear spin moment of the nuclei and an applied magnetic field, causing the nuclear levels to be split into $2(I+1)$ substates. [136-138] Transitions between the excited state and the ground state occur only where m_I changes by 0 or 1, and in the case of a transition between the $I = 3/2$ and the $I = 1/2$ substates there are six possible transitions, **fig. 2.14.**, separated by a distance proportional to the total effective magnetic field, B_{eff}.

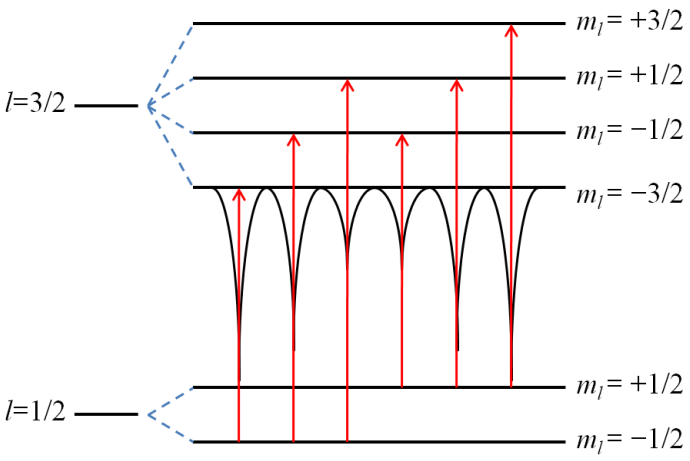

Figure 2.14. Magnetic splitting of energy levels into multiple substates, in the application of a magnetic field, producing a sextet of lines upon the Mössbauer spectra for an ^{57}Fe sample.

While the line positions are related to the energy of the split substates the intensity of each is related to the angle at which the gamma-rays and the nuclear spin moment interact, while this does not affect the ratio of the intensity of the outer or inner lines the middle lines can have values between 0 and 4 times that of the inner lines, **eq. 2.12.**

Equation 2.12.

$$(outer : middle : inner) = 3 : \left(\frac{(4\sin^2\theta)}{(1+\cos^2\theta)}\right) : 1$$

For polycrystalline samples in no applied field the middle lines are often twice the intensity of the inner. Further problems for high spin Fe^{3+} containing compounds can occur when the iron cations are separated over a considerable distance leading to asymmetric broadening of peaks related to magnetic relaxation. This can be a particular problem for magnetically ordered materials with crystallites that are larger than a single magnetic domain, which leads to the appearance of fully magnetically split six-line spectra, however below the size of a single magnetic domain superparamagnetism can lead to anomalous readings.[136-138]

2.5.5. Instrumentation

All Mössbauer spectra presented in this work were recorded and interpreted by Professor Davie Evans at the University of Hull, using ES-Technology MS-105 Mössbauer spectrometer, in zero magnetic field at 78 K, with a 900 MBq ^{57}Co source in a rhodium matrix at ambient temperature. Spectra were referenced against 25 μm iron foil at 298 K and spectrum parameters were obtained by fitting with Lorentzian curves. Under a nitrogen atmosphere samples were ground with boron nitride before mounting in the sample holder.

2.6. Structural Determination - ICP-AES

Inductively coupled plasma atomic emission spectroscopy (ICP-AES) uses the specific characteristic wavelengths of electromagnetic radiation emitted from excited atoms to qualify and quantify the cations present within a sample.

2.6.1. ICP Torch

Argon plasma is used to excite electrons within the atoms present in the sample, this is created by pumping argon gas through an ICP torch consisting of three concentric quartz tubes, where it is ignited using a Tesla unit. The plasma is maintained through application of an electromagnetic field (radio waves) generated using an induction or radiofrequency coil, **fig. 2.15.** The radiofrequency coil is kept separated from the plasma by the quartz tubing which is cooled using an outer flow of argon gas, primarily used to feed the plasma. As the argon stream is ionized a stable cloud of electrons and ionized argon is created,

this flows toward the magnetic field of the radiofrequency coil. The ionised plasma is kept from damaging the quartz tubes by an auxiliary gas flow acting as a tangential stream, limiting the damage to these.

A small amount of pre-digested sample (dissolved in conc. HCl) is then nebulised using an argon carrier stream and injected into the plasma jet through the central quartz tube. As the sample passes through the plasma it is ionized and excited due to the intense heat, creating a plume in which the elements are free of molecular association. As the sample ions relax to their ground state electromagnetic radiation characteristic of the elements present is emitted, the point at which this happens within the plasma is heavily dependent upon the temperature and ionization energy of the sample.[132, 133, 139, 140]

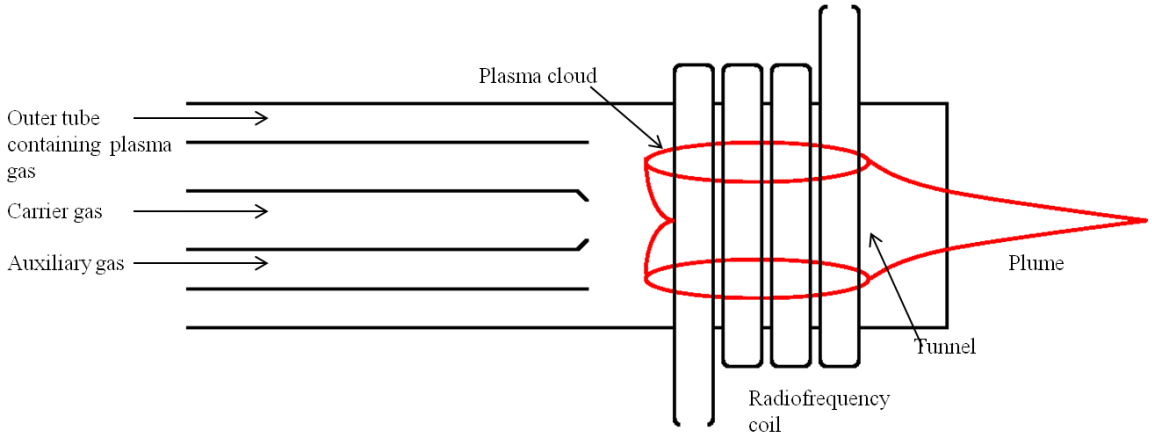

Figure 2.15. Schematic diagram of ICP torch, where tangential streams of argon gas are used to create a plume of plasma into which an aerosol spray of the sample can be injected, causing the electronic excitation of the ions within the aerosol and subsequently allow for their qualification and quantification.

2.6.2. Sample Analysis

When the aerosol is introduced into the argon plasma the energy exchanged causes any molecules to become dissociated into atoms, the huge excess of energy within the plasma enables free electrons to remove outer electrons from the atoms creating positive cations,

the energy of the argon atoms being 15.76 eV. Although metals become completely ionized (ionization energies 7-8eV), non-metals or metalloids present within the sample are not usually fully ionized due to their higher ionization energies (approximately 12eV). Any remaining energy further excites the ion removing outer electrons into higher orbitals, **fig. 2.16.**

The ions only remain in the excited state induced by the plasma for short periods before falling back to more energetically favourable states. The energy difference between the energy levels is emitted as electromagnetic radiation, at either visible or ultra-violet wavelengths. Many lines occur within the spectra, due to the many potential energy levels that the ion can be excited to and several intermediate steps that the ion can relax to. A great number of these potential lines can be used to quantify the amount of the elements present within the sample; however careful consideration must be made when choosing the wavelength of light so as to avoid spectral interference.

For sample analysis one wavelength of the emission band is desirable. The desired wavelength is separated via a diffraction grating. The photons from the line are eventually detected using either a photomultiplier tube (PMT) or solid state detector ideally with as little energy loss between emission and detection as possible. The intensity of light emitted is then related to the concentration present within the sample.

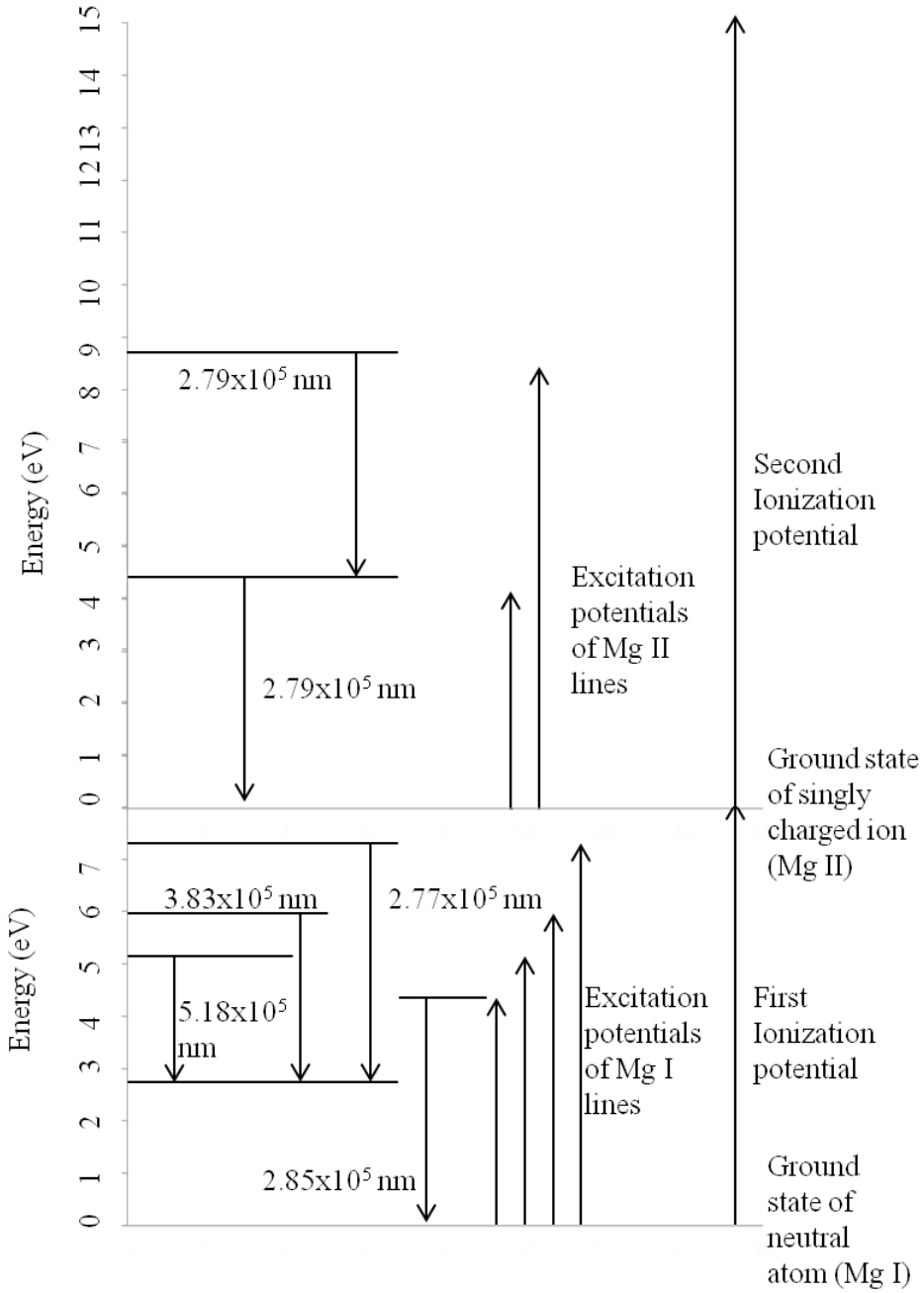

Figure 2.16. Energy level diagram for the excitation of magnesium, when placed into an argon plasma, for ICP analysis. Multiple excitations can be seen yielding multiple relaxations and the emission of different wavelengths of electromagnetic radiation, which can be used for qualification and quantification.

2.6.3. Calibration and Quantification

The relationship between intensity of the band and the mass of the element present is a proportional one. At low concentrations it is usually satisfactory to use only two standards to create a suitable calibration graph, a blank and a standard slightly more concentrated than the metal to be analysed. A greater number of standards can be used to create the calibration, although if there is no spectral interference this is often not necessary. The concentration of the upper calibration should be a factor of 100 above the detection limit to ensure good reproducibility and by being only slightly higher in concentration that the samples to be analysed reducing the error incurred by extrapolation, **fig. 2.17.**

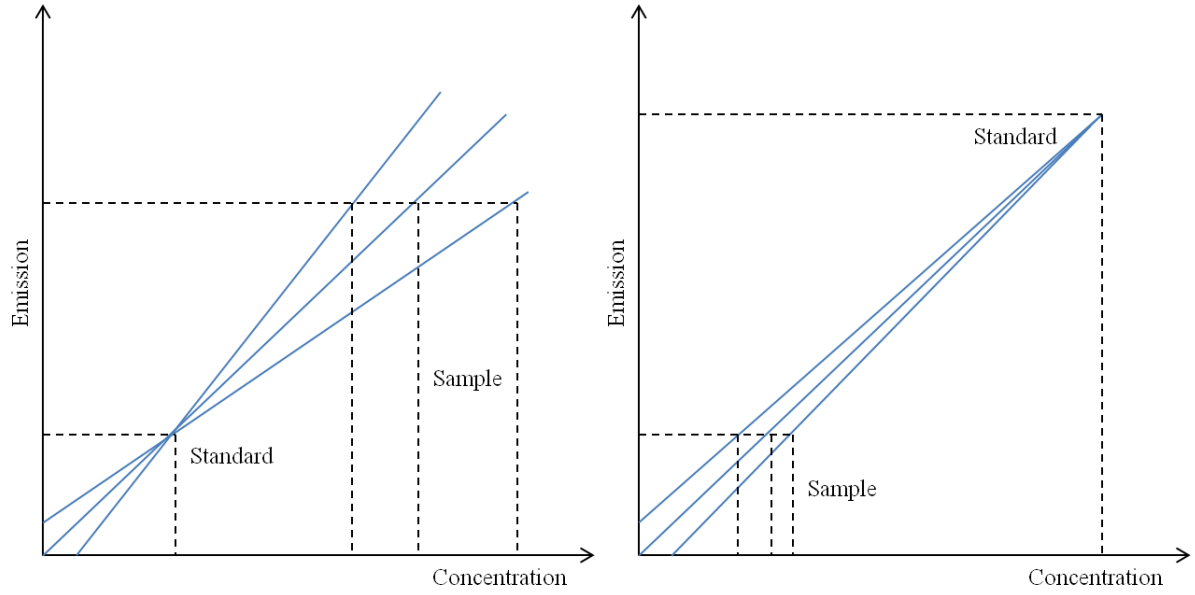

Figure 2.17. Error incurred due to extrapolation when determining concentration using too low a concentration of standard (right) and when too high a concentration is used (left).

Once the intensity of the band in the samples spectrum is known the concentration can be found from the calibration graph, and the weight percentage of the element within the

sample calculated. The weight percentage is calculated using the element(s) molecular mass to calculate the ratio of metals and therefore the molecular formula of the solid.

2.7. Determination of Particle Size Using Transmission Electron Microscopy (TEM)

Transmission electron microscopy is a powerful tool for electron diffraction spectroscopy and imaging. It is primarily used for imaging of nanoparticles and calculation of particle size in the nanotechnology field, if the nanoparticle images are clear enough and the particles prove to be non-agglomerated.

2.7.1. Instrumentation

TEM works much in the same way as conventional visible light microscopy. A beam of electrons is focussed upon a thin layer of the sample, prepared by dispersing the sample in a volatile solvent and applying this to the sample holder before letting the solvent, **fig. 2.18.** The beam that has been diffracted by the solid is then magnified through a series of lenses and condenser systems so that the beam is focussed onto the recording media, illuminated by a coherent plane-wave allowing the optics to form a negative image. [141, 142]

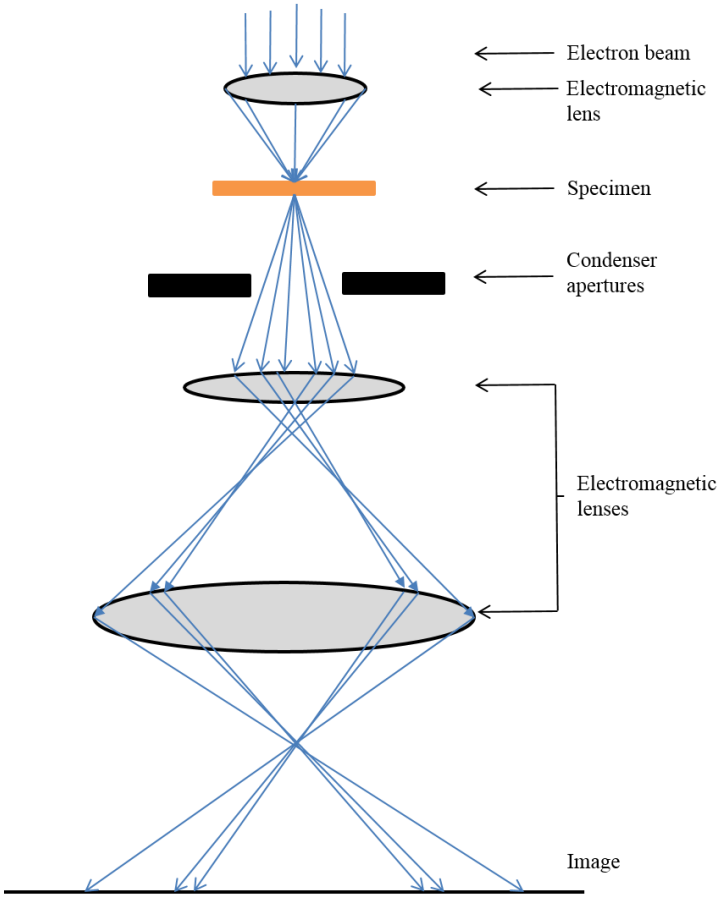

Figure 2.18. Schematic representation of transmission electron microscope (TEM), where an electron beam is first focussed onto a sample through a set of electromagnetic lenses, and the resulting diffracted electron beam is then used to create an image on an X-ray sensitive camera.

2.7.1.1. Electron Gun

The electron gun is responsible for the generation of the stream of electrons and their acceleration toward the sample. Several types of electron gun are used depending upon the source of the beam of electrons and their use; including Tungsten filament which are able to withstand high temperatures a LaB_6 single crystals which have longer lifetimes producing more intense electron beams at lower temperatures. Field emission guns however are most commonly used, producing more intense beams with a smaller energy spread, while operating at room temperature.

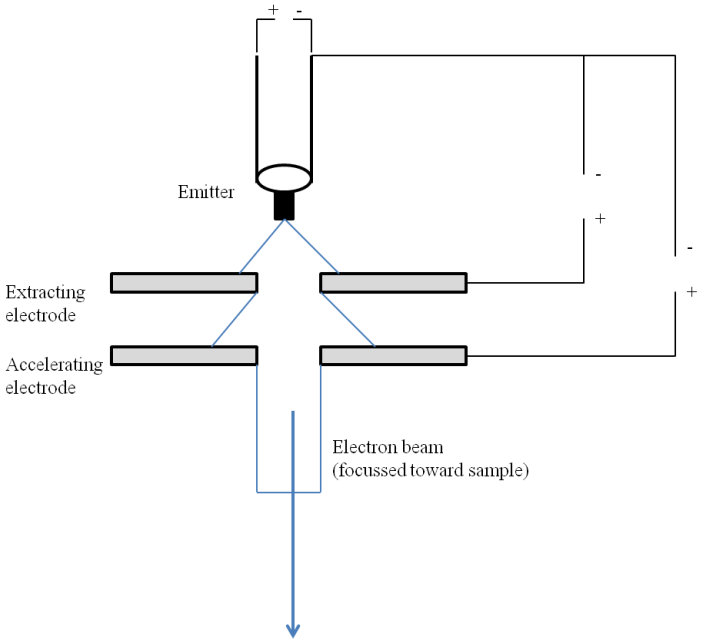

Figure 2.19. Schematic diagram of an electron gun, similar to an X-ray tube where electrons are accelerated away from a filament through the use of a potential difference, in this case the electrodes also act as apertures, focussing the electron beams.

The field emission gun uses the field emission effect, in which a highly charged electric field is applied to a metal crystal (the emitter) within a high pressure vacuum (10^{-8} Pa). A potential difference is then applied over the extracting electrode, a metal plate with a central hole, causing electrons to be emitted via the tunnelling effect. The beam of electrons emitted is focussed through the hole in the extracting electrode, and a second accelerating electrode used to accelerate these toward the sample, **fig. 2.19.** The wavelength of the beam can be calculated, **eq. 2.13.**, using Planck's constant, h, the mass of the electron, m_e, and the electrons velocity, v.

Equation 2.13.

$$\lambda = \frac{h}{m_e v}$$

By adjusting the potential difference placed over the two electrodes the energy and therefore the intensity of the electron beam can be altered, altering the image contrast.[143]

2.7.1.2. Lenses

A system of electromagnetic lenses is used to focus the beam of electrons diffracted by the sample onto the imaging equipment. Each lens can be individually focussed by altering the current within the lens coils. A series of condenser apertures are used to eliminate any electrons scattered from the beam by the lenses eliminating the production of X-rays from interactions between the electrons and the microscope housing.

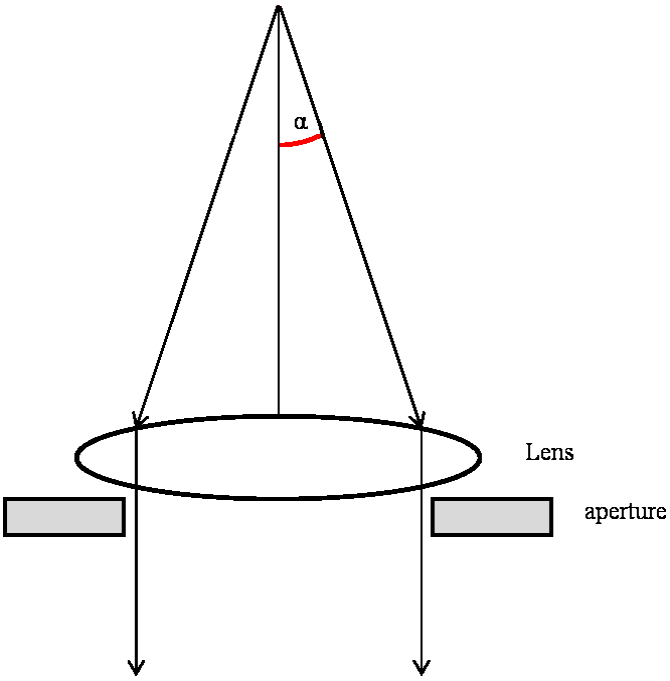

Figure 2.20. Representation of the semi angle, α, and its relationship with the resolution.

The objective lens placed below the specimen determines the resolution of the image. The resolution, *r*, of the microscope can be calculated, **eq. 2.14.**, using the wavelength of the electrons, λ, the refractive index of the medium between the object and the lens, μ, and the semi angle, α, above which the electron beam is stopped by the aperture, **fig. 2.20.**

Equation 2.14.

$$r = \frac{0.61\lambda}{\mu \sin \alpha}$$

The resolution can be increased (a decrease in *r*) by either decreasing the wavelength or by increasing either the refractive index of the lenses or the size of the aperture. The resolution of the TEM is limited by diffraction of the electrons which have shorter wavelengths than X-rays they have smaller Bragg angles leading to a resolution ≈ 1Å. The projector lens has a fixed focus designed to focus the electron beam into the recording equipment.

2.7.1.3. Image capture

The most commonly used techniques for recording TEM images are photographic film, imaging plates, real time video CCD cameras, and slow scan CCD cameras. Both photographic film and imaging plates can be used to record TEM images and diffraction patterns, but suffer from long development times and require additional software for analysis. The Real time video CCD cameras are used for focussing of the microscope image and searching small areas of the overall image and are rarely used for image acquisition. Slow-scan CCD cameras are commonly used for image capture producing high quality images and allowing for immediate data analysis.

2.8. BET Analysis using Tristar 3000

Two types of BET analysis exist for the determination of the amount of a gas adsorbed onto a solids surface, those relying on volumetric methods (the method discussed here) and those relying upon gravimetric methods.

To enable the determination of the adsorbents physisorption isotherm the adsorbent is first out gassed to remove any physisorbed species from its surface, before placing the adsorbent under a high vacuum (≈ 10 mPa). The chamber containing the adsorbent is then flushed with an inert gas, usually the adsorptive, to ensure surface cleanliness. This process is then cycled several times depending upon the nature of the adsorbent.[144]

After the final cycle of out gassing has taken place a known quantity of the pure gas is flushed over the adsorbent at constant temperature. As this gas is adsorbed the pressure within the vessel falls until equilibrium is achieved, the amount of gas adsorbed at the equilibrium point can then be calculated. The dead space volume is pre-calculated from the samples density or through filling the vessel with a non-adsorbent gas. The adsorption isotherm is constructed by following the variation in the volume of gas adsorbed over a range of pressures, the shape of which is heavily dependent upon the nature of the adsorbent.

2.8.1. Physiorption Isotherms

Depending upon the nature of the particles (solid, macro/meso/micro porous) the adsorption isotherms may take several different shapes, **fig. 2.21.**

Type *I* isotherms are exhibited by microporous solids which have an external surface area, where the amount of adsorption depends upon the volume of the micropore rather than the internal surface area.

Type *II* isotherms are exhibited by non-porous and macroporous solids where there is unrestricted adsorption for both the monolayer and multilayer. Point B, **fig. 2.21.**, is the point at which multilayer adsorption occurs and the linear section following this can be used to calculate the single point surface area.

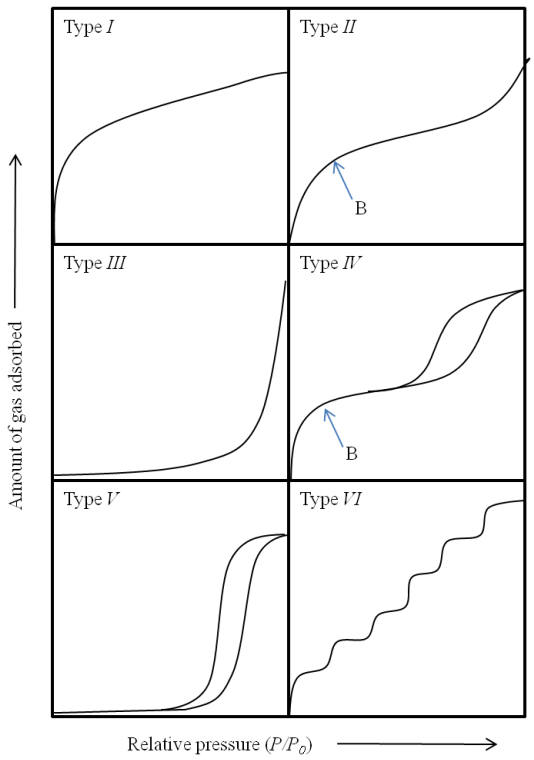

Figure 2.21. Visual representations of physisorption isotherms seen for the absorption/desorption of inert gasses onto different solid surfaces.[144, 145]

Type *III* isotherms are rarely exhibited, as they show gradual curvature and no definitive point B. These types of isotherms are usually associated with nitrogen adsorbing onto polyethylene where the interactions between adsorbate molecules have a greater effect.

Type *IV* isotherms are attributed to mesoporous materials in which capillary condensation occurs, particularly when adsorption of the adsorbant are similar to the type *II* isotherm, however desorption of the adsorbant occurs at lower relative pressures.

Type *V* isotherms only occur for porous adsorbents in which the adsorbent-adsorbate interaction is weak.

Type *VI* isotherms are the result of stepwise adsorption onto a non-porous surface. The step height represents the capacity of each monolayer while the sharpness of each step is heavily temperature dependent.

2.8.2. Calculation of Surface Area

Estimations of a samples surface area can be made through use of the "single point method" where the data from any single point in the BET range (the linear section after point B, **fig. 2.21.**) can be used. At any point upon the BET range as the BET constant, *C*, is assumed to be large enough for the intercept of the isotherm to be 0. The capacity of the monolayer, $\boldsymbol{n_m}$, can be calculated, **eq. 2.16.**, from the amount of substance, *n*, and the relative pressure of the adsorptive, P/P^0.

Equation 2.16.

$$n_m = n(1 - P/P^0)$$

The specific surface area, *a*, can then be determined, **eq. 2.17.**, from the average area occupied by each molecule within the monolayer, σ (for $N_{2(g)}$ = 0.162 nm^2 at 77 K).[145]

Equation 2.17.

$$a = n_m L \sigma$$

Where *L* is Avogadro's constant. The value of σ may change depending upon the temperature and the nature of the adsorptive and can be calculated, **eq. 2.18.** from the packing factor, *f*, for a hexagonal close packed system (1.091) and the molar mass of the adsorptive, *M*, and density, ρ.

Equation 2.18.

$$\sigma = f \left({}^{M}/_{\rho L} \right)^{2/3}$$

For more accurate measurement of the surface area the BET surface area must be calculated using the BET equation, **eq. 2.19.**

Equation 2.19.

$$\frac{{}^{p}/_{p^0}}{n\left(1-{}^{p}/_{p^0}\right)} = \frac{1}{n_m C} + \frac{C-1}{n_m C}\left({}^{p}/_{p^0}\right)$$

where *C* is the BET constant. If a BET plot is made of $(P/P^0)/(\mathbf{n}(1-P/P_0))$ against p/p^0 the slope and intercept of the line can be used to calculate $\boldsymbol{n}_m$ and *C*, **eq. 2.20 and 2.21.**

Equation 2.20.

$$n_m = \frac{1}{s+i}$$

And,

Equation 2.21.

$$c = \left(\frac{s}{i}\right) + 1$$

The specific surface area, *a*, can then be calculated in the same way as when using the single point method. Application of the full BET equation overcomes the assumption that the intercept equals 0 for a significantly high BET constant, which can cause significant errors within the single point method.

2.8.3. Calculation of Particle Size

Calculation of a nanoparticles size from either the BET or single point surface area, *S*, **eq. 2.22.** The particles are assumed to be spherical, the diameter, ϕ (nm), which can be calculated if the density, ρ, is known.[31]

Equation 2.22.

$$\Phi = \frac{6000}{\rho S}$$

The diameter calculated, however, can only be taken as an approximation as slight changes in density are often seen between bulk and nanomaterials. It is also assumed the particles are not aggregated, and that the isotherm is that of a type *II* compound.

2.9. Determination of Magnetic Properties Using Vibrating Sample Magnetometry

Characterisation of magnetic properties is performed using superconducting quantum interference devices (SQUIDs) or vibrating sample magnetometers (VSM), allowing magnetic properties such as saturation, coercivity and remanence to be calculated, from the hysteresis loops measured.

2.9.1. Vibrating Sample Magnetometry (VSM)

Vibrating sample magnetometry uses a variation upon the induction method, in which an electrical current is induced within a circuit by the movement of the sample placed within an applied magnetic field. The change in the magnetic induction in the space between a pair of electromagnetic pick up coils is measured when the sample is vibrated at 90° to the field which is magnetizing it.[13, 16, 146] An alternating current with a fixed frequency is generated within the pickup coils due to Faraday's law of induction as the sample is vibrated, **fig. 2.22.**, the change in induction, *B*, can then be related to the magnetization of the sample, *M*, **eq. 2.23.**

Equation 2.23.

$$B = B_0 + \mu_0 M$$

where μ_0 is the samples magnetic permeability. When the sample is within the magnetizing field the magnetic induction can be calculated through application of the magnetic fields strength, **eq. 2.24.**

Equation 2.24.

$$B = \mu_0(H + M)$$

Conversely the magnetic induction when the sample is vibrated out of the magnetic field can be calculated by, **eq. 2.25.**

Equation 2.25.

$$B = \mu_0 H$$

Therefore the change in the induction can then be calculated, **eq. 2.26.**

Equation 2.26.

$$\Delta B = \mu_0 M$$

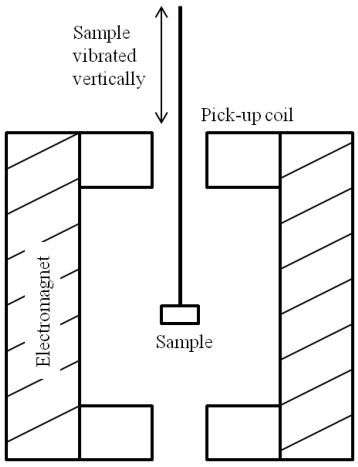

Figure 2.22. Schematic Diagram of a vibrating sample magnetometer, where a vibrating sample is subjected to an alternating magnetic field by electromagnets and the effect of the field strength monitored electrically through a pick up coil.

From the plot of the samples magnetization at variable field strengths a hysteresis loop is created, from which the materials saturation magnetization, M_s, magnetic remanence, M_r, and magnetic coercivity, H_c, can be calculated.

3.0. Method Development

Microreactors have been used to successfully synthesise nanoparticles.[98] The droplet coalescence technique for instance has been used to produce a wide variety of nanoparticles using microreactors, and the production of CdSe quantum dots, due to their fluorescence properties, has been automated using "black box" procedures which are crucial toward the scaling up to industrial scale.[114, 147-150]

The main challenge presented is producing nanoparticles so that particle adhesion upon the microreactor walls does not occur as this leads to blocking and inhomogeneous particle growth. Throughout this work the terms adhesion and blocking will be referred to, it is important to note that these are not the same thing. Particle adhesion refers to the build-up of particles upon the microreactor walls, which leads to an increase in back pressure due to narrowing of the channels, however the reagent flow still continues through the microreactor. Blocking refers to the point at which particle adhesion to them icroreactors has become thick enough to completely prevent the flow of reagents through the microchannels.

This has been achieved on proof of concept devices by intricate microreactor design or *ad hoc* modifications to existing microreactors, allowing the droplet coalescence or co-axial flow techniques, which prevent adhesion to the microchannel walls by isolating the nanoparticles from these.[100]

Microreactors utilising droplet coalescence use intricate microreactor designs and surfactants to continuously produce droplets of reagents with consistent volume in an immiscible carrier phase. The parameters within the microreactor (*e.g.* channel size, which affects the flow regime, and droplet size, flow rate, and surfactant concentration) can be used to adjust droplet size and therefore tune nanoparticles size.[101] The nanoparticles once produced are confined within the droplet preventing their adhesion to

the microreactors walls. Co-axial flow microreactors use a series of inlets designed to insert a single flow of reagents into the centre of another. Under laminar flow conditions the reagents mix through diffusion across the interface between the outer and inner flows. As the reaction proceeds at the interface between the two flows, particle adhesion does not occur upon the microreactor walls.

Both the droplet coalescence and co-axial flow techniques would be difficult to replicate upon a large scale, as it would prove difficult to run hundreds of these microdevices simultaneously in parallel, under identical conditions, e.g. the large volume of viscous immiscible carrier phase, required when using the droplet coalescence technique can lead to pressure drops on large scale systems.

As microreactors for the synthesis of organic chemicals and polymers are already in use in industry it appeared expedient to "reverse engineer" a technique for use on a pre-existing industrially used microreactor, rather than designing and producing a completely new synthetic microfluidic system, particularly as these microreactor designs have already been shown to be able Scaled up for larger scale syntheses.[151] When using these commercially available microreactors the design of the microreactors remains fixed, and no *ad hoc* adjustments can be made. The designs of the microreactors which were provided by Chemtrix.BV (**appendix 1**) are tailored toward liquid phase organic reactions, performed by the confluence of multiple reagent flows under laminar flow conditions.[152] All reactor designs comprise of one etched layer and one cover plate, with isotropic channels of a depth of 60 μm and width of 300 μm, the channel length and the number of inlets varies with design, **fig. 3.1.** As the reactor designs were not obviously suited toward the production of nanoparticles and no *ad hoc* modifications could be made to prevent particle adhesion, a technique had to be developed so as to enable nanoparticle production using these systems while limiting these problems, herein the development of this method is discussed.

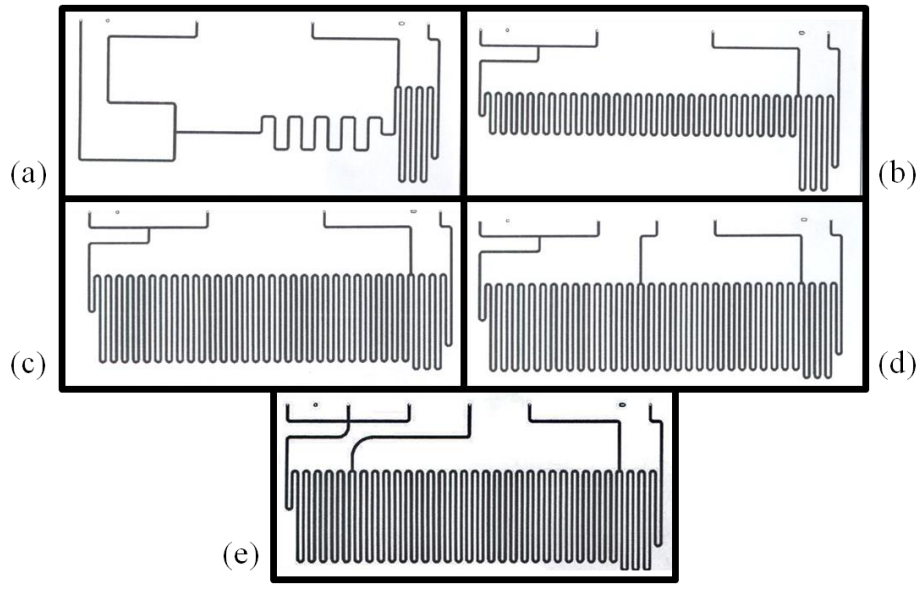

Figure 3.1. Microreactor designs 3021 (a), 3022 (b), 3023(c), 3024(d), and 3025 (e), used when developing the continuous flow focused technique. The exact details of each of these designs including microchannel dimensions can be found in the appendices.

3.1.1. Initial Experiment Design

Microreactor 3025 comprised of one etched layer and one cover plate, with isotropic channels of a depth of 60 μm and width of 300 μm (volume 10 μl). The reactor design allows for the confluence of three single reagent flows at the cross junction, which can be used to form droplets by shearing of the aqueous flow using an immiscible carrier phase. The cross junction was considered to be similar to two T-junctions placed next to one another, due to the large width of the microchannels (300 μm). Production of droplets using T-junctions occurs by introducing the reagent stream perpendicularly into an immiscible carrier stream. The perpendicular nature of the flows causes droplet formation via a mechanism of tearing, shearing and pinching of the reagent flow by the carrier flow.[106, 153] **Fig. 3.2.**, shows a schematic of microreactor 3025 set up for these experiments.

Encapsulation of the aqueous flows was hypothesised to occur in one of two ways, depending upon the flow rate ratio between the carrier and aqueous phases. The reagents would either be present as small droplets not contacting the microreactor walls when the total flow rate ratio was low, **fig. 3.3.a.**, due to the effect of flow rate upon capillary number, or plugs of the aqueous phases which contact the microreactor walls would be formed at higher total flow rate, as more disorganised flow regimes are favoured, **fig. 3.3.b**. Mixing of the reagents within the droplets would then occur across the interface within the droplet by the slow process of diffusion, and possibly through chaotic advection caused by the movement of the droplet through the U-bend within the serpentine microchannel.[106, 154]

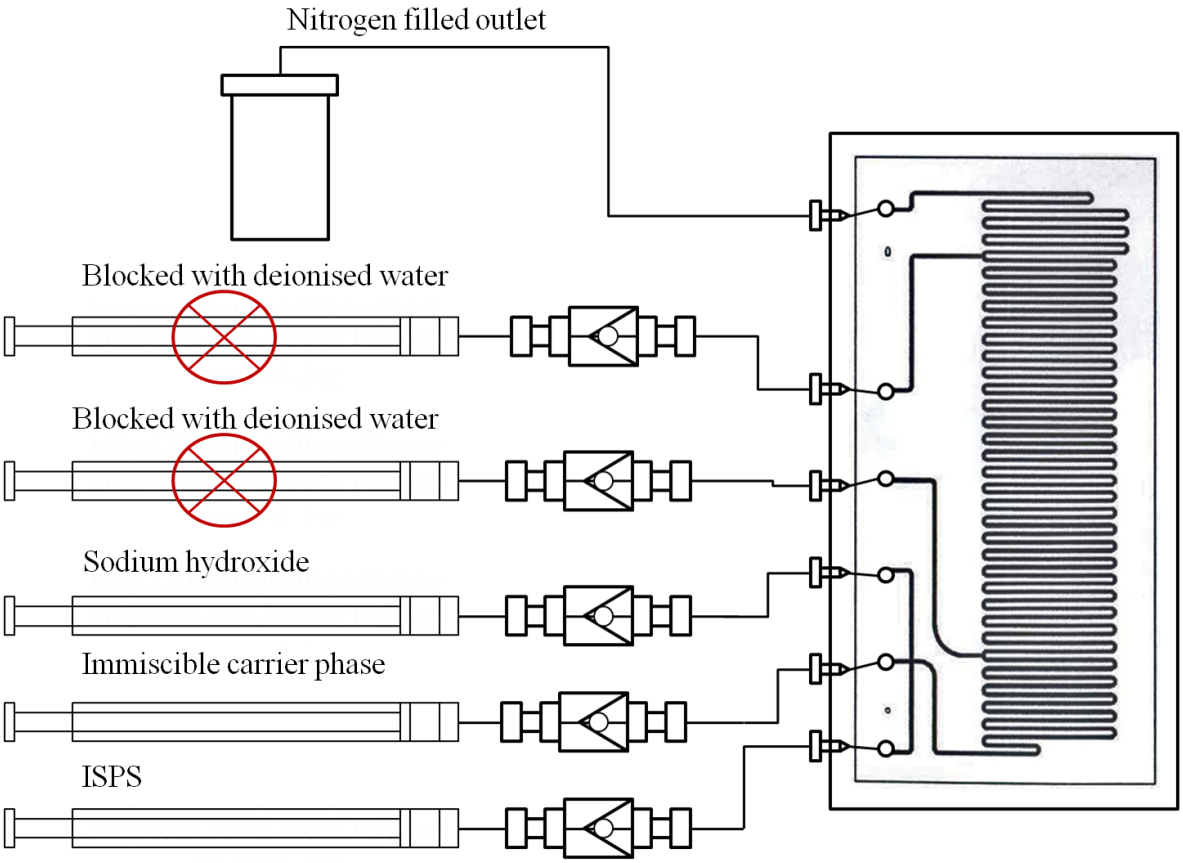

Figure 3.2. Schematic design of the initial droplet coalescence experiment using microereactor design 3025, in which the three inlets at the T-Junction are used, to create a droplet of two merged aqueous flows using an immiscible carrier phase. The remaining inlets are blocked.

Initially a flow of hexane was used as the immiscible carrier phase due to its lower toxicity and environmental impact than that of the perfluorocarbon oils commonly used in proof of concept research. The hexane flow was pumped through the central inlet at a high flow rate (800 µl hr^{-1}) so that the two reagent flows, an iron salts precursor solution (ISPS), and a concentrated base solution pumped into the central channel perpendicularly through the outer channels.

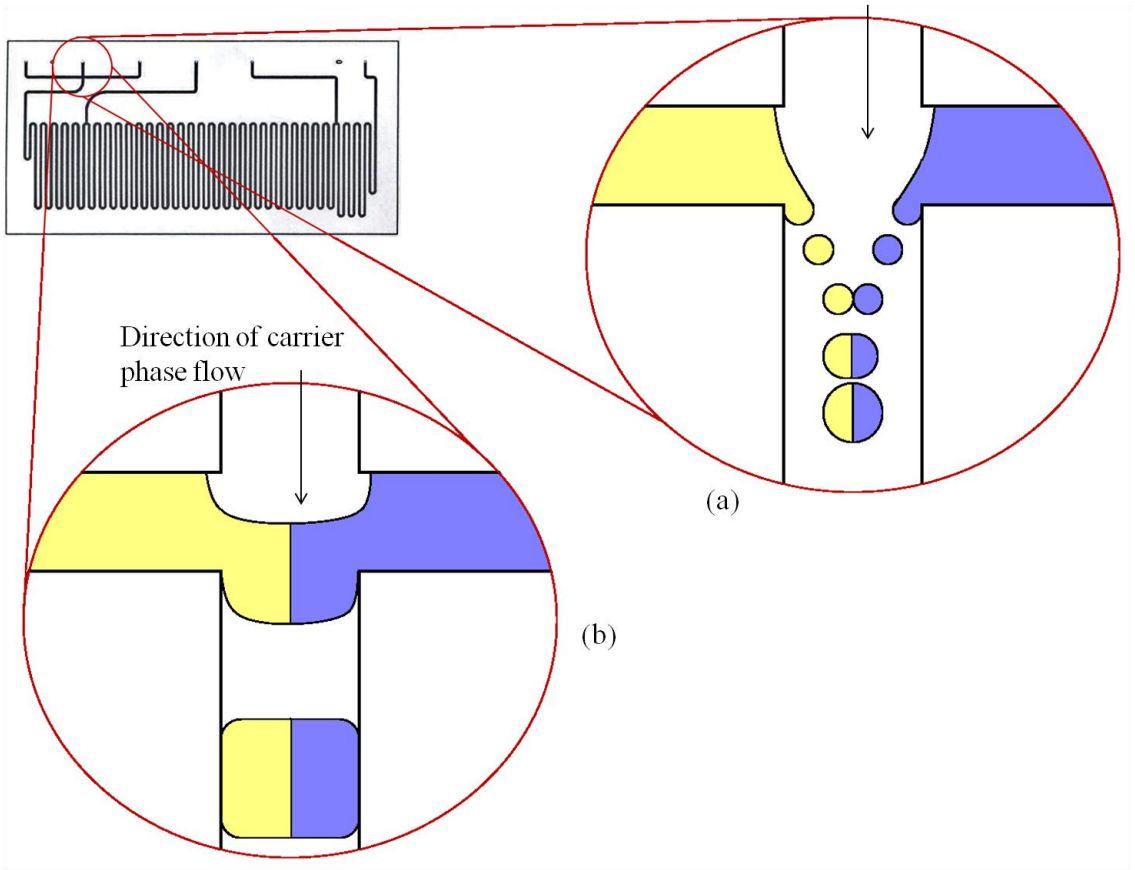

Figure 3.3. Hypothesised droplet formation in the cross-junction of microreactor 3025, where droplets were hypothesised to form first before merging due to the higher flow rate (a), or where plugs were hypothesised to form at low flow rate ratios, by the two aqueous streams first merging and then being pushed through the microchannel as a plug (b).

The ISPS was formed from a mixture of $FeSO_4.7H_2O$ (0.0125 mol dm^{-3}), $Fe_2(SO_4)_3.xH_2O$ (0.0125 mol dm^{-3}) dissolved in hydrochloric acid (0.11 mol dm^{-3}). Sodium hydroxide (0.2 mol dm^{-3}) was used as the base. These were pumped into the microreactor using Chemyx mechanical syringe pumps at 400 µl hr^{-1}, while the immiscible carrier phase was infused into the microreactor at a rate of 800 µl hr^{-1} (total flow rate = 1600 µl hr^{-1}). These flow rates were the equivalent of those used in the work of Frenz et.al., of which this droplet coalescence method was based upon.[108] Iron sulphates (iron (II) sulphate and/or iron (III) sulphate) and iron chlorides (iron (II) chloride and/or iron (III) chloride), are well documented with the reaction of iron(II) chloride and iron (III) chloride with a strong

base (tetramethyl ammonium hydroxide) the most commonly used reaction[19, 155] sodium hydroxide was chosen as the base for its lower toxicity and environmental impact in comparison to the ammonium hydroxide variants (tetramethylammonium hydroxide), used in other works, keeping in mind the idea of making this technique as compatible with industry as possible.

Shearing of the reagent streams was observed to produce large polydisperse plugs, with precipitate adhesion occurring upon the microreactor walls, culminating in back pressure issues and blocking of the microreactor, **fig. 3.4.** The cause of the precipitate adhesion to the microreactor walls was considered to be due to the hydrophilic nature of the glass microchannel surface. The aqueous reagents caused droplets, of what was initially intended to be the immiscible carrier phase, to form within the aqueous reagent streams, due to the preferential wetting of the microreactor walls by the aqueous reagents instead of the silicone oil. The preferential wetting of the microreactor walls by the aqueous reagents, allowed the walls of the microchannels to act as sites for nucleation and growth of the nanoparticles, leading quickly to particle adhesion of the nanoparticles, and increased back pressure. The passing of a droplet of silicone oil through the aqueous reagents was seen to disrupt some of the adhesion, forcing this from the walls, but did not prevent particle adhesion enough to prevent blocking of the microchannel by the nanoparticles. To solve this, a series trial and error experiments were adopted and development of a technique attempted for synthesis of IONs within the microreactor using droplet coalescence.

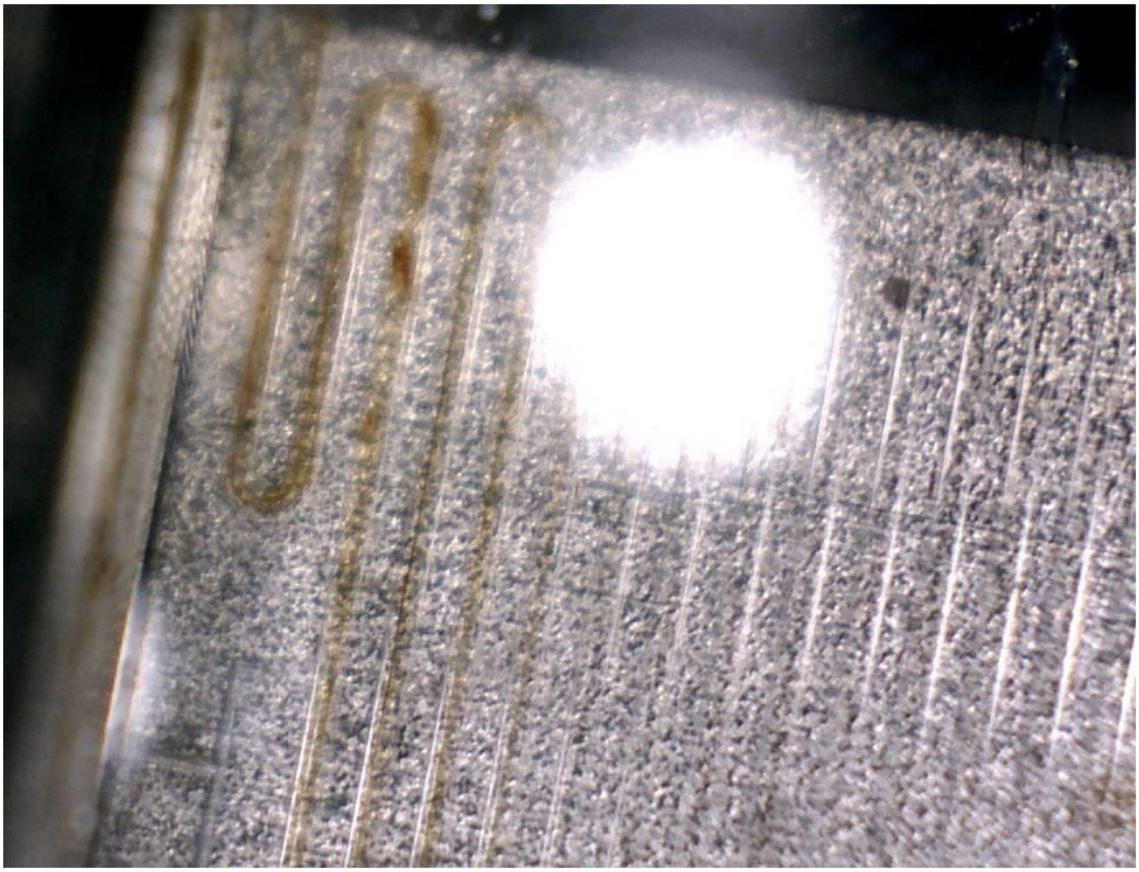

Figure 3.4. Nanoparticle build up upon the walls of the microreactor during the initial droplet coalcescence method experiment. A thin coating of nanoparticles was oserved upon the micrreactor walls. This formed in the area of the microchannel just after the cross junction, it is hypothesised that this occurred due to the preferential wetting of the microchannel walls allowing these to act as a site for nucleation and growth of the nanoparticles, so that droplets of silicone oil were instead transported through the aqueous reagent flows.

3.1.2. Hydrophobic or Hydrophilic Microchannels

As the failure of the initial experiment was due to the preferential wetting of the microreactor walls by the aqueous phases, the surface of the microreactor walls was modified to become hydrophobic, enabling the immiscible carrier phase to preferentially wet the walls, partially stabilising the droplets, so that the reagent flows were

encapsulated and the reaction would proceed without precipitate adhesion to the microreactor walls.

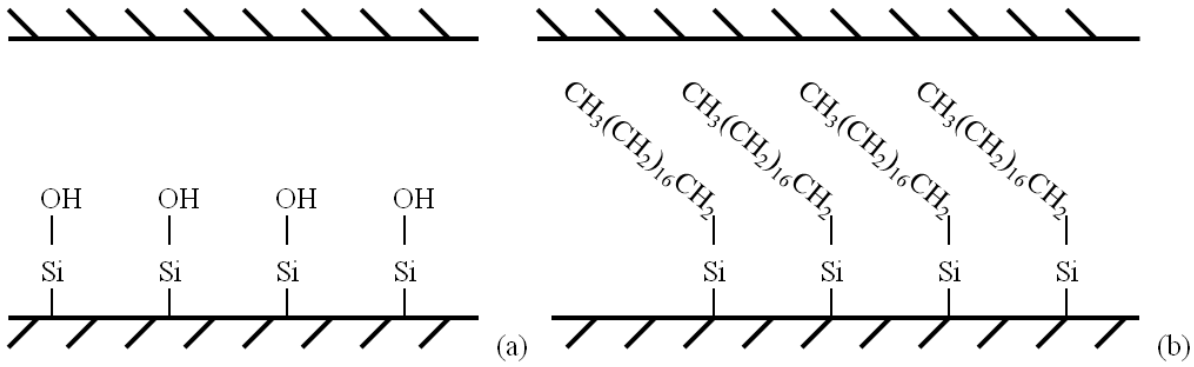

Figure 3.5. Diagrams of a normal hydrophilic microchannel wall (a), and hydrophobic microchannel wall coating after heating of chlorodimethyl-octadecysilane while being infused through the microreactor at a constant rate (b).

The surface of the microreactor walls was coated in a hydrophobic layer by heating (80 ˚C) a solution of chlorodimethyl-octadecylsilane (chlorodimethyl-octadecylsilane in toluene, 0.1 g ml^{-1}) which was pumped through the microreactor at 200 µl hr^{-1}. This causes coating of the silica surface with long chain hydrocarbon groups, $CH_3(CH_2)_{16}CH_2$-, **fig. 3.5.** This method was suggested by Dr. C.Wiles, and is commonly used by CHEMTRIX.BV., when developing methods which require a temporary hydrophobic coating on the channels surface. The thermal decomposition of chlorodimethyl-octadecylsilane is a commonly used method for the synthesis of silica nanoparticles with hydrophobic surfaces.[156]

The experimental method laid out in **section 3.1.1.**, was then re-performed using the hydrophobic chip. Droplet formation was noted within the microreactor and initially the reaction appeared to proceed within these, noted by a colour change within the droplets, which became progressively darker throughout the serpentine portion of the microreactor. Precipitation however, did not take place exclusively within the droplets, as particle adhesion was noted to occur, but over a much greater area of the serpentine microchannel.

Problems with reproducibility were also noted as when repeated extensive blocking occurred throughout the serpentine microchannel due to this particle adhesion.

3.1.3. Choice of Carrier Phase

As the problem of particle adhesion could not be solved through changing the hydrophobicity of the microreactor surface, the type of carrier phase was altered in an attempt to better encapsulate the reagents. Wang *et.al.*, were seen to use silicone oil as a carrier phase when producing gold nanoparticles using the droplet coalescence technique, within a simple proof of concept design.[147] Switching from hexane to silicone oil could also have been advantageous due to its heat transport properties and higher boiling point (> 200 °C compared to 69 °C for hexane), which could be expedient if higher temperatures were required for formation of more highly crystalline nanoparticles. Silicone oil has a lower toxicity than either hexane or perfluorocarbon oils. The experimental procedure and microreactor setup remained the same as that used in previous experiments using the microreactor with the hydrophilic coating, not that used in **section 3.1.2.**, **fig. 3.2.**, with the exception of the PEEK tubing used. The PEEK tubing had a larger internal diameter (ID) of 125 μm, to cope with the extra pressure involved with pumping the more viscous silicone oil.

Plugs of uniform size were initially seen, and appeared to contain the reagents, as a colour change was noted within them, becoming progressively darker when moving through the microreactor. Precipitate adhesion was also noted to occur more slowly upon the microreactor walls, the length of time required for complete blocking of the microchannel to occur was seen to increase from 30 seconds to several minute.

3.1.4. Altering Flow Rate Ratio

Testing the use of different carrier phases was concluded by altering the flow rates of these; as the flow rate can have a large effect upon the flow regimes present within the microchannel, and preventing the wetting of the walls by the aqueous phases.[88] It was further hypothesised that at higher flow rates the precipitate build up upon the microreactor walls would also be disrupted due to the force implied by the reagents moving through the microchannel at a higher rate. The flow rates of the aqueous reagents was altered between 100 to 800 µl hr^{-1}, while the flow rate of the carrier phase was kept constant at 800 µl hr^{-1}.

3.1.4.1. Silicone oil

When using flow rates greater than 800 µl hr^{-1} and 500 µl hr^{-1}, (carrier phase and aqueous phases respectively), a greater proportion of droplets were seen to contain the reagents, due to a darkening of these as they moved through the microreactor. Precipitate adhesion along the inlet was also noted as well as the serpentine microchannel, but seen to be greatly reduced. Disruption of the precipitate adhesion was noted, as some was seen to become displaced due to the pressure build up behind. The precipitate was seen to first shift slightly along the microchannel before breaking loose from the surface and breaking up as it is pushed out of the microreactor, **fig. 3.6.** Back pressure issues however, led to poor reducibility, with leakages occurring at check valves and luerlocks.

At flow rates of 800 µl hr^{-1} to 400 µl hr^{-1}, carrier phase to aqueous phase, precipitate adhesion was seen to be more severe, occurring at the cross-junction, leading to blow through of precipitate. At aqueous flow rates between 400 µl hr^{-1} and 100 µl hr^{-1}, particle adhesion led to blocking of the microreactor in under 5 minutes.

3.1.4.2. Hexane

At flow rates higher than 800 to 400 µl hr^{-1}, carrier phase to aqueous phase, particle adhesion was still observed , but total blocking of the microchannel prevented, however pressure issues were seen to occur due to the narrowing of the channels by the particle adhesion, leading to an increase in back pressure. At flow rates less than 800 µl hr^{-1} to 400 µl hr^{-1}, carrier phase to aqueous phase, droplets with near uniform sizes were seen, however particle adhesion led to blocking within a minute of the reactions being run (approx. 20 µl of ISPS) the lower flow rates appeared to not provide enough force to remove particles from the microreactor walls.

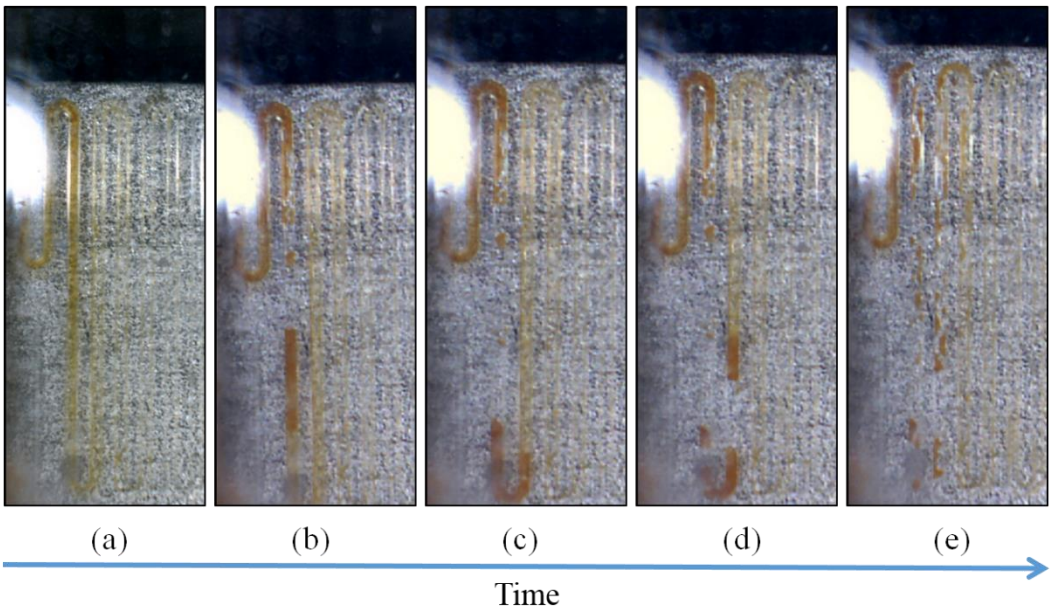

Figure 3.6. Precipitate adhesion to the microchannel walls and its subsequent "un-blocking" as the pressure builds up behind the precipitate. First precipitate begins to build up on the walls (a), this builds up until a point of critical mass is reached (b), where the enough particles have adhered to the microchannel walls to affect the flow rate. Pressure behind the blockage then increases, shunting this further through the serpentine microchannel (c), this gradually loosens the blockage (d), until it has broken up enough to be blown through the microreactor (e). The entire process happens over the course of a few seconds.

Due to the technical limitations, the leaking at check valves, luerlocks, and on occasion syringes breakage, flow rate above 800 μl hr^{-1} for both the oil flow rate and both aqueous reagent streams were not attempted when using either carrier phase.

3.1.5. Altering pH of Reagents

The solutions of iron salts used by both Frenz *et.al.*, and Abou-Hassan *et.al.*, employed hydrochloric acid to stabilise the Fe^{2+} cations against oxidation.[102, 108] It was hypothesised that the concentration of the acid present in the ISPS could also be used to help delay the formation of precipitate, as this would first be neutralised by the base, owing to the faster diffusion rates of H^+ and OH^- in comparison to that of the Fe^{2+} or Fe^{3+} cations. If precipitation is delayed so that precipitate adhesion upon the microreactor walls was spread over a greater area or lessened by this delay, the force of higher flow rates could be used to prevent complete blocking of the microchannel.

A slight increase in the concentration of hydrochloric acid in the ISPS (10% v/v to 15% v/v) led to the delaying of precipitate formation until the serpentine portion of the microchannel, allowing for a greater volume of reagents to be used, instead of blocking after 100 μl of ISPS was pumped into the microreactor, blocking would not occur until 300-400 μl of ISPS was pumped into the microreactor.

When concentration of the sodium hydroxide solution was increased, precipitation occurred much faster, often leading to clogging of the microreactor at the cross junction as was expected. The increase in back pressure created by the precipitate, was seen to loosen the blockages and at concentrations of 2.00 mol dm^{-3} precipitation but was not enough to cause complete blocking, much of the build-up was seen to be blown through the microreactor.

3.1.6. Summary - Adapting Droplet Coalescence Method

Encapsulation of the co-precipitation reaction between an ISPS and base, within an immiscible carrier phase, without the use of surfactants, was attempted. Several different parameters were adjusted in an attempt to find a set of conditions in which the reaction could be performed without blocking the microreactor due to precipitate build up, allowing for the technique to be used reliably. It was observed that droplet shearing occurred at the cross junction of microreactor design 3025, however the precipitate synthesised adhered to the microreactor walls leading to blocking of the microreactor, this was thought to be due to the preferential wetting of the microreactor walls by the aqueous reagents. A hydrophobic surface was created within the chip to prevent this, however, particle adhesion was found to spread throughout the serpentine portion of the microchannel, leading to substantial blocking. A series of parameters were then altered in an attempt to control this particle adhesion. The carrier phase was altered from hexane to silicone oil, increasing the time taken for particle adhesion to occur, allowing for greater volumes of reagents to be used before blocking occurred. The flow rates of the aqueous phase were tailored to further prevent blocking, at higher flow rates the volume of reagents which could be used before this occurred, was seen to double, although at these high flow rates back pressure issues, in the form of leakages from the connections

and valves, were also noted. To further decrease particle adhesion the pH of the reagents was decreased, although decreasing particle adhesion was noted, blocking was still seen to occur. Therefore a change of technique was implemented, and the continuous flow technique adapted to produce IONs within the microreactor.

3.2. Continuous Flow Techniques

Continuous flow techniques utilise the scaling phenomenon of laminar flow to keep streams of fluids separated, this in effect allows for the control of the reactions using time, as the mixing of reagents is based upon rates of diffusion across the microchannel, discussed in detail in **section 1.5.**[88]

As mixing is predominantly diffusion based under laminar flow conditions, theoretically nanoparticles can be synthesised with highly controlled sizes. Microreactors utilising continuous flow, however, often suffer from particle adhesion to the microreactor walls and related blocking due to wetting of the microchannel walls.[157-159]

Ion	Molecular Diffusion Coefficient (m^2s^{-1}) [160, 161]	Diffusion Distance (m)	Diffusion Time (s)
Fe^{2+}	1.44×10^{-5}	3×10^{-4}	0.0031
Fe^{3+}	1.81×10^{-5}	3×10^{-4}	0.0025
OH^-	5.27×10^{-5}	3×10^{-4}	0.0008
H^+	1.87×10^{-5}	3×10^{-4}	0.0024

Table 3.1. Calculated diffusion times across a microchannel for several common ions used within this work, based on molecular diffusion coefficients obtained from the CRC handbook of physical chemistry.[160, 161]

Previous work by Abou Hassan *et.al.* had utilised continuous flow in their co-axial flow technique which helped to prevent adhesion.[102] The failure to adapt the droplet coalescence technique for use upon commercial microreactor systems led to the use of the continuous flow technique upon the commercially available microreactor systems. The complex nozzle design used by Abou Hassan *et al.*, could not be replicated upon the mircroreactor systems used in this work and as such the co-axial flow technique could not be used. This groups work did suggest however that the particle adhesion upon the microreactor walls could be limited, if not completely prevented, using a continuous flow technique.

3.2.1. Initial Continuous Flow Experiment

Initially chip design 3025 was used; a flow of MilliQ water was pumped through the central inlet, separating the two reagent flows within the serpentine microchannel, **fig. 3.7.** The flow of MilliQ water was used as it was thought that it would prevent particle adhesion at the cross junction, as the reagent streams would first have to diffuse through this before reacting with each other. The concentration of iron (II) sulphate and iron (III) sulphate within the ISPS were 0.01 and 0.02 M respectively, made by mixing equal volumes of the two iron salts solutions. A solution of 1.00 M NaOH was used as a base. Higher flow rates could now also be utilised without back pressure issues, each flow was introduced into the microreactor at 1000µl hr^{-1} per flow (total flow rate = 3000 µl hr^{-1}).

Particle adhesion upon the microreactor walls occurred before 50 µl of reagents could be pumped into the microreactor, approximately 1 minute into the experiment, leading to blocking.

In an attempt to solve this, the reagents were further diluted ($FeCl_2$ = 0.005 M, $FeCl_3$ = 0.01 M), however, this led to no nanoparticle formulation as the concentrations then appeared to be too low.

Several sets of experiments were therefore devised to investigate the effect of several parameters upon nanoparticle formation, and adhesion, including the chip design to limit particle adhesion while ensuring they were still formed.

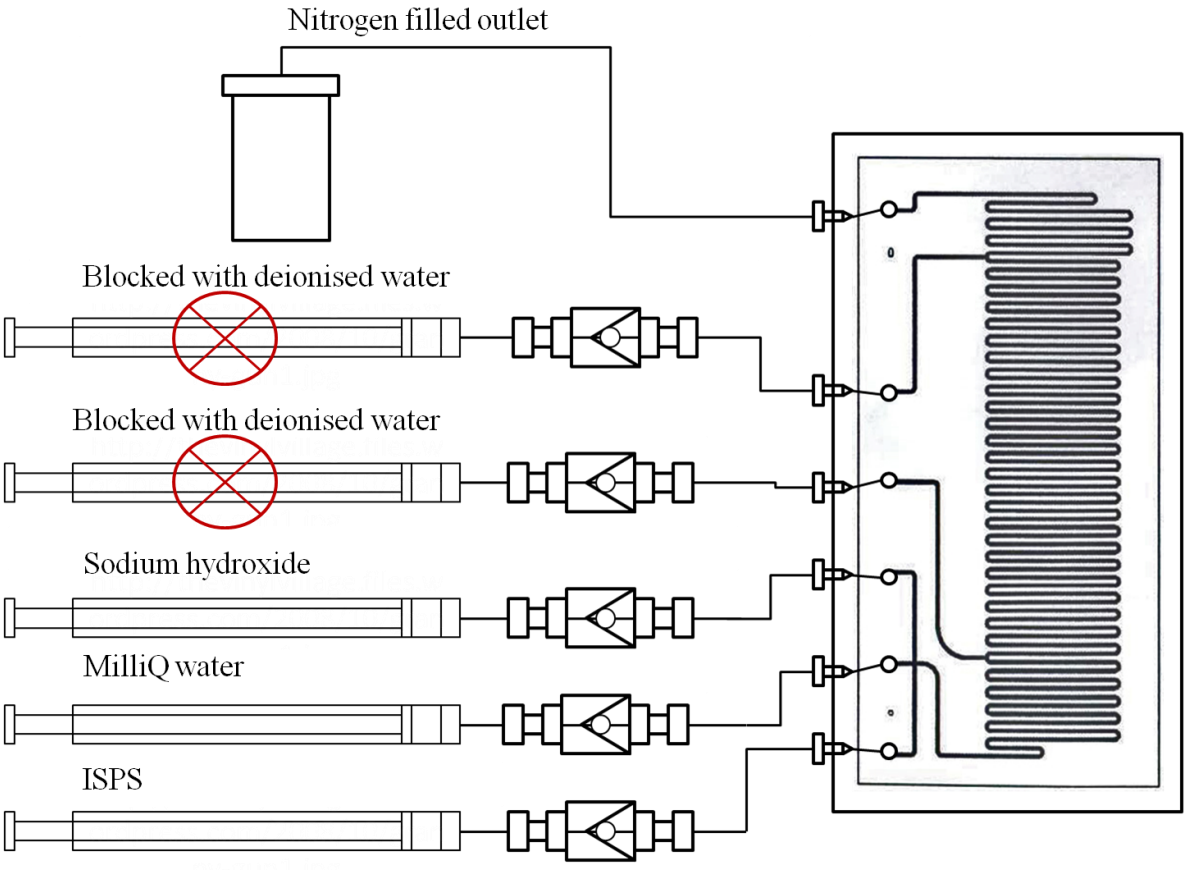

Figure 3.7. Schematic diagram of the attempt to synthesise iron oxide nanoparticles using microreactor design 3025, an ISPS and NaOH base, were infused through the outer inlets of the cross-junction while a central flow of MilliQ water, was used to seperate and dilute reagents.

3.2.2. Altering Flow Rate of Reagent Streams

The flow rates of the reagents were first altered in an attempt to limit the particle adhesion, due to the effect this had upon particle adhesion when using the droplet coalescence technique. Microreactor design 3021 was implemented; this design allows for the confluence of two flows at a T-junction, with a relatively short residence time as only a small length of serpentine microchannel is present, **fig. 3.8.**

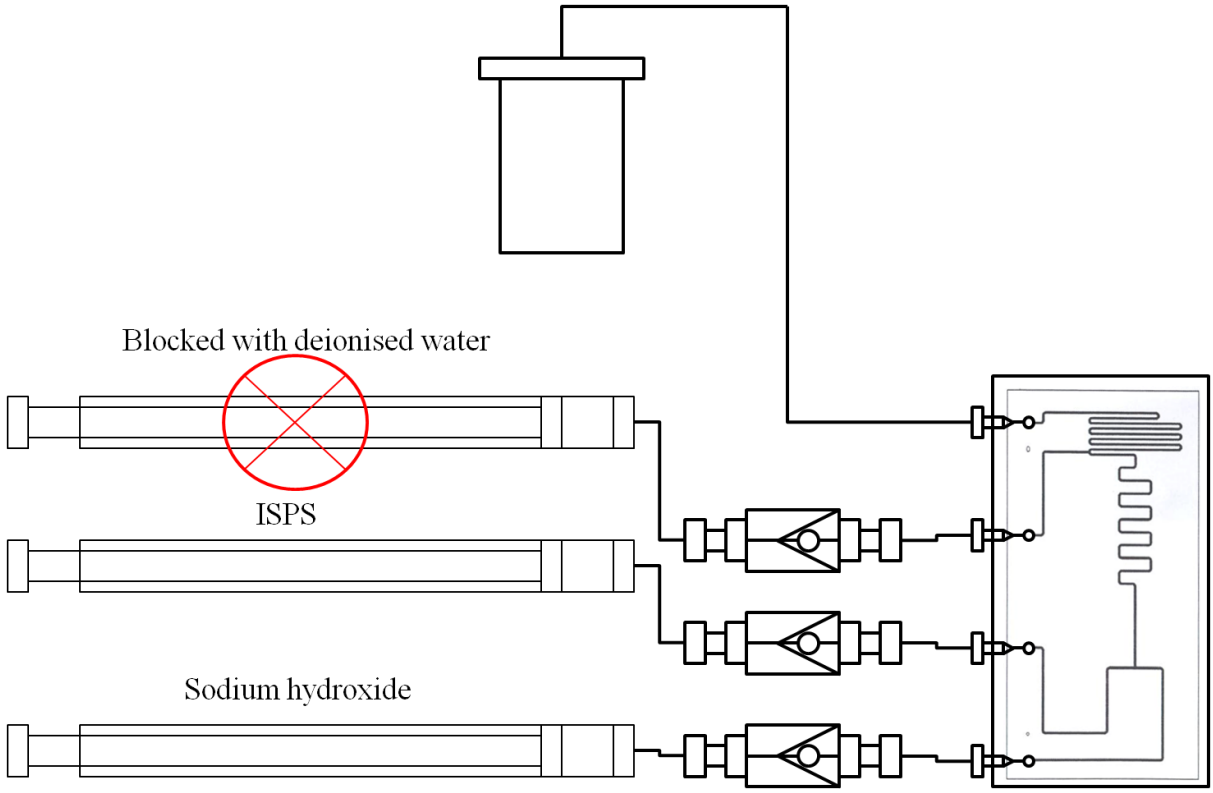

Figure 3.8. Schematic diagram of microreactor 3021, used to test the effect of different flow rates (total flow rate 2000 - 6000 µl hr^{-1}) upon particle adhesion when utilising continuous flow. Particle detachment from the microreactor walls was noted to increase with increasing flow rate, leading this to be "blown through" and collected at the outlet.

The concentrations of both iron (II) sulphate and iron (III) sulphate salts were (0.01 and 0.02 mol dm^{-3}, respectively) in the ISPS, the sodium hydroxide (1.00 M) solution was

used as a base, each flow was injected into the microreactor at varying flow rates (1000 - 3000 μl hr^{-1} per flow, total flow rate 2000 - 6000 μl hr^{-1}).

At a flow rate of 1000 μl hr^{-1} per flow particle adhesion was seen to increase rapidly with blocking of the channels occurring after 100 μl of ISPS had been pumped into the microreactor (approx. 2 minutes). As the flow rate of the flows was increased toward 2000 μl hr^{-1} per flow the time taken for total blocking to occur could be seen to increase (approx. 5 minutes). Particle detachment from the microreactor walls was also noted to increase, leading this to be "blown through" and collected at the outlet.

At flow rates of 2000 – 3000 μl hr^{-1} per flow, constant blow through of precipitate was noted and the volume of reagents required for complete blocking to occur was seen to increase to ≈ 400 μl (approx. 8 minutes of running time). Blocking of the microreactor was still seen to occur however, even at maximum flow total flow rate of 3000 μl hr^{-1} per flow, and therefore particle adhesion could not be controlled through simply controlling the flow rate.

3.2.3. Effect of Increasing Acid Concentration in ISPS upon Particle Adhesion

As increasing acid concentration was seen to limit the particle adhesion whens using droplet coalescence, the concentration of acid within the ISPS was increased (H_2SO_4 from 0.11 M to 0.45 M, 0.5 M, or 0.55 M) when performing the continuous flow reactions. Microreactor design 3023 was used, where confluence of the reagent streams occurs at a T-junction, with a longer microchannel than design 3021. The ISPS was altered as the iron (II) sulphate and iron (III) sulphate salts were dissolved in dilute sulphuric acid the concentration of which was varied. The iron (II) sulphate, iron (III) sulphate, and sodium hydroxide concentrations were kept at those used in the previous experiment (0.01 M,

0.02 M, and 1.00 M, respectively) an excess of sodium hydroxide was employed to induce precipitation, **fig. 3.9.** Each flow was pumped into the chip at 1000 μl hr^{-1}.

As when hydrochloric acid was employed to delay precipitation when droplet coalescence was used to synthesis IONs, an increase in the volume of ISPS was noted before blocking occurred was noted. When the iron salts were dissolved in sulphuric acid (0.45 mol dm^{-3}), particle adhesion upon the microreactor walls was noted leading to blockages near the inlet. The amount of particle adhesion was seen to be reduced when the sulphuric acid concentration was increased to 0.5 mol dm^{-3} and no blocking was seen to occur, at concentrations of sulphuric acid greater than 0.55 mol dm^{-3}, however, this concentration was often seen to be too high, dissolving particles at the outlet.

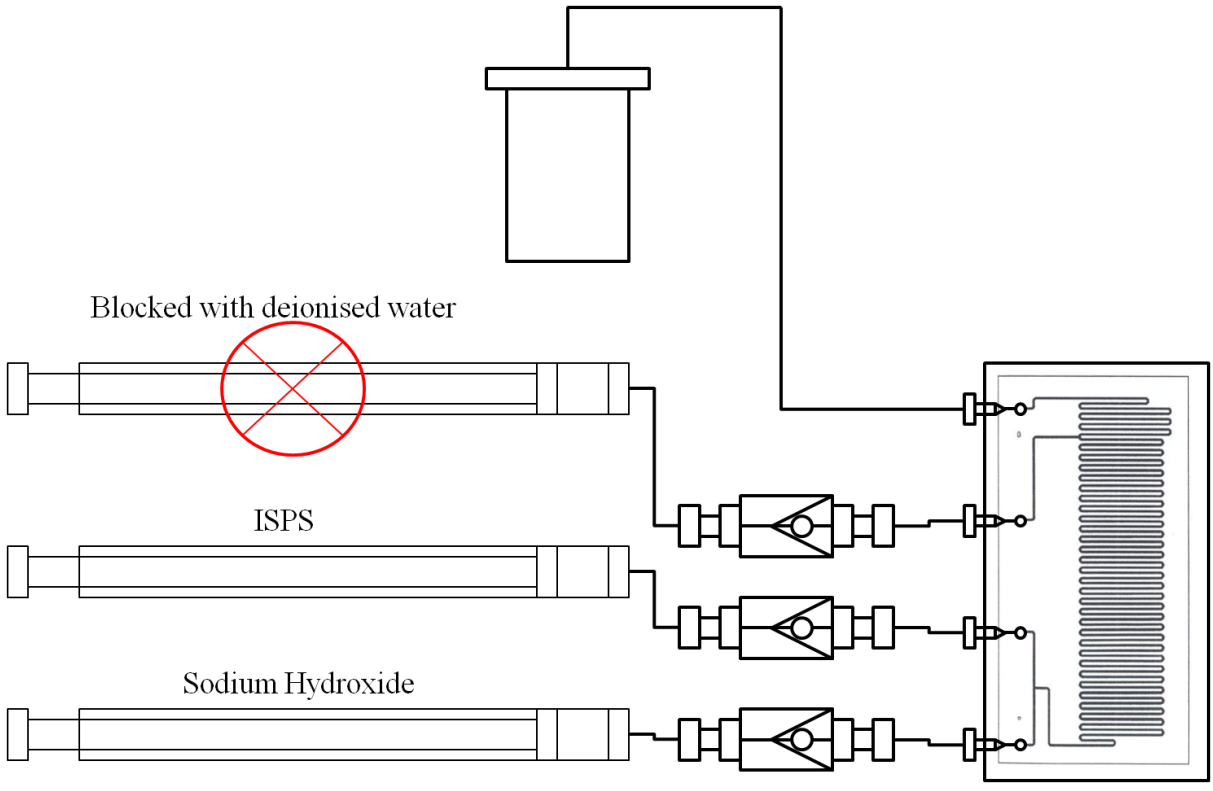

Figure 3.9. Schematic diagram of microreactor 3022 system used when investigating the effect of increasing acid concentration upon particle adhesion.

3.2.4. Flow Focussing of the Reagent Streams

Although altering the acid concentration and flow rate of the reagents had made a significant difference in limiting adhesion to the microreactor walls, both failed to solve the problem of blocking caused by particle adhesion. An idea was finally conceived in which the ISPS was constrained in 2D laterally across the microchannel by the sodium hydroxide flows, similar to the constraining of the nanoparticles in 3D in the co-axial flow technique performed by Abou-Hassan *et.al.*[102]

By constraining the flow of the ISPS laterally across the microchannel it was thought that precipitate adhesion would be reduced. Inserting the ISPS flow between two flows of sodium hydroxide would create two interfaces between the reagent streams, widening the area upon which adhesion occurred, **fig. 3.10.**, but preventing particle adhesion upon the sides of the microchannel, as the interfaces between the flows contact only the horizontal walls at the top and bottom of the microchannel, limiting particle adhesion to the vertical surfaces. As the area over which adhesion occurs will be larger upon the horizontal surfaces, leading to a thinner layer of precipitate build up, an increasing number of nanoparticles would be needed to create a blockage and exposing a larger number of particles to the force of the flow, disrupting adhesion and loosening this from the walls.

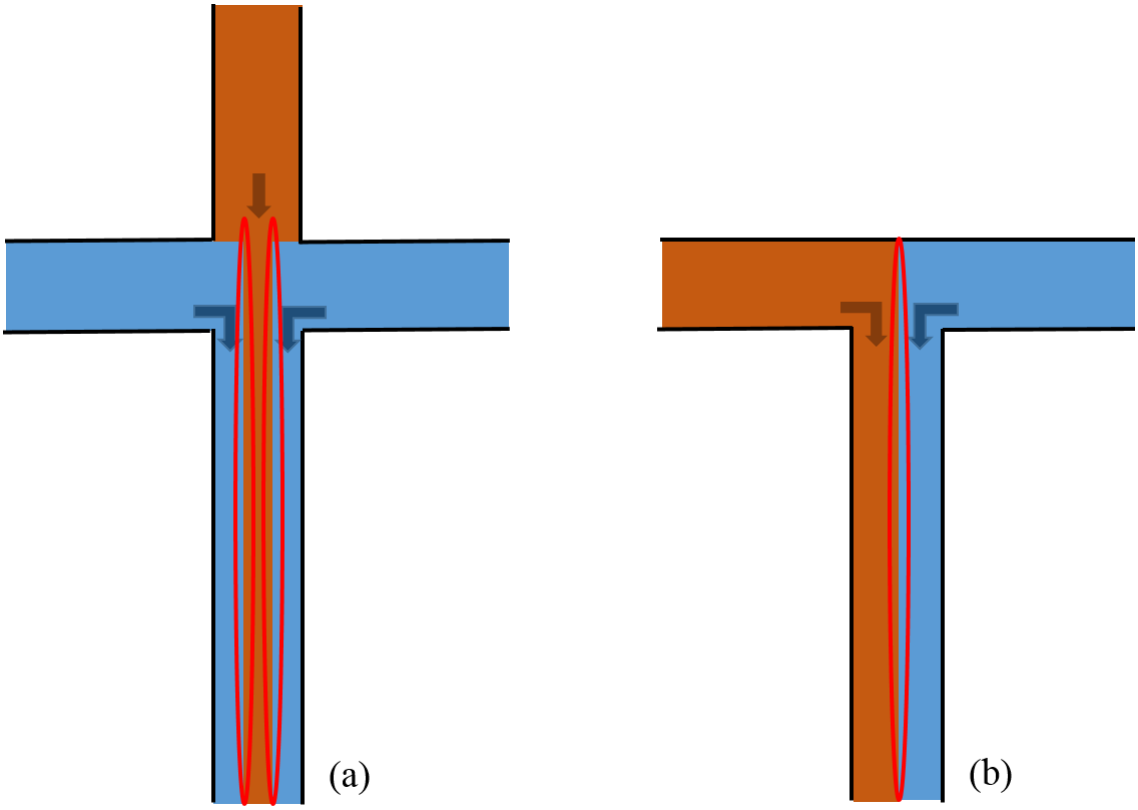

Figure 3.10. Diagrams of the interfaces between the flows, in the flow focussed reactor design the area at which particle adhesion could occur at the interface between the flows is larger (a), compared to that of the non-flow focussed (b), due to the two flows of base (blue) which will diffuse into the central ISPS flow (red).

Initially an iron salts precursor solution containing iron (II) sulphate (0.01mols dm^{-3}) and iron (III) sulphate (0.02 mol dm^{-3}) dissolved in deionised water, was introduced into the central inlet of microreactor design 3025 at a flow rate of 1000 µl hr^{-1}. Simultaneously two flows of sodium hydroxide (1.00 mols dm^{-3}) were introduced into the outer inlets (see **fig. 3.11.**) at a flow rate of 1000 µl hr^{-1} per flow (Total flow rate for the system = 3000 µl hr^{-1}), at these flow rates the Reynolds number of the system is 5.03, and the fluids act under laminar flow conditions, the reaction proceeding by diffusion of the base into the ISPS, due to the shorter diffusion times of the base (OH^- = 8.5 x10^{-4} s) in comparison to the divalent and trivalent iron cations (Fe^{2+} = 3.1 x10^{-3} s and Fe^{3+} = 2.5 x10^{-3} s).

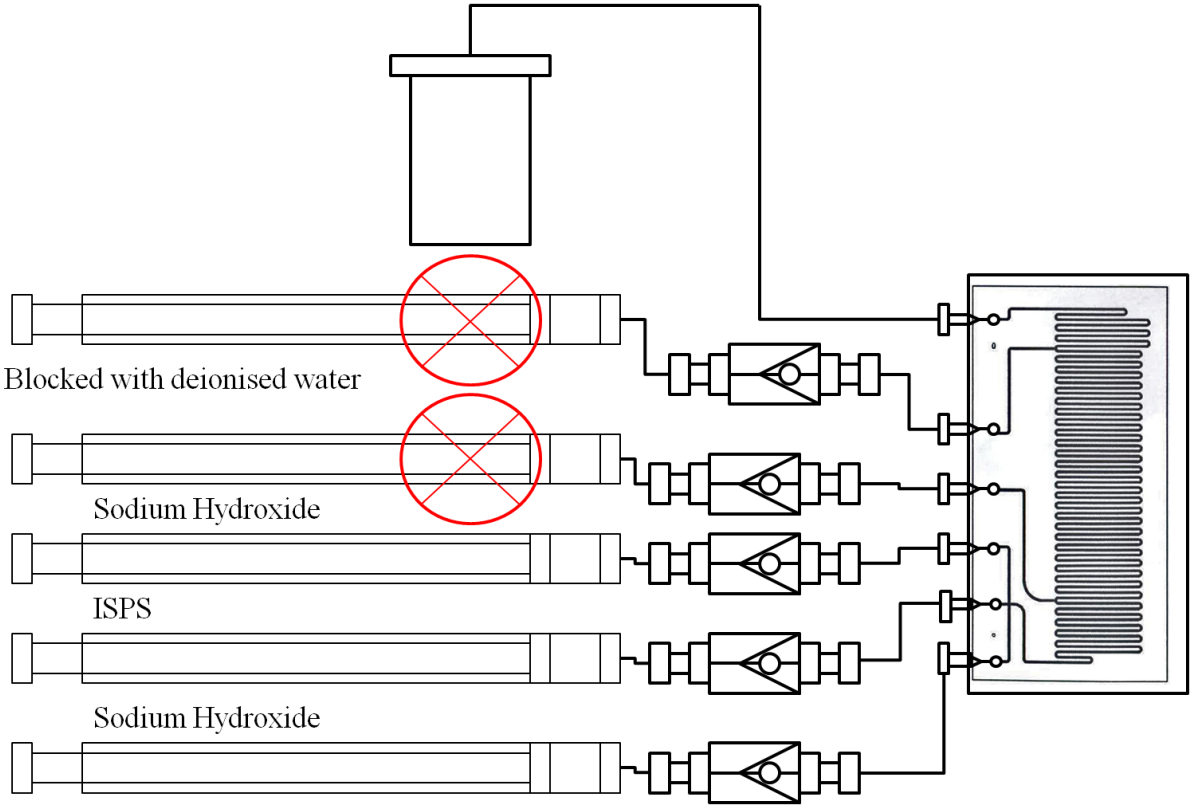

Figure 3.11. Schematic design of microreactor 3025, used for continuous flow focussing, and the formation of nanoparticles without the blocking of the microreactor.

A small amount of particle adhesion was noted to have occurred after 200 µl of each reagent had been pumped into the reactor, and no increase in particle adhesion was noted by the completion of the run after 800 µl of each reagent was pumped through the reactor. The flow rate ratio of the inner to outer flows was altered in an attempt to reduce the amount of precipitate adhesion further; the ideal flow rate ratio was found to be 1:1. The microreactor could be used continuously for 30, 1 hour runs (e.g. 1000 µl of ISPS was used per run), before cleaning was required; any product was collected and dried in an argon atmosphere. The powder X-ray diffraction pattern was recorded over the range $10 < 2\theta° < 80$ with a step time of 30s, **fig. 3.12.**

X-ray diffraction analysis showed the precipitate collected to contain a mixture of Fe_3O_4, γ-Fe_2O_3, as well as α-Fe_2O_3, Na_2SO_4, $NaHSO_4$ and unidentifiable impurities. Several crystallographic databases have been consulted in trying to determine what the

unidentified impurities may be. So while a technique had now been devised for particle synthesis using these microreactors the reagents had to be altered to form nanoparticles of the correct phase.

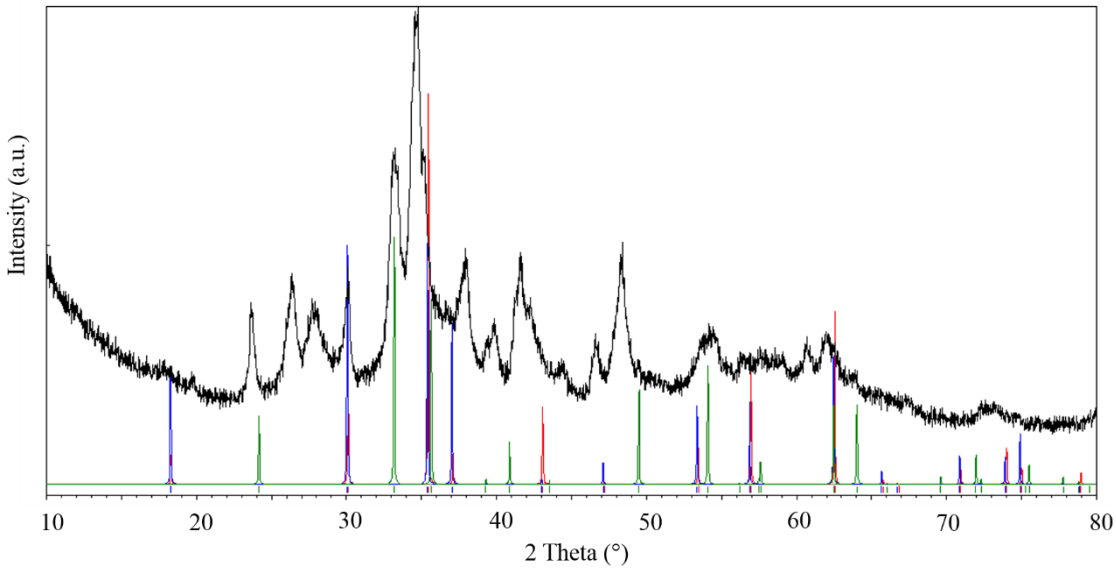

Figure 3.13. Powder X-ray diffraction pattern of the product produced when divalent and trivalent iron sulphate salts were used to form the ISPS. The PXRD pattern is displayed along with the peak positions of Fe_3o_4 (red), γ-Fe_2O_3 (blue), and α-Fe_2O_3 (green), and the product can be seen to not be the desired product Fe_3O_4, or the possible other forms of iron oxide.

The failure to produce either spinel phase of iron oxide was thought to be due to the use of the iron sulphates instead of iron chlorides. Iron sulphate salts can often be seen to lead to the formation of unusual iron compounds such as Jarosite or Schwertamite.[19] Subsequently the reagents were changed so as to remove any sulphate from the system. The iron salts precursor solution was formed by mixing $FeCl_2$ (0.01 mol dm^{-3}) and $FeCl_3$ (0.02 mol dm^{-3}) each dissolved in hydrochloric acid (1.10 mol dm^{-3}, 100 ml); a solution of sodium hydroxide (1.00 mol dm^{-3}) was also prepared. Both sets of reagents were pumped into their respective microreactor inlets at 1000 µl hr^{-1} per flow (total flow rate 3000 µl hr^{-1}), the residence time of which equates to 13.8 s.

When using this technique the microreactor was found to be able to perform 40 runs (40 x 1 ml volumes of ISPS used) without significant particle adhesion to the microreactor walls. After 40 runs cleaning of the microreactor with dilute sulphuric acid was undertaken as a precautionary measure. Powder X-ray diffraction patterns were obtained for this precipitate over the range of $10 < 2\theta° < 80$, with a time per step of 25s. The phase obtained was identified as a spinel phase iron oxide, the type of iron oxide e.g. Fe_3O_4 or γ-Fe_2O_3 could not be determined, **fig. 3.13.**

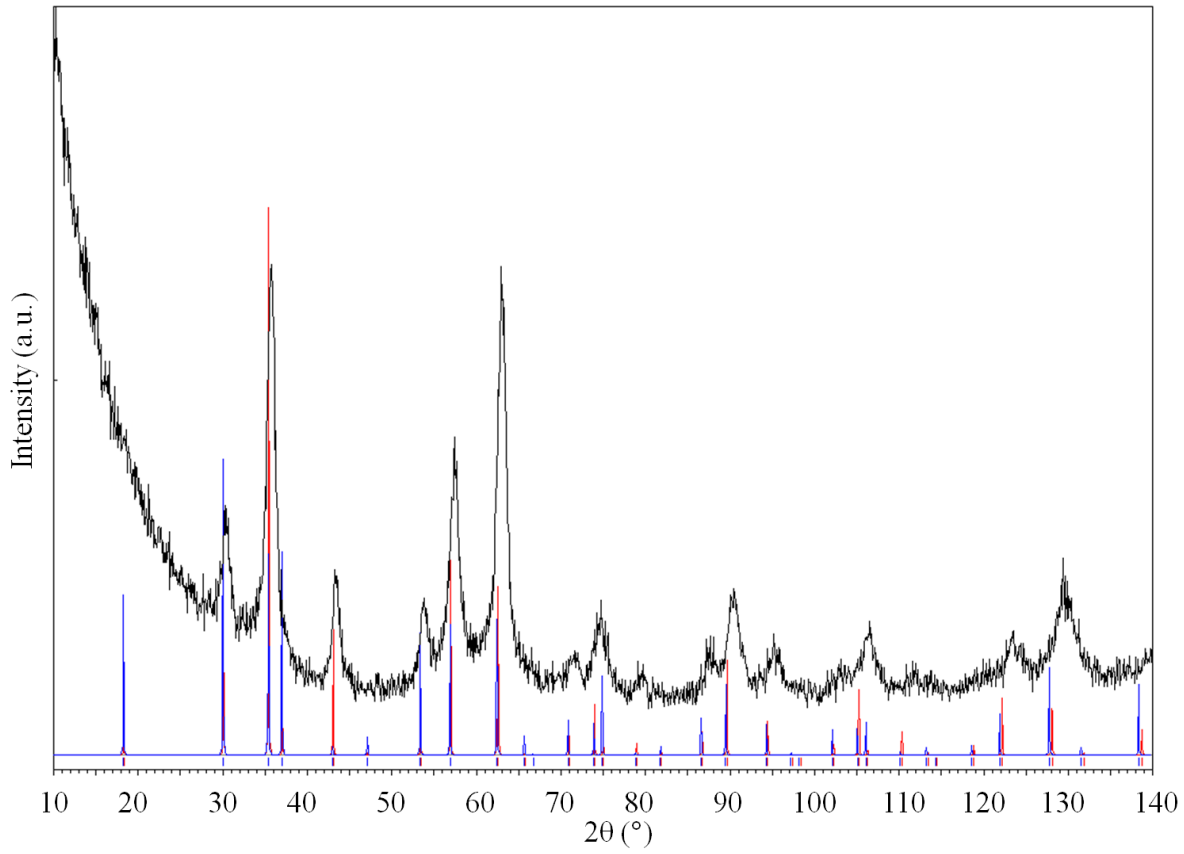

Figure 3.13. Powder X-ray diffraction pattern of product produced when divalent and trivalent iron chloride salts were used to form the ISPS, compared against Fe_3O_4 (*Fd3-m*, red) and γ-Fe_2O_3 (*Fd3-m*, blue).

3.2.5. Summary

A continuous flow method was adapted to allow for the synthesis of iron oxide nanoparticles with limited particle adhesion to the microreactor walls. This was performed through the careful manipulation of several parameters, and implementation of different microreactor designs. Increasing the total flow rate of the reagent flows increased the total volume of reagents needed to cause blocking of the microreactor, due to the force applied to the precipitate build up causing its detachment from the microreactors surface. The concentration of acid used to dissolve the divalent and trivalent iron sulphate salts was increased to further limit precipitate adhesion and prevent precipitation until the serpentine portion of the microreactor. This was seen to decrease with increasing acid concentration, however, when a concentration of 10% V/V sulphuric acid led to the inhibition of particle formation. Finally a flow focussed approach was used this in conjunction with the above parameters which allowed for the microreactor to be used for prolonged periods without blocking. The precipitate formed from the sulphate salts however proved not to form spinel phase iron oxide; the reagents were altered accordingly, so as to allow for the production of these spinel phases.

4.0. Continuous Flow Focussing Technique: Synthesis and Analysis of Iron Oxide Nanoparticles (IONs)

The continuous flow focussing technique was shown to be able to produce spinel phase iron oxide nanoparticles. The nanoparticles however need to be further characterised and their size dependent properties explored to help tailor them toward specific applications. Biomedical applications for example rely upon superparamagnetism by groups of nanoparticles, which occurs only when the nanoparticles diameters are below approximately 30 nm.[19] The size of the nanoparticles and their agglomerations therefore need to be characterised in order to gain control over the resultant magnetic properties and hence why microreactors have been used to synthesise these.[102, 108, 113, 114]

Synthesis of iron oxide nanoparticles (IONs) was performed using the flow focussing technique, the development of which was discussed in **Section 3.2.4.** To recap, deoxygenated solutions of an ISPS, prepared by the mixing of equal volumes of stoichiometricly concentrated $FeCl_2$ (0.01 M) and $FeCl_3$ (0.02 M) dissolved in HCl (1.10 M), was pumped into the central inlet of the microreactor simultaneously with two flows of sodium hydroxide solution into the outer inlets at 1000 μl hr^{-1} per flow (total flow rate = 3000 μl hr^{-1}). The precipitate produced was collected under nitrogen before being magnetically decanted from the supernatant and washed with ethanol and deionised water and dried in an inert atmosphere at 100 °C. A schematic diagram of the microreactor set up is shown in, **fig. 4.1.**

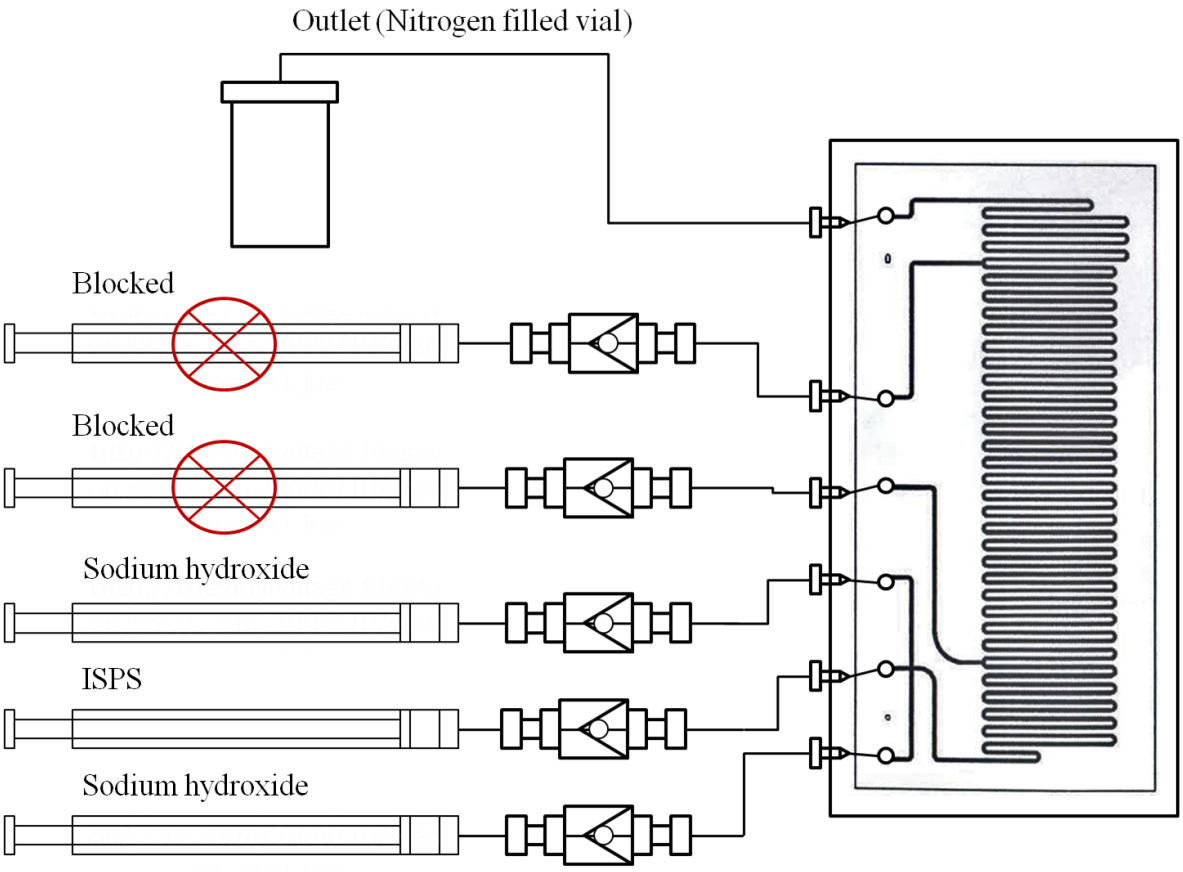

Figure 4.1. Schematic design of microreactor 3025, used for continuous flow focussing, and the formation of iron oxide nanoparticles without the blocking of the microreactor.

Powder X-ray diffraction patterns of the precipitate were recorded over the range of $10 \leq 2\theta° \leq 140$, with a step size of 0.02 ° and a time per step of 25 s, **fig. 4.2.** The predominant phase was revealed to be spinel phase iron oxide, in the form of either γ-Fe_2O_3 or Fe_3O_4. The determination of which of these phases was present however could not initially be made due to the similarities between their diffraction patterns. Occasionally the diffraction pattern of bulk γ-Fe_2O_3 contains peaks relating to the superlattice reflections at 6.68 ° and 7.61 ° 2θ, indicating the case of the $P4_12_12$ unit cell, however these could not be detected due to the high background and peak broadening.[27]

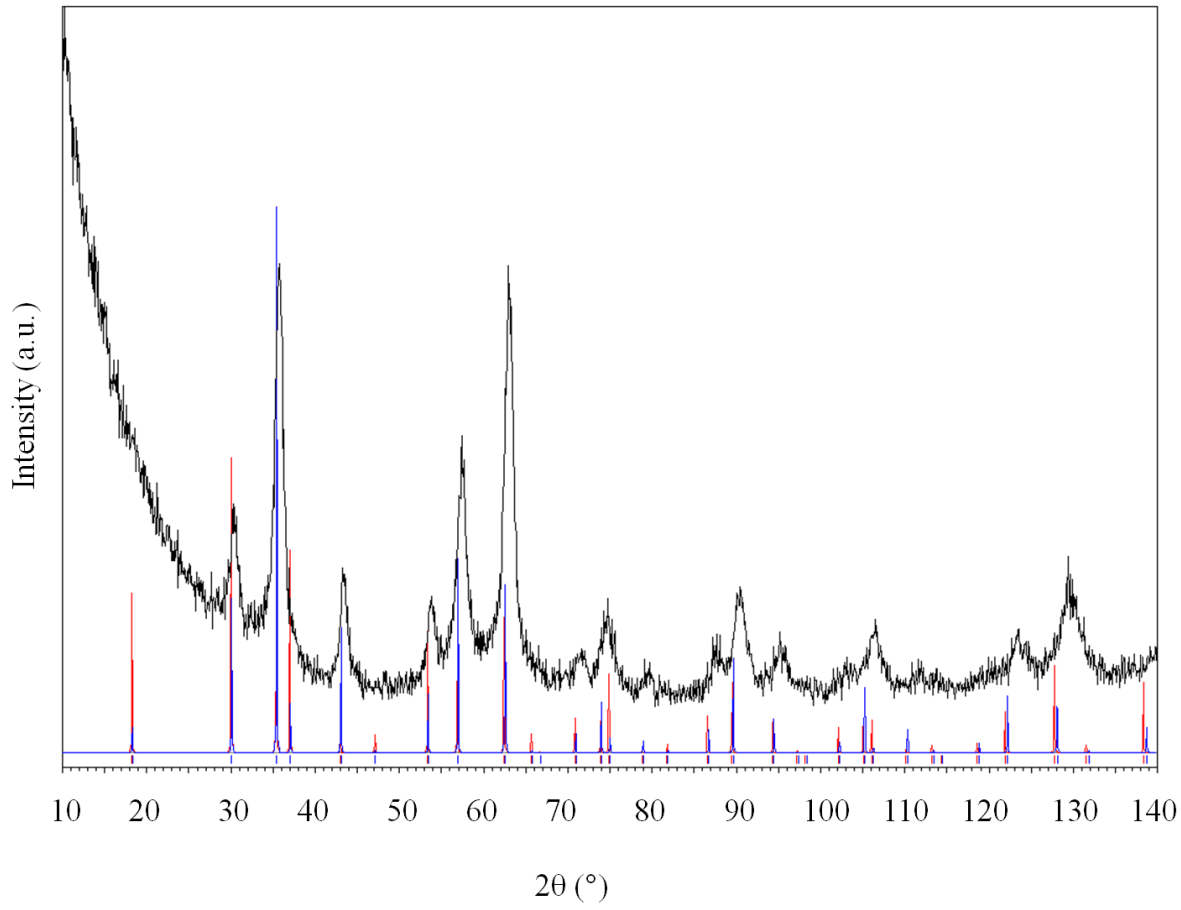

Figure 4.2. Powder X-ray diffraction pattern of the IONs produced using the microreactor, the peaks in the PXRD can be seen to be relatively broad suggesting the nanoscale of the particles and the pattern can be seen to consist of Fe_3O_4 (*Fd3-m*), red, and γ-Fe_2O_3 (*Fd3-m*), blue.[24, 29]

4.0.1. Qualitative and Quantitative Phase Analysis

Fourier Transform Infra-red spectroscopy was further employed to distinguish between γ-Fe_2O_3 and Fe_3O_4; spectra were recorded over the range 1000-375 cm^{-1} at a nominal resolution of 4 cm^{-1}. The fingerprint region revealed bands that match those of Fe_3O_4, however upon closer inspection, some degradation of the two broad bands at 586 cm^{-1} and 430 cm^{-1} was also noted, **fig. 4.3.**, suggesting the presence of γ-Fe_2O_3, due to the decreased symmetry within the unit cell. The IONs were therefore thought to contain a mixture of Fe_3O_4 and γ-Fe_2O_3 phases. Detailed studies by other groups have found IONs

with diameters < 20 nm contain both spinel phases of iron oxide and are present as iron deficient magnetite $Fe_{3-\delta}O_4$.[31]

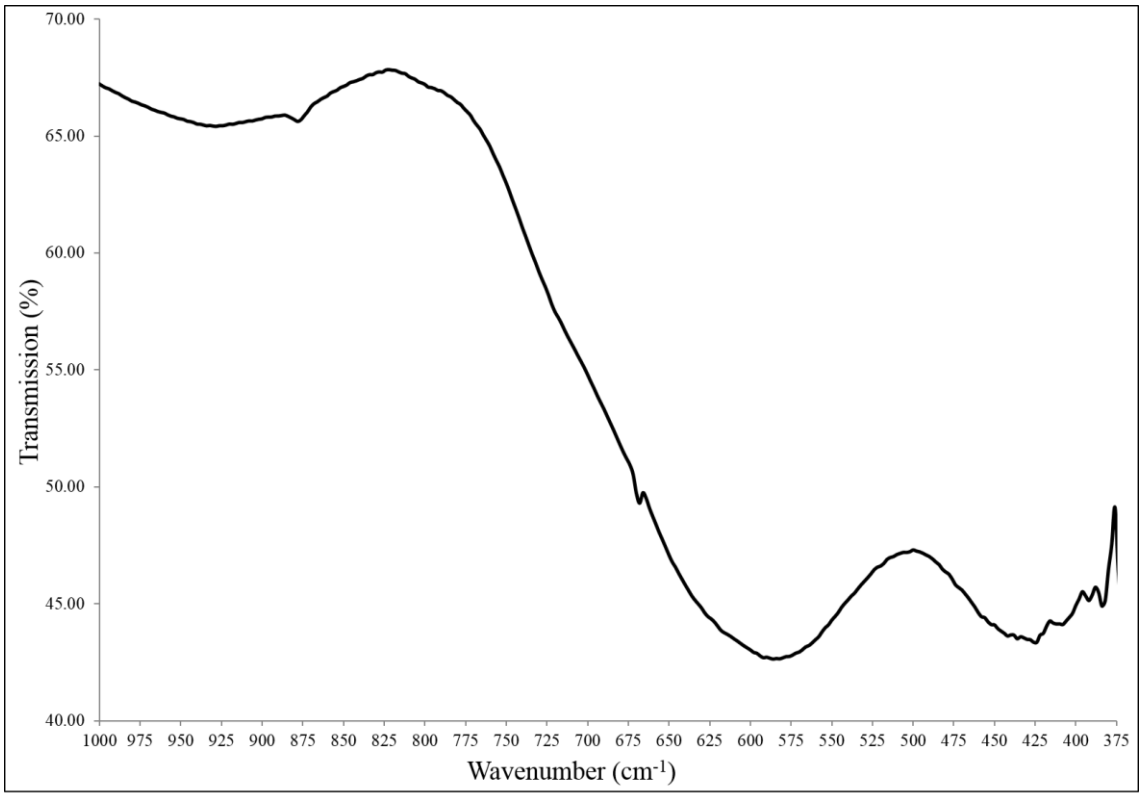

Figure 4.3. FTIR spectrum of the fingerprint region of the iron oxides. While two bands can be seen to be largely present at 580 cm^{-1} and 425 cm^{-1}, suggesting Fe_3O_4, some degradation of the band at lower wavenumber between 425 cm^{-1} and 375 cm^{-1} can also be seen, suggest the presence of γ-Fe_2O_3.

Attempts were made at quantifying the weight percentage of γ-Fe_2O_3 and Fe_3O_4 phases within the nanoparticles after their presence had been confirmed using FTIR. A modified approach was taken to that used by Kim *et. al.*, discussed in greater detail in **Chapter 5**.[129] PXRD patterns were recorded over the range $55 \leq 2\theta\ ° \leq 65$, with a step size of 0.02 °, and a time per step of 28 s. Three patterns were taken and the intensities added to increase the intensity of the reflections, enabling the two peaks within the range to be deconvoluted into those relating to their respective (511) and (440) reflections. From the

(440) reflections the nanoparticles were found to contain a percentage weight of 52.87 ± 5.79 % γ-Fe_2O_3 and 49.63 % ± 4.68 Fe_3O_4.

As the exact phase of the nanoparticles has been calculated it is possible to calculate the percentage yield of the nanoparticles, 97.06%.

It has been suggested, however that the space time yield would provide a more accurate representation of how efficient the microreactor is in synthesising nanoparticles. Space time yields are traditionally used for the calculating the efficiency of catalysts where the amount of converted reactant is compared to the volume of the catalyst and how long the reagents were flowed through this, in a flow reactor.[162-165] To convert to calculate the space time yield for the microreactor used here, the yield of the reagents was considered (converted amount of reactant) the volume of reactant used to achieve this yield and the time it took to produce this, **eq. 4.1.**

Equation 4.1.

$$Space\ Time\ Yield\ (mol\ l^{-1}\ hr^{-1}) = \frac{Converted\ amount\ of\ a\ reactant}{volume\ of\ reactor \times time}$$

The space time yield calculated for the above continuous flow focussed technique used in microreactor 3025 is 4.48 mol l^{-1} hr^{-1}. Unfortunately as this technique for comparing different types of microreactors is commonly used by chemical engineers working with organic reagents, the details given by other groups are insufficient to calculate space time yields for these other techniques and therefore cannot be compared to our technique.

4.0.2. Determination of Particle Size

An estimation of the nanoparticles diameter was made using the Scherrer equation using the peak at 35.8° 2θ, corresponding to the (311) reflection of Fe_3O_4, chosen due to its high

intensity; from this the nanoparticle diameter was estimated to be 6.72 ± 0.72 nm, as the Scherrer formulae calculates the mean crystallite diameter.[127, 128] Although the standard deviation appears large, approximately 10% of the overall size, this would not prove to be of great significance if the nanoparticles were to be used for biomedical applications. Currently marketed IONs based MRI contrast agents have diameters of > 20 nm once they have been coated, and then taking into account the standard deviation our nanoparticles would still be smaller in size, although care would be needed to be taken if any coatings were later applied.[4, 166] TEM images of the nanoparticles which were taken at a voltage of 120 kV, showed the nanoparticles to be roughly spherical, and highly agglomerated. Due to the agglomeration automatic size analysis could not be attempted using image analysis software. Manual size analysis may prove to be unintentionally biased if performed, **fig. 4.4.**

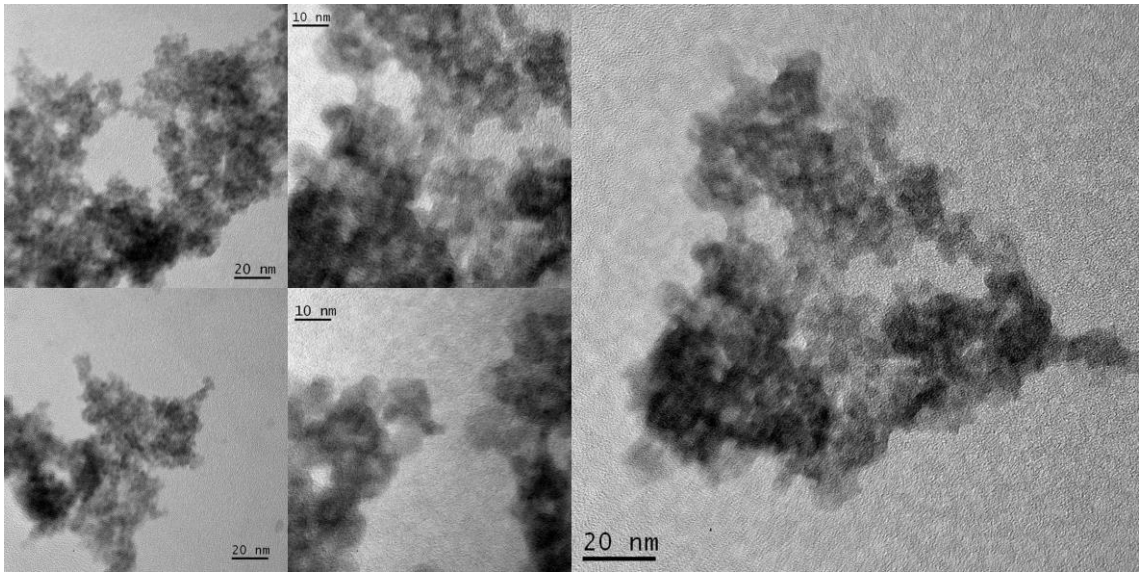

Figure 4.4. TEM images of the nanoparticles produced using the 2D-contnuous flow focussed technique. It can clearly be seen that the nanoparticles are generally spherical in morphology and highly agglomerated, hence no accurate measurement of the nanoparticles size could be made from these. Reaction conditions, microreactor designs, flow rate = 3000 µl hr^{-1}, residence time 13.8 s, ISPS contains, [$FeCl_2$] = 0.01 M, [$FeCl_3$] = 0.02 M, dissolved in [HCL] = 1.10 M, and the base NaOH = 1.00 M.

A major issue however would prove to be the agglomeration of the nanoparticles, as no attempt was made to surface stabilise the nanoparticles against this using surface bound molecules (typically surfactants, citrate, amino acids, or long chain polymers). This aggregation is undesirable as the aggregates can be over 100 nm in diameter and therefore significantly decrease the half-life of the nanoparticles within the blood stream.[2]

BET analysis performed using $N_{2(g)}$ as the adsorptive gas, at a temperature of 77.3 K, showed the nanoparticles to be non-porous with uniform surfaces (type *II* isotherm). A BET surface area of 136.99 cm^3g^{-1} was calculated from the isotherm.

The BET surface area was used to provide further evidence of nanoparticles agglomeration, as the average diameter calculated from this was 17.18 nm, and therefore almost three times that calculated from PXRD data.

Further estimation of the nanoparticles size has been made from the magnetization curve by plotting a Langevin curve to the hysteresis loop of the nanoparticles, and the particle size can be estimated by fitting of the data with a Log-normal law of parameters, the particle size was estimated to be 3.4 ± 0.7 nm.[102]

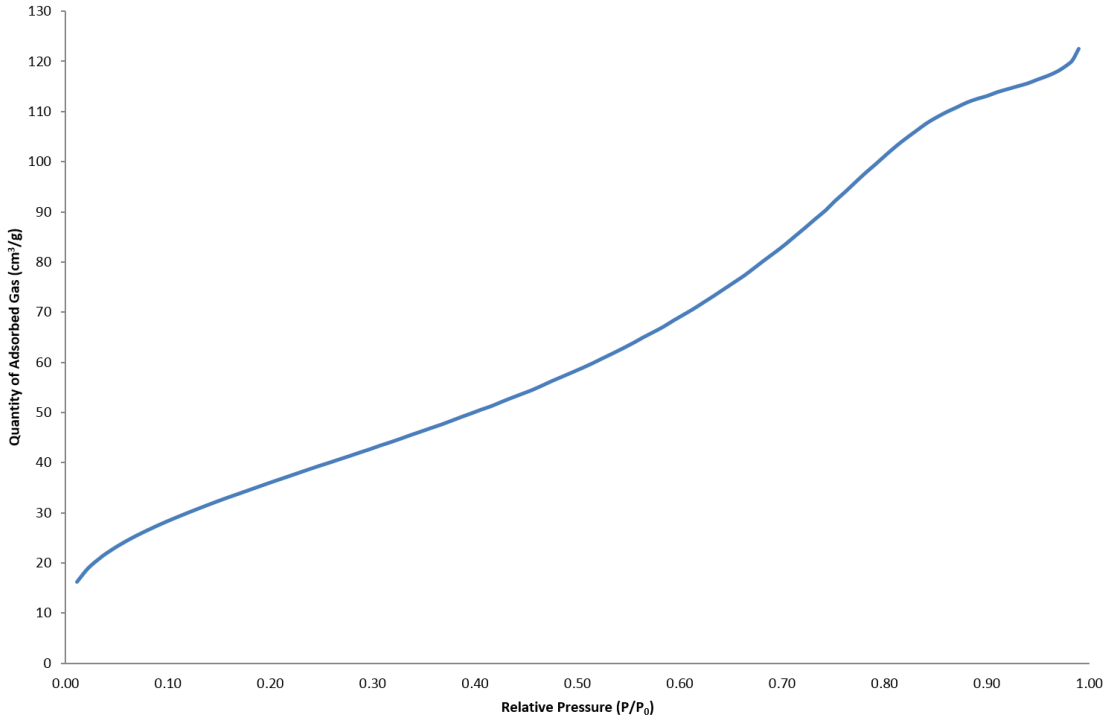

Figure 4.5. BET isotherm of the nanoparticle produced using the 2D-continuous flow focussed technique, showing a type II isotherm indicative of non-porous or macroporous solids where there is unrestricted adsorption for both the monolayer and multilayer.[19]

4.0.3. Analysis of Magnetic Properties

Vibrating sample magnetometry was performed, using field strength of 10000 Oe, a sensitivity of 0.01 emu, and a time per step of 0.1 s. The hysteresis loop recorded is used to investigate the magnetic nature of the nanoparticles, the hysteresis loop shows characteristically negligible values of magnetic coercivity and remanence, 14.5 Oe and 0.00415 emu g^{-1}, respectively, suggesting they act as near ideal superparamagnets. Initially magnetization of the sample increases rapidly with increasing field strength, this gradually slows until the plateau where the saturation magnetisation is reached, **fig. 4.5.** The plateau, however, is not reached even at field strengths of 10000 Oe, and is replaced by a much slower rate of magnetisation in comparison to the initial magnetisation, at this

point the magnetic saturation is approximated to 32.9 emu g^{-1} at 10000 Oe. As the polydispersity of the sample is approximately ± 1.0 nm, this cannot be responsible for the large range in magnetisations seen in **fig. 4.5.;** instead it further suggests the formation of aggregates, as large aggregates will have a larger magnetic saturation.

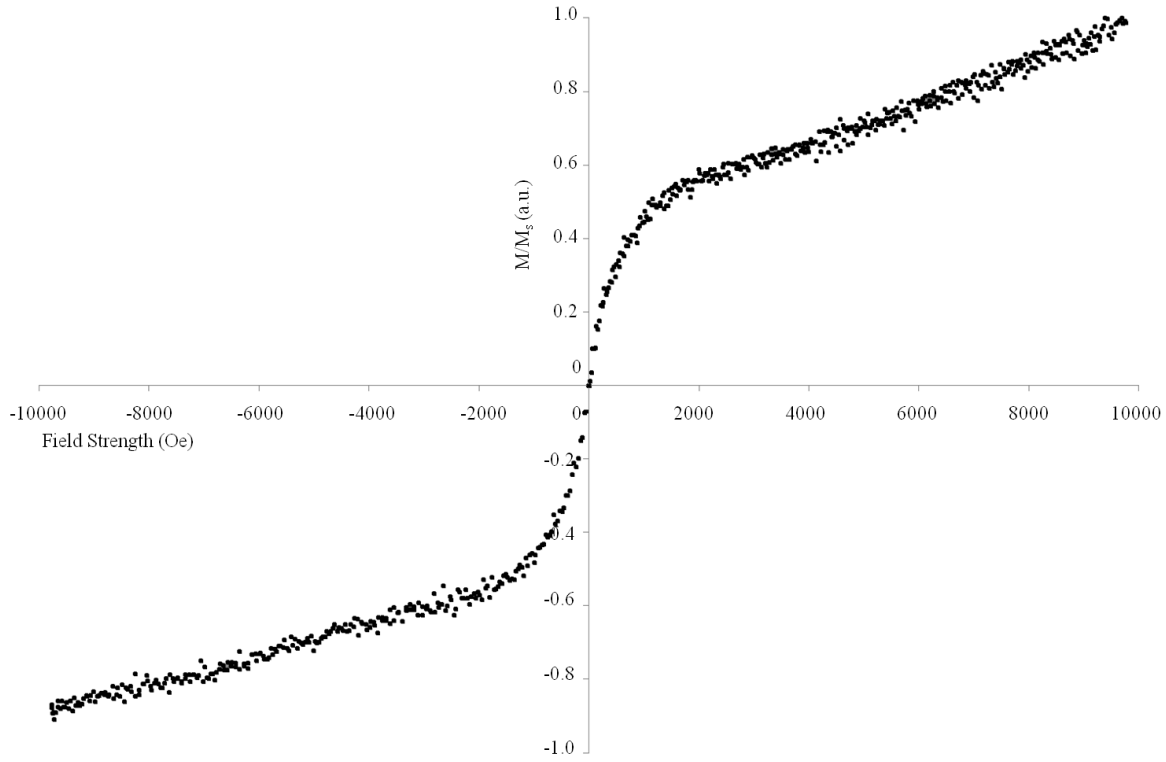

Figure 4.5. Hysteresis loop of iron oxide nanoparticles produced using the microreactor. The low values of both coercivity and remanence and the lack of a hysteresis loop suggest the nanoparticles to be superparamagnetic in nature. However the large deviation in magnetic saturations suggest that the nanoparticle are of either highly varied size or are forming agglomerates.

4.1. Comparison between Synthetic Techniques in Microreactors

Magnetic iron oxide nanoparticles have been synthesised prior to this work using *ad-hoc* microreactors, using the droplet coalescence, co-axial flow and thermal decomposition techniques.[102, 108, 113, 114] A comparison therefore needed to be drawn between the different

synthetic techniques and the continuous flow focussing technique upon commercially available microreactors and nanoparticles produced in batch. Full details of other microfluidic techniques for the synthesis of IONs are given in **chapter 1**.

Abou Hassan *et.al.*, synthesised IONs with a diameter of approximately 7 nm, using an *ad hoc* microreactor designed to utilise the co-axial flow technique.[102] A precursor solution of iron salts (c = 10^{-2} M, with a 1:2 ratio of Fe^{2+}: Fe^{3+}) with concentrations on the same scale as the continuous flow focussing technique was inserted into the centre of a flow of tetramethylammonium hydroxide (0.172 M), at a total flow rate 30000 µl hr^{-1} with an estimated residence time of 10 s. The surfactant didodecyldimethyl ammonium bromide (DDAB) was used in an attempt to prevent aggregation of the nanoparticles and to remove them from any un-reacted starting reagents by quick solvent extraction.

Frenz *et.al.*, synthesised IONs with diameters of 4 ± 1 nm using the droplet coalescence technique.[108] In which an *ad hoc* microreactor with a novel hydrodynamic coupled nozzle was used to generate droplets of a precursor ($FeCl_2$ = 30 x10^{-3} M and $FeCl_3$ = 60 x10^{-3} M, dissolved in 0.5 M HCl) and ammonium hydroxide (2 M), a surfactant in the form of the ammonium salt of perfluorinated polyether was used to stabilize the droplets. The droplets were then coalesced by placing an AC voltage (200 V, at 30 kHz) across the microchannel. Several flow rates were tested for coalescence of the droplets using the hydrodynamic coupled nozzle, however, to synthesise particles with the sizes quoted a total flow rate of 830 µl hr^{-1} (flow rate of oil = 650 µl hr^{-1}, flow rate of iron salts = 60 µl hr^{-1}, and flow rate of ammonium hydroxide = 120 µl hr^{-1}) was used. As no details of the microreactor length are given a residence time for the crystals within the microreactor cannot be calculated.

Kumar *et.al.*, synthesised IONs upon an *ad hoc* microreactor with diameters of 3.6 ± 0.8 nm.[114] A capillary based droplet reactor was used to synthesise and instantly coalesce droplets of an iron salts precursor ($FeCl_2$ = 0.02 M, $FeCl_3$ = 0.04 M, and

dextran = 0.05 M dissolved in 0.4 M HCl) and ammonium hydroxide (28 %V/V). Dextran acted as both a surfactant for the stabilisation of the droplets in the Octadecene carrier phase. After coalescence the droplets passed through a heating stage and heated at 60 °C, to aid particle growth and crystallisation. The total flow rate of the system 48000 μl hr^{-1} (flow rate of carrier = 36000 μl hr^{-1}, flow rate of iron salts = 7980 μl hr^{-1}, and flow rate of ammonium hydroxide = 4020 μl hr^{-1}) corresponding to a residence time (including the heating capillary) of 540 s.

4.1.1. Co-Precipitation Reaction in Batch

A batch co-precipitation reaction was performed using equal concentrations and volume ratios to those used in the continuous flow focussing technique. To do this an ISPS was first made by mixing of $FeCl_2$ (0.01 M) in HCl (1.10 M, 100 ml) and $FeCl_3$ (0.02 M) in HCl (1.10 M, 100 ml). The ISPS (50 ml) was then deoxygenated under nitrogen atmosphere for 30 mins with constant agitation (stirring at 500 rpm). To this NaOH (100 ml, 1.00 M) was added to induce precipitation of the nanoparticles. Any nanoparticles were collected via magnetic decantation and dried in an inert atmosphere. Powder X-ray diffraction patterns of the precipitate were recorded over the range of $10 \leq 2\theta\ ° \leq 140$, with a step size of 0.02 ° and a time per step of 25 s, and the phase confirmed as spinel phase iron oxide. The nanoparticles diameter was calculated from these patterns by application of the Scherrer equation using the peak relating to the (311) reflection of either phase.

4.1.2. Comparison of Nanoparticle Size

In comparison to our technique, **table 4.1.**, it can be seen that the nanoparticles produced using the continuous flow focussing technique are of similar sizes as those produced by the co-axial flow and droplet coalescence techniques, the droplet coalescence technique in particular is thought to provide a greater degree of control in nanoparticles size and polydispersity than continuous flow based techniques as the volume of reagents available for nucleation and growth is constrained.

Nanoparticles properties were also compared to those of the nanoparticles produced in batch. The nanoparticles prepared using the continuous flow focussing technique were 6.72 ± 0.72 nm and those produced in batch 8.2 ± 1.5 nm, respectively.

Technique	Particle Size (nm)	Reagent Concentration (mol dm^{-3})	Total Flow Rate ($\mu l\ hr^{-1}$)	Residence Time (s)	Surfactant
Continuous Flow Focussing	6.72 ± 0.72	1.00 x 10^{-2} ($FeCl_2$) 2.00 x 10^{-2} ($FeCl_3$)	3000	13.8	None
Co-axial Flow (Abou-Hassan *et.al.*[102])	7.0	1.00 x 10^{-2} ($FeCl_2$) 1.00 x 10^{-2} ($FeCl_3$)	24600-30000	10-48	DDAB
Droplet Coalescence (Frenz *et.al.*[108])	4.0 ± 1.0	240 x 10^{-3} ($FeCl_2$) 480 x 10^{-3} ($FeCl_3$)	830	*	None
Droplet Coalescence (Kumar *et.al.*[114])	3.6 ± 0.8	2.00 x 10^{-2} ($FeCl_2$) 4.00 x 10^{-2} ($FeCl_3$)	40020	235	Dextran

Table 4.1. Comparison of the sizes of nanoparticles produced by different microfluidic techniques and conditions that may affect this size. * indicates unknown literature value.

4.1.3. Comparison of Nanoparticle Phase

Although the size of the nanoparticles has a great effect upon their magnetic properties, so can the phase of which the IONs are comprised. The magnetic saturation which is often used to compare different nanoparticles can differ by as much as 20% depending upon the whether the phase of the nanoparticles is Fe_3O_4 or γ-Fe_2O_3.[19] Therefore accurate determination of the unit cell structure and the weight percentage of the phases within the

nanoparticles need to be carried out, the full method for doing this is explained in chapter 5, however it is summarised here for convenience. PXRD patterns were recorded for the IONs produced in bulk, over the range $55 \leq 2\theta\ ° \leq 65$, with a step size of 0.02 ° and a time step of 28 s. Three patterns were taken and the intensities added to increase the counts from the (440) reflections the nanoparticles produced in bulk were found to contain a percentage weight of 74.02 ± 8.10 % γ-Fe_2O_3 and 26.04 ± 2.45 % Fe_3O_4. Using the same technique the weight percentage of γ-Fe_2O_3 was lower in the nanoparticles produced in the continuous flow focussing technique, 52.87 ± 5.79 % γ-Fe_2O_3 and 49.63 % ± 4.68 Fe_3O_4, respectively. The percentage weights of γ-Fe_2O_3 and Fe_3O_4 shown in both the sample produced using the continuous flow focussing technique and bulk synthesis is likely due to their size, as nanoparticles with diameters ≥ 20 nm tend toward a core shell structure of Fe_3O_4 surrounded by γ-Fe_2O_3, due to surface oxidation.[31] While those with diameters ≤ 20 nm tend toward a mixture of the two phases, e.g. $Fe_{3-\delta}O_4$. While other groups have produced spinel phase iron oxide nanoparticles, data and/or full structure determination has not been reported.[102, 108, 114]

After calculating the phase of both the IONs produced in batch and using the continuous flow focussed technique in the microreactor, both the percentage yield and space time yield for both techniques can be calculated, **table 4.2**

2D continuous flow focussed technique:

$$\boldsymbol{STY}\ (\boldsymbol{mol\ l^{-1}hr^{-1}}) = \frac{\boldsymbol{Mass}\ (\boldsymbol{g}) \times \left((\boldsymbol{Wt\%\ \gamma - Fe_2O_3}(\%) \times \boldsymbol{RMM\ \gamma - Fe_2O_3(mol/g)}) + (\boldsymbol{Wt\%\ \gamma - Fe_2O_3}(\%) \times \boldsymbol{RMM\ \gamma - Fe_2O_3(mol/g)})\right)}{\boldsymbol{Volume\ of\ reactor}\ (\boldsymbol{l}) \times \boldsymbol{reaction\ time}\ (\boldsymbol{hr})}$$

$$\boldsymbol{STY} = \frac{\mathbf{0.090} \times \left(\left({}^{\mathbf{52.9}}/_{\mathbf{100}}\right) \times \mathbf{159.7}\right) + \left(\left({}^{\mathbf{49.6}}/_{\mathbf{100}}\right) \times \mathbf{231.51}\right)}{\mathbf{10 \times 10^{-3} \times 5}} = \mathbf{358.7\ mol\ l^{-1}hr^{-1}}$$

Batch production of IONs (Co-precipitation)

$$\boldsymbol{STY} = \frac{\mathbf{0.016} \times \left(\left({}^{\mathbf{74.0}}/_{\mathbf{100}}\right) \times \mathbf{159.7}\right) + \left(\left({}^{\mathbf{46.0}}/_{\mathbf{100}}\right) \times \mathbf{231.51}\right)}{\mathbf{50 \times 10^{-3} \times 1}} = \mathbf{56.0\ mol\ l^{-1}hr^{-1}}$$

Technique	Percentage yield (%)	Space time yield (mol l^{-1} hr^{-1})
Continuous Flow Focussed	**97.06**	**358.7**
Batch	**89.01**	**56.0**

Table 4.2. Percentage yields of IONs obtained using the continuous flow focussed technique and in batch, and the respective space time yields for both reactor set ups, the continuous flow focussed technique can be seen to be 22 times more efficient than the batch reaction.

Space time yields were calculated using the method and equations outlined at the beginning of this chapter, on comparison of the continuous flow focussed method can be shown to provide an improvement of 6.4 times in terms of space time yield over the batch method.

4.1.4. Comparison of Magnetic Properties

The magnetic saturation of the nanoparticles is often measured to compare different magnetic nanoparticles. A high magnetic saturation is often required for the majority of applications, where other magnetic properties are more application specific, hence in the majority of literature dealing with superparamagnetic nanoparticles only the saturation magnetisation is quoted.

The magnetic saturation of the IONs synthesised using the continuous flow technique can be seen to be comparable to that of the IONs synthesised in batch, 32.09 and 34.11 emu g^{-1}, respectively. The decrease in the magnetisation between the two is thought to be due to their size, with the batch nanoparticles being larger; an increase in size has been seen to cause an increase in magnetic saturation.[31] The magnetic saturation of the nanoparticles

produced using the continuous flow focussing technique is seen to be lower than that of the nanoparticles produced by Kumar *et. al.*, using the droplet coalescence technique, the cause of this is the extra heating stage that was used to increase the particles crystallinity which would help increase the overall magnetic saturation.[114] The magnetic saturation of the nanoparticles produced using the continuous flow technique is more favourable than those synthesised using the co-axial flow technique, **table 4.3.**[102] No data was presented upon the magnetic saturation of the nanoparticles produced using the droplet coalescence technique by Frenz *et.al.*, The nanoparticles were confirmed to be superparamagnetic, however, evidenced by their normalized hysteresis loop.[108]

Technique	Phase	Type of Magnetism	Magnetic Saturation (emu g^{-1})
Continuous Flow Focussing	γ-Fe_2O_3 & Fe_3O_4	Ferrimagnetic (superparamagnetic)	32.09
Bulk	γ-Fe_2O_3 & Fe_3O_4	Ferrimagnetic (superparamagnetic)	34.11
Co-axial[102]	γ-Fe_2O_3 or Fe_3O_4	Ferrimagnetic (superparamagnetic)	26.71†
Droplet Coalescence[114]	γ-Fe_2O_3 & Fe_3O_4	Ferrimagnetic (superparamagnetic)	58.00

Table 4.3. Comparison of the magnetic properties of the nanoparticles synthesised in using techniques presented in the literature and the continuous flow focussed technique. Again it can be seen that the magnetic properties of the nanoparticles produced by the continuous flow focussed technique are on the same scale as those produced using other techniques. * Calculated from data given in the article or from supplementary information

4.1.5. Comparison Summary

When the physical properties of the iron oxide nanoparticles produced using the continuous flow focussing technique are compared to those produced using *ad-hoc* microreactors or bulk syntheses, those produced with the continuous flow technique have similar or more favourable properties. The mean size and standard deviation of the nanoparticles are comparable to those produced using the droplet coalescence technique while being smaller and with a smaller standard deviation than those produced using any other synthesis technique.

The phase composition of the nanoparticles produced using continuous flow focussing contains less γ-Fe_2O_3 than those nanoparticles produced in batch, 52.9 ± 5.8 % γ-Fe_2O_3 and 49.6 % ± 4.7 Fe_3O_4 produced using the continuous flow technique compared to 74.0 ± 8.1% γ-Fe_2O_3 and 26.0 ± 2.5% Fe_3O_4 when produced in batch, the percentage error in these values was calculated from the measuring of "blind" sample discussed in **chapter 5**. the The magnetic properties of both are also similar showing superparamagnetism and magnetic saturations of 32.09 and 34.11 emu g^{-1}, respectively. This was however smaller than those of the IONs produced by Kumar *et.al.,* 53.30 emu g^{-1}.[83, 114]

In terms of efficiency the continuous flow technique produces nanoparticles with a higher percentage yield (97.06% compared to 89.00%) and a higher space time yield (0.3930 mol l^{-1} hr^{-1} compared to 0.00176 mol l^{-1} $hr^{-1)}$ than the batch technique.

4.2. Critical Evaluation of TEM Images of Synthesised Nanoparticles

Ideally for IONs to be used for any application their size must be carefully controlled, reaction parameters such as flow rate, concentration, and temperature have been seen to have an effect upon particle size by altering the rates of nucleation and growth, this has been particularly noted in the synthesis of silver and barium sulphate nanoparticles, and CdSe quantum dots.[167-169]

Iron oxide nanoparticles produced at different synthesis parameters, temperature, concentration, and total flow rate, were imaged using TEM. While these images cannot be used quantitatively, due to poor imaging contrast, a critical qualitative interpretation of the images is given below.

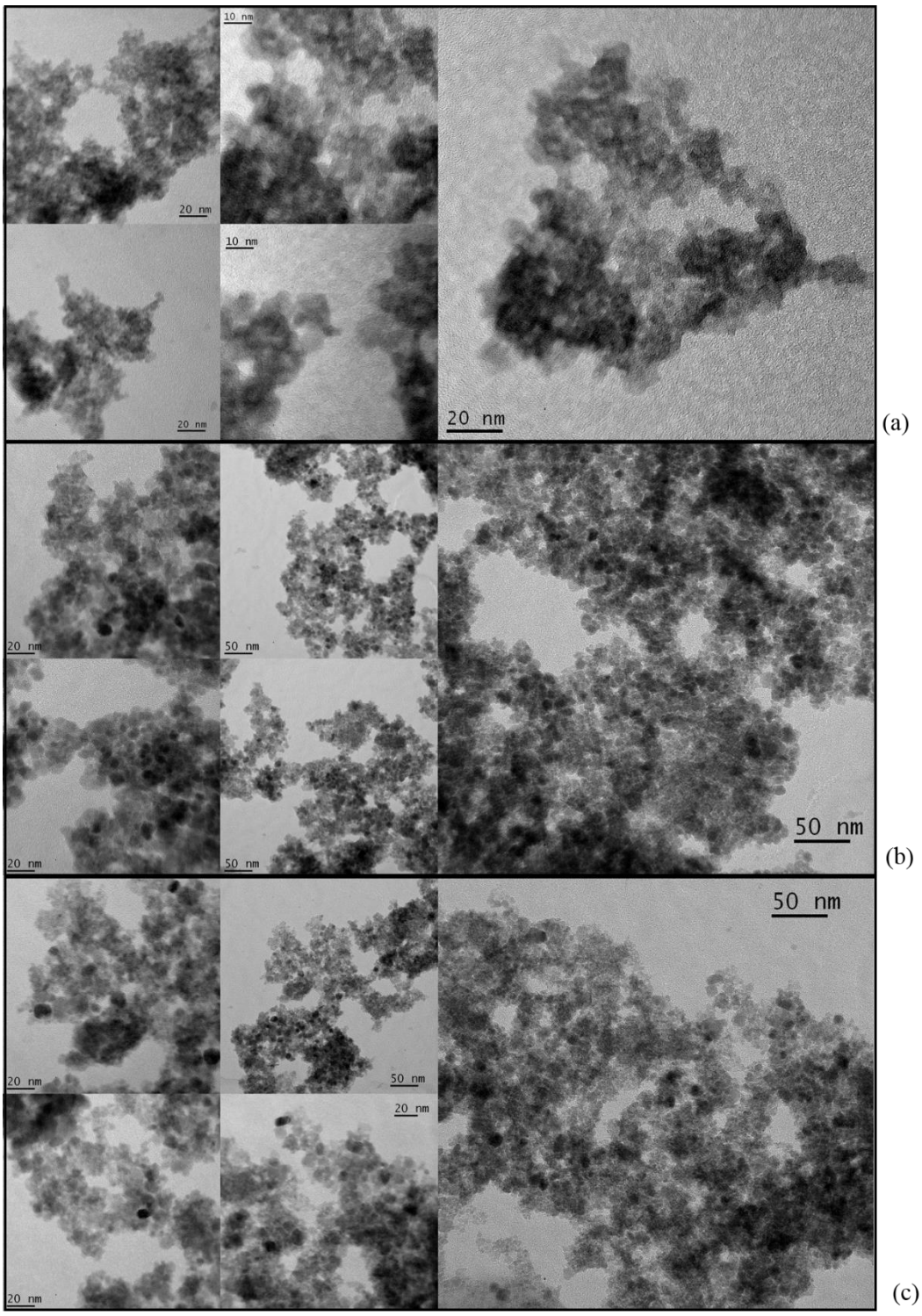

Figure 4.6. TEM pictures of nanoparticles synthesised at temperatures of 25.5 °C (a), 75.5 °C (b), and 95.5 °C (c). As noted below the particles can be seen to be roughly spherical and highly agglomerated due to the lack of surface stabilisers. Reaction conditions, microreactor designs, flow rate = 3000 µl hr^{-1}, residence time 13.8 s, ISPS contains, [$FeCl_2$] = 0.01 M, [$FeCl_3$] = 0.02 M, dissolved in [HCL] = 1.10 M, and the base NaOH = 1.00 M.

The particles produced are approximately spherical though some can be seen to show edges, although this could be due to the images contrast, **fig. 4.6.**, and **fig. 4.7.**

The particles are highly agglomerated, the main reason for this being the lack of surface coating agents, causing them to agglomerate to reduce their high surface energy. Secondly the nanoparticles are also highly magnetic and the field generated by the electron beam would cause some agglomeration, again due to the lack of a surface coating agent prior to TEM analysis.

The contrast and agglomeration issues mean that the TEM images can only be used for qualitative, demonstrative purpose, rather than quantitative analysis, and it is not prevalent to use them to calculate the particle size or the size distribution. The overall image contrast and particle agglomeration prevent the usual use of software for the automatic calculation of particle size, and any manual measurement of the size may lead to an unintentional biasing of the result, as the easiest particles to measure, those at the edges of the agglomerate, may be smaller than those in the bulk, **fig. 4.8.** Given more time this could be achieved through the use of PXRD if more precipitate was collected and application of the Scherrer formulae would yield the particle sizes of these.

Therefore the only conclusions that can possibly be drawn from these TEM images, are that all nanoparticles independent of reaction conditions are seen to be spherical and highly agglomerated.

All TEM images of nanoparticles are included in appendix 2 in the electronic supplementary information included on disk with this thesis. **Fig. 4.7.**, and **fig. 4.8.**, below show TEM images of nanoparticles produced at various concentrations and flow rates.

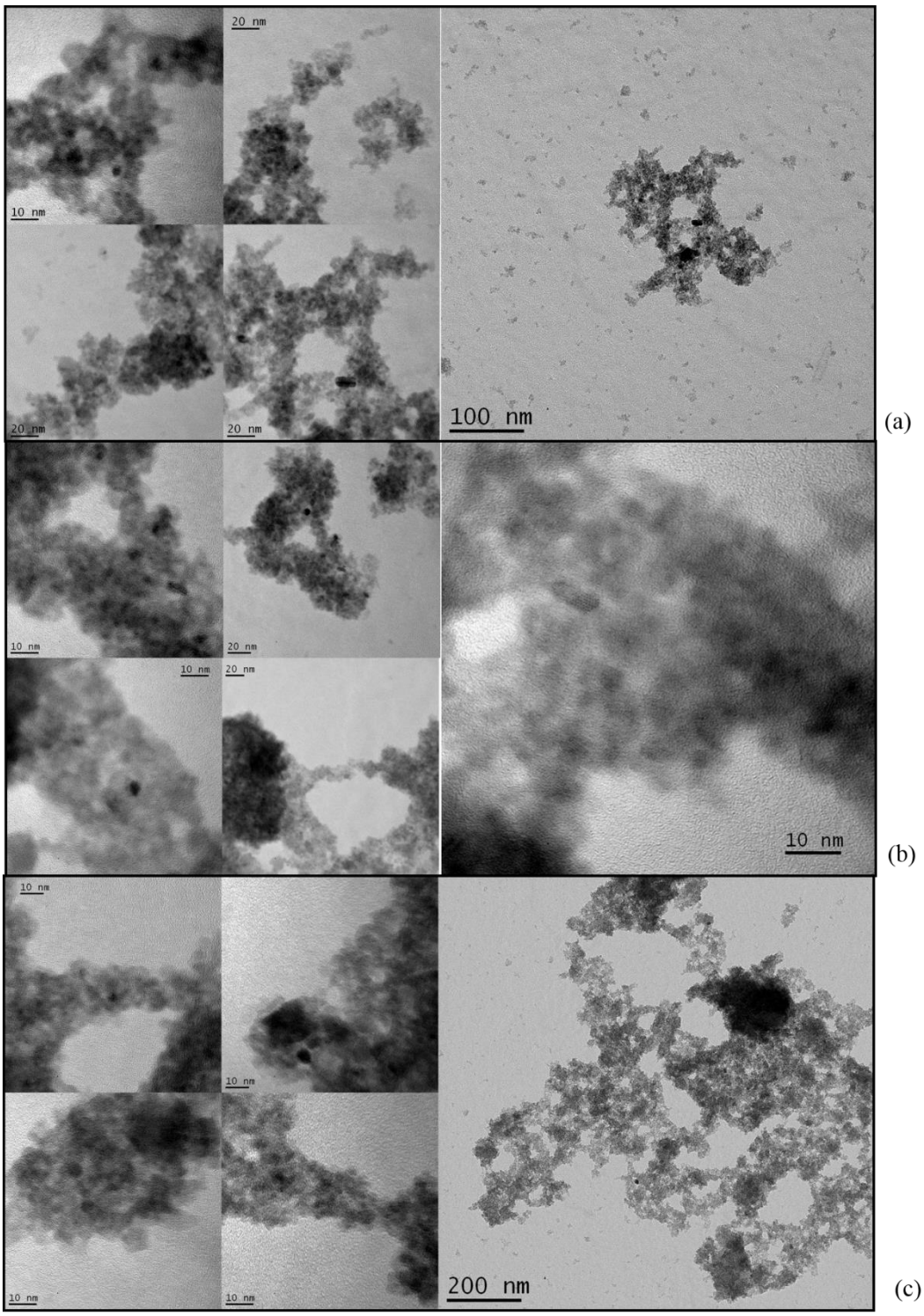

Figure 4.7. Iron oxide nanoparticles synthesised using different concentrations of $FeCl_2$ and $FeCl_3$, $FeCl_2$ = 0.14 M and $FeCl_3$ = 0.28 M (a), $FeCl_2$ = 0.15 M and $FeCl_3$ = 0.30 M (b), $FeCl_2$ = 0.16 M and $FeCl_3$ = 0.32 M (c). All nanoparticles can be seen to be approximately spherical and highly agglomerated.

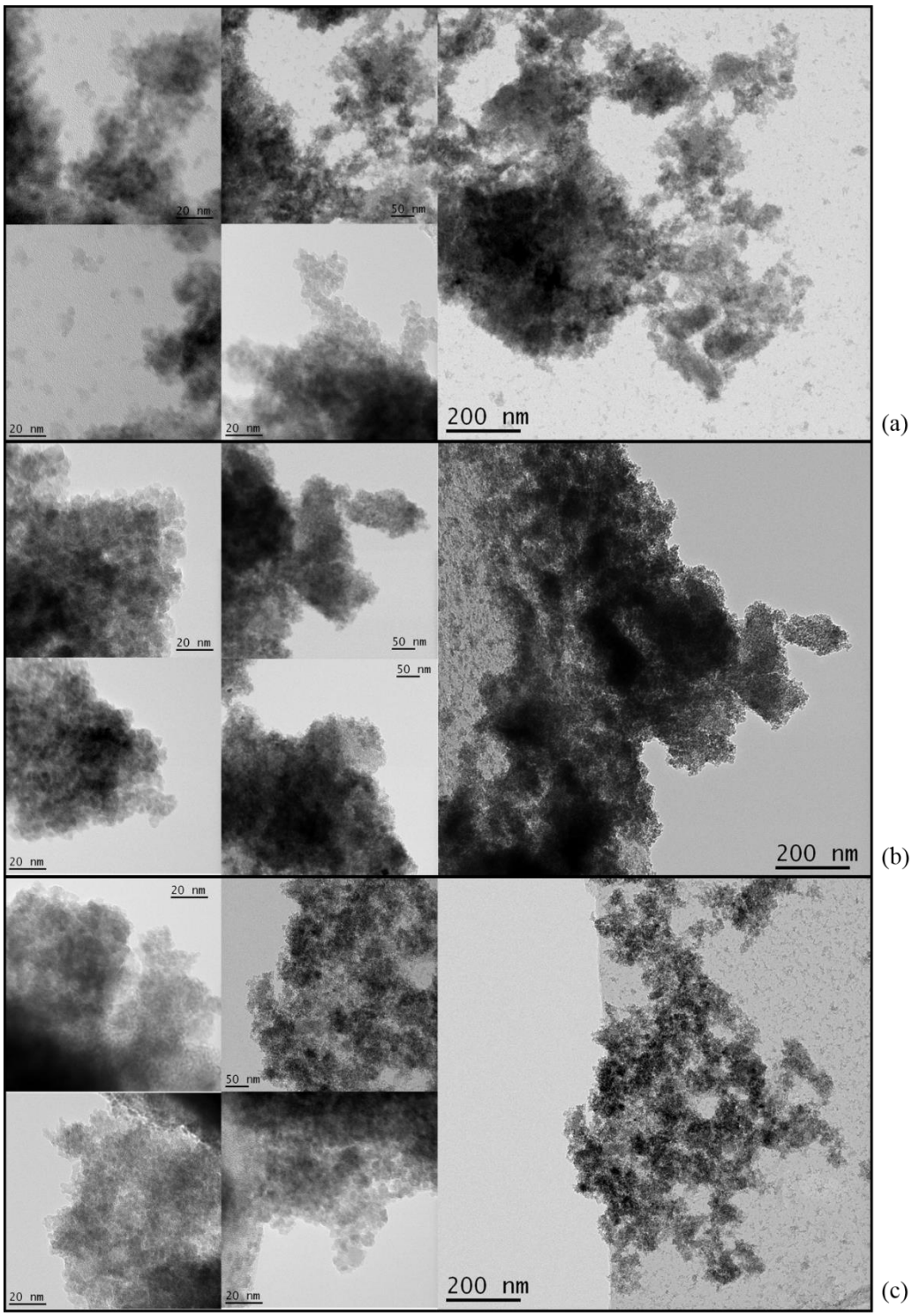

Figure 4.8. TEM images of the iron oxide nanoparticles at different total flow rates, 2250 µl hr^{-1} (a), 4500 µl hr^{-1} (b), and 6000 µl hr^{-1} (c).

4.3. Conclusions

The iron oxide nanoparticles produced using the continuous flow technique, were seen to be of a very small size with a standard deviation approximately one tenth of this (6.72 ± 0.72 nm), and calculated from PXRD data via the Scherrer Formula. The standard deviation in the particle size ≈ 10% should not cause a great difference in either the magnetic properties of the nanoparticles, or their half-life in the blood stream, if they were to be used for biomedical applications.[2]

The phase of the nanoparticles was seen to be a mixture of γ-Fe_2O_3 and Fe_3O_4, using FTIR. The amount of these two phases present in the nanoparticles was further evaluated using a calibration technique developed by Kim *et al.*, and adapted here for our purposes.[129] The nanoparticles were seen to comprise of 52.87 ± 5.79 % γ-Fe_2O_3 and 49.63 % ± 4.68 Fe_3O_4, this allowed for the calculation of the percentage yield of 97.06 %. The nanoparticles were also seen to be superparamagnetic in nature from the use of VSM. A critical evaluation of TEM images of nanoparticles produced at different synthesis parameters was then made, although no sizing information could be drawn from these due to the quality of the images, and without implying any unintentional size bias by measuring particle sizes manually.

A comparison was then drawn between the technique and the others currently presented in the literature, in short the nanoparticles produced are on a par with those produced using the droplet coalescence method in terms of size and standard deviation in this. They also have magnetic saturations greater than those produced using the co-axial flow method. When compared to nanoparticles produced in batch their size and magnetic saturation are seen to be smaller and with much smaller standard deviations in size.

Space time yields of the 2D flow focussed technique and the same reaction performed in batch upon the bench top were calculates showing the 2D flow focused technique to be over 6.4 times more efficient.

5.0. Controlling the Phase of Iron Oxide Nanoparticles

The IONs produced in both the batch and continuous flow focussing process contained a mixture of both Fe_3O_4 and γ-Fe_2O_3 phases. The Fe_3O_4 phase would prove more favourable in terms of potential magnetic applications, due to its higher magnetic saturation, while γ-Fe_2O_3 is the more chemically stable of the two phases.[19] It would therefore be advantageous to be able to control the amount of either of these phases within the nanoparticles to tailor their properties toward specific applications, of which the first step would be the ability to produce nanoparticles containing only Fe_3O_4 or γ-Fe_2O_3 phases.

A lack of analysis techniques exists for ways in which to easily quantify the amount of these two phases present within the nanoparticles, and due to the chemical instability of Fe_3O_4, i.e. it easily oxidizes, it would therefore be favourable to develop a technique capable of determining both the presence and quantity of the two phases within the nanoparticles at once. Mössbauer spectroscopy can be used, however, there is a risk of sample oxidation during sample preparation in this technique, and the technique is extremely specialised, requiring specialist equipment and analysis is required to be able magnetically split the resulting spectra, determining both the presence and quantity of both phases. It is therefore often used to compliment other analyses rather than be the primary method of analysis.[31, 84, 136, 137]

Herein the development of an X-ray diffraction procedure to analyse the nanoparticles phase both qualitatively and quantitatively is discussed along with the attempted synthesis of single phase Fe_3O_4 and γ-Fe_2O_3 nanoparticles using both batch and the continuous flow focussing technique.

5.1. Quantification of Fe_3O_4 and γ-Fe_2O_3 within Nanoparticles

X-ray diffraction methods do exist which allow for the quantification of different phases within mixtures; however, they mostly rely upon phases having different crystallographic structures. As both Fe_3O_4 and γ-Fe_2O_3 possess the inverse spinel structure, and show little difference in lattice parameter, when the tripling of the unit cell of γ–Fe_2O_3 is taken into account, many of these techniques cannot be used to differentiate between the phases. Further to this both contain the same elements nullifying the use of atomic scattering factors to determine any differences.[127-129]

Further complications arise from the sample size, and the need for samples to remain pure. A method in which an internal standard would be added to the sample to allow for phase quantification, would, due to the small sample size, prove to be destructive and non-beneficial. These factors rule out the majority of quantitative X-ray diffraction techniques that could be used for analysis of IONs.

5.1.1. Peak Deconvolution Method: Kim *et. al.* Method

A non-destructive method for the quantification of Fe_3O_4 and γ-Fe_2O_3 within a binary mixture of the two, using PXRD has been developed. It is reliant upon the similarity in structure of the two phases, and the associated intensity of their overlapping peaks seen in the PXRD patterns of the two phases, this often appears as peak asymmetry.[129] In summary, calibration mixtures of Fe_3O_4 and γ-Fe_2O_3 were prepared at different weight percentages, *wt%*. PXRD patterns were recorded over the ranges of $56 \leq 2\theta° \leq 58.5$ and $61 \leq 2\theta° \leq 64$, using a step size of 0.01° and time per step of 10 s. These ranges corresponded to the (511) and (440) reflections of both Fe_3O_4 and γ-Fe_2O_3.[170-173] Each PXRD pattern was recorded in triplicate and the intensity relating to $k_{\alpha 2}$ radiation

removed, before an average intensity for the triplicate data was calculated. The MDI Jade 6.5. program was then used to deconvolute the asymmetric peaks into their symmetric components, each relating to the two phases. The quantity of each phase can then be calculated from the ratio of the two intensities, the "integrated intensity fraction", through the gradient and intercept of the calibration graph, **eq. 5.1.**

Equation 5.1.

$$\left[\frac{I_{(511)Maghemite}}{I_{(511)Maghemite} + I_{(511)Magnetite}}\right] = kw_{maghemite}$$

A linear calibration graph was obtained by plotting the integrated intensity fraction in percent, against the weight percentage within the calibrants. The values used for the calibration graph in the work of Kim *et.al.* are summarised in, **table 5.1.** Theoretically the calibration graph should be linear, passing through the origin, as if 0 wt% of Fe_3O_4 is present in a binary mixture of it and γ-Fe_2O_3 the sample must be purely γ-Fe_2O_3, and vice versa, if 0 wt% of γ-Fe_2O_3 is present the sample must be purely Fe_3O_4. Realistically this is not the case, sample eccentricities (peak broadening due to defects and strain), and the nature of the diffractometer (e.g. performing step wise scans with a goniometer) can cause changes in the intensity and position of the peaks.

The detection limit for the calibration graph was calculated from the root mean square error (RMSE), **eq. 5.2.**, the difference between the predicted and measured values, based upon the calibration graph trendline. The detection limit was found to be 9.5 wt%.

Equation 5.2.

$$Detection\ Limit = 3 \times \frac{RMSE}{Gradient}$$

Gradient	Intercept	R^2	Detection limit (wt%)
1.0136	-0.2371	0.9941	9.5

Table 5.1. The gradient, intercept, coefficient of determination and detection limit of the calibration graph created by Kim *e al.* using their technique of taking the average intensity of peaks relating to the [511] reflection of Fe_3O_4 and γ -Fe_2O_3.

5.1.2. Use of the Peak Deconvolution Method

The method of Kim *et al.*, appears to provide a quick, efficient and non-destructive method for the quantification of Fe_3O_4 and γ-Fe_2O_3 phases within nanoparticles, and was used in this work, to determine the weight percentages of γ-Fe_2O_3 and Fe_3O_4. In using this method for detection of the two phases within our nanoparticles using our own machinery, some considerations must be taken into account.

Firstly, the nanoparticles produced in the work of Kim *et al.*, were significantly larger in size, 33.8 ± 20.6 nm in diameter, than the nanoparticles produced in this work, and from the PXRD patterns presented in their work, are also more crystalline due to the synthesis method. The nanoparticles produced by Kim *et.al.* therefore possess a much larger diffracting volume than those in this work, which may also be more crystalline, producing much sharper peaks in the corresponding PXRD patterns, making detection and deconvolution of overlapping peaks much easier.[129]

Secondly, the calibration graph used in their work was made using a state of the art Rigaku diffractometer, and using more powerful peak profiling software in the form of the MDI Jade 6.5 program, neither of which were available for use in this work. The Bruker D5000 diffractometer which was in use at the University of Hull, uses both a different radiation source, detector and method of recording the intensity of diffracted X-rays, to the one

used by Kim *et.al.,* and therefore construction of our own calibration graph was required.[129]

Taking into account these considerations, some minor statistical analysis was used to obtain the calibration graph used in this work, including the use of the Dixon Q Test to remove statistical outliers, and eliminate any gross errors.

5.1.2.1. Preparation of Calibration Standards

Calibration standards were prepared by the intimate mixing of commercial γ-Fe_2O_3 nanoparticles (≤ 50 nm, the smallest commercially available γ-Fe_2O_3 nanoparticles available at the time) and bulk (≈ 1 μm) Fe_3O_4 particles. Nanoparticles of Fe_3O_4 were not used as these are often seen to have deficient iron content $Fe_{3-\delta}O_4$, which in effect is a mixture of the γ-Fe_2O_3 and Fe_3O_4 phases that the detection of is being attempted, and would therefore adversely affect the weight percentages in the calibrants.[24, 26, 28, 29] It must be highlighted that bulk Fe_3O_4 can still possess iron deficiencies, however, it is much less likely due to the large size of the nanoparticles, and provided they are kept under inert conditions, should possess very few iron deficiencies.[31, 84] The disadvantage of using bulk Fe_3O_4 is that it will lead to the production of sharper, less broad, peaks related to Fe_3O_4 in the PXRD patterns of the calibrants.

PXRD patterns of the binary mixtures, were recorded in triplicate, over the range $55 \leq 2\theta\ ° \leq 65$, with a step size of 0.02 ° and a time step of 28 s, to record the intensity of the peaks relating to the (511) and (440) reflections. A 0.02 ° step size was used in this work instead of the 0.01 ° step size used by Kim *et. al.* as from experience when working with the Bruker D5000 diffractometer, and the nanoparticls produced in this work a 0.02 ° step size produced clearer peaks with less noise upon the signal.

5.1.2.2. Peak Deconvolution

Peak deconvolution was performed upon the combined PXRD patterns using the XFit software program, chosen due to its recommendation by the CCP14 group PXRD group, as an alternative to the unavailable MDI JADE 6.5. program.[130, 174]

There are several steps in the peak deconvolution process;

- Collection of PXRD data and removal of the peaks the $k_{\alpha 2}$ radiation. The $k_{\alpha 2}$ contribution must be removed as it can cause the appearance of a second peak to the primary, which may be mistaken for the deconvoluted peaks, unfortunately this also causes an intensity decrease.
- Either "averaging" or "summing" of the intensity data of the scans which were performed in triplicate. The two methods effect the data slightly differently, as the main problem with this deconvoution method is obtaining enough counts to allow for an accurate deconvolution of the peak, the data presented throughout this work uses the summed rather than the averaged data. The difference between these two methods and the effect they have upon the final data is discussed further in **section 5.5.**
- Convert file to the .CPI format. Performed using the CONVX program.
- Symmetric peaks are then placed at the peak positions where at the positions of the theoretical peak positions of γ-Fe_2O_3 and Fe_3O_4 are upon the 2θ scale.
- XFit was then used to plot two symmetric peaks so that they fit the asymmetric peak, **fig. 5.1.**
- The intensities of these two symmetric peaks, for each calibrant were then used to create the calibration graph, **fig 5.2.**

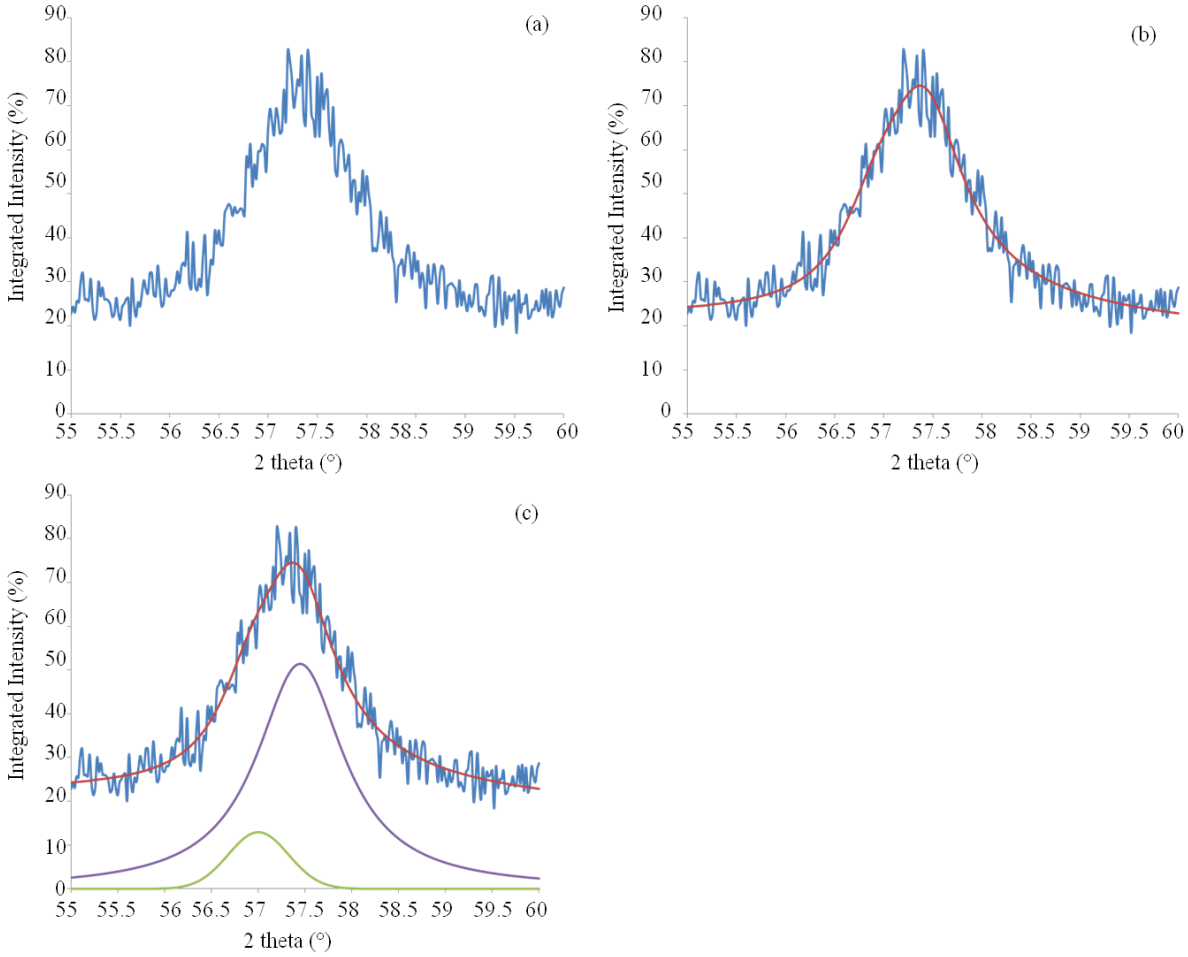

Figure 5.1. Peak deconvolution of a (511) reflection, where the X-ray data, blue (a), is first loaded into X-fit. The asymmetry of the PXRD data can be clearly seen if an assymetric peak is fitted to it, red (b). The raw PXRD data is deconvoluted into the symmetric peaks of Fe_3O_4, green, and γ-Fe_2O_3, purple, (c).

5.1.2.3. Statistical Testing of Data

A calibration graph was created by plotting the calculated integrated intensity, the contribution of each phase to the overall intensity, against the weight percentage of the phase respective phase in the calibrant. The most grossly erroneous point, if one was present, was removed from the graphs by application of the Dixon Q test to these calculated values by comparison to where the point should theoretically be present. A Q

value for a 95% level of confidence, which is taken as standard when developing a new analysis technique was used, as a relatively new technique was being adapted and developed for use with our own equipment, and use of the Dixon Q test therefore seemed expedient.[132, 133]

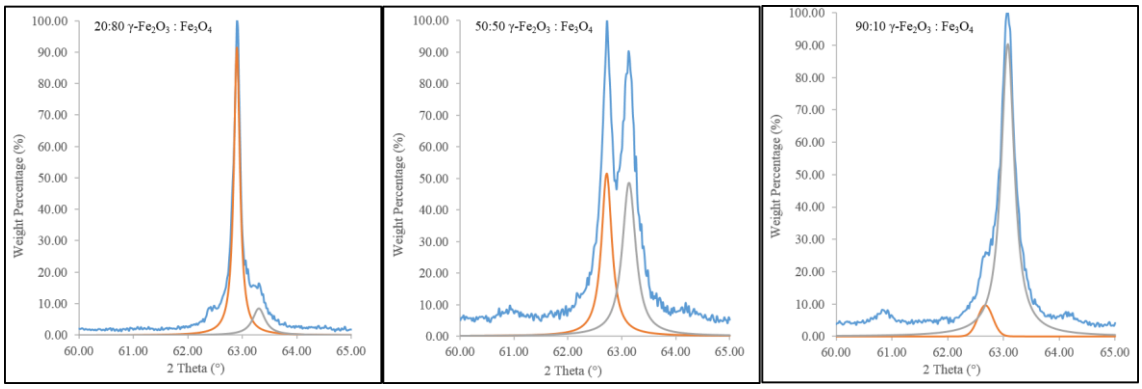

Figure 5.2. Deconvolutions of [440] peaks for calibrants made from 20% (right), 50% (centre) and 90% γ-Fe_2O_3 (left), in which the original X-ray diffraction data, has been deconvoluted into the peaks relating to Fe_3O_4 (orange) and γ-Fe_2O_3 (grey), the integrated intensities of the two are then used to construct the calibration graphs.

The Dixon Q test is a widely used statistical analysis tool for the removal of gross errors, **eq. 5.3.**, in which a data point differs excessively from that which is expected. Grossly erroneous data points can often be noticed easily by eye, however, it was thought prudent to obtain statistical evidence for this. The Dixon Q test uses a critical value, Q_{crit}, which if less than the experimental value, Q_{exp}, the data point associated with the Q_{exp} value is said to be erroneous. The Q_{crit} for a 95% factor of confidence (e.g. a 1 in 20 chance that the retention/rejection of a data point is wrong), for 19 observations, is 0.356. Therefore if Q_{exp} is greater than 0.356 for any data point it is removed, as it is considered to be erroneous.

Equation 5.3.

$$Q_{exp} = |x_q - x_n|/w$$

To perform the test, the difference between the suspect data point, x_q, and where the point should occur upon the theoretical trendline is taken. The theoretical trendline would pass through the origin and have a gradient of 1, as logically if only γ-Fe_2O_3 is present within a binary mixture, then 100% of the intensity must be contributed from this.

The difference between the actual and theoretical points was then calculated. These differences were then sorted from highest to lowest, and the difference between each of the initial differences, and their next nearest point calculated, x_n. The modulus of these values was then taken, and divided by the spread of the entire data set, *w*. The spread of the data was calculated by taking the square root of the number of values being analysed divided by the largest difference minus the smallest.

The quantity given by dividing the modulus of the data values by the spread of the data set is the Q_{exp} value, which was then compared to the Q_{crit} and if found to be greater than this the respective data point was labelled as erroneous. The single largest outlier calculated using the test, was then removed from the graph, as the Dixon Q test can be used to remove only a single outlier.

The Grubb's test which is able to removal multiple statistical outliers has also been suggested as an alternative to the Dixon Q test. However this is unsuitable for such small data sets, those with less than 25 points, and when used to perform removal of erroneous data has caused the calibration graphs to differ greatly from the theoretical trendline.[131]

The tables of the calculated integrated intensities of the calibrants, their Q values and the detection limits for each calibration graph used in this work can be found in the electronic appendices.

5.1.2.4. Detection Limit and Mean Square Error

The detection limits for the individual calibration graphs were calculated using the method suggested in the text book *Fundamentals of Analytical Chemistry*, rather than using the formula presented in the work of *Kim* et.al.[129, 132] The minimum detectable quantity, Δx_{min}, **eq. 5.4.**, can be determined from the standard deviation in the calibrants, s_b, and is dependent upon the level of confidence in the results, *t*.

Equation 5.4.

$$\Delta x_{min} = t s_b \sqrt{\frac{N_1 + N_2}{N_1 N_2}}$$

where, N_1 and N_2 are the number of points being compared and the degree of freedom, respectively.

5.1.5. Error Calculation

The error values calculated for each of the percentages of the two phases within the nanoparticles, was calculated by performing blind testing upon a calibrant with known amounts of the two phases present.

A blind calibrant was prepared by a second member of the research team by the intimate grinding of γ-Fe_2O_3 nanoparticles and bulk Fe_3O_4. The weights of each phase used equated to the calibrant containing 60% γ-Fe_2O_3 and 40% Fe_3O_4.

Multiple PXRD patterns of the (440) reflection of the calibrant were taken and the intensity added and deconvoluted, before comparing this to the calibration graph, which yielded values of 70.50% γ-Fe_2O_3 and 42.85% Fe_3O_4. The difference between these values and the actual weight percentages of the two phases present was then calculated. The error upon the values was calculated to be ± 15% of the weight percentage of γ-Fe_2O_3,

and ± 7% of the weight percentage of Fe_3O_4. These errors may seem particularly high, however it must be remembered that this is only a prototype technique.

In summary, the calibration graphs constructed using the added intensity data of the (440) reflections, of the tetragonal unit cell of γ-Fe_2O_3 ($P4_12_12$) are to be used throughout this work, **fig. 5.3.**

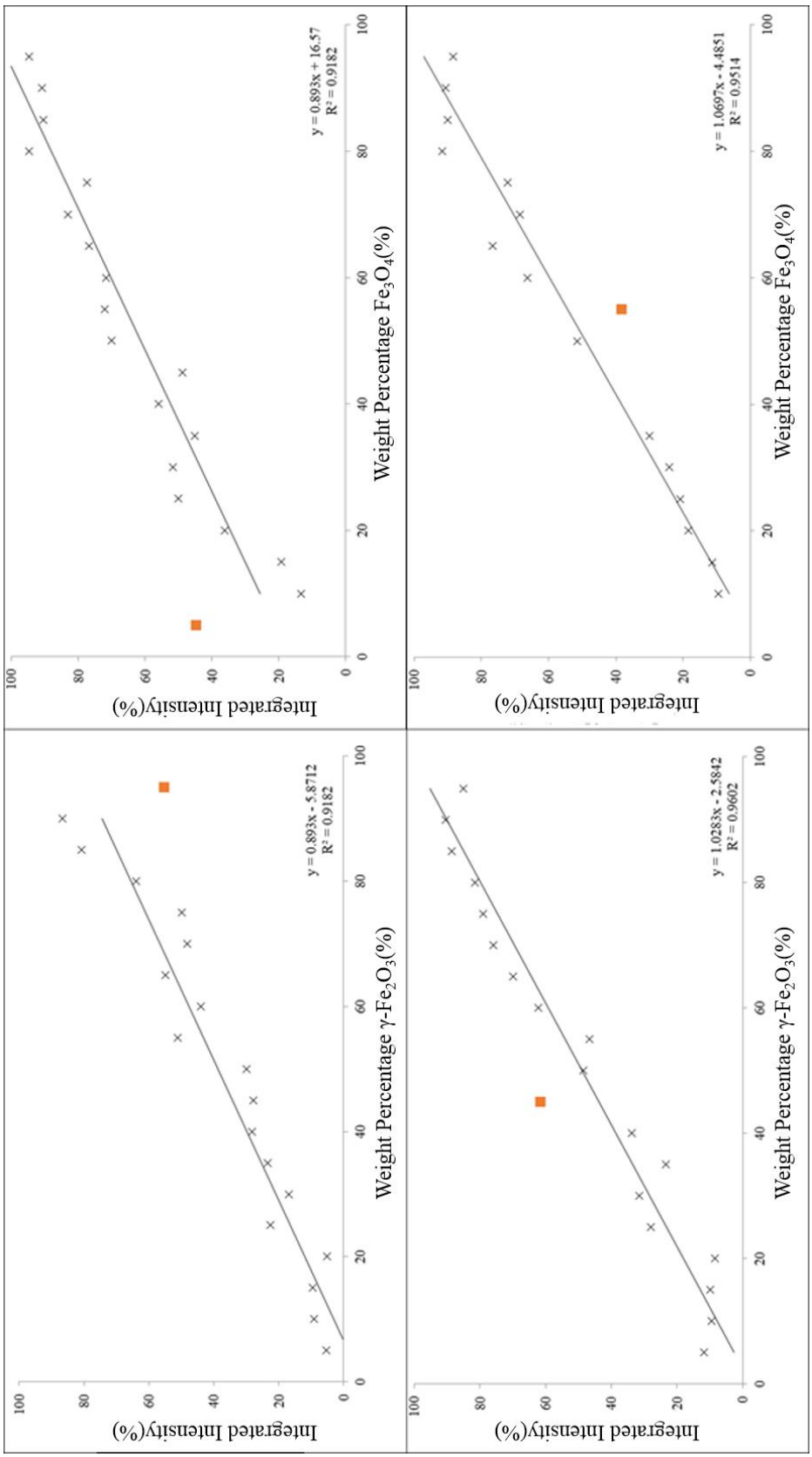

Figure 5.3. Calibration graphs constructed when the summed intensity of multiple PXRD patterns for each calibrant was used, where (511) γ-Fe_2O_3 (a), (511) Fe_3O_4 (b), (440) γ-Fe_2O_3 (c), and (440) Fe_3O_4 (d).

5.2. Synthesis of γ-Fe_2O_3 Nanoparticles

Single phase γ-Fe_2O_3 IONs were synthesised via the introduction of an oxidizing agent so that all of the Fe^{2+} content of Fe_3O_4 present in the IONs was oxidized, forming γ-Fe_2O_3 nanoparticles.

5.2.1. Synthesis of γ-Fe_2O_3 Nanoparticles in Batch

Nanoparticles with higher weight percentages of γ-Fe_2O_3 were synthesised via oxidation of IONs produced by the co-precipitation of divalent and trivalent iron salts, **eq. 5.5 and 5.6.**

Equation 5.5.

$$FeCl_2 + 2FeCl_3 + 8NaOH \rightarrow Fe_3O_4 + 4H_2O + 8NaCl$$

followed by;

Equation 5.6.

$$2Fe_3O_4 + \frac{1}{2}O_2 \rightarrow 3\gamma - Fe_2O_3$$

H_2O_2 was chosen as the oxidizing agent as the more commonly used nitric acid, is incompatible with Polyethyletherketone (PEEK) of which the microreactor housing, tubing and adapters are constructed.[152]

The experimental procedure outlined in **section 2.1.2.**, was used to form IONs in batch, before oxidation of these by the addition of the relative concentration of hydrogen peroxide (50 ml).

Powder X-ray diffraction patterns revealed each sample to be pure spinel phase, with no impurities present. The peak deconvolution technique, was then used to determine the

weight percentage of the two phases within the nanoparticles. Multiple PXRD patterns of the (511) and (440) reflections were recorded over the range $55 \leq 2\theta° \leq 65$. The percentages of γ-Fe_2O_3 and Fe_3O_4 within each sample were calculated from the added intensity data of the (440) reflections using the peak deconvolution technique, and the calibration graph constructed using the (440) reflections of both γ-Fe_2O_3 and Fe_3O_4 using the added intensity data, **fig. 5.3.** The weight percentages calculated using the calibration graph were plotted against the concentration of H_2O_2, **fig. 5.4.**

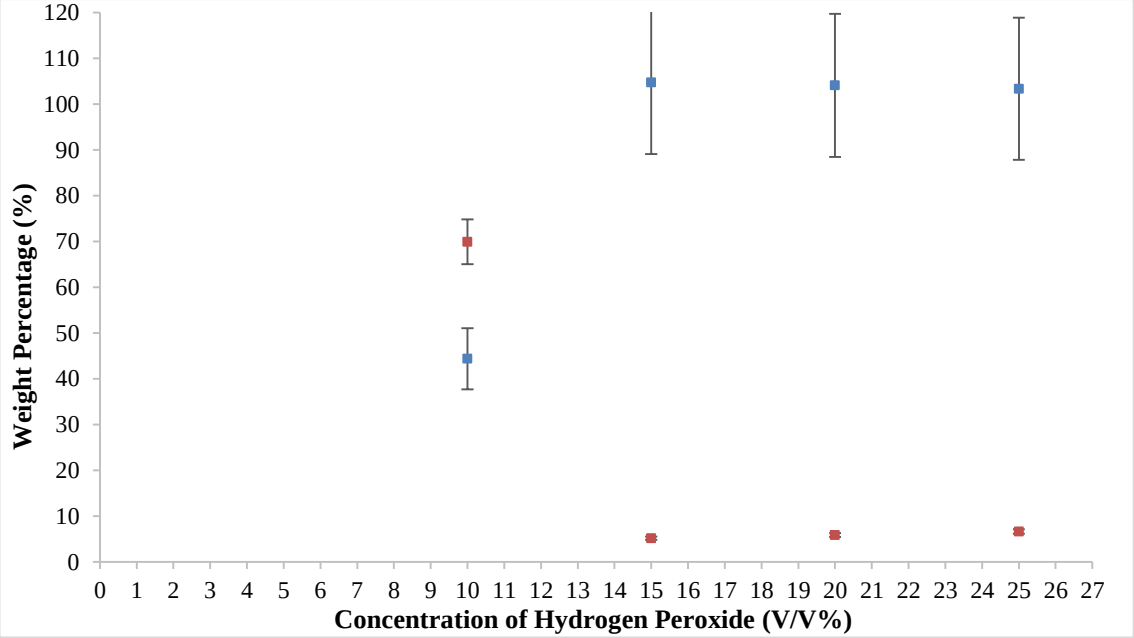

Figure 5.4. Plot of the weight percentages of γ-Fe_2O_3 and Fe_3O_4 calculated to be in the nanoparticles vs. concentration of hydrogen peroxide used as an oxidation agent for oxidation of Fe_3O_4 (orange) to γ-Fe_2O_3 (blue) in the nanoparticles.

The weight percentage of γ-Fe_2O_3 was seen to increase with increasing concentration of hydrogen peroxide. A hydrogen peroxide concentration of 15 V/V% was required to form completely γ-Fe_2O_3 nanoparticles 104.8 ± 11.9 %, and 5.1 ± 0.5 %, as the detection limit for Fe_3O_4 at a 95% confidence limit is 19.15 %, it can therefore be assumed that the

nanoparticles comprise of pure γ-Fe_2O_3, as below it cannot be said whether any Fe_3O_4 is present within the sample.

The reaction was taken forward for the attempted synthesis of pure γ-Fe_2O_3 nanoparticles using hydrogen peroxide upon the microreactor system.

5.2.2. Synthesis of γ-Fe_2O_3 Nanoparticles using Microreactors

The continuous flow focussing technique used for the synthesis of IONs was adapted to allow for the continuous synthesis of pure γ-Fe_2O_3 nanoparticles. The microreactor design allows for the initial production of IONs, with a mixture of γ-Fe_2O_3 and Fe_3O_4 phases being present, before oxidising these, through the addition of a flow of H_2O_2 through the inlet previously blocked with deionised water, **fig. 5.5.** Under laminar flow conditions oxidation of the nanoparticles proceeds by the diffusion of the hydrogen peroxide across the microchannel, before it can selectively oxidize the Fe^{2+} ions present in Fe_3O_4 to Fe^{3+}. The use of H_2O_2 as the oxidizing agent led to several technical issues due to its decomposition into O_2 and H_2O, which is catalysed by iron oxide, **eq. 5.7.**

Equation 5.7.

$$H_2O_2 \xrightarrow{Fe_2O_3} H_2O + \frac{1}{2}O_2$$

The decomposition was required for the oxidation process but leads to the formation of bubbles or plugs of gas within the microreactor system, which disrupt the laminar flow of the system, introducing some chaotic mixing of reagents, and causing problems with back pressure.

As this technique involves the oxidation of the IONs within the microreactor system, a quenching reagent would usually be used to prevent over oxidation in the outlet vial. Within the stock bottle the decomposition of hydrogen peroxide is prevented by the

addition of a stabilizing agent, however, it would likely have little effect in this case with the IONs in the collection vessel acting as a catalyst. A "salt ice" bath was instead employed to cool the collection vessel, and reduce the rate of decomposition of any un-reacted H_2O_2 present within it, and therefore oxidation mainly takes place within the microreactor.

The experimental procedure was outlined in **section 2.2.2.**, hydrogen peroxide (30 V/V %) was used as the oxidizing agent. The precipitate produced was collected under nitrogen and cooled using the "salt ice" bath, before the supernatant (including any un-reacted H_2O_2) was removed via magnetic decantation, and washed with ethanol, and deionised water before being dried in an inert atmosphere at 100 ℃ to remove any additional water content, **fig. 5.5.**

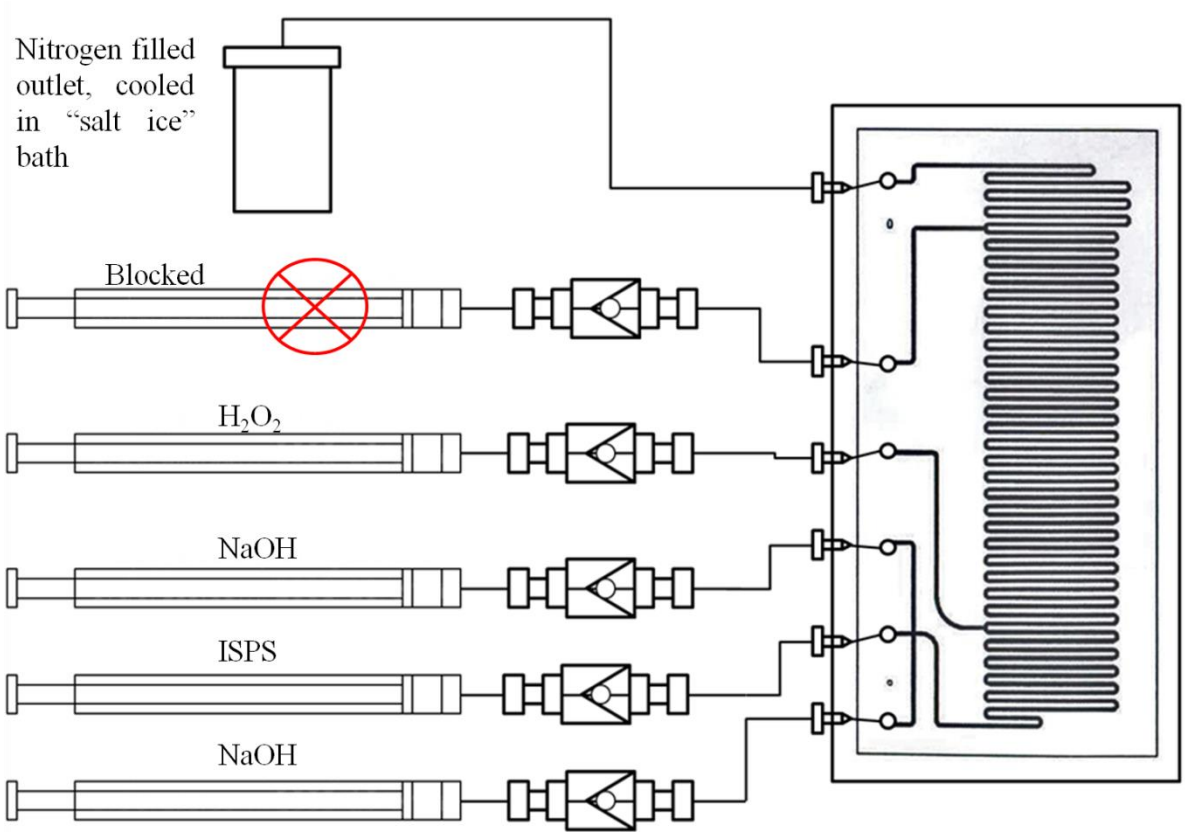

Figure 5.5. Schematic microreactor design for the synthesis of pure γ-Fe_2O_3 nanoparticles, the same set-up is used as when producing "ordinary" ION's, with the addition of a flow of H_2O_2 as an oxidizing agent through the 4th inlet, to oxidize the nanoparticles formed from the reaction of the ISPS with the sodium hydroxide.

The peak deconvolution technique was used to determine the weight percentage of the two phases within the nanoparticles. PXRD patterns of the precipitate were recorded over the range of $55 \leq 2\theta\ ° \leq 65$, and the peak corresponding to the (440) reflection of Fe_3O_4, and γ-Fe_2O_3 deconvoluted, the intensities of the deconvoluted peaks were then compared to the calibration graph compared to the calibration graph, **fig.5.6.** The weight percentages of Fe_3O_4 and γ-Fe_2O_3 were calculated to be 20.8 ± 1.5 % and 91.8 ± 13.8 %, respectively, suggesting that the nanoparticles were almost completely γ-Fe_2O_3, as the detection limit for Fe_3O_4 is 19.15 %. Due to the high concentration of hydrogen peroxide used, and comparing this with the results obtained for the synthesis of γ-Fe_2O_3 in batch, and those obtained by other groups, it is quite likely that the nanoparticles produced do contain such

a large proportion of γ-Fe_2O_3. The actual structure of this, whether a small core of Fe_3O_4 surrounded by a large shell of γ-Fe_2O_3, or interspersed unit cells of the two phases is beyond the scope of this work.[31, 84]

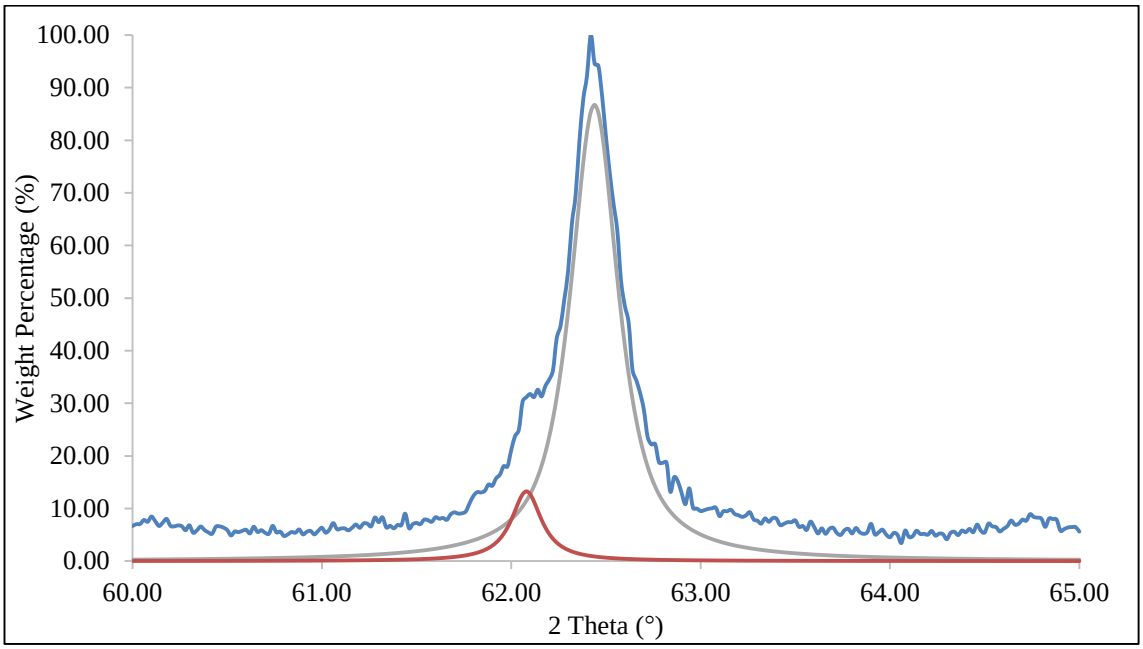

Figure 5.6. Deconvolution of the [440] peak for the IONs produced in the microreactor using H_2O_2 as an oxidizing agent, into its respective peaks for Fe_3O_4 (orange) and γ-Fe_2O_3 (grey). A slight shoulder to the peak can be seen hinting at the presence of some Fe_3O_4, however the percentage of γ-Fe_2O_3 calculated is within the detection limit for this, and as such the sample is likely to be almost completely γ-Fe_2O_3.

To confirm that the IONs produced using the modified continuous flow focussing technique, composed of nearly entirely γ-Fe_2O_3, a titration against $KMnO_4$ was performed, so that the percentage of Fe^{2+} within the sample could be calculated, **eq. 5.8.**

Equation 5.8.

$$MnO_4^- + 8H^+ + 5Fe^{2+} \rightarrow Mn^{2+} + 4H_2O + 5Fe^{3+}$$

The weight percentage of Fe_3O_4 calculated from the Fe^{2+} content in the solution was 0.104 ± 0.375 %, as such the amount of Fe_3O_4 within the sample is negligible and the sample thought to consist purely of γ-Fe_2O_3.

Further evidence of the production of single phase nanoparticles was provided from the Mössbauer spectra of the nanoparticles, recorded and interpreted by Professor David Evans at the University of Hull using an ES-Technology MS-105 Mössbauer spectrometer, and the parameters obtained by fitting the data with Lorentzian curves, **fig. 5.7.**

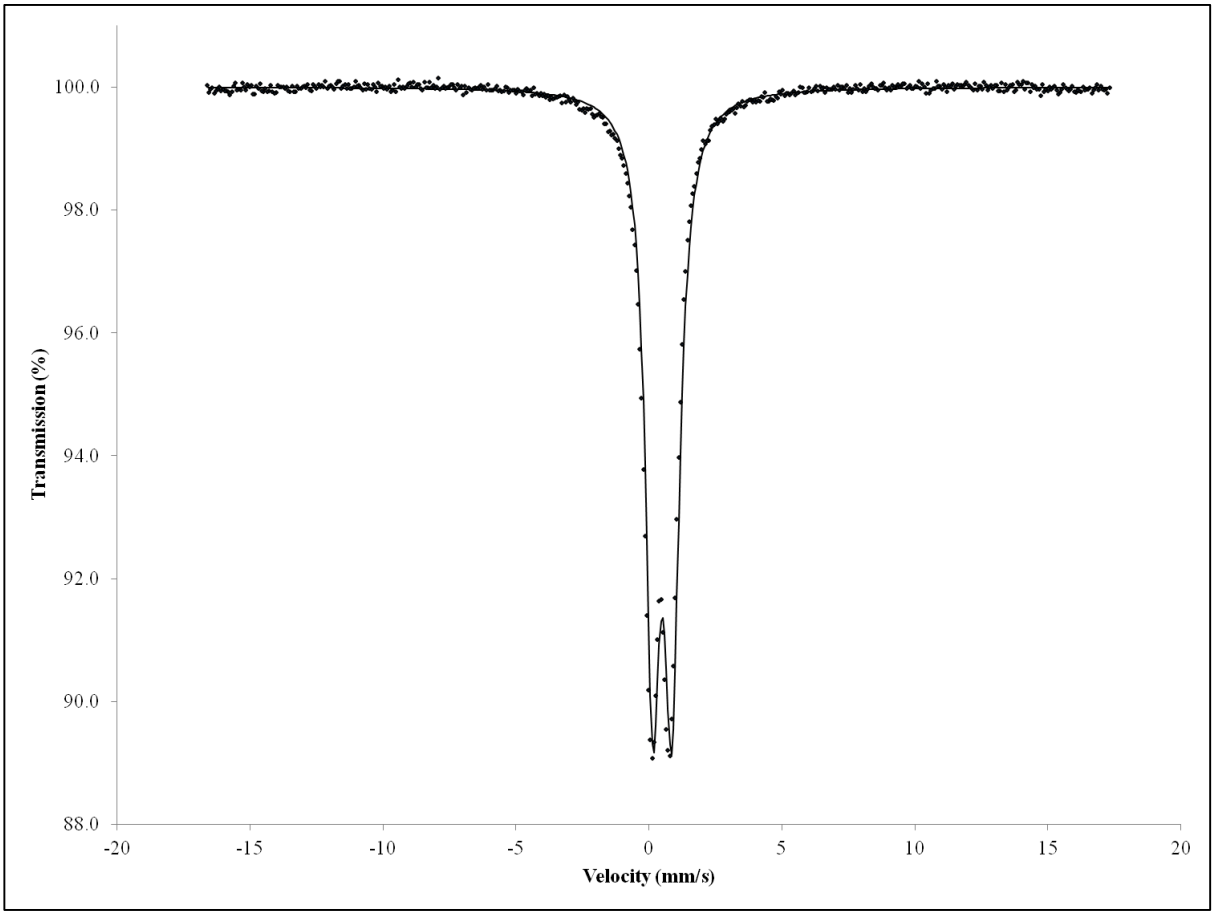

Figure 5.7. Mössbauer spectrum of γ-Fe_2O_3 nanoparticles synthesised using microreactor, showing the doublet spectrum of a superparamagnetic compound, and although little information can therefore on the compounds structure from this spectrum, only a single doublet can be seen to be produced suggesting the nanoparticles are of a single phase.

The well-defined single quadrupole, split doublet is indicative of single phase superparamagnetic particles. If the temperature were to be further lowered or the sample placed within a magnetic field, then a sextet spectrum can be expected to be obtained as the superparamagnetic relaxation time would be greater (slower) than that of the Larmor procession frequency of the ^{57}Fe nucleus. The isomer shift and quadrupole splitting are similar to that reported for IONs produced by other groups, **table 5.2.**[32, 33, 175]

As only a single phase can be seen to be present in the Mössbauer spectrum, and along with the results obtained from both the titration and application of the calibration graph the IONs produced in the microreactor are thought to purely comprise of γ-Fe_2O_3.

Sample	Isomer Shift ($mm\ s^{-1}$)	Quadropole Splitting ($mm\ s^{-1}$)	Line Width ($mm\ s^{-1}$)
γ-Fe_2O_3 IONs synthesised in microreactor	0.45	0.72	0.34
IONs [149]	0.40-0.49	0.60-0.65	

Table 5.2. Comparison of Mössbauer of the isomer shift and quadropole splitting of the doublet obtained for the pure γ-Fe_2O_3 IONs produced in this work and those of similar ION's in the literature.

5.3. Synthesis of Pure Fe_3O_4 Nanoparticles

The synthesis of nanoparticles with higher weight percentages of Fe_3O_4 would be favourable for the increased magnetic saturation.[19] Whether the synthesis of pure Fe_3O_4 nanoparticles is practically achievable is of debate, due to its rapid oxidation to the intermediate iron deficient, $Fe_{3-\delta}O_4$, phase in any atmosphere which is not inert. Therefore while the formation of pure Fe_3O_4 nanoparticles may not be practically possible,

increasing the weight percentage of Fe_3O_4 would still be favourable and the implementation of a reproducible route to their synthesis would be beneficial.

5.3.1. Altering Weight Percentage of Fe_3O_4 in IONs in Batch

Fe_3O_4 nanoparticles were synthesised using the same co-precipitation reaction used to synthesise IONs in batch, **section 2.1.2.** $NaBH_4$ was used as a reducing agent and a competitor to oxidation of Fe^{2+} to Fe^{3+}, by generating a reducing atmosphere due to the decomposition of $NaBH_4$ with water, **eq. 5.9.** Much of the $NaBH_4$ was consumed in this decomposition reaction; however a fraction was able to prevent oxidation or reduce the Fe^{3+}.

Equation 5.9.

$$NaBH_4 + 2H_2O \rightarrow NaBO_2 + 4H_2$$

A potential problem was that of the reduction of the nanoparticles lead to formation of the pure metal. The $NaBH_4$ solution was therefore tested at several concentrations, to see if this would cause reduction to the pure metal.[176]

PXRD patterns of the precipitate collected revealed no crystalline impurities to be present, and the presence of both pure Fe nanoparticles and NaCl were ruled out at all concentrations of $NaBH_4$. The percentage weight of Fe_3O_4 in each of the samples was calculated using the peak deconvolution method, by adding the data obtained for the (440) reflections of cubic Fe_3O_4 and tetragonal γ-Fe_2O_3 from multiple scans, and comparing the calculated intensities to the calibration graph, **fig 5.8.**

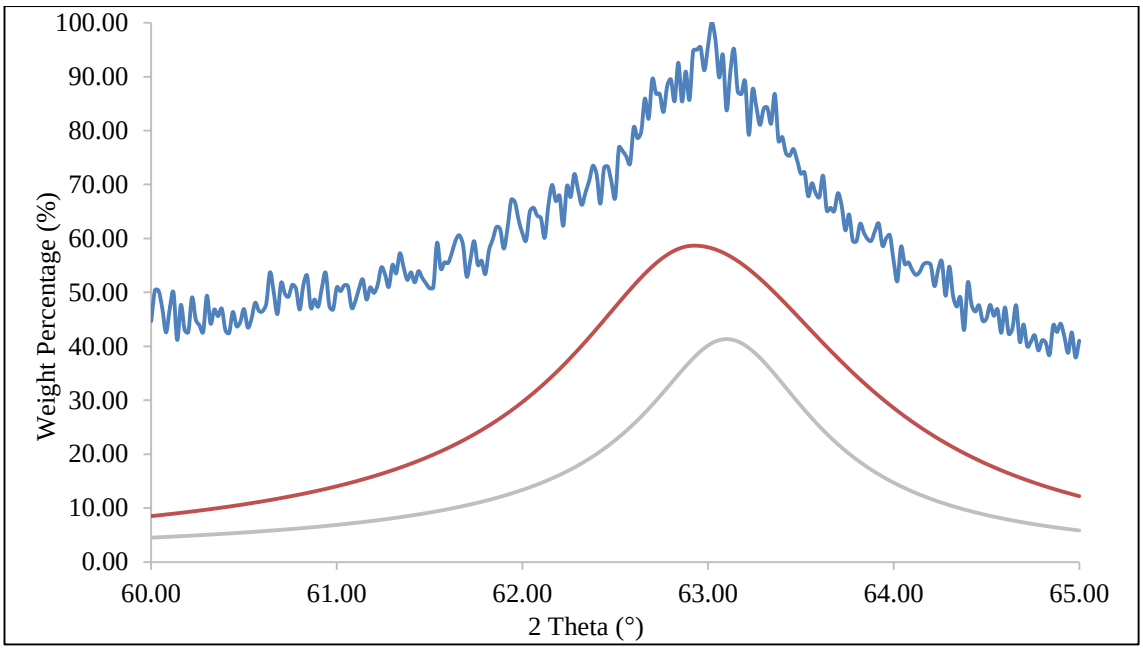

Figure 5.8. IONs produced in batch when 0.30 M $NaBH_4$ was used as a reducing agent in an attempt to synthesise nanoparticles with a higher weight percentage of Fe_3O_4, where the [440] peak has been deconvoluted into the corresponding peaks for Fe_3O_4 (orange) and γ-Fe_2O_3 (grey).

An increase in the weight percentage of Fe_3O_4 was seen with increasing $NaBH_4$ concentration, **fig. 5.9.** The weight percentage of Fe_3O_4 within the nanoparticles, was not seen to be that much greater than that which was present without the use of $NaBH_4$, the nanoparticles were seen to constitute of 59.8 ± 6.4 % Fe_3O_4 and 42.2 ± 3.9 % γ-Fe_2O_3, and it would appear that that the synthesis of "pure" Fe_3O_4 nanoparticles could not be achieved with such low concentrations of $NaBH_4$. Attempted conversion of the reaction for use with the continuous flow focussing technique upon the microreactors was still made.

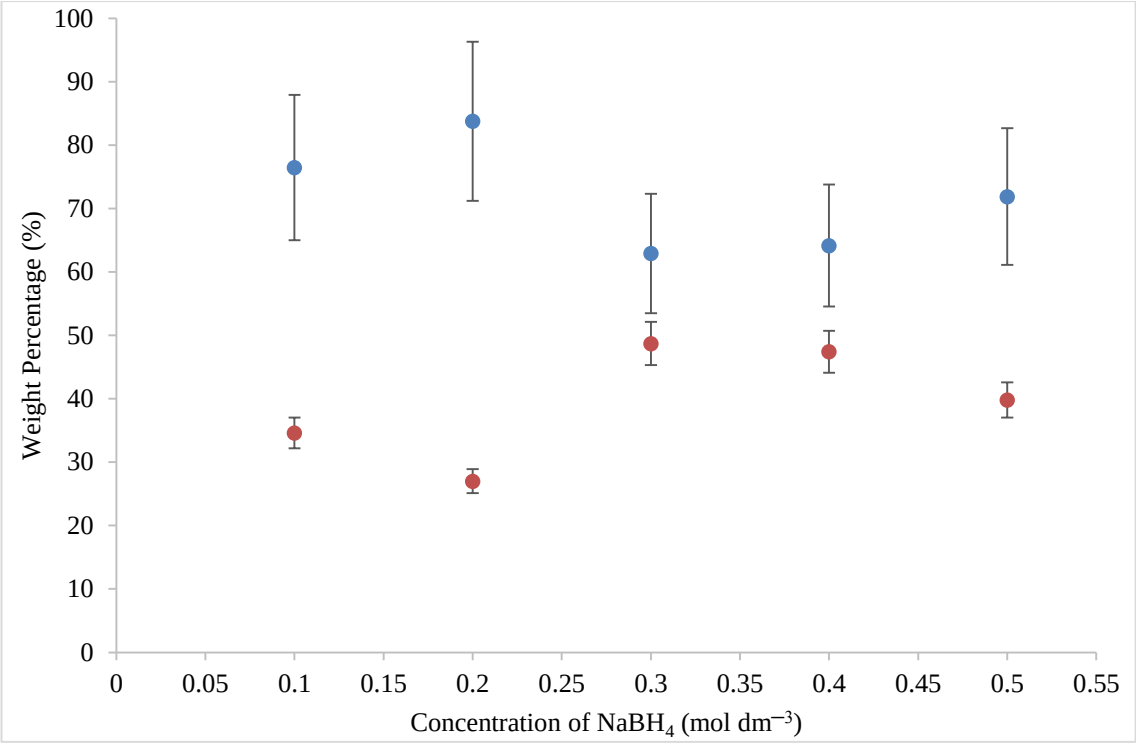

Figure 5.9. Plot of the weight percentages of Fe_3O_4 (orange) and γ-Fe_2O_3 (blue) within the IONs produced when $NaBH_4$ was used as a reducing agent at various concentrations. Little increase in the amount of Fe_3O_4 was seen within the nanoparticles with increasing concentrations of $NaBH_4$.

5.3.2. Synthesis of Fe_3O_4 Nanoparticles using Microreactors

The continuous flow focussing technique used for the synthesis of IONs was modified to allow for the synthesis of nanoparticles with increased weight percentages of Fe_3O_4, similar to when hydrogen peroxide was used to produce nanoparticles with increased weight percentages of γ-Fe_2O_3, replacing the flow of H_2O_2 with a flow of $NaBH_4$ dissolved in dry ethanol, **fig. 5.10.**

Ideally the microreactor design would allow for the initial production of IONs, before addition of the $NaBH_4$. It was thought that the large volume of water would act as a quench of the $NaBH_4$, causing it to completely decompose within the microreactor, and no further reduction would occur in the collection vial.

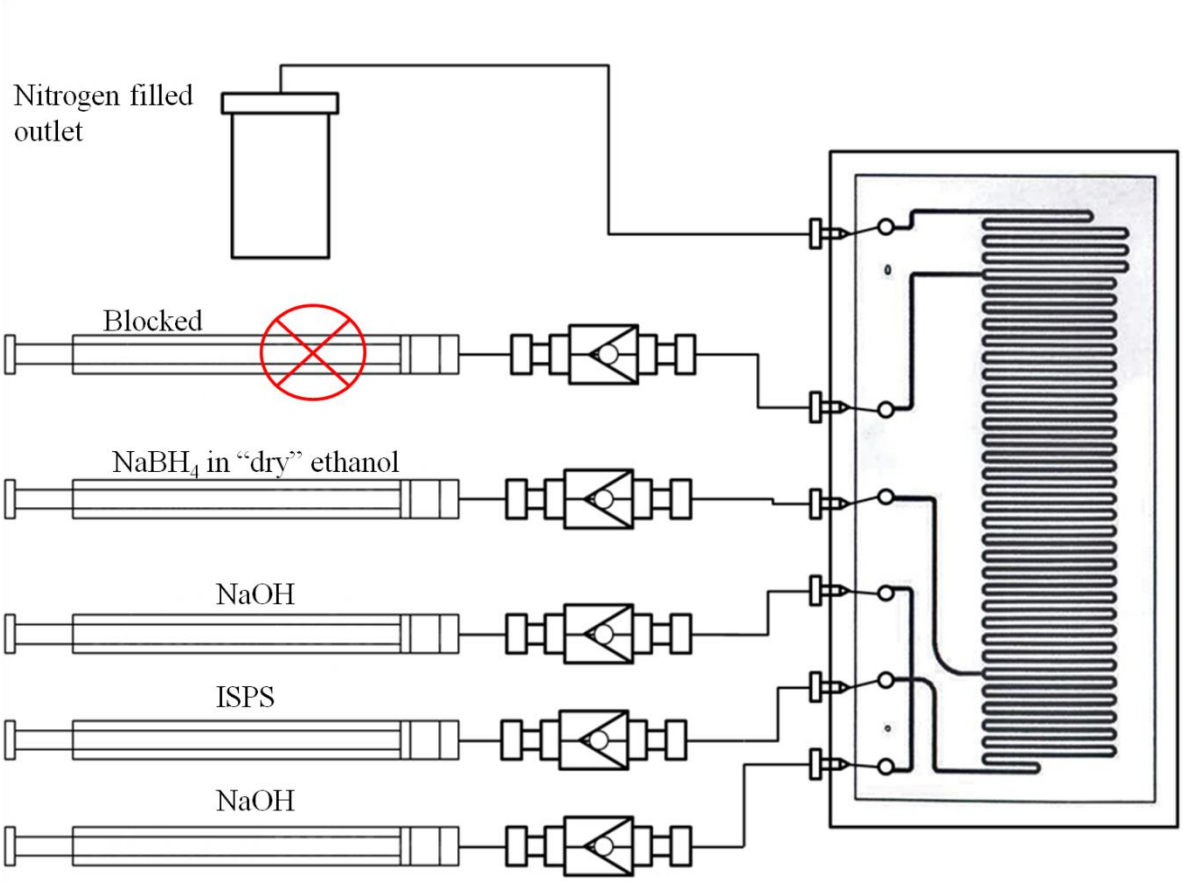

Figure 5.10. Schematic microreactor design for the synthesis of pure Fe_3O_4 nanoparticles, the same set-up is used as when producing "ordinary" ION's with the addition of a flow of $NaBH_4$ in dry ethanol as a reducing agent through the 4th inlet, to oxidize the nanoparticles formed from the reaction of the ISPS with the sodium hydroxide.

Unfortunately no precipitate could be collected, due to several technical problems. Primarily due to pressure problems associated with the decomposition of $NaBH_4$, which was far more vigorous than that of H_2O_2, leading to the formation of large plugs of H_2 gas being produced. This affected the pressure within the microreactor, and therefore the flow rate of reagents, and any results obtained could not be guaranteed to be reproducible. Fouling of the microreactor was seen to occur on a regular basis due to the formation of insoluble $NaBO_2$. This was particularly prominent in the PEEK tubing leading from the outlet to the collection vessel, the PEEK tubing itself was found to react with the $NaBH_4$,

due to reduction of the ketones to alcohols, which led to the tubing becoming brittle, leading to cracking.[177] An alternative reducing agent would therefore have to be found to be able to produce these nanoparticles using this microreactor set-up.

5.4. Conclusions

A previously reported peak deconvolution technique based upon the ratio of the intensities of selected diffraction peaks was adapted and developed for the determination of the percentage of γ-Fe_2O_3 and Fe_3O_4 within the IONs produced in this work.[129] The technique required some adaptation to be used in this work, so that the weight percentage of γ-Fe_2O_3 and Fe_3O_4 in the nanoparticles already produced using the 2D flow focussing technique. The technique used here should at best be viewed as a prototype due to the large errors that are calculated for it, and further refinement is required for more accurate phase determination. There are also several theoretical considerations that pose questions about the technique that are discussed in the "Further Discussions" section, **section 5.5.**
As both phases were found to be present in these nanoparticles it was theorised that the percentages of these may be controllable using oxidizing and reducing agents. It proved possible to synthesise nearly pure γ-Fe_2O_3 nanoparticles through the use of hydrogen peroxide, in both batch and in the microreactor. This however did prove difficult to control due to iron oxide acting as a catalyst for the decomposition of hydrogen peroxide and therefore causing further over oxidation of the sample. With more careful selection of the oxidizing agent it is likely that the weight percentage of γ-Fe_2O_3 can be more accurately controlled. Nitric acid would be the most likely candidate, if the microreactor housing and tubing can be made of a resistant polymer, or glass tubing could be employed. The production of nanoparticles with higher weight percentages of Fe_3O_4 through the use of sodium borohydride as a reducing agent and oxidation competitor proved to be far

more problematic. In batch the nanoparticles were found to contain weight percentages similar to those produced without the use of sodium borohydride as a reducing agent suggesting that this had little effect upon the weight percentage of Fe_3O_4 present in the nanoparticles. This may is probably due to the sodium borohydride reacting with the large excess of water present in the aqueous reagents. An alternative explanation may be that the rate of oxidation of Fe_3O_4 to γ-Fe_2O_3 is significantly fast enough to counter act the effect of the sodium borohydride, although if this was the case higher percentages of γ-Fe_2O_3 would be expected in the nanoaprticles originally produced in the microreactor, compared to those produced using sodium borohydride. The reaction was also attempted in the microreactor, however due to the extremely fast rate of decomposition of Sodium borohydride, in the microreactor large back pressure problems were encountered.

5.5. Further Discussion

Although the peak deconvolution method developed by Kim *et.al.*, and used in this work offers an all in one technique for the qualification and quantification of γ-Fe_2O_3 and Fe_3O_4, there are some points of the underlying solid state theory that require discussion. Firstly, should the average intensity or the combined intensity of the multiple PXRD patterns be used? Kim *et.al.* used averaged data to increase the signal to noise ratio, however, the low intensities of the peaks prove to be difficult to deconvolute.[129] As a large amount of noise would greatly affect the shape of the peak over a small range of intensities and therefore the amount of the two phases present.[129] Taking an average of multiple scans does decrease the amount of noise seen upon the PXRD pattern, as would increasing the scan length. The overall intensity of the peak, however, will remain on the same scale as the original patterns and therefore still be quite low, which can cause difficulties when deconvoluting the peaks using XFit.[130, 174]

The addition of the PXRD patterns can also decrease the amount of noise present upon the PXRD patterns, by amplifying the intensity of the peaks rather than the background noise, which occurs randomly, and would cancel out over multiple patterns. This also increases the overall intensity of the peaks, helping with their deconvolution, although a "noisier" pattern is observed in comparison to the averaged intensity.

To test which of the two methods produced the more accurate calibration graphs, multiple PXRD patterns were recorded for the calibrants over the range $55 \leq 2\theta\ ° \leq 65$, with a step time of 28 s, and a step size of 0.02 °. Deconvolution of the recorded patterns was performed using the method proposed in **section 5.1.2.2.**, with the peak positions of the (511) and (440) reflections set at those of the Fe_3O_4 (*Fd3-m*) and γ-Fe_2O_3 (*P4₁2₁2*) phases both space groups were chosen as they represent those most similar to those used in the work of Kim *et.al.*[129] Calibration graphs were then created from the data sets and the most grossly erroneous point removed after application of the Dixon Q test, **fig. 5.11.**, and **fig. 5.12.**

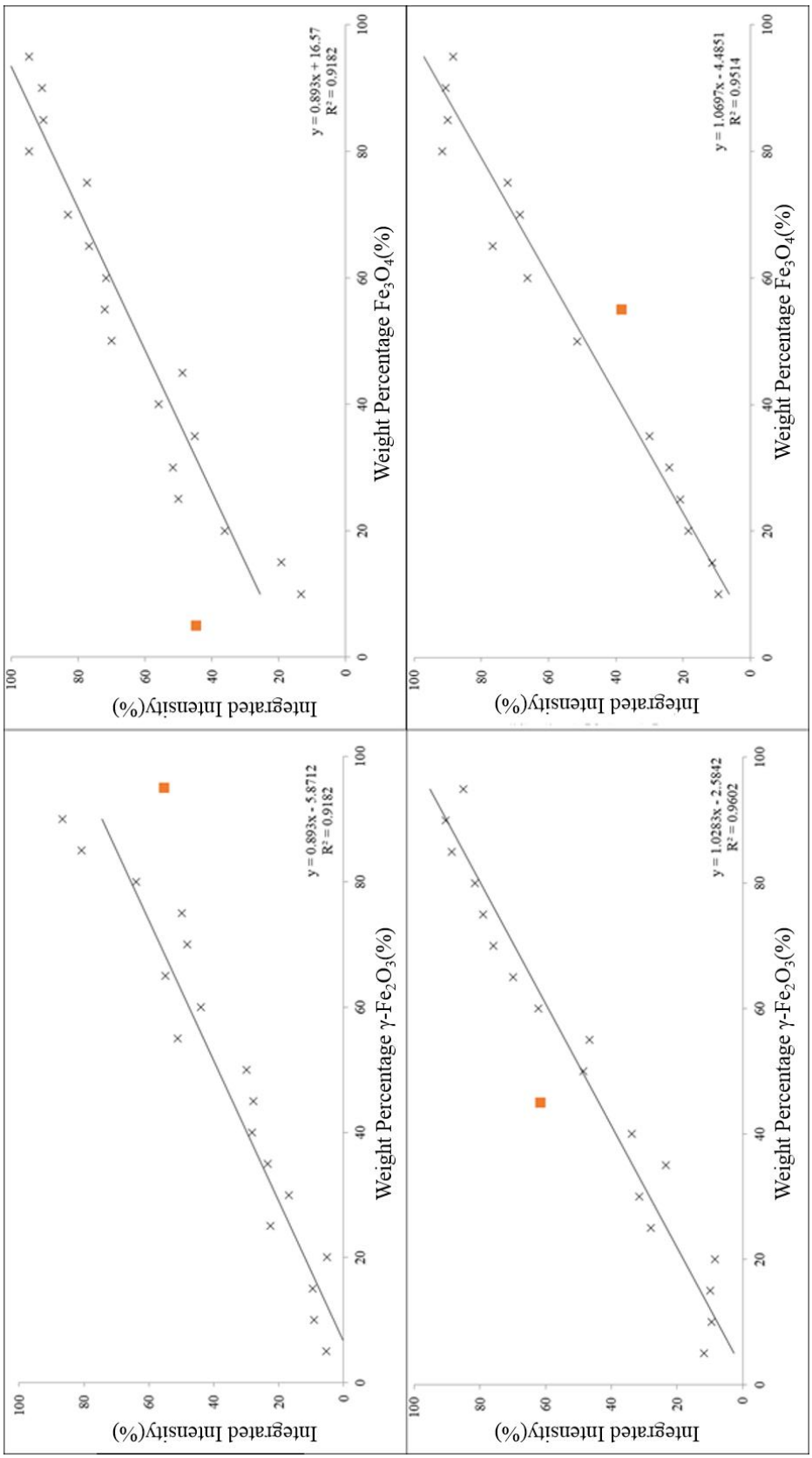

Figure 5.11. Calibration graphs constructed when the summed intensity of multiple PXRD patterns for each calibrant was used, where (511) γ-Fe_2O_3 (a), (511) Fe_3O_4 (b), (440) γ-Fe_2O_3 (c), and (440) Fe_3O_4 (d).

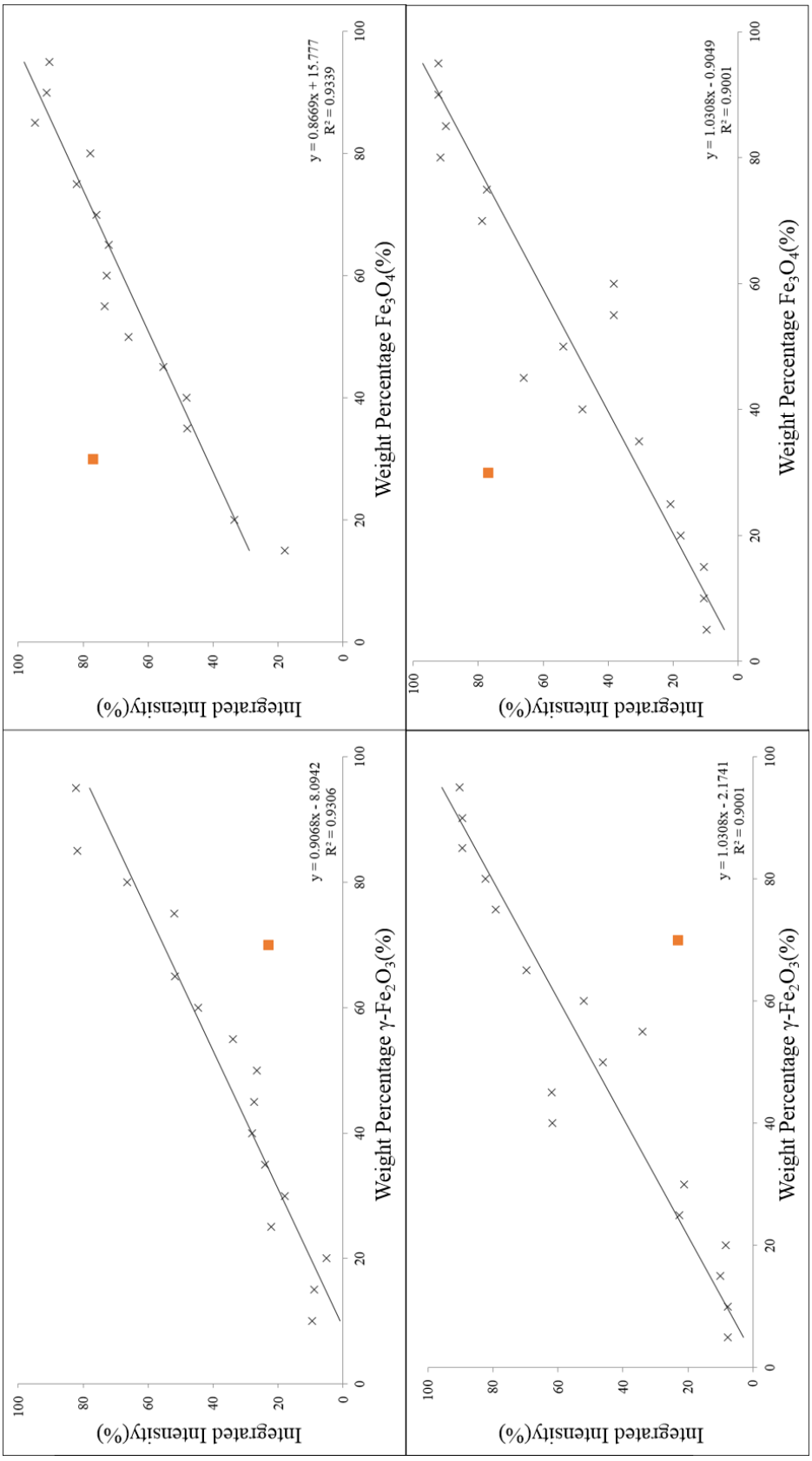

Figure 5.12. Calibration graphs constructed when the averaged intensity of multiple PXRD patterns for each calibrant was used, where (511) γ-Fe_2O_3 (a), (511) Fe_3O_4 (b), (440) γ-Fe_2O_3 (c), and (440) Fe_3O_4 (d).

To test which calibration graphs were the most accurate, the intercept and gradient of the calibration graphs were compared to the theoretical intercept and gradient, which should be 0 and 1 respectively, as well as looking at the calculated detection limits for each graph, **table 5.3.**

Method			Gradient	Difference	Intercept	R^2	Detection limit (wt%)
Averaged Method	(511)	γ-Fe_2O_3	0.847	-0.153	-6.978	0.829	13.0
		Fe_3O_4	0.859	-0.141	-3.051	0.819	20.6
	(440)	γ-Fe_2O_3	0.967	-0.033	-1.517	0.783	18.5
		Fe_3O_4	0.967	-0.033	4.866	0.783	30.2
Addition Method	(511)	γ-Fe_2O_3	0.893	-0.107	-5.871	0.918	13.8
		Fe_3O_4	0.893	-0.107	16.570	0.918	17.4
	(440)	γ-Fe_2O_3	1.028	0.028	-2.584	0.960	12.2
		Fe_3O_4	1.070	0.070	-4.485	0.951	29.1

Table 5.3. Gradient intercept, coefficient of determination and detection limits for the calibration graphs (fig. 5.2. and fig. 5.3.) produced using the summed and averaged PXRD intensity data, the calibration graph for the [440] reflection using the summed data, addition method, can be seen to be most accurate, with a gradient and intercepts closest to the theory, while having the most accurate coefficient of determination.

From the above table it can be seen that the calibration graphs produced using the (511) reflection are more inaccurate in terms of their gradients, deviating further from the

theoretical gradient than those produced using the (440) reflection. This may be due to the positions of the two (511) reflections being much closer, compared to that of the (440), and also of weaker intensity than the (440) reflections. Both of these factors make the deconvolution process using the X-fit software more difficult, and are likely a cause of this inaccuracy.

When looking at the differences between the two methods, the difference between the gradient of the actual and theoretical trend lines, the average method can be seen to deviate more than those of the addition method. When looking at the intercepts however the opposite trend can be seen with the calibration graphs constructed using the averaged method being closer to the theoretical intercept than those of the addition method, mainly due to the large difference seen in the intercept of the Fe_3O_4 calibration graph constructed using the (511) calibration graphs. No real conclusion can therefore be drawn by solely comparing the gradients and intercepts of the calibration graphs to that of the theory.

The R^2 values which represent the fit of the data to the trend line do suggest that the calibration graphs produced using the additions method may be slightly more accurate. As the R^2 values for these are closer to 1, the ideal value than those using the averaged method, suggesting that the data is more consistent and less likely to be erroneous. This was likely due to the increased intensity used in the deconvolution process, making this easier to perform with the Xfit software. Finally the detection limits for each method must be considered, with the lower the better. The detection limits for the additions method can be seen to be consistently smaller than those of the averaged method, with the exception of the γ-Fe_2O_3 calibration graph based upon the (511) reflection using the average method which is slightly smaller than that using the addition method.

Based upon the above observations it was concluded that the addition method was the more accurate of the two, likely due the increased intensity of the reflections used within the deconvolution process, which produces calibration graphs with gradients closer to that

expected from the underling theory, as well as more ideal R^2values and detection limits, than the averaged methods.

A second question relates to traditional solid state theory, which set of peak positions for γ-Fe_2O_3 should be used in the deconvolution process, those relating to the cubic (*Fd3-m*) or tetragonal (*$P4_12_12$*) phase (**table 5.4.)**? Classical solid state theory would suggest the use of the peak positions relating to the cubic unit cell (*FD3-m*) of both phases. The unit cell used by Kim *et. al.*, was a tetragonal unit cell, with positions close to that of those of the *$P4_12_12$* unit cell of γ-Fe_2O_3.[129, 170-173] The *$P4_12_12$* unit cell also represents the most thermodynamically stable form of γ-Fe_2O_3 and would therefore be a more realistic choice to base the deconvolution technique upon than the less stable cubic *FD3-m* phase. Another problem in using the cubic unit cell of γ-Fe_2O_3 is that the peak positions of the two cubic phases are closer, and would therefore require higher resolutions scans to be deconvoluted, which would prove difficult with IONs due to the associated peak broadening.

Compound	Reflection	Peak Position (°)
Fe_3O_4 (Cubic, *Fd3-m*)[24]	(511)	56.958
	(440)	62.545
γ-Fe_2O_3 (Tetragonal, $P4_12_12$)[29]	(511)	57.369
	(440)	63.001
γ-Fe_2O_3 (Cubic, *Fd3-m*)[178]	(511)	57.130
	(440)	62.735

Table 5.4. The peak position of the (511) and (440) reflections relating to Fe_3O_4 and γ-Fe_2O_3, obtained from the experimental work of various researchers.

The unit cell parameters of the cubic Fe_3O_4 (*FD3-m*), and both the cubic and tetragonal unit cells of γ-Fe_2O_3 (*FD3-m*, and $P4_12_12$) are very similar, when the tripling of the c-axis of the tetragonal unit cell is taken into account, making it difficult to model the amount of phases present in bulk samples through classical Rietveld refinement, and extremely difficult, if not impossible for nanoparticle samples. Therefore calibration graphs using both the cubic and tetragonal unit cells were constructed and the gradients, intercepts, R^2, and detection limits, considered when deciding which calibration graphs would prove to be the most accurate.

As the calibration graphs created using the (511) reflection and averaged method, were shown to be more inaccurate than those produced using the (440) reflection and the addition method, a set of calibration graphs using the (440) reflection of the Fe_3O_4 (*Fd3-m*), and γ-Fe_2O_3 ($P4_12_12$), and the additions method, were compared to a set also prepared using the additions method and (440) reflection of Fe_3O_4 (*Fd3-m*), and γ-Fe_2O_3 (*Fd3-m*), **table 5.5.**

Unit Cell Used for Graph	Phase	Gradient	Difference	Intercept	R^2	Detection limit (wt%)
Tetragonal *P4₁2₁2* Unit Cell	γ-Fe_2O_3	1.0283	0.0283	-2.5842	0.9602	12.2
	Fe_3O_4	1.0697	0.0697	-4.4851	0.9514	29.1
Cubic *Fd3-m* Unit Cell	γ-Fe_2O_3	1.0932	0.0932	-7.3811	0.9677	18.04
	Fe_3O_4	1.0996	0.0996	-3.2156	0.9734	8.39

Table 5.5. Gradient, intercept and coefficient of determination, along with the detection limit at 95% confidence of the calibration graphs created using the additions method and two different unit cells of γ-Fe_2O_3. The calibration graph produced using the $P4_12_12$ unit cell can be seen to tie in most closely with the theory.

From the above table the gradient and intercepts of the calibration graphs produced using the *P4₁2₁2* unit cell are closer to the theoretical gradient and intercept, 1 and 0, respectively. The R^2 values, which represent the fit of the trendline to the data set are closer to 1 for the *Fd3-m* unit cell, suggesting a better fit of the data to the plotted trendline for this graph suggesting a greater deviation in the data points from their theoretical positions, which is further seen in the calculated detection limits using this unit cell. The detection limits for the calibration graphs using the tetragonal (*P4₁2₁2*) unit cell can be seen to detect a lower weight percentage of γ-Fe_2O_3; however, the calibration graphs using the cubic (*FD3-m*) cell can detect a lower percentage of Fe_3O_4.

As the gradient and intercept of the calibration graphs produced using the tetragonal unit cell, are closer to the theoretical gradient and intercept, but the R^2 and detection limits

favour the calibration graphs based upon the cubic unit cell, no definitive conclusion can be drawn upon which unit cell should be used to construct the calibration graphs used in this work. As such throughout this work the calibration graphs constructed from the tetragonal ($P4_12_12$) unit cell as this ties in most closely with the work of Kim *et.al.*[129] Further work is required upon this technique however to further reduce the detection limits upon the calibration graphs, and to provide more evidence as to the underlying solid state theory that the calibration graph is based upon.

6.0. Cation Substitutions in Fe_3O_4

Cation substitutions of transition metals with similar sizes, for iron in Fe_3O_4 have been extensively studied. Substitutions of cobalt, manganese and zinc have been extensively investigated, with partial substitution often seen as providing a route for the tuning of magnetic properties.[179-182] More rarely performed are cation substitutions of tin and vanadium into Fe_3O_4 have also been performed.[49, 54]

This chapter discusses the work carried out to prepare transition metal substituted Fe_3O_4 samples via a modified co-precipitation approach. The process was then adapted for use in the continuous flow focussing technique, to set up a methodology for the preparation of these compounds using microreactors. To the best of the author's knowledge, no attempts have yet been made at performing cation substitution reactions using microreactors, only pure cobalt ferrite ($CoFe_2O_4$) nanoparticles have so far been synthesised using microreactors.[121]

6.1. Substitution of Divalent Metals (M^{2+}) in Batch

Partial substitution of divalent metal (M^{2+}) cations (e.g. Co^{2+}, Mn^{2+}, Zn^{2+}, and Sn^{2+}) was achieved via co-precipitation from a solution of a stoichiometric mixture of transition metal salts.

A modified Iron Salts Precursor Solution (mod-ISPS) was prepared by the mixing of stoichiometric volumes of MCl_2, $FeCl_2$, and $FeCl_3$ dissolved in HCl, the exact method is given in **section 2.1.1.** The divalent iron content was replaced with an equivalent amount of the divalent metal cation salt (**table 6.1.**). NaOH used again as a base.[108]

Divalent cation substitution;

$$xMCl_2 + (1-x)FeCl_2 + 2FeCl_3 + 8NaOH \rightarrow\rightarrow M_xFe_{3-x}O_4 + 4H_2O + 8NaCl$$

Volume of MCl_2 (0.01M) (ml)	Volume of $FeCl_2$ (0.01M) (ml)	Volume of $FeCl_3$ (0.02M) (ml)	Predicted Percentage of Substitution in Fe_3O_4, in terms of total Fe content (%)	Predicted Formula of Compound
1.25	11.25	12.5	3.33	$M_{0.1}Fe_{2.9}O_4$
2.50	10.00		6.66	$M_{0.2}Fe_{2.8}O_4$
3.75	8.75		10.00	$M_{0.3}Fe_{2.7}O_4$
5.00	7.50		13.33	$M_{0.4}Fe_{2.6}O_4$
6.25	6.25		16.66	$M_{0.5}Fe_{2.5}O_4$

Table 6.1. Volume of reagents used for synthesising cation substituted IONs and the predicted formulae from these if 100% of reagents react.

6.1.1. Co^{2+} Substituted Fe_3O_4 via Co-precipitation

Powder X-ray diffraction patterns of the precipitate were recorded over the range of $20 \leq 2\theta° \leq 80$, with a step size of 0.02° and a time step of 15 s. The PXRD patterns of the $Co_xFe_{3-x}O_4$ ($0.0 \leq x \leq 0.5$) series match the pattern of iron oxide showing that the spinel structure is maintained, in agreement with the literature, **fig. 6.1.**[35, 179, 183, 184] No Co containing secondary phases can be detected within any of the patterns.

A shift in the position of the reflections is noted for all samples in comparison to that of un-substituted nanoparticles. A small shift of the peaks towards higher 2 theta positions is seen, indicating a smaller unit cell, which is consistent with the substitution of Co for Fe in either its divalent or trivalent, located upon the octahedral sites, due to its smaller

ionic radii in a crystal lattice (Co^{2+}(6, H.S.) = 0.745 Å, Co^{3+}(6, H.S.) = 0.610 Å, and Fe^{2+}(6, H.S.) = 0.780 Å, Fe^{3+}(6, H.S.) = 0.645 Å).[185] The increase in 2 theta angle is shown more clearly observed for samples where x = 0.1 and 0.4, but less observable for those where x = 0.2, 0.3 and 0.5.

Calculation of the lattice parameters was performed using the Checkcell program, $CoFe_2O_4$ *a* = 8.384(5) Å (*Fd3-m*) used as model, **fig. 6.2.**[184] A decrease in lattice parameter was seen with increasing percentage of $CoCl_2$ in the initial solution indicating a decrease in the unit cell volume, as would be expected for the substitution of Co^{2+} for Fe^{2+} based upon the effective ionic radii of the ions calculated by R. D. Shannon.[185]

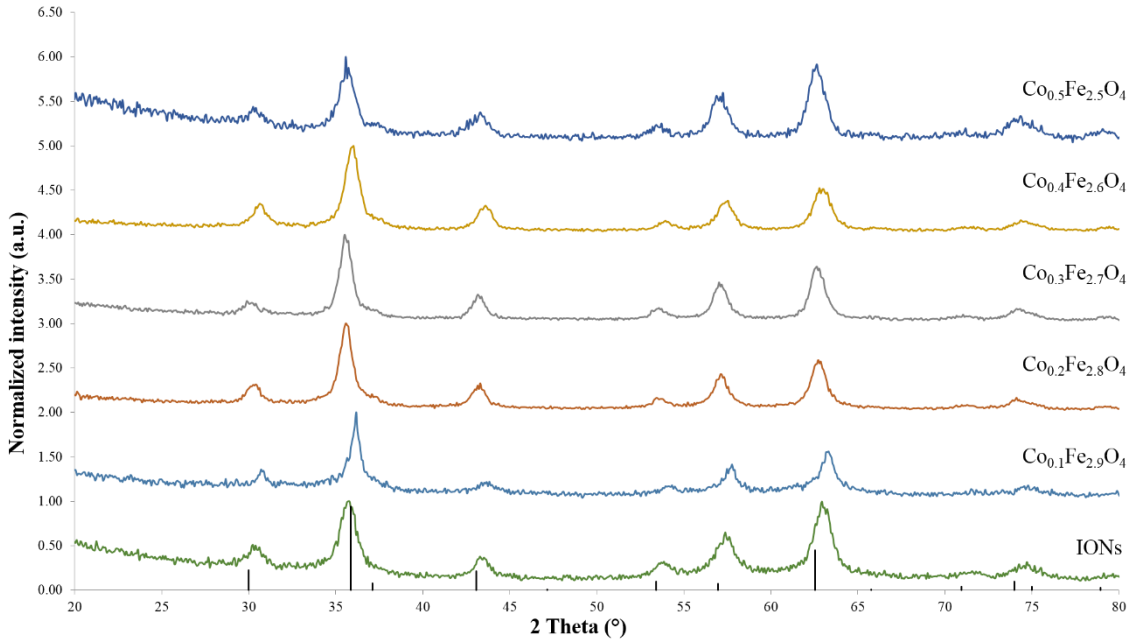

Figure 6.1. PXRD patterns for the $Co_xFe_{3-x}O_4$ ($0 \leq x \leq 0.5$) series of substituted IONs. The general spinel phase can be seen to be maintained from the peak positions of this (black), a slight shift in the patterns is seen suggesting some substitution in each, while the peaks broadness suggest the compounds to be nanoparticular in nature.

ICP-AES was used to determine the amount of cobalt present within each sample. An increase in Co content within the nanoparticles was seen with increasing $CoCl_2$ content

in solution, **fig. 6.2.** This agrees with the increasing lattice parameter noted with increasing $CoCl_2$ content in solution and therefore suggests successful substitution of Co^{2+} for Fe^{2+}. The amount of Co present within each sample can be seen to be less than amount of Co in the initial reagent solution. This may be due to the washing away of some of the Co being washed away during the synthesis and subsequent washing steps. From the ICP-AES data the general formula of the nanoparticles can be recalculated, **table 6.2.**

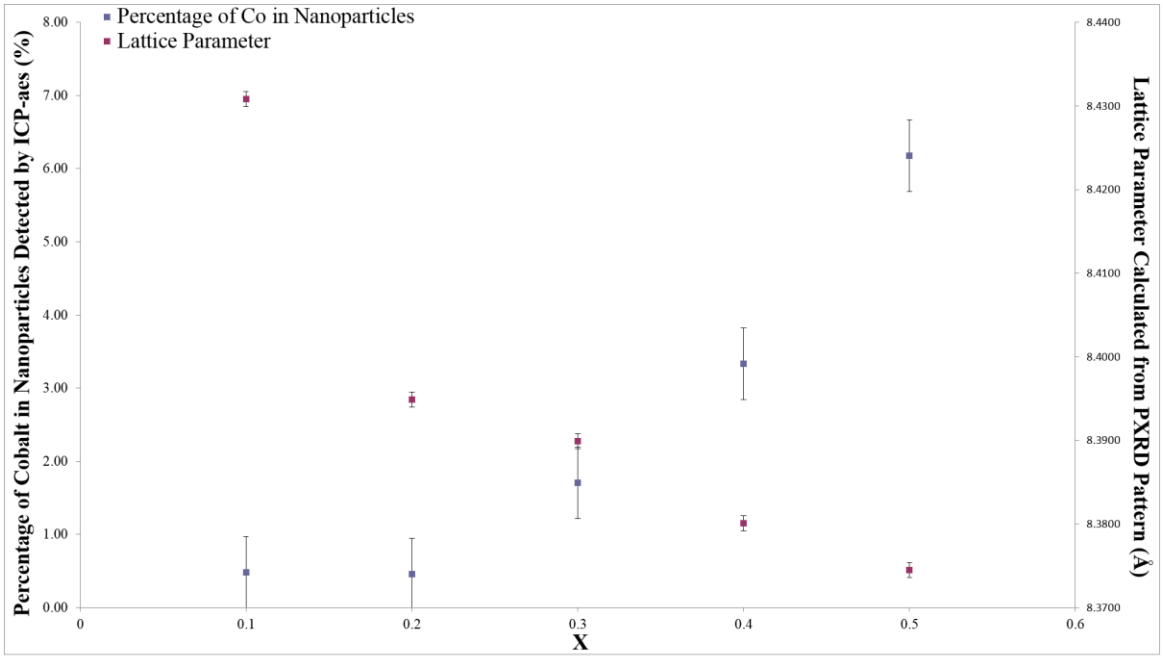

Figure 6.2. Plot of actual Co content calculated from the ICP data, and the lattice cell parameter of the nanoparticles calculated from the positions of the peaks in the PXRD pattern versus the predicted amount of cobalt, x, in the $Co_xFe_{3-x}O_4$ series.

The general formulae are calculated for the Fe_3O_4 inverse spinel structure, rather than that of γ-Fe_2O_3 in accordance with current literature.[35, 179, 180, 183, 184] The assumption that Fe_3O_4 – type spinel compounds have been obtained is supported by the presence of a 2+ metal, absent in the Fe_2O_3-type spinel compounds. The degassing of the initial reagent solutions in the synthesis and the storage of the samples in an inert environment were

performed to avoid the oxidation of the 2+ metal. XPS could confirm the presence of Co and Fe in a 2+ oxidation state.

Percentage of $CoCl_2$ in Initial Solution (%)	Predicted Formula of Compound	Actual Percentage of Co in Nanoparticles (%)	Actual Formula of Compound	Lattice Cell Parameter (Å)	Particle Size (nm)
3.33	$Co_{0.1}Fe_{2.9}O_4$	0.46	$Co_{0.01}Fe_{2.99}O_4$	8.430(8)	14.58
6.66	$Co_{0.2}Fe_{2.8}O_4$	1.70	$Co_{0.05}Fe_{2.95}O_4$	8.394(9)	9.39
10.00	$Co_{0.3}Fe_{2.7}O_4$	3.33	$Co_{0.10}Fe_{2.90}O_4$	8.389(9)	10.84
13.33	$Co_{0.4}Fe_{2.6}O_4$	6.18	$Co_{0.19}Fe_{2.81}O_4$	8.380(1)	9.36
16.66	$Co_{0.5}Fe_{2.5}O_4$	14.47	$Co_{0.43}Fe_{2.57}O_4$	8.374(5)	8.16

Table 6.2. Predicted and actual formulae for the $Co_xFe_{3-x}O_4$ series of Co^{2+} substituted nanoparticles, with the calculated lattice parameter and particle size calculated using the Scherrer equation. The formulae are based upon the amount of Co detected through ICP and the presumption that the compound possesses the Fe_3O_4 structure, as is standard from the literature.

The substituted nanoparticles were seen to be larger, approximately 3 times larger, than the un-substituted nanoparticles, 6.72 ± 0.72 nm.

6.1.2. Mn^{2+} Substituted Fe_3O_4 via Co-precipitation

Powder X-ray diffraction patterns of the $Mn_xFe_{3-x}O_4$ ($0.0 \leq x \leq 0.5$) series were recorded over the range of $20 \leq 2\theta\ ° \leq 80$ with a step size of 0.02 ° and step time of 28 s. The patterns showed that the spinel structure is maintained throughout the whole range of

substittutions, **fig. 6.3.** [36, 39] A shift toward lower 2 theta angles, was seen with increasing Mn^{2+} concentration in the initial solution, suggesting an increase in unit cell size, which is consistent with the substitution of Mn^{2+} for Fe^{2+}, due to the difference in the ionic radii, (Fe^{2+} = 0.780 Å, and Mn^{2+} = 0.830 Å). No difference would be observed however if the substitution of Mn^{3+} for Fe^{3+} occurred instead of substitution of Mn^{2+} for Fe^{2+}, (Mn^{3+} = 0.645 Å and Fe^{3+} = 0.645 Å).

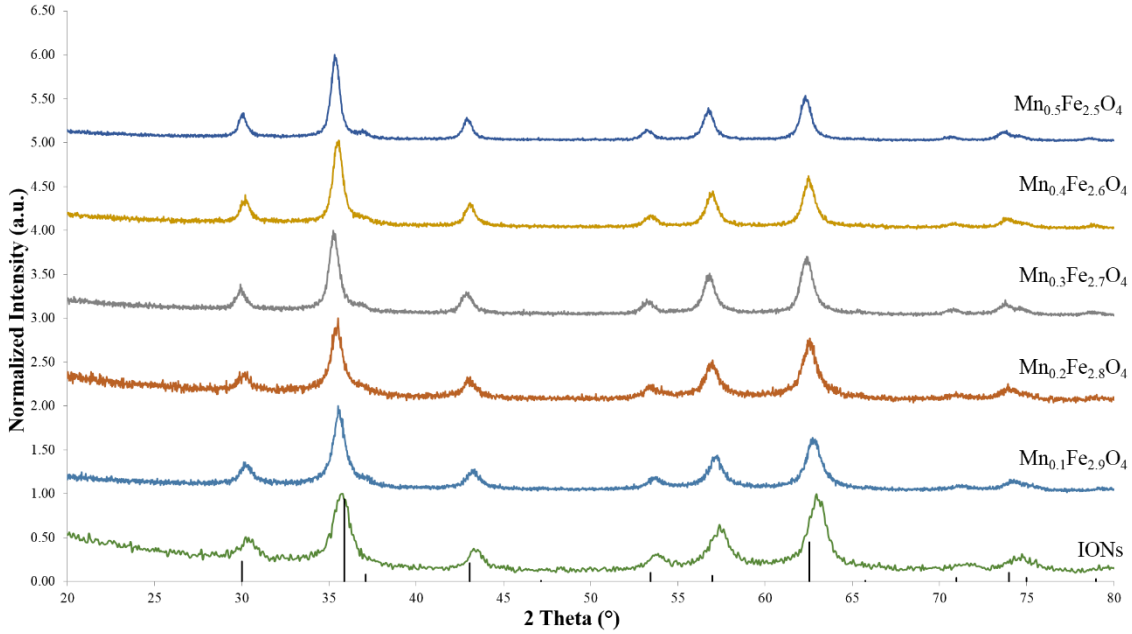

Figure 6.3. PXRD patterns for the $Mn_xFe_{3-x}O_4$ series of substituted IONs. The general spinel phase can be seen to be maintained from the peak positions of this (black), a slight shift in the patterns is seen suggesting some substitution in each, while the peaks broadness suggest the compounds to be nanoparticular in nature.

The site occupancy for Mn substituted nanoparticles cannot be determined using only PXRD as the scattering factors of both Mn and Fe are very similar, Rietveld refinement can be used to calculate this from the scattering factors, but has not been performed in this work due to the difficulties associated with trying to fit low intensity broad peaks in the refinement process.

It has been suggested that Mn^{2+} has little preference for octahedral or tetrahedral sites and will occupy both.[41] Manganese ferrite ($MnFe_2O_4$) was found to have an intermediate spinel phase with 20% inversion, e.g. 20% of the Mn^{2+} occupies the octahedral holes in place of Fe^{3+}, $[Mn_{0.80}Fe_{0.20}]_{Tet}[Fe_{1.80}Mn_{0.20}]_{Oct}O_4$. This is particularly relevant in the case of nanoparticles, as it has been suggested that up to 80% inversion can occur, $[Mn_{0.20}Fe_{0.80}]_{Tet}[Fe_{1.20}Mn_{0.80}]_{Oct}O_4$. [39, 41, 186] The nanoparticles produced in this work have sizes of 11 - 15 nm and a large degree of inversion would be expected, as for nanoparticles with sizes of approximately 4 nm the degree of inversion was shown to be 63.0 ± 1.8%.[41] Lattice parameters were calculated using Checkcell program, $MnFe_2O_4$, a = 8.3950 Å, (*Fd3-m*) was used as a model. [24, 29, 39] An increase in lattice parameter, and therefore an increase in the unit cell volume was observed with increasing $MnCl_2$ concentration in solution, **fig. 6.4.**

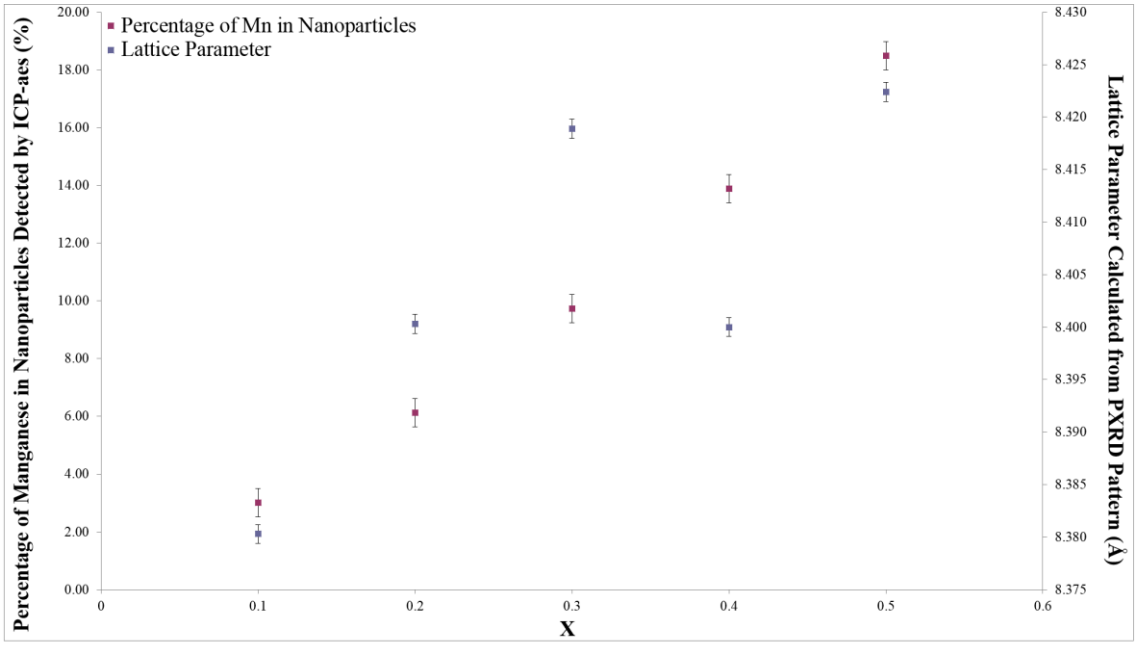

Figure 6.4. Plot of actual Mn content and the lattice cell parameter of the nanoparticles calculated from the positions of the peaks in the PXRD pattern versus the predicted amount of cobalt, x, in the $Mn_xFe_{3-x}O_4$ series.

The percentage of manganese present within the IONs was seen to increase linearly with an increasing percentage of $MnCl_2$ in the initial solution. From this the formulae of the nanoparticles was calculated, **table 6.3.** The percentage of Mn substituted into the nanoparticles can be seen to be much closer to that predicted from the percentage present in solution, compared to the case of $Co_xFe_{3-x}O_4$ series. The amount of Mn substituted into the nanoparticles, of predicted formulae $Mn_{0.4}Fe_{2.6}O_4$ and $Mn_{0.5}Fe_{2.5}O_4$, was higher than predicted; the cause of which is unclear. However, it is hypothesised that this may be due to a loss of Fe when washing the samples, see **section 6.1.3.** As the general formulae are calculated from the ratio of Mn to Fe, any decrease in the Fe content would result in a greater amount of Mn within the nanoparticles.

Percentage of Mn in Initial Solution (%)	Predicted Formula of Compound	Actual Percentage of Mn in Nanoparticles (%)	Formula of Compound	Lattice Parameter (Å)	Particle Size (nm)
3.33	$Mn_{0.1}Fe_{2.9}O_4$	3.02	$Mn_{0.09}Fe_{2.91}O_4$	8.380(3)	11.09
6.66	$Mn_{0.2}Fe_{2.8}O_4$	6.12	$Mn_{0.18}Fe_{2.82}O_4$	8.400(3)	12.20
10.00	$Mn_{0.3}Fe_{2.7}O_4$	9.74	$Mn_{0.29}Fe_{2.71}O_4$	8.418(9)	12.80
13.33	$Mn_{0.4}Fe_{2.6}O_4$	13.88	$Mn_{0.42}Fe_{2.58}O_4$	8.400(1)	12.84
16.66	$Mn_{0.5}Fe_{2.5}O_4$	18.49	$Mn_{0.55}Fe_{2.45}O_4$	8.422(4)	15.21

Table 6.3. Predicted and actual formulae for the $Mn_xFe_{3-x}O_4$ series of Mn^{2+} substituted nanoparticles, with the calculated lattice parameter and particle size calculated using the Scherrer equation.

6.1.3. Zn^{2+} Substituted Fe_3O_4 via Co-precipitation

The most studied substituted ferrite structure is the zinc substituted ferrites ($Zn_xFe_{3-x}O_4$). Zn^{2+} cannot be oxidized, and has a preference for the tetrahedral holes, tending toward the formation of spinel phase compounds, rather than the inverse spinel. Substitution of Zn^{2+} into the nanoparticles was achieved through the co-precipitation method. Powder X-ray diffraction patterns were recorded for the $Zn_xFe_{3-x}O_4$ ($0.0 \leq x \leq 0.5$) series, over the range $20 \leq 2\theta\ ° \leq 80$, with a step size of 0.02 °, and time step of 28 s, **fig 6.5.**

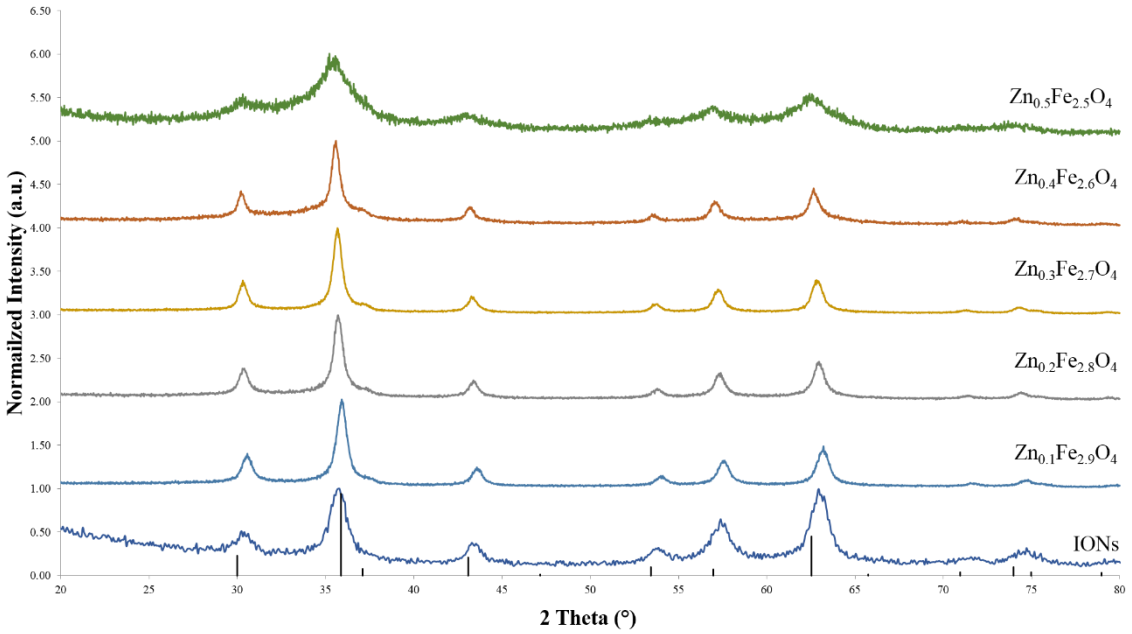

Figure 6.5. PXRD patterns for the $Zn_xFe_{3-x}O_4$ series. The general spinel phase can be seen to be maintained from the peak positions of this (black), a slight shift in the patterns is seen suggesting some substitution in each, while the peaks broadness suggest the compounds to be nanoparticular in nature.

PXRD patterns of the nanoparticles show the spinel phase to be maintained, in agreement with literature.[187] $Zn_{0.5}Fe_{2.5}O_4$ pattern showed significant peak broadening, although the position of the peaks can be associated with the positions of those expected for the spinel

phase other impurities cannot be ruled out. A shift toward higher 2 theta angle would be predicted when Zn^{2+} is substituted into the spinel structure for Fe^{2+} due to the difference between the ionic radii of the two cations (Zn^{2+}(4, H.S.) = 0.60 Å, and Fe^{2+} (4, H.S.) = 0.63 Å). A shift toward lower 2 theta angle is observed with increasing $ZnCl_2$ concentration solution however, consistent with literature. A shift toward lower 2 theta angle was observed by *Singh et.al.* with an increase in Zn content to $x \leq 0.5$, due to the redistribution of cations upon the octahedral sites, with Zn^{2+} preference for tetrahedral sites.[44] In the inverse spinel structure of Fe_3O_4 the tetrahedral holes are occupied by Fe^{3+}, however Zn^{2+} has a much greater affinity for the tetrahedral holes, and therefore replaces the Fe^{3+} upon the tetrahedral sites, with the Fe^{3+} instead occupying the octahedral holes. This leads to an increase in unit cell size due to Zn^{2+} larger ionic radii than Fe^{3+} when occupying both octahedral and tetrahedral holes, (Zn^{2+} (4, H.S.) = 0.600 Å, Zn^{2+} (6, H.S.) = 0.740 Å, and Fe^{3+} (4, H.S.) = 0.645 Å, Fe^{3+} (6, H.S.) = 0.490 Å). When $x \geq 0.6$ the unit cell size decreases and would be accompanied by a shift back toward higher 2 theta angle.[44]

An increase in the lattice parameters calculated using the Checkcell program, $ZnFe_2O_4$, a = 8.437(5) Å (*Fd3-m*) used as model, suggests that the unit cell increases with increasing Zn^{2+} content.

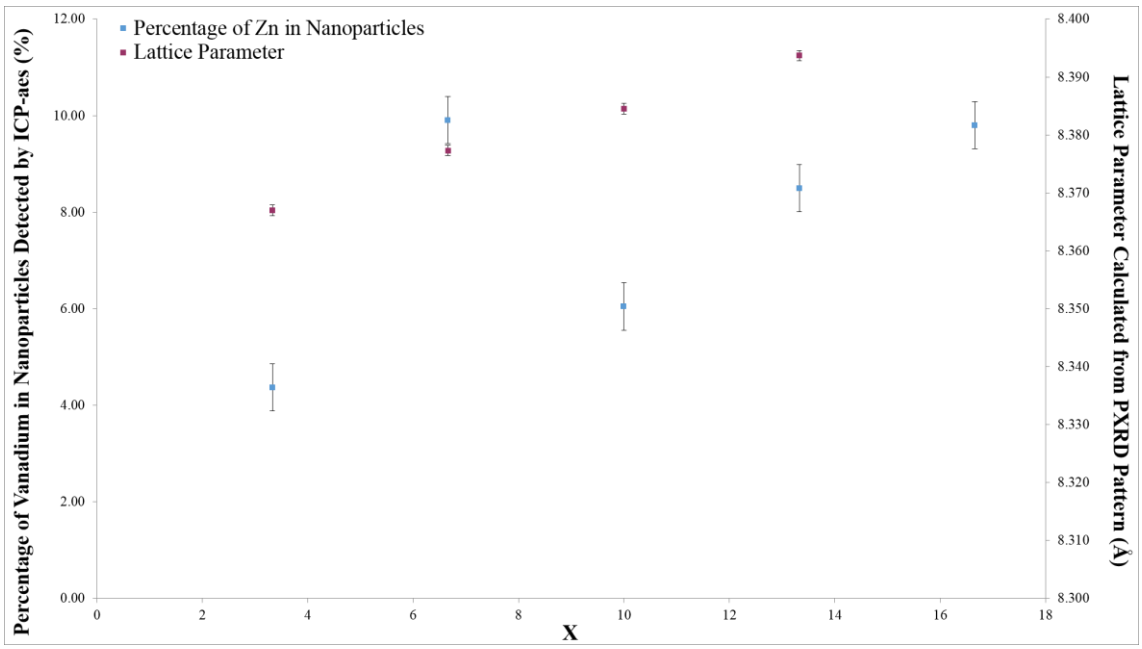

Figure 6.6. Plot of actual Zn content and the lattice cell parameter of the nanoparticles calculated from the positions of the peaks in the PXRD pattern versus the predicted amount of Zinc, x, in the $Zn_xFe_{3-x}O_4$ series.

A near linear increase in the Zn content was seen with increasing $ZnCl_2$ concentration in solution, **fig. 6.6.** Unlike the $Co_xFe_{3-x}O_4$ and $Mn_xFe_{3-x}O_4$ series of compounds, the percentage of Zn found within the $Zn_xFe_{3-x}O_4$ series was always larger than that predicted. This was attributed to the removal of iron containing impurities in the washing stage.

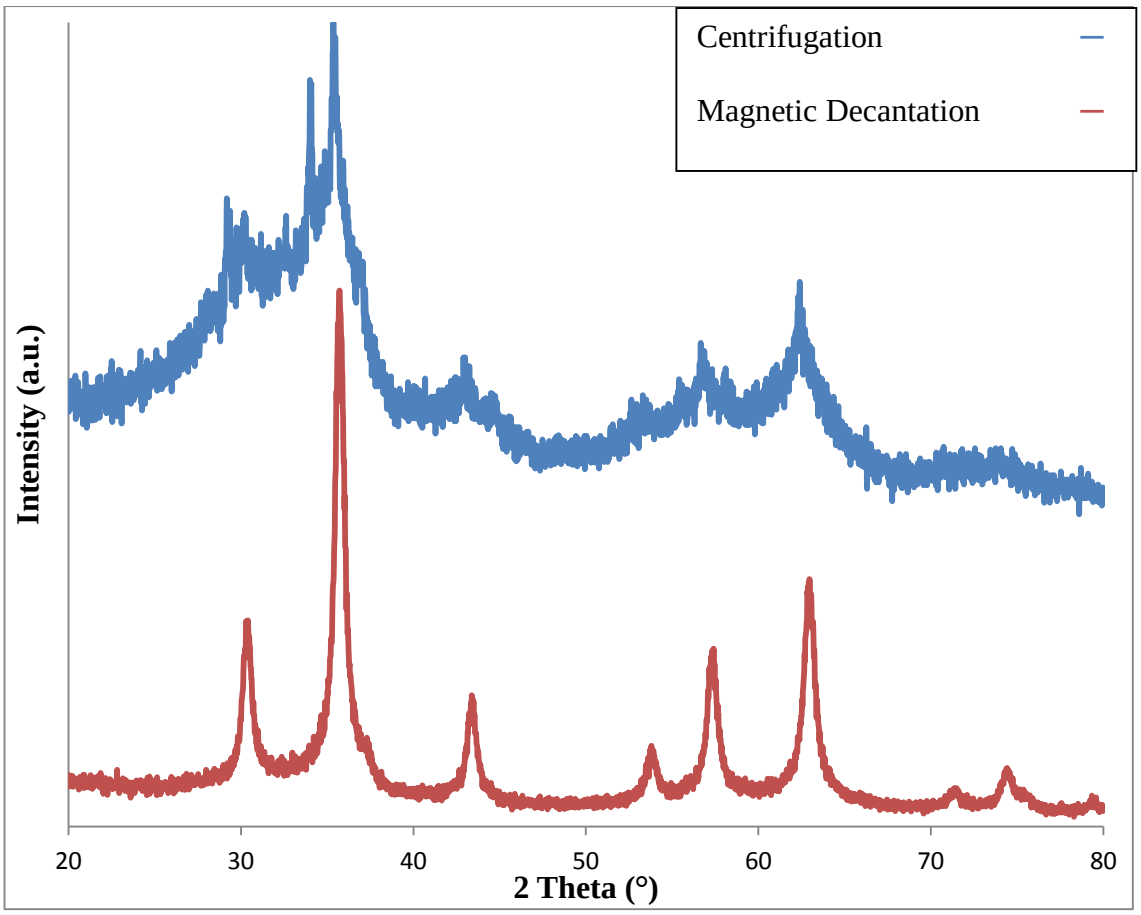

Figure 6.7. PXRD patterns of $Zn_{0.2}Fe_{2.8}O_4$ when isolated by centrifugation or magnetic decantation. The pattern obtained from the sample which was centrifuged contains other impurities compared to that which has been separated via magnetic decantation.

To test the assumption that Fe content was being lost through the production of Fe containing impurities a second sample of $Zn_{0.2}Fe_{2.8}O_4$ was synthesised and the nanoparticles removed from the supernatant using centrifugation rather than magnetic decantation. PXRD patterns recorded for this over the range $20 \leq 2\theta\ ° \leq 80$, with a step size of 0.02 °, and time step of 28 s, and can be seen to contain multiple impurities, in comparison to that in which magnetic decantation was used, **fig. 6.7.**

Percentage of $ZnCl_2$ in Initial Solution (%)	Predicted Formula of Compound	Actual Percentage of Zn in Nanoparticles (%)	Formula of Compound	Lattice Cell Parameter (Å)	Particle Size (nm)
3.33	$Zn_{0.1}Fe_{2.9}O_4$	4.37	$Zn_{0.13}Fe_{2.87}O_4$	8.367(1)	12.25
6.66	$Zn_{0.2}Fe_{2.8}O_4$	9.90	$Zn_{0.30}Fe_{2.70}O_4$	8.377(3)	13.98
10.00	$Zn_{0.3}Fe_{2.7}O_4$	6.04	$Zn_{0.18}Fe_{2.82}O_4$	8.384(5)	14.38
13.33	$Zn_{0.4}Fe_{2.6}O_4$	8.49	$Zn_{0.25}Fe_{2.75}O_4$	8.393(7)	9.77
16.66	$Zn_{0.5}Fe_{2.5}O_4$	9.80	$Zn_{0.29}Fe_{2.71}O_4$	N/A	N/A

Table 6.4. Predicted and actual formulae for the $Zn_xFe_{3-x}O_4$ series of Zn^{2+} substituted nanoparticles, with the calculated lattice parameter and particle size calculated using the Scherrer equation. The amount of zinc present in the nanoparticles was calculated as a mean from two sets of ICP data both showing that for the attempted formation of the $Zn_{0.2}Fe_{2.8}O_4$ an increase in doping occurs.

6.1.4. Sn^{2+} Substituted Fe_3O_4 via Co-precipitation

Sn^{2+} substitution in Fe_3O_4 was achieved through the co-precipitation method. $SnCl_2.2H_2O$ was used as the source of Sn^{2+}, and dissolved in HCl (1.10 M) avoiding hydrolysis of the $SnCl_2$ to Sn(OH)Cl, an insoluble impurity. Substitution of Sn^{2+} in Fe_3O_4 proved to be difficult, presumably due to the much larger size of Sn^{2+} in comparison to Fe^{2+} (Sn^{2+} (6, H.S. = 0.93 Å, and Fe^{2+} (6, H.S.) = 0.78 Å).[160] No greater than 4% substitution could be achieved in any of the samples as evidenced by the ICP-AES results, **fig. 6.8.**

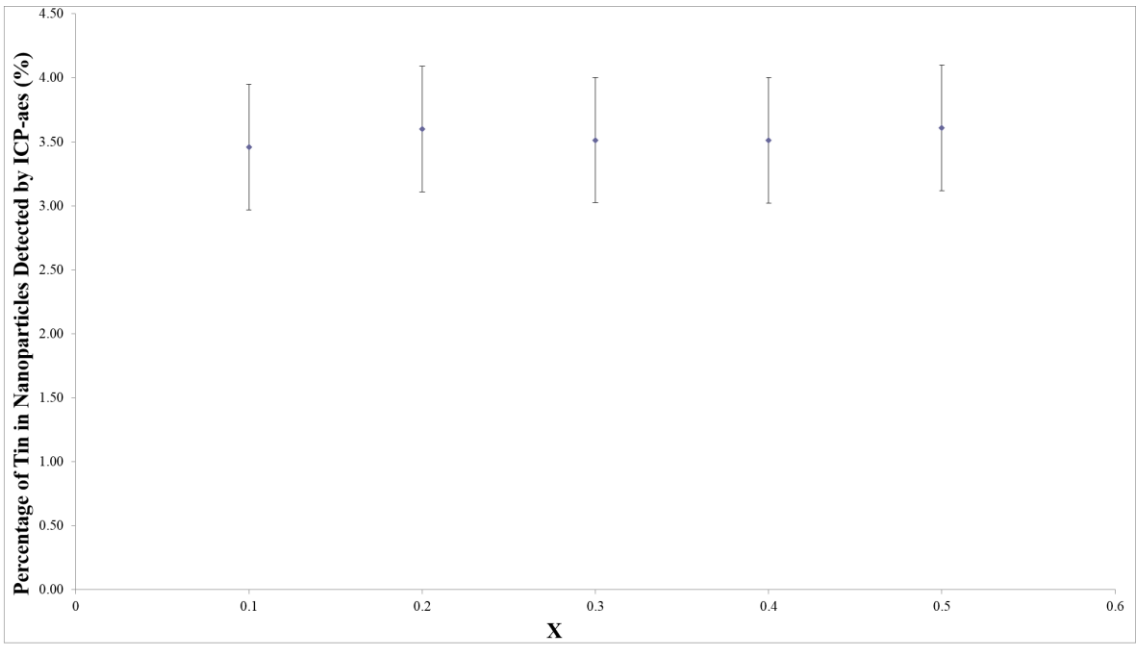

Figure 6.8. Plot of actual Sn content against x in the $Sn_xFe_{3-x}O_4$ series. The percentage of Sn present in the nanoparticles was calculated from ICP and little changes is shown between attempted substitution and what is actually achieved.

Powder X-ray diffraction patterns were recorded over the range of $20 \leq 2\theta\ ° \leq 80$ with a step size of 0.02 ° and step time of 28 s. The inverse spinel phase can be seen to be maintained for all samples in the series $Sn_xFe_{3-x}O_4$, **fig. 6.9.** With higher levels of attempted substitution (x = 0.3, 0.4 and 0.5) the PXRD patterns were seen to broaden significantly, suggesting a loss of crystallinity, and although the peaks do match those of the inverse spinel phase, no indexing can be accurately performed. The lattice parameters calculated for $Sn_{0.1}Fe_{2.9}O_4$ and $Sn_{0.2}Fe_{2.8}O_4$, were 8.337(1) and 8.339(3) Å, respectively, close to that of Fe_3O_4 (8.394(1) Å), further suggesting little substitution of Sn^{2+}.[24] The predicted and actual formulae of the compounds predicted are given in **table 6.5.**, assuming that all compounds have the spinel type structure. The presence of a small amount of NaCl was seen in the pattern of $Sn_{0.4}Fe_{2.6}O_4$, produced during the synthesis and not completely removed during the washing process, however no Sn containing impurities were observed.

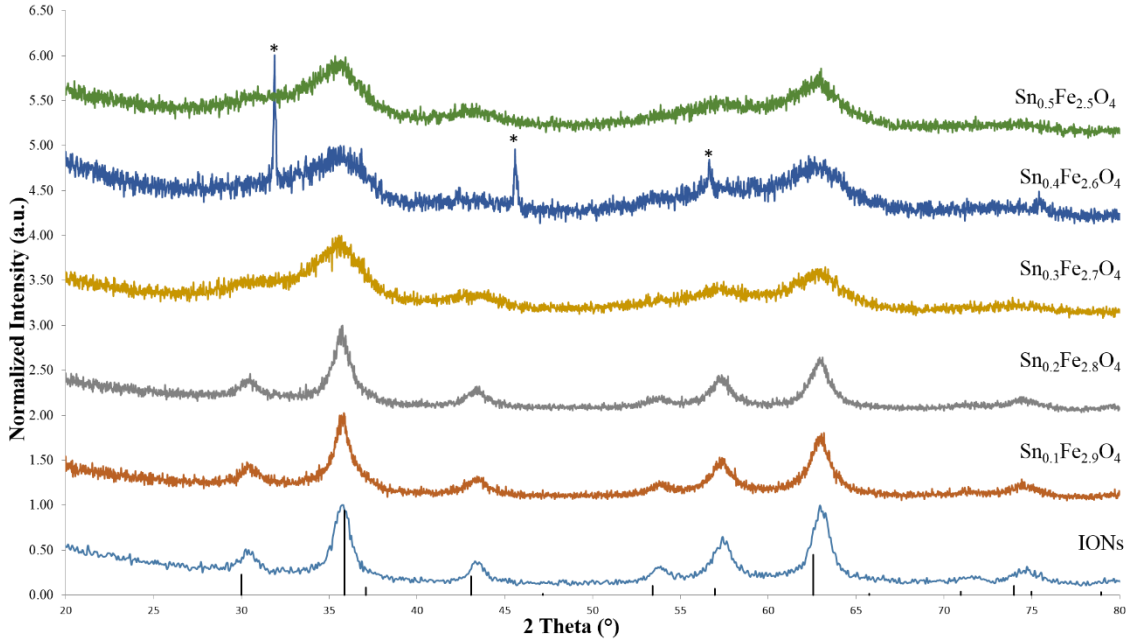

Figure 6.9. PXRD patterns for the $Sn_xFe_{3-x}O_4$ series. * indicate NaCl peaks. The general spinel structure (black) is maintained for both the $Sn_{0.1}Fe_{2.9}O_4$ and $Sn_{0.2}Fe_{2.8}O_4$ nanoparticles, but is lost when higher substitutions are attempted.

The degradation of the PXRD patterns for samples where x = 0.3, 0.4 and 0.5, could be explained by the reduction of Fe^{3+}, leading to the formation of a greater amount of weakly magnetic impurities and affecting the formation of the inverse spinel phase iron oxides, hence the low amount of substitution, and the broadness of the peaks. This may be due to the reduction of Fe^{3+} to Fe^{2+} as Sn^{2+} in the form of $SnCl_2.2H_2O$, acts as a weak reducing agent.[188] Furthermore the substitution of Sn^{4+} for Fe^{2+} is ruled out as no α-Fe_2O_3 is detected in the PXRD patterns of the $Sn_xFe_{3-x}O_4$ series. At present the formation of the $Sn_xFe_{3-x}O_4$ series has mainly been reported where α-Fe_2O_3 was used as the precursor, through hydrothermal synthesis.[54] Berry *et.al.*, have suggested the formation of a stable Sn substituted α-Fe_2O_3 phase may be due to the substitution of Sn^{4+} which occupies defect clusters, where 3 Sn^{4+} locally replace 4 Fe^{3+} maintaining an overall charge balance and preventing reduction of Fe^{3+}, which may explain why a spinel phase compound is not formed as this charge stabilisation would not occur.[53, 189] The formation of a

superparamagnetic α-Fe_2O_3 compound has been suggested through synthesis using high energy ball milling.[52]

Percentage of $SnCl_2$ in Initial Solution (%)	Predicted Formula of Compound	Actual Percentage of Sn in Nanoparticles (%)	Actual Formula of Compound	Lattice Cell Parameter (Å)	Particle Size (nm)
3.33	$Sn_{0.1}Fe_{2.9}O_4$	3.49	$Sn_{0.10}Fe_{2.90}O_4$	8.337(1)	7.89
6.66	$Sn_{0.2}Fe_{2.8}O_4$	3.60	$Sn_{0.11}Fe_{2.89}O_4$	8.339(3)	7.29
10.00	$Sn_{0.3}Fe_{2.7}O_4$	3.51	$Sn_{0.11}Fe_{2.89}O_4$*		
13.33	$Sn_{0.4}Fe_{2.6}O_4$	3.51	$Sn_{0.11}Fe_{2.89}O_4$*		
16.66	$Sn_{0.5}Fe_{2.5}O_4$	3.61	$Sn_{0.11}Fe_{2.89}O_4$*		

Table 6.5. Predicted and actual formulae for the $Sn_xFe_{3-x}O_4$ series of Sn substituted nanoparticles, with the calculated lattice parameter and particle size calculated using the Scherrer equation. * Patterns not significantly crystalline to allow for calculation of particle size or lattice parameter.

6.2. Substitution of Trivalent Transition Metals (M^{3+}) in Batch

Substitution of trivalent cations was attempted by replacing Fe^{3+} with V^{3+}, using VCl_3 as the V source. A mod-ISPS was prepared by the mixing of stoichiometric volumes of the VCl_3, $FeCl_2$ and $FeCl_3$ dissolved in HCl, and precipitated using NaOH solution as a base, **table 6.6.**, for specific volumes. The exact method is given in **section 2.1.1.**

Trivalent cation substitution;

$$xMCl_3 + FeCl_2 + (2-x)FeCl_3 + 8NaOH \rightarrow M_xFe_{3-x}O_4 + 4H_2O + 8NaCl$$

Volume of VCl_3 (0.01M) (ml)	Volume of $FeCl_3$ (0.02M) (ml)	Volume of $FeCl_2$ (0.01M) (ml)	Predicted Percentage of Substitution in Fe_3O_4, in terms of total Fe content (%)	Predicted Formula of Compound
5.00	22.5	25	6.66	$V_{0.2}Fe_{2.8}O_4$
10.00	20		13.33	$V_{0.4}Fe_{2.6}O_4$
15.00	17.5		20.00	$V_{0.6}Fe_{2.4}O_4$
20.00	15.00		26.66	$V_{0.8}Fe_{2.2}O_4$
25.00	12.50		33.32	$V_{1.0}Fe_{2.0}O_4$

Table 6.6. Volume of reagents for mod-ISPS and predicted formulae of the $V_xFe_{3-x}O_4$ series of V^{3+} substituted nanoparticles, with the calculated lattice parameter and particle size calculated using the Scherrer equation.

PXRD patterns of the precipitate were recorded over the range of $20 \leq 2\theta\ ° \leq 80$ with a step size of 0.02 ° and a time step of 28 s, **fig. 6.10.** The inverse spinel phase is maintained for the entire $Fe_{3-x}V_xO_4$ series, a small amount of sodium chloride can be seen in the pattern of $Fe_{2.7}V_{0.3}O_4$. Very little change in the 2 theta angle was expected with increasing V substittuion, due to the similar ionic radius in comparison to Fe, 0.640 and 0.645 Å, respectively, and no obvious shift is seen in the peaks of the V substittuted compounds in comparison to the unsubstittuted nanoparticles. If V^{5+} had been substittuted into the compounmds in place of V^{3+} a shift toward higher 2 theta angles would be observed due to the much smaller ionic radius of V^{5+} (V^{5+}, H.S., (6) = 0.54 Å, and V^{3+}, H.S., (6) = 0.64 Å). A shift toward higher angle is observed only for the $V_{0.5}Fe_{2.5}O_4$. NaCl is noted as an impurity in the pattern of $V_{0.3}Fe_{2.7}O_4$.

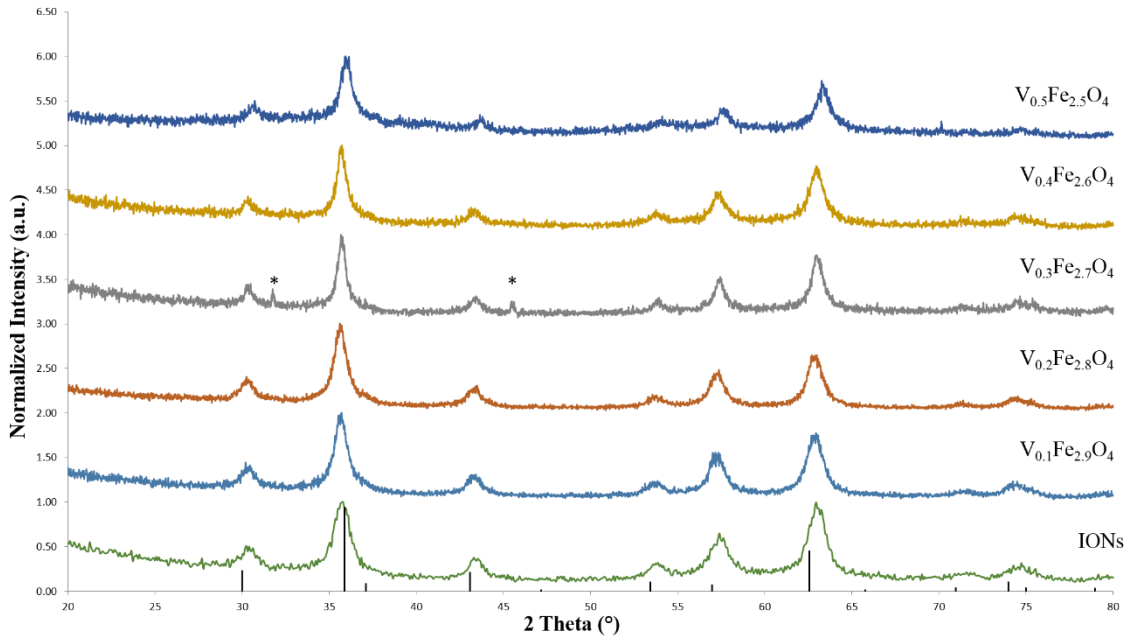

Figure 6.10. PXRD patterns for the $V_xFe_{3-x}O_4$ series. The general spinel structure (black) can be seen to be maintained for all patterns with some broadening and shifting of peaks, as well as some NaCl impurity in the pattern of $V_{0.3}Fe_{2.6}O_4$. * note the peaks associated with NaCl.

An increase in the percentage of V in the nanoparticles was seen with increasing VCl_3 concentration in solution, **fig. 6.11.** The V content within the nanoparticles was much lower than that in solution; as with Co, Mn, and Zn substitution, this was attributed to the formation of impurities, which are lost during magnetic decantation process. Taking into account that no V containing impurities were detected it can be inferred that all V content is substituted into the spinel structure, thus the general formulae for each compound was calculated from this data, and compared to the lattice parameter calculated from the unit cell. The lattice parameter calculated from PXRD data shows a general increasing trend with increasing vanadium content although the trend is not particularly linear like the V content calculated from ICP.

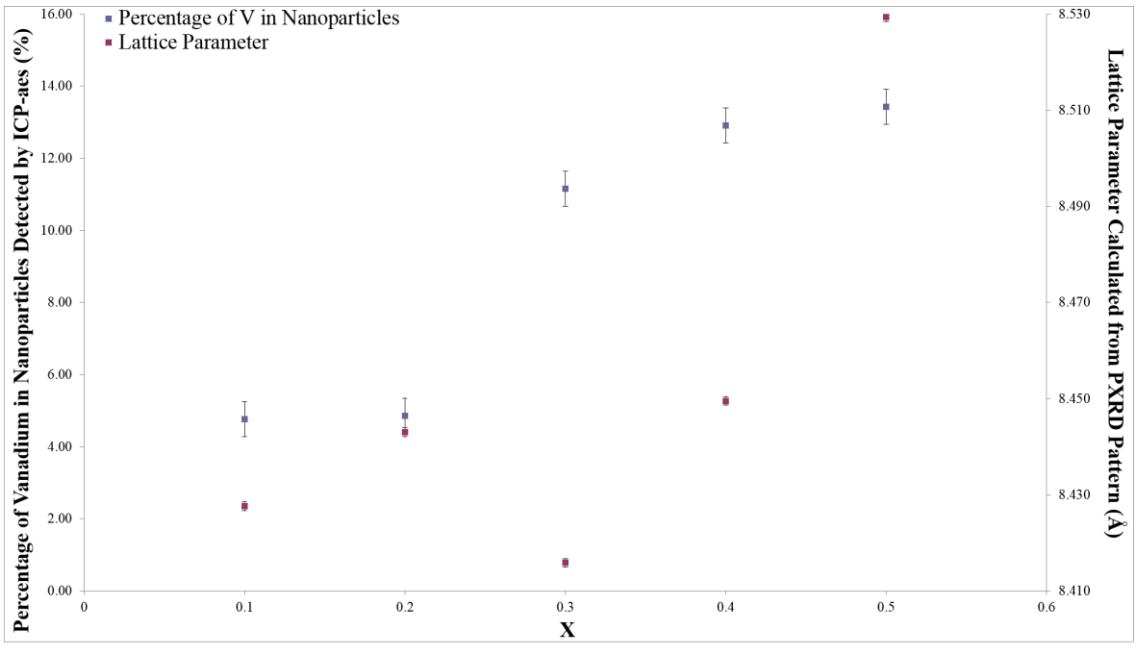

Figure 6.11. Plot of actual Vanadium content and the lattice cell parameter of the nanoparticles calculated from the positions of the peaks in the PXRD pattern versus the predicted amount of Vanadium, x, in the $V_xFe_{3-x}O_4$ series.

As with many of the substitution reactions of other transition metals, notably Mn, the issue of substituting V^{3+} for Fe^{3+} results in complicated site occupancies. Substitution of V^{3+} has been shown to result in some of the Fe^{2+} being shifted from the octahedral onto the tetrahedral holes, where the general formula of $[Fe^{2+}{}_{\alpha}, Fe^{3+}{}_{1-\alpha}]_{Tet}[Fe^{2+}{}_{1-\alpha}, Fe^{3+}{}_{1-x}, V^{3+}{}_{x}]_{Oct}O_4$ has been suggested for V substituted ferrites.[50, 51, 190] Therefore the shift of the pattern of the $V_{0.5}Fe_{2.5}O_4$ could also be due to the "shifting" of cations onto different unit cell sites, although in this case it was not the direct preference of the octahedral over the tetrahedral site of the V^{3+} that effects the unit cell structure but the effect it has upon the Fe^{2+} ion.

Percentage of VCl_3 in Initial Solution (%)	Predicted Formula of Compound	Actual Percentage of V in Nanoparticles (%)	Actual Formula of Compound	Lattice Cell Parameter (Å)	Particle Size (nm)
6.66	$V_{0.2}Fe_{2.9}O_4$	0.14	$V_{0.14}Fe_{2.86}O_4$	8.428	9.98
13.33	$V_{0.4}Fe_{2.8}O_4$	0.15	$V_{0.15}Fe_{2.85}O_4$	8.443	11.11
20.00	$V_{0.6}Fe_{2.7}O_4$	0.33	$V_{0.33}Fe_{2.67}O_4$	8.416	14.82
26.66	$V_{0.8}Fe_{2.6}O_4$	0.39	$V_{0.39}Fe_{2.61}O_4$	8.450	12.23
33.32	$V_{1.0}Fe_{2.5}O_4$	0.40	$V_{0.40}Fe_{2.60}O_4$	8.529	8.92

Table 6.7. Predicted and general formula of V^{3+} substituted nanoparticles, with the calculated lattice parameter and particle size calculated using the Scherrer equation.

6.3. Substitution of Divalent Transition Metals (TM^{2+}) Using Microreactors

Following the substitution co-precipitation reaction, metal substitution in Fe_3O_4 was carried out in microreactors using the continuous flow focussing technique. Zinc substitution, i.e. the preparation of the $Zn_xFe_{3-x}O_4$ series, proved the least problematic and was therefore chosen as a starting point for the novel approach to the synthesis of metal substituted Fe_3O_4 nanoparticles. The ISPS was modified (mod-ISPS) as in the batch reactions, where the $FeCl_2$ content, was partially replaced with $ZnCl_2$, **table 6.8.**

Volume of $ZnCl_2$ (0.01 M) (ml)	Volume of $FeCl_2$ (0.01 M) (ml)	Volume of $FeCl_3$ (0.02 M) (ml)	Predicted Percentage of Zn Substituted for Fe (%)	Predicted Formula of Compound
1.25	11.25	12.5	3.33	$Zn_{0.1}Fe_{2.9}O_4$
2.50	10.00		6.66	$Zn_{0.2}Fe_{2.8}O_4$
3.75	8.75		10.00	$Zn_{0.3}Fe_{2.7}O_4$

Table 6.8. Volume of reagents for zinc doped iron oxide nnaoparticles and the predicted formulae of the nanoparticles formed within the microreactro.

The mod-ISPS was pumped into the central inlet of the microreactor simultaneously with two flows of sodium hydroxide, through the outer inlets at 1000 μl hr^{-1} per flow (total flow rate = 3000 μl hr^{-1}). The temperature was held at 25.5 room temperature of the lab when performing the substitution in batch), as when un-substituted IONs were synthesised by the Labtrix Start Unit. The precipitate produced was collected under nitrogen before being magnetically decanted from the supernatant and washed with ethanol and deionised water. The washed precipitate was then dried in an inert atmosphere at 100 °C for 24 hours. A schematic diagram of the microreactor set up is shown in **fig. 6.12.**

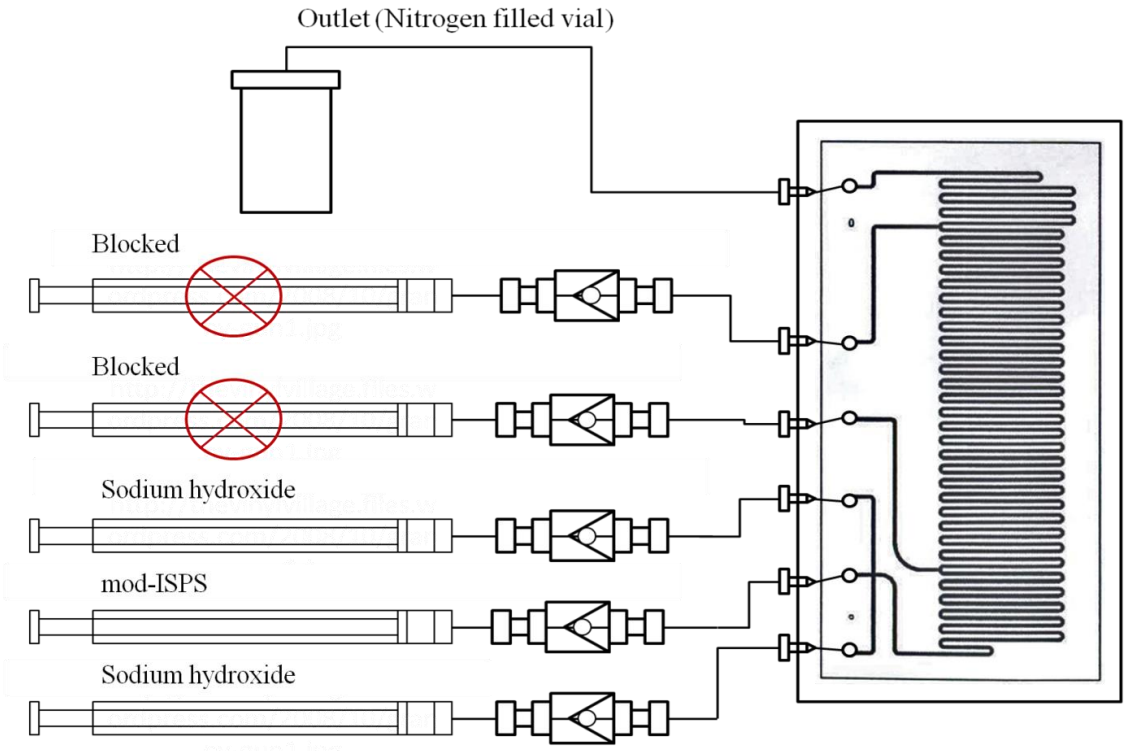

Figure 6.12. Schematic diagram for microreactor set up for used in that attempted formation of zinc doped iron oxide nanoparticles. Where a modified version of the ISPS is used to perform the attempted cation substitution reaction.

PXRD patterns were recorded for the samples over the range $20 \leq 2\theta\ ^\circ \leq 80$, with a step size of 0.02 ° and a time step of 28 s per step, **fig. 6.13**. PXRD patterns of the $Zn_xFe_{3-x}O_4$ series, show that the spinel structure is maintained, although all patterns suffer badly from peak broadening, and the presence of impurities cannot be ruled out. The broadness of the peaks is indicative of their low crystallinity, hence a heating stage during or after the reaction in the microfluidics reactors may be required.

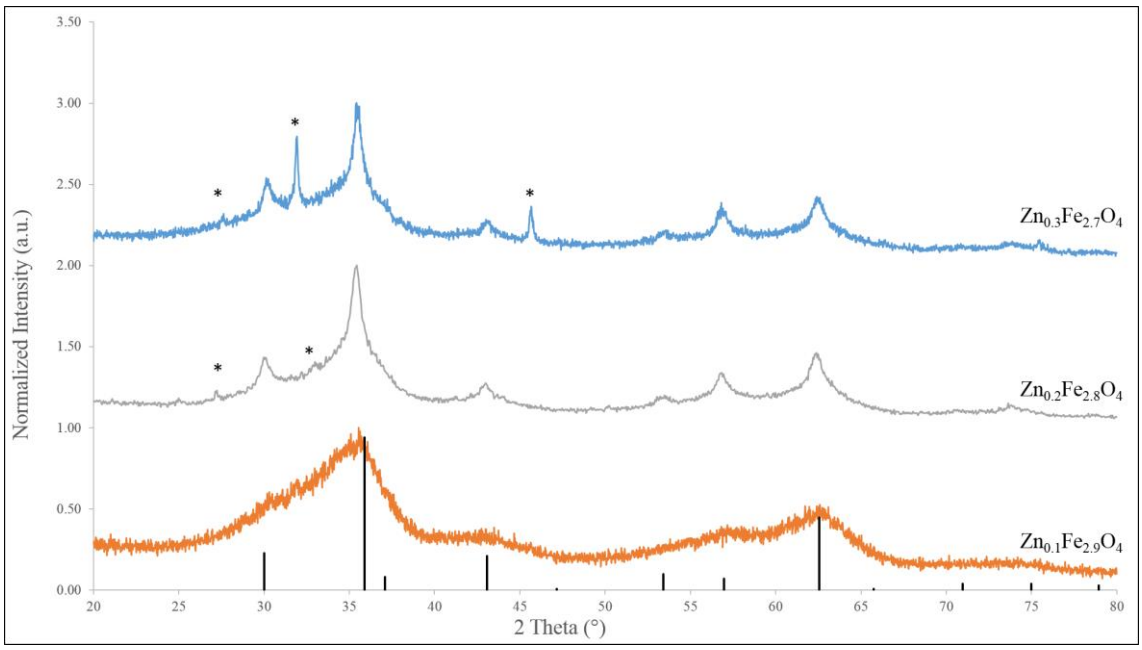

Figure 6.13. PXRD patterns of the $Zn_XFe_{3-x}O_4$ nanoparticles formed when Zn2+ substitution is attempted using the continuous flow focussed technique in a microreactor. The Spinel structure can be seen to be present as the very broad peaks of the nanoparticles can be seen to be in the correct position, suggesting a lack of crystallinity and potential presence of impurities. * denotes NaCl impurities.

Mössbauer spectra for the three $Zn_xFe_{3-x}O_4$ (x = 0.1, 0.2, 0.3) were recorded, on an ES-Technology MS-105 Mössbauer spectrometer, **fig. 6.14.** Spectra were referenced against 25 μm iron foil at 298 K and spectrum parameters were obtained by fitting with Lorentzian curves.

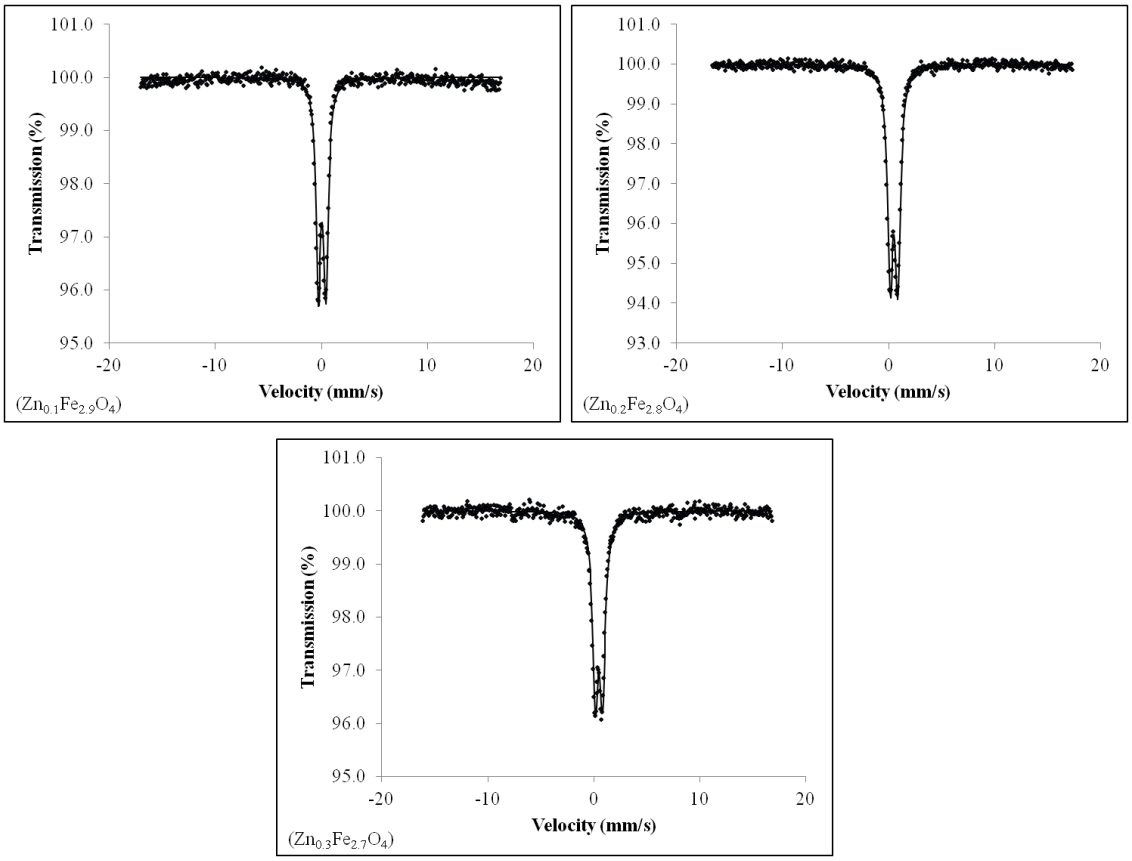

Figure 6.14. Mössbauer spectra for zinc ferrites synthesised using continuous flow focussing. Each can be seen to be a doublet spectra suggesting a superparamagnetic spinel phase, however some peaks may be hidden in the baseline of the $Zn_{0.3}Fe_{2.7}O_4$ suggesting that the substitution of the Zn^{2+} into the structure maybe having some effect upon the nanoparticles magnetism.

No impurities were detected in the spectra, although close inspection of the baseline of the spectrum of the sample $Zn_{0.3}Fe_{2.7}O_4$ shows some deviation, which may be due to a very small amount of another iron oxide (Fe_3O_4 or γ-Fe_2O_3) or a very broad six-line hyperfine component of the spectra.

Sample	Isomer shift (mm/s)	Quadrupole Splitting (mm/s)	Half Width at Half Maximum (mm/s)
$Zn_{0.1}Fe_{2.9}O_4$	0.43 ± 0.02	0.71 ± 0.02	0.27 ± 0.02
$Zn_{0.2}Fe_{2.8}O_4$	0.45 ± 0.02	0.71 ± 0.02	0.31 ± 0.02
$Zn_{0.3}Fe_{2.7}O_4$	0.43 ± 0.02	0.70 ± 0.02	0.33 ± 0.02
$ZnFe_2O_4$ Singh *et.al.*[165]	0.32 ± 0.02	0.40 ± 0.02	0.41 ± 0.02
$ZnFe_2O_4$ Ahn *et.al.* [166]	0.39 ± 0.02	0.59± 0.02	N/A

Table 6.9. Mossbauer parameters for the zinc substituted ferrites synthesised using continuous flow focusing and comparison values taken from literature.

The Mössbauer isomer shift and quadropole splitting were seen to be of the same order as those seen in literature, **table 6.9.**[191-193] The well defined doublet seen in all spectra is common for nanosized zinc ferrite systems, displaying superparamagnetic behaviour. The isomer shift for each sample was higher than that seen for $ZnFe_2O_4$ nanoparticles (0.33 - 0.35 mm/s), indicating that some Fe^{2+} may be present, as these values are closer to those expected for superparamagnetic Fe_3O_4 at 80 K (0.40 - 0.46 mm/s).[45, 175] If the temperature were to be further lowered then a sextet spectrum would likely be obtained as the superparamagnetic relaxation time would be greater (slower) than that of the Larmor procession frequency of the ^{57}Fe nucleus. [137, 194] An increasing trend in the half width at half maximum was noted with increasing zinc content, suggesting that the zinc content is affecting the particles magnetic properties particularly those associated with superparamagnetism. Further to this, the deviation from the baseline in the spectrum of $Zn_{0.3}Fe_{2.7}O_4$, may indicate that the relaxation rate has been affected, and the deviation may be due to the sample being close to the blocking temperature at which point the

expected sextet, due to quadrupole splitting, and is starting to emerge from the background or baseline.

ICP analysis revealed an increasing trend in the amount of Zn present within the nanoparticles with increasing $ZnCl_2$ concentration in the initial solution. As with the $Zn_xFe_{3-x}O_4$ compounds made in bulk those produced in the microreactor were seen to contain a higher percentage of Zn than that present in solution. This was again due to the production of impurities, lost in the washing process.

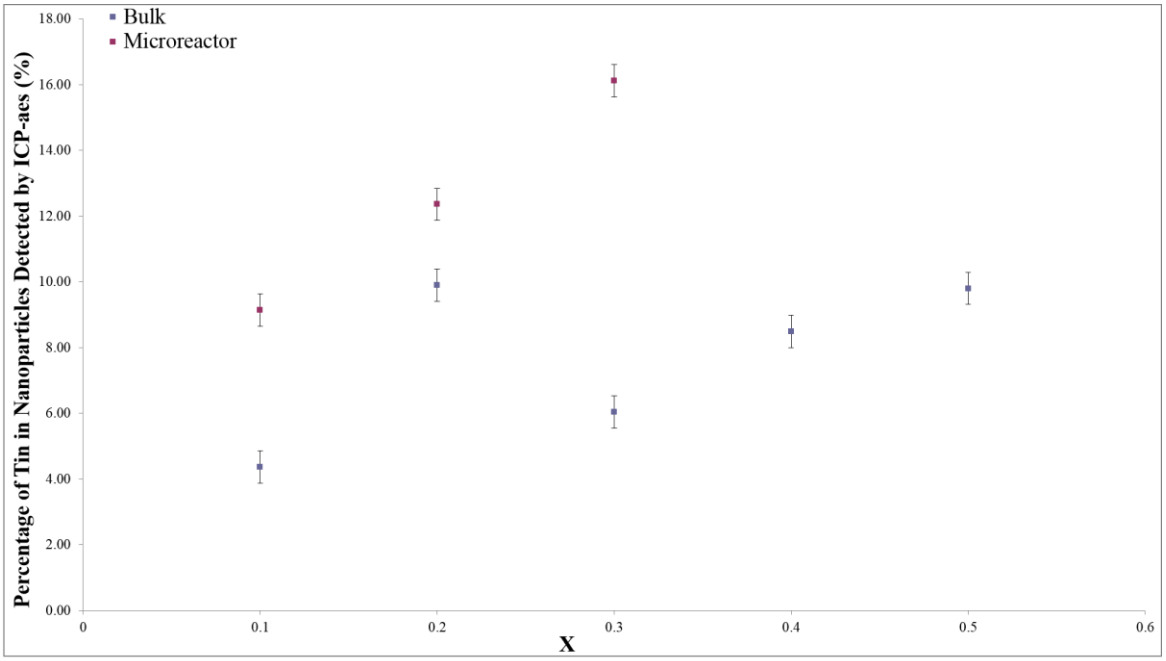

Figure 6.15. Plot of the actual Zn content in the $Zn_xFe_{3-x}O_4$ series nanoparticles, for those produced in both the microreactor (red) and those produced in batch (blue). The amount of Zn^{2+} nanoparticles substituted into the nanoparticles can be seen to be higher for those produced in the microreactor than those in batch.

When the batch and microreactor ICP data for Zn substitution are compared, those produced within the microreactor can be seen to have an increased amount of substitution, probably due to the controlled diffusion of reagents allowed by the use of microreactors in comparison to co-precipitation methods, **fig. 6.15.**

Using the ICP data the general formulae of the compounds were calculated, **table 6.10**. The general formulae also show that even the lowest amount of substitution achieved within the microreactor was equivalent to the highest amount of substitution obtained when the reactions were performed in bulk, suggesting the use of the microreactor provides a much more efficient way of synthesising cation substituted IONs.

Percentage of $ZnCl_2$ in Initial Solution (%)	Predicted Formula of Compound	Percentage of Zn in Nanoparticles (%)	Formula of Compound
3.33	$Zn_{0.1}Fe_{2.9}O_4$	9.14	$Zn_{0.27}Fe_{2.73}O_4$
6.66	$Zn_{0.2}Fe_{2.8}O_4$	12.36	$Zn_{0.37}Fe_{2.63}O_4$
10.00	$Zn_{0.3}Fe_{2.7}O_4$	16.14	$Zn_{0.48}Fe_{2.52}O_4$

Table 6.10. Predicted and actual substitution of Zinc into the nanoparticles. The formulae are based upon Fe_3O_4 consistent with literature.

6.4. Conclusions

Cation substitution of several transition metals (Co^{2+}, Mn^{2+}, Zn^{2+}, Sn^{2+} and V^{3+}) in Fe_3O_4 was performed using a modified co-precipitation reaction. In general an increase in the amount of cation substitution was seen with an increasing amount present within the presence in the initial reagents. The amount of substituted cations was often seen to differ from that predicted, due to impurities lost during the washing steps.

The synthesis of a series of $Zn_xFe_{3-x}O_4$ compounds was attempted using the continuous flow focussing technique. Zn was chosen as the most suitable for this, as the substitution into the spinel phase iron oxide has been most researched; and Zn^{2+} has a clear preference for the tetrahedral sites over the octahedral. The nanoparticles produced in the microreactor were confirmed as single phase by both Mössbauer and PXRD although the

PXRD patterns did show very broad peaks. The Mössbauer spectra showed the nanoparticles to be superparamagnetic, due to the doublet present instead of the expected sextet, the parameters of the doublet were also seen to be close to those of $ZnFe_2O_4$ suggesting substitution had occurred. The amount of Zn substitution into the nanoparticles was seen to increase when synthesised within the microreactor, in comparison to those produced in bulk. This was thought to be due to the controlled rate of diffusion and mixing of the reagents within the microreactor. Production of Zn substituted nanoparticles was therefore thought to be more efficient when performed using microreactors. Controlling the amount of substitution however may prove more difficult due to the production of non-magnetic impurities.

7.0. Conclusions

The work described in this thesis demonstrates the development of an adaptable microfluidic technique for the synthesis of iron oxide nanoparticles, using commercially available microreactor devices. Spinel phase iron oxide nanoparticles were synthesised and a degree of control over the phase of these was obtained by further adaptation and development of the technique.

It has been demonstrated that through careful manipulation of experimental parameters that a microfluidic technique for the synthesis of nanoparticles can be reverse engineered, for use on commercial microreactors. Microreactors therefore need no longer be designed specifically for certain reactions, as is common, but premade microreactors can be easily adapted for the synthesis of nanoparticles even if their primary application is not for this, moving microfluidics away from being a "proof of concept field" by overcoming the problem of first user premium. To prove this, the microreactors used throughout this work have been specifically designed for the synthesis of organic liquids and light weight polymers, not solids, and are already implemented in the chemical industryhowever through a process of reverse engineering, spinel phase iron oxide nanoparticles have been produced. These nanoparticles have been analysed and seen to possess comparable physical and magnetic properties to those produced using microreactors specifically designed for the synthesis of nanoparticles.

As currently the main focus of research into spinel phase iron oxide nanoparticles is for use in the biotechnology industry as either MRI contrast agents or hyperthermia treatments for arteriosclerosis and cancer, demonstrating the ability to produce nanoparticles with consistently small sizes, and magnetic properties is crucial to their continued use in the biotechnology industry. By using microdevices which are already used in the chemical synthesis industry, the author feels that this work has laid the

groundwork for the ability to continually produce nanoparticles with structures tailored toward specific applications on an industrial scale.

Manipulation of structural changes has been widely studied in bench and solid state reactions, in an attempt to study and gain control over the magnetic properties of spinel phase iron oxide nanoparticles. This work has seen the use and further development of a simple technique relying upon powder X-ray diffraction for the quantification of Fe_3O_4 and γ-Fe_2O_3, through peak deconvolution, which until now has proved difficult due to their similar crystallographic structures.

No work before this research, had been conducted into the subjects of phase manipulation or cation substitution of nanoparticles using microreactor technology. This work has demonstrated that the phase of spinel iron oxide nanoparticles can be converted and controlled through the addition of oxidizing agents, allowing the nanoparticle structures to be converted from Fe_3O_4 to γ-Fe_2O_3, increasing the nanoparticles chemical stability. The reverse reaction, converting Fe_3O_4 to γ-Fe_2O_3, to increase the magnetic properties of the nanoparticles, was also attempted with less success, suggesting the choice of reducing agent needs to be more carefully considered.

Cation substitution is the more common technique for manipulating the structure of spinel phase iron oxide nanoparticles, and their subsequent magnetic properties in bench and solid state reactions. This work demonstrates that cation substitution reactions can also be easily performed using microreactors, allowing for the production of zinc substituted ferrites ($Zn_xFe_{3-x}O_4$).

8.0. Further Work

As the nanoparticles synthesised in this work were primarily designed for use as either MRI contrast agents or hyperthermia treatments, the magnetic relaxivity of these must first be calculated, along with the T_1 and T_2 relaxation times.

Any further work based upon the work presented in this thesis, would also have several technical issues to consider. Firstly the crystallinity of the nanoparticles prepared in microreactors would need to be addressed. Throughout this work attention has been drawn toward peak broadness, while a broadening of peaks in PXRD patterns is expected for nanoparticles, it is also indicative of poorly crystalline samples, and efforts would need to be taken to address this, as increasing the nanoparticles crystallinity would help to make the nanoparticles magnetic properties more favourable, particularly in increasing the particles magnetic saturation. A growing trend has recently appeared for the addition of heating stages to microreactors for improvement of nanoparticle crystallinity after formation. This has been avoided in this work as no form of pressure regulation (e.g. the use of a back pressure regulator) has been used, and a change in the temperature inevitably will lead to a change in the pressure of the system. It would be relatively easy however, to increase the length of the outlet tubing and use an oil bath to create a heating section after nanoparticle formation has taken place in the microreactor, **fig. 8.1.** A more effective route however, maybe to use this in conjunction with ethylene glycol based reagents, rather than the aqueous solutions currently used, allowing for temperatures of up to 196 °C to be utilised.

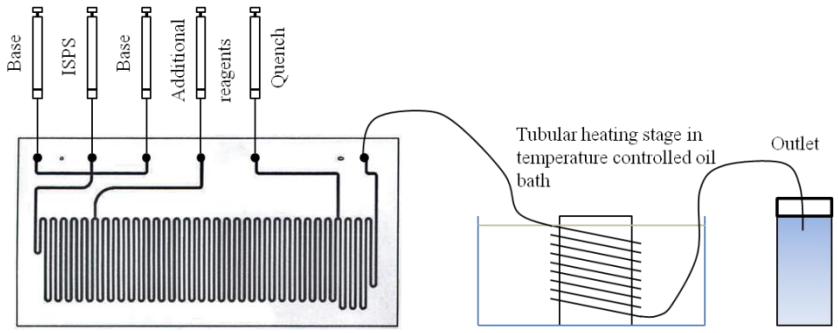

Figure 8.1. Preliminary design of microreactor system used for continuous flow focussing approach with external heating stage for improved crystallinity.

The peak deconvolution method used for determination and quantification of the two phases of iron oxide within the nanoparticles would also require continued development. While the error upon the calibration graph and the associated detection limits are low for a technique in the early stages of development, further improvements could be made. The use of a more modern diffractometer would likely provide well defined X-ray diffraction patterns, enabling better determination of the peak asymmetry, while the use of more powerful peak fitting software, e.g. Jade 6.0., would allow for more accurate deconvolution of the peaks, yielding more accurate weight percentages of the Fe_3O_4 and γ-Fe_2O_3 phases within the nanoparticles.

Finally addressing the long-term goal of the project needed to be addressed in the "scaling out" or "scaling up" of the reaction to enable large scale, or on-site production of the nanoparticles using these systems. The most easily achievable way of doing this would be to move from the Chemtrix.BV Labtrix Start system currently used toward their currently marketed pilot plant Kiloflow system. Alternatively a "black-box" system like those employed by the group of A.J. deMello, could be conceived, in which a combination of FTIR and Nanosight were used to provide continuous analysis of the size and phase of the nanoparticles, allowing for a "black box" computer program to allow for continuous control of reaction parameters, **fig. 8.2.**

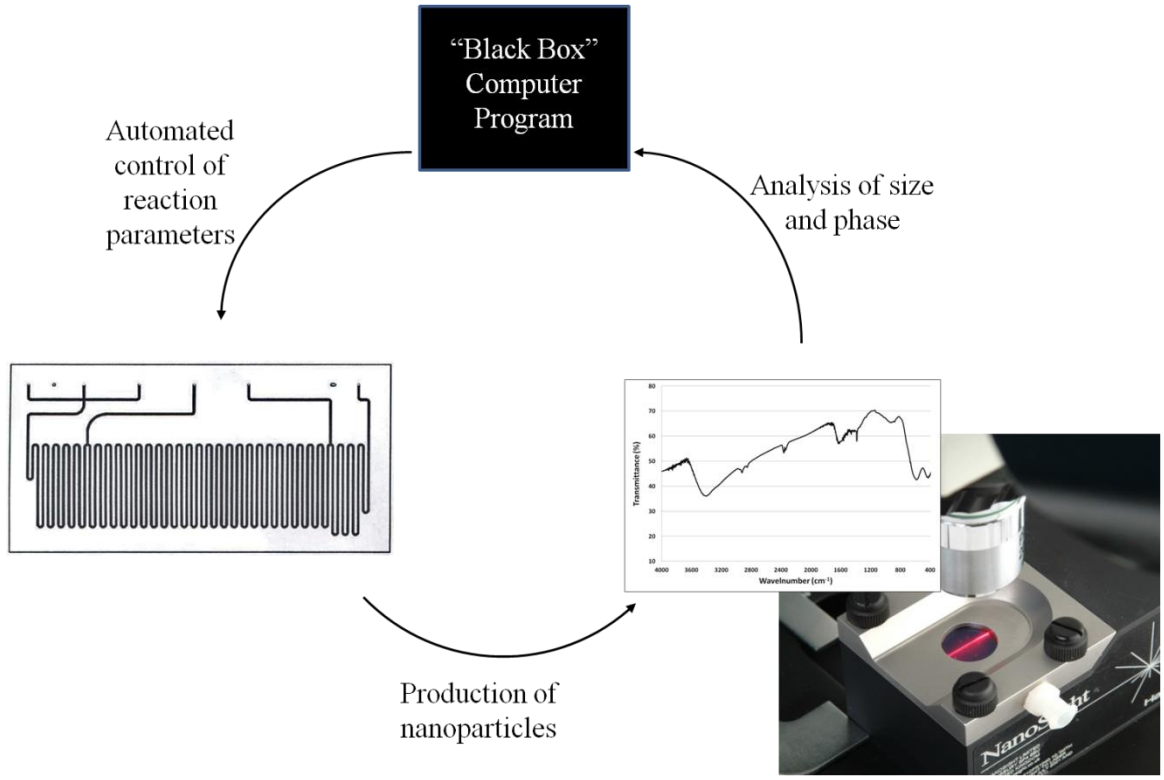

Figure 8.2. Schematic representation of automation process, through "black boxing" to enable automated production of nanoparticles.

9.0. References

1. E. Kim, K. Lee, Y. M. Huh and S. Haam, *J Mater Chem*, 2013, **1**, 729.
2. R. R. Qiao, C. H. Yang and M. Y. Gao, *J Mater Chem*, 2009, **19**, 6274-6293.
3. A. Saraste, S. G. Nekolla and M. Schwaiger, *Cardiovac Res*, 2009, **83**, 643-652.
4. H. B. Na, I. C. Song and T. Hyeon, *Adv Mater*, 2009, **21**, 2133-2148.
5. Z. R. Stephen, F. M. Kievit and M. Zhang, *Mater Today*, 2011, **14**, 330-338.
6. Q. A. Pankhurst, J. Connolly, S. K. Jones and J. Dobson, *J Phys D Appl Phys*, 2003, **36**, 167-181.
7. Y. Gossuin, P. Gillis, A. Hocq, Q. L. Vuong and A. Roch, *Adv Rev*, 2009, **1**, 299-310.
8. E. D. Smolensky, H. Y. E. Park, Y. Zhou, G. Rolla, M. Marjanska, M. Botta and V. C. Pierre, *J Mater Chem B*, 2013, **1**, 2818-2828.
9. S. Laurent, S. Dutz, U. O. Hafeli and M. Mahmoudi, *Adv Colloid Interfac*, 2011, **166**, 8-23.
10. M. Johanssen, U. Gneveckow, L. Eckelt, A. Feussner, N. Waldofner, S. A. Loening, A. Jordan, R. Scholz, S. Deger and P. Wust, *Int J Hyperther*, 2005, 1-11.
11. M. Johannsen, B. Thiesen, P. Wust and A. Jordan, *Int J Hyperther*, 2010, **26**, 790-795.
12. D. S. Mathew and R. S. Juang, *Chem Eng J*, 2007, **129**, 51-65.
13. J. P. Jakubovics, *Magnetism and Magnetic Materials*, Second edn., The Institute of Materials, 1994.
14. D. H. Martin, *Magnetism in Solids*, First edn., Iliffe Books Ltd., 1967.
15. L. Smart and E. Moore, *Solid State Chemistry, An Introduction*, Second edn., Chapman & Hall, Chapman & Hall, 2-6 Boundary Row, London, SE1 8HN, UK, 1995.
16. J. Crangle, *Solid State Magnetism*, First edn., Edward Arnold, 1991.
17. S. Bdanta and W. Kleemann, *J Phys D Appl Phys*, 2009, **42**, 1-28.
18. P. Weiss, *J. Phys. Rad.*, 1909, **6**, 661.
19. R. M. Cornell and U.Schwertmann, *The Iron Oxides: Structure, Properties, Reactions, Occurences and Uses.*, Second edn., Wiley-VCH, 2003.
20. A. R. West, *Basic Solid State Chemistry*, Second edn., John Wiley & Sons Ltd, 2000.
21. J. K. Burdett, G. D. Price and S. L. Price, *J Amer Chem Soc*, 1982, **104**, 92-95.
22. J. K. Burdett, G. D. Price and S. L. Price, *J Amer Chem Soc*, 1984, **104**, 92-95.
23. J. K. Burdett, *Chemical Bonding in Solids*, First edn., Oxford University Press, 1995.
24. M. E. Fleet, *J Solid State Chem*, 1986, **62**, 75-82.
25. K. J. Gallagher, W. Feitknecht and U. Mannweiler, *Nature*, 1968, **217**, 1118-1121.
26. C. Greaves, *J Solid State Chem*, 1983, **49**, 325-333.
27. T. J. Bastow, A. Trinchi, M. R. Hill, R. Harris and T. H. Muster, *J Magn Magn Mater*, 2009, **321**, 2677-2681.
28. R. Grau-Crespo, A. Y. Al-Baitai, I. Saadoune and N. H. De Leeuw, *J Phys Conden Mat*, 2010, **22**, 7.
29. J. E. Jorgensen, L. Mosegaard, L. E. Thomsen, T. R. Jensen and J. C. Hanson, *J Solid State Chem*, 2007, **180**, 180-185.
30. R. Zboril, M. Mashlan and D. Petridis, *Chem Mater*, 2002, **14**, 969-982.
31. J. S. Salazar, L. Perez, O. de Abril, T. P. Lai, D. Ihiawakrim, M. Vazquez, J. M. Greneche, S. Begin-Colin and G. Pourroy, *Chem Mater*, 2011, **23**, 1379-1386.
32. M. D. Carvalho, F. Henriques, L. P. Ferreira, M. Godinho and M. M. Cruz, *J Solid State Chem*, 2013, **201**, 144-152.

33. J. B. Yang, X. D. Zhou, W. B. Yelon, W. J. James, Q. Cai, K. V. Gopalakrishnan, S. K. Malik, X. C. Sun and D. E. Nikles, *J ApplPhys*, 2004, **95**, 7540-7542.
34. C. C. Huang, K. Y. Chuang, C. P. Chou, M. T. Wu, H. S. Sheu, D. B. Shieh, C. Y. Tsai, C. H. Su, H. Y. Lei and C. S. Yeh, *J Mater Chem*, 2011, **21**, 7472-7479.
35. L. B. Tahar, L. S. Smiri, M. Artus, A. L. Joudrier, F. Herbst, M. J. Vaulay, S. Ammar and F. Fievet, *Mater Res Bull*, 2007, **42**, 1888-1896.
36. D. Carta, M. F. Casula, A. Falqui, D. Loche, G. Mountjoy, C. Sangregorio and A. Corrias, *J Phys Chem C*, 2009, **113**, 8606-8615.
37. E. A. Schultz-Sikma, H. M. Joshi, Q. Ma, K. W. MacRenaris, A. L. Eckermann, V. P. Dravid and T. J. Meade, *Chem Mater*, 2011, **23**, 2657-2664.
38. C. Wende, K. Olimov, H. Modrow, F. E. Wagner and H. Langbein, *Mater Res Bull*, 2006, **41**, 1530-1542.
39. M. J. Akhtar and M. Younas, *Solid State Sci*, 2012, **14**, 1536-1542.
40. M. G. Goodarz Naseri, E. B. Bin Saion, H. A. Abbastabar Ahangar, N. Hashim and A. H. Shaari, *J Magn Magn Mater*, 2011, **323**.
41. C. N. Chinnasamy, A. Yang, S. D. Yoon, K. Hsu, M. D. Shultz, E. E. Carpenter, S. Mukerjee, C. Vittoria and V. G. Harris, *J Appl Phys*, 2007, **101**.
42. J. C. Waerenborgh, M. O. Figueiredo, J. M. P. Cabral and L. C. J. Pereira, *J Solid State Chem*, 1994, **111**, 300-309.
43. C. Barcena, A. K. Sra, G. S. Chaubey, C. Khemtong, J. P. Liu and J. Gao, *Chem Comm*, 2008, 2224-2226.
44. J. P. Singh, G. Dixit, R. C. Srivastava, H. M. Agrawal, V. R. Reddy and A. Gupta, *J Magn Magn Mater*, 2012, **324**, 2553-2559.
45. M. Atif, S. K. Hasanain and M. Nadeem, *Solid State Comm*, 2006, **138**, 416-421.
46. V. A. Pool, M. T. Klem, J. Holroyd, T. Harris, E. Arenholz, M. Young, T. Douglas and Y. D. Idzerda, *J Appl Phys*, 2009, **105**.
47. B. Behdadfar, A. Kermanpur, H. Sadeghi-Aliabadi, M. del Puerto Morales and M. Mozaffari, *J Magn Magn Mater*, 2012, **324**, 2211-2217.
48. J. C. Bernier and P. Poix, *Ann Chim France*, 1967, **1967**, 81-89.
49. X. Liang, S. Zhu, Y. Zhong, J. Zhu, P. Yuan, H. He and J. Zhang, *ApplCatal B-Environ*, 2010, **97**, 151-159.
50. V. Nivoix and B. Gillot, *Solid State Ionics*, 1998, **111**, 17-25.
51. V. Nivoix, P. Perriat, P. Tailhades and B. Gillot, *CR Acad Sci B*, 1997, **325**, 279-286.
52. O. N. C. Uwakweh, R. Mas, C. Morales, P. Vargas, J. Silva, A. Rosa, N. Lopez, R. P. Moyet and Y. Cardona, *J Mater Eng Perform*, 2011, **20**, 1157-1162.
53. F. J. Berry, C. Greaves, J. G. McManus, M. Mortimer and G. Oates, *J Solid State Chem*, 1997, **130**, 272-276.
54. Y. Ling, G. Wang, D. A. Wheeler, J. Z. Zhang and Y. Li, *Nano Lett*, 2011, **11**, 2119-2125.
55. A. Tavakoli, M. Sohrabi and A. Kargari, *Chem Pap*, 2007, **61**, 151-170.
56. A. H. Lu, E. L. Salabas and F. Schuth, *Angew Chem Int Edit*, 2007, **46**, 1222-1244.
57. S. Laurent, D. Forge, M. Port, A. Roch, C. Robic, L. V. Elst and R. N. Muller, *Chem Rev*, 2008, **108**, 2064-2110.
58. E. Darezereshki, M. Ranjbarb and F. Bakhtiaric, *J Alloy Comp*, 2010, **502**, 257-260.
59. O. Karaagac, H. Kockar, S. Beyaz and T. Tanrisever, *Ieee T Magn*, 2010, **46**, 3978-3983.
60. S. Nigam, K. C. Barick and D. Bahadur, *J Magn Magn Mater*, 2011, **323**, 237-243.

61. G. Utkan, F. Sayar, P. Batat, S. Ide, M. Kriechbaum and E. Piskin, *J Colloid Interfac Sci*, 2011, **353**, 372-379.
62. B. R. Jarrett, M. Frendo, J. Vogan and A. Y. Louie, *Nanotech* 2007, **18**, 7.
63. J. L. Viota, F. J. Arroyo, A. V. Delgado and J. Horno, *J Colloid Interfac Sci*, 2010, **344**, 144-149.
64. Z. J. Wang, H. Zhu, X. L. Wang, F. Yang and X. R. Yang, *Nanotech*, 2009, **20**, 10.
65. S. Mohapatra, S. K. Mallick, T. K. Maiti, S. K. Ghosh and P. Pramanik, *Nanotech*, 2007, **18**, 9.
66. Y. Sun, G. Guo, B. Yang, W. Cai, Y. Tian, M. He and Y. Liu, *Physica B*, 2011, **406**, 1013-1016.
67. M. Joselevich and F. J. Williams, *Langmuir*, 2008, **24**, 11711-11717.
68. X. Peng, Y. Wang, X. Tang and W. Liu, *Dyes Pigments*, 2011, **91**, 26-32.
69. M. P. S. de Almeida, K. L. Caiado, P. P. C. Sartoratto, D. Silva, A. R. Pereira and P. C. Morais, *J Alloys Comp*, 2010, **500**, 149-152.
70. A. Bumb, M. W. Brechbiel, P. L. Choyke, L. Fugger, A. Eggeman, D. Prabhakaran, J. Hutchinson and P. J. Dobson, *Nanotech*, 2008, **19**, 6.
71. L. Han and Y. Wei, *Mater Lett*, 2012, **70**, 1-3.
72. P. Dutta, A. Manivannan, M. S. Seehra, N. Shah and G. P. Huffman, *Phys Rev B*, 2004, **70**.
73. A. Demortiere, P. Panissod, B. P. Pichon, G. Pourroy, D. Guillon and B. Donnio, *Nanoscale*, 2011, **3**, 225-232.
74. P. Guardia, J. Perez-Juste, A. Labarta, X. Batlle and L. M. Liz-Marzan, *Chem Comm*, 2010, **46**, 6108-6110.
75. T. Hyeon, S. S. Lee, J. Park, Y. Chung and H. Bin Na, *J Amer Chem Soc*, 2001, **123**, 12798-12801.
76. C. Qin, C. Li, Y. Z. Hu, J. F. Shen and M. X. Ye, *Colloid Surface A*, 2009, **336**, 130-134.
77. C.-H. Ho, C.-P. Tsai, C.-C. Chung, C.-Y. Tsai, F.-R. Chen, H.-J. Lin and C.-H. Lai, *Chem Mater*, 2011, **23**, 1753-1760.
78. P. Guardia, A. Labarta and X. Batlle, *J Phys Chem C*, 2011, **115**, 390-396.
79. S. H. Sun, H. Zeng, D. B. Robinson, S. Raoux, P. M. Rice, S. X. Wang and G. X. Li, *J Amer Chem Soc*, 2004, **126**, 273-279.
80. R. Qin, F. Li, W. Jiang and L. Liu, *J Mater Sci Technol*, 2009, **25**, 69-72.
81. H. Zeng, P. M. Rice, S. X. Wang and S. H. Sun, *J Amer Chem Soc*, 2004, **126**, 11458-11459.
82. G. Gao, P. Huang, Y. Zhang, K. Wang, W. Qin and D. Cui, *Cryst Eng*, 2011, **13**, 1782-1785.
83. S. Ge, X. Y. Shi, K. Sun, C. P. Li, C. Uher, J. R. Baker, M. M. B. Holl and B. G. Orr, *J Phys Chem C*, 2009, **113**, 13593-13599.
84. C. J. Belle, A. Bonamin, U. Simon, J. Santoyo-Salazar, M. Pauly, S. Begin-Colin and G. Pourroy, *Sensor Actuator*, 2011, **160**, 942-950.
85. T. Taniguchi, K. Nakagawa, T. Watanabe, N. Matsushita and M. Yoshimura, *J Phys Chem C*, 2009, **113**, 839-843.
86. H. Deng, X. L. Li, Q. Peng, X. Wang, J. P. Chen and Y. D. Li, *Angew Chem Int Edit*, 2005, **44**, 2782-2785.
87. C. Hu, Z. Gao and X. Yang, *J Magn Magn Mater*, 2008, **320**, L70-L73.
88. P. Tabeling, *Introduction to Microfluidics*, Oxford University Press, 2005.
89. A. Manz, D. J. Harrison, E. M. J. Verpoorte, J. C. Fettinger, A. Paulus, H. Ludi and H. M. Widmer, *J Chromatogr*, 1992, **593**, 253-258.
90. B. H. Weigl and P. Yager, *Science*, 1999, **283**, 346-347.

91. J. B. Knight, A. Vishwanath, J. P. Brody and R. H. Austin, *Phys Rev Lett*, 1998, **80**, 3863-3866.
92. R. P. Oda, M. A. Strausbauch, A. F. R. Huhmer, N. Borson, S. R. Jurrens, J. Craighead, P. J. Wettstein, B. Eckloff, B. Kline and J. P. Landers, *Anal Chem*, 1998, **70**, 4361-4368.
93. M. A. Northrup, B. Benett, D. Hadley, P. Landre, S. Lehew, J. Richards and P. Stratton, *Anal Chem*, 1998, **70**, 918-922.
94. A. Y. Fu, C. Spence, A. Scherer, F. H. Arnold and S. R. Quake, *Nat Biotechnol*, 1999, **17**, 1109-1111.
95. A. E. Kamholz, B. H. Weigl, B. A. Finlayson and P. Yager, *Anal Chem*, 1999, **71**, 5340-5347.
96. J. C. T. Eijkel, A. Prak, S. Cowen, D. H. Craston and A. Manz, *J Chromatogr*, 1998, **815**, 265-271.
97. G. M. Whitesides, *Nature*, 2006, **442**, 368-373.
98. M. Pumera, *Chem Comm*, 2011, **47**, 5671-5680.
99. J. B. Edel, R. Fortt, J. C. deMello and A. J. deMello, *Chem Comm*, 2002, 1136-1137.
100. A. Abou-Hassan, O. Sandre and V. Cabuil, *Angew Chem Int Edit*, 2010, **49**, 6268-6286.
101. C. X. Zhao, L. Z. He, S. Z. Qiao and A. P. J. Middelberg, *Cheml Eng Sci*, 2011, **66**, 1463-1479.
102. A. Abou Hassan, O. Sandre, V. Cabuil and P. Tabeling, *Chem Comm*, 2008, 1783-1785.
103. P. Atkins and J. De Paula, *Physical Chemistry*, 8th Edition edn., Oxford University Press, 2006.
104. A. M. Nightingale, S. H. Krishnadasan, D. Berhanu, X. Niu, C. Drury, R. McIntyre, E. Valsami-Jones and J. C. deMello, *Lab Chip*, 2011, **11**, 1221-1227.
105. J. D. Tice, H. Song, A. D. Lyon and R. F. Ismagilov, *Langmuir*, 2003, **19**, 9127-9133.
106. H. Song, J. D. Tice and R. F. Ismagilov, *Angew Chem Int Edit*, 2003, **42**, 768-772.
107. D. R. Link, E. Grasland-Mongrain, A. Duri, F. Sarrazin, Z. D. Cheng, G. Cristobal, M. Marquez and D. A. Weitz, *Angew Chem Int Edit*, 2006, **45**, 2556-2560.
108. L. Frenz, A. El Harrak, M. Pauly, S. Begin-Colin, A. D. Griffiths and J. C. Baret, *Angew Chem Int Edit*, 2008, **47**, 6817-6820.
109. H. Song, M. R. Bringer, J. D. Tice, C. J. Gerdts and R. F. Ismagilov, *Appl Phys Lett*, 2003, **83**, 4664-4666.
110. P. Watts and C. Wiles, *Chem Comm*, 2007, 443-467.
111. C. Wiles and P. Watts, *Chem Comm*, 2011, **47**, 6512-6535.
112. C. H. Zhao, L. He, S. Z. Qiao and A. P. J. Middelberg, *Chem Eng Sci*, 2011, **66**, 1463-1479.
113. T. Miyake, T. Ueda, N. Ikenaga, H. Oda and M. Sano, *J Mater Sci*, 2005, **40**, 5011-5013.
114. K. Kumar, A. M. Nightingale, S. H. Krishnadasan, N. Kamaly, M. Wylenzinska-Arridge, K. Zeissler, W. R. Branford, E. Ware, A. J. deMello and J. C. deMello, *J Mater Chem*, 2012, **22**.
115. Q. Dai, D. Berman, K. Virwani, J. Frommer, P. O. Jubert, M. Lam, T. Topuria, W. Imaino and A. Nelson, *Nano Lett*, 2010, **10**, 3216-3221.
116. S. Krishnadasan, R. J. C. Brown, A. J. deMello and J. C. deMello, *Lab Chip*, 2007, **7**, 1434-1441.
117. A. Abou-Hassan, J.-F. Dufreche, O. Sandre, G. Meriguet, O. Bernard and V. Cabuil, *J Phys Chem C*, 2009, **113**, 18097-18105.

118. A. Abou-Hassan, R. Bazzi and V. Cabuil, *Angew Chem Int Edit*, 2009, **48**, 7180-7183.
119. N. Hassan, V. Cabuil and A. Abou-Hassan, *Angew Chem Int Edit*, 2013, **52**, 1994-1997.
120. A. Abou-Hassan, O. Sandre, S. Neveu and V. Cabuil, *Angew Chem Int Edit*, 2009, **48**, 2342-2345.
121. A. Abou-Hassan, S. Neveu, V. Dupuis and V. Cabuil, *RSC Adv*, 2012, **2**, 11263-11266.
122. W. Clegg, *Crystal Structure Determination*, Oxford University Press, 1998.
123. J. Pickworth Glusker and K. N. Trueblood, *Crystal Structure Analysis a Primer*, Second edn., Oxford University Press, 1985.
124. M. T. Weller, *Inorganic Materials Chemistry*, Oxford Science Publications, 1994.
125. W. H. Bragg and W. L. Bragg, *X-rays and Crystal Structure*, G. Bell and Sons Ltd, 1915.
126. R. E. Dinnebier and S. J. L. Billinge, *Powder Diffraction: Theory and Practice*, RSC Publishing, 2008.
127. R. Jenkins and R. L. Snyder, *Introduction to X-ray Powder Diffractometry*, Wiley & Sons, Inc., 1996.
128. H. P. Klug and L. E. Alexander, *X-ray Diffraction Procedures*, John Wiley & Sons, 1974.
129. W. Kim, C. Y. Suh, S. W. Cho, K. M. Roh, H. Kwon, K. Song and I. J. Shon, *Talanta*, 2012, **94**, 348-352.
130. R. W. Cheary and A. A. Coelho, CCP14 Powder diffraction Libary-Daresbury laboratory, Warrington, England, Editon edn., 1996.
131. J. N. Miller, *Statistics and Chemometrics for Analytical Chemistry*, Harlow; Prentice Hall, Sixth edn., 2010.
132. D. A. Skoog, D. M. West and F. J. Holler, *Fundamentals of Analytical Chemistry*, Seventh edn., Harcourt College Publishers, 1996.
133. F. W. Fifield and D. Kealey, *Principles and Practice of Analytical Chemistry*, Fourth edn., Blackie Academic & Professional, 1995.
134. M. Davies, *Infra-red Spectroscopy and Molecular Structure; An Outline of the Principles*, Elsevier Publishing Company, 1963.
135. R. T. Conley, *Infrared Spectroscopy*, Allyn and Bacon, inc., 1966.
136. L. H. Bowen, E. De Grave and R. E. Vandenberghe, *Mossbauer Spectroscopy Applied to Magnetism and Materials Science*, Plenum Press, 1993.
137. T. E. Cranshaw, B. W. Dale, G. O. Longworth and C. E. Johnson, *Mossbauer Spectroscopy and its Applications*, First edn., Cambridge University Press, 1985.
138. RSC Mossbauer Spectroscopy Group, http://www.rsc.org/Membership/Networking/InterestGroups/MossbauerSpect/.
139. J. Nolte, *ICP Emission spectrometry: A Practical Guide*, Wiley-VCH, 2003.
140. S. J. Hill, *Inductively Coupled Plasma Spectrometry and its Applications*, Sheffield Academic Press Ltd, 1999.
141. X. Zou, S. Hovmoller and P. Oleynikov, Oxford Scholarship Online, Editon edn., 2011.
142. S. J. Pennycook and P. D. Nellist, eds. S. J. Pennycook and P. D. Nellist, Springer, Editon edn., 2011.
143. J. Ltd., *JEOL Ltd. Documents and Downloads*, http://www.jeol.com/RESOURCES/DocumentsandDownloads/tabid/350/Default.aspx?EntryId=84.
144. K. S. W. Sing, D. H. Everett, R. W. Haul, L. Moscou, R. A. Pierotti, J. Rouquerol and T. Siemieniewska, *Pure Appl Chem*, 1985, **57**, 603-619.
145. S. Brunauer, P. H. Emmett and E. Teller, *J Amer Chem Soc*, 1938, **60**, 309-319.

146. D. Jiles, *Introduction to Magnetism and Magnetic Materials*, First edn., Chapman & Hall, 1995.
147. W. Wang, C. Yang, X. Q. Cui, Q. L. Bao and C. M. Li, *Microfluid Nanofluid*, 2010, **9**, 1175-1183.
148. E. M. Chan, A. P. Alivisatos and R. A. Mathies, *J Amer Chem Soc*, 2005, **127**, 13854-13861.
149. S. A. Khan, A. Gunther, M. A. Schmidt and K. F. Jensen, *Langmuir*, 2004, **20**, 8604-8611.
150. A. M. Nightingale and J. C. de Mello, *J Mater Chem*, 2010, **20**, 8454-8463.
151. C. Wiles, *Chem Today*, 2011, **29**, 32-33.
152. C. Wiles, Chemtrix.BV, www.Chemtrix.com, 2012.
153. C. X. Zhao and A. P. J. Middelberg, *Chem Eng Sci*, 2011, **66**, 1394-1411.
154. F. Sarrazin, L. Prat, N. Di Miceli, G. Cristobal, D. R. Link and D. A. Weitz, *Chem Eng Sci*, 2007, **62**, 1042-1048.
155. S. Santra, R. Tapec, N. Theodoropoulou, J. Dobson, A. Hebard and W. H. Tan, *Langmuir*, 2001, **17**, 2900-2906.
156. P. Das, A. Saha, A. R. Maity, S. C. Ray and N. R. Jana, *Nanoscale*, 2013, **5**, 5732-5737.
157. J. Wagner and J. M. Kohler, *Nano Lett*, 2005, **5**, 685-691.
158. Y. J. Song, R. S. Li, Q. Q. Sun and P. Y. Jin, *Chem Eng J*, 2011, **168**, 477-484.
159. Z. L. Xue, A. D. Terepka and Y. Hong, *Nano Lett*, 2004, **4**, 2227-2232.
160. *Handbook of Chemistry and Physics*, 72nd edn., CRC Press Inc., 1991-1992.
161. *Handbook of Chemistry and Physics*, 76th edn., CRC Press Inc., 1995-1996.
162. R. A. Bourne, X. Han, M. Poliakoff and M. W. George, *Angew Chem Int Edit*, 2009, **48**, 5322-5325.
163. R. A. Bourne, R. A. Skilton, A. J. Parrott, D. J. Irvine and M. Poliakoff, *Org Process Res Dev*, 2011, **15**, 932-938.
164. A. J. Parrott, R. A. Bourne, G. R. Akien, D. J. Irvine and M. Poliakoff, *Angew Chem Int Edit*, 2011, **50**, 3788-3792.
165. J. G. Stevens, R. A. Bourne, M. V. Twigg and M. Poliakoff, *Angew Chem Int Edit*, 2010, **49**, 8856-8859.
166. N. Tran and T. J. Webster, *J Mater Chem*, 2010, **20**, 8760-8767.
167. S. Krishnadasan, J. Tovilla, R. Vilar, A. J. deMello and J. C. deMello, *J Mater Chem*, 2004, **14**, 2655-2660.
168. G. A. Patil, M. L. Bari, B. A. Bhanvase, V. Ganvir, S. Mishara and S. H. Sonawane, *Chem Eng Process*, 2012, **62**, 69-77.
169. D. Jeevarathinam, A. K. Gupta, B. Pitchumani and R. Mohan, *Chem Eng J*, 2011, **173**, 607-611.
170. W. Deer, R. Howie and J. Zussman, J., *Rock Forming Minerals*, **5**, 73.
171. D. Lindsley, *Mineral Society of America*, 1976, L-18. http://www.minsocam.org/
172. *Dana's System of Mineralogy*, 7th edn, 1976.
173. *The NBS Alloy Data Center: Permuted Materials Index*, 1967, 698.
174. A. Martorana, R. Gerbasi, A. Marigo and R. Zannetti, *Comput Phys Comm*, 1984, **34**, 145-151.
175. A. A. A. Aljabali, J. E. Barclay, O. Cespedes, A. Rashid, S. S. Staniland, G. P. Lomonossoff and D. J. Evans, *Adv Funct Mater*, 2011, **21**, 4137-4142.
176. K. J. Carroll, D. M. Hudgins, S. Spurgeon, K. M. Kemner, B. Mishra, M. I. Boyanov, L. W. Brown, M. L. Taheri and E. E. Carpenter, *Chem Mater*, 2010, **22**, 6291-6296.
177. J. Clayden, N. Greeves, S. Warren and P. Wothers, *Organic Chemistry*, First edn., Oxford University Press, 2008.

178. V. Petkov, P. D. Cozzoli, R. Buonsanti, R. Cingolani and Y. Ren, *J Amer Chem Soc*, 2009, **131**, 14264.
179. S. Chakrabarti, S. K. Mandal and S. Chaudhuri, *Nanotech*, 2005, **16**, 506-511.
180. G. V. M. Jacintho, A. G. Brolo, P. Corio, P. A. Z. Suarez and J. C. Rubim, *J Phys Chem C*, 2009, **113**, 7684-7691.
181. Y. Pu, X. Tao, X. Zeng, Y. Le and J. F. Chen, *J Magn Magn Mater*, 2010, **322**, 1985-1990.
182. B. Behdadfar, A. Kermanpur, H. Sagdeghi-Aliabadi, M. del Puerto Morales and M. Mozaffari, *J Magn Magn Mater*, 2012, **324**, 2211-2217.
183. Y. Pu, X. Tao, X. Zeng, Y. Le and J.-F. Chen, *J Magn Magn Mater*, 2010, **322**, 1985-1990.
184. G. Vaidyanathan, S. Sendhilnathan and R. Arulmurugan, *J Magn Magn Mater*, 2007, **313**, 293-299.
185. R. D. Shannon, *Acta Crystallogr*, 1976, **A32**, 751-767.
186. S. Calvin, E. E. Carpenter and V. G. Harris, *Appl Phys Lett*, 2012, **81**, 3828-3830.
187. H. Ehrhardt, S. J. Campbell and M. Hofmann, *J Alloy Comp*, 2002, **339**, 255-260.
188. N. N. Greenwood and A. Earnshaw, *Chemistry of the Elements*, Second edn., Butterworth-Heinemann Ltd., 1997.
189. F. J. Berry, C. Greaves, O. Helgason, J. McManus, H. M. Palmer and R. T. Williams, *J Solid State Chem*, 2000, **151**, 157-162.
190. M. Nohair, D. Aymes, P. Perriat and B. Gillot, *Vibrational Spectroscopy*, 1995, **9**, 181-190.
191. J. P. Singh, R. C. Srivastava, H. M. Agrawal and R. P. S. Kushwaha, *Hyperfine Interact*, 2008, **183**, 221-228.
192. L. H. Singh, R. Govindaraj, G. Amarendra and C. S. Sundar, 57th DAE Solid State Physics Symposium, Bombay, INDIA, 2012.
193. Y. Ahn, E. J. Choi, S. Kim, D. H. An, K. U. Kang, B. G. Lee, K. S. Baek and H. N. Oak, *J Korean Phys Soc*, 2002, **41**, 123-128.
194. K. K. P. Srivastava, *J Phys Condens Mat*, 2003, **15**, 549-560.

Appendix 1.

A1.1. Microreactor Designs and Details.

Chip Design 3021(T-mixer reactor with three inlets and one outlet)

Channel Width = 300 µm

Channel Depth = 60 µm

Reactor Volume = 1.0 µl

Quench Volume = 1.5 µl

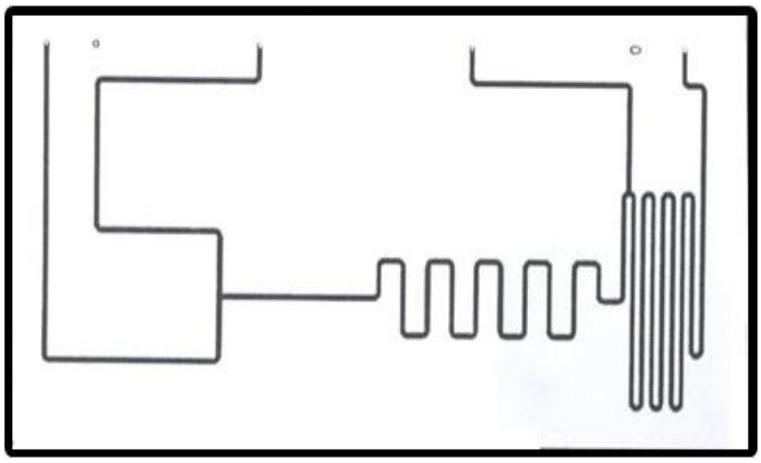

Chip Design 3022 (T-mixer reactor with three inlets and one outlet)

Channel Width = 300 µm

Channel Depth = 60 µm

Reactor Volume = 5.0 µl

Quench Volume = 1.5 µl

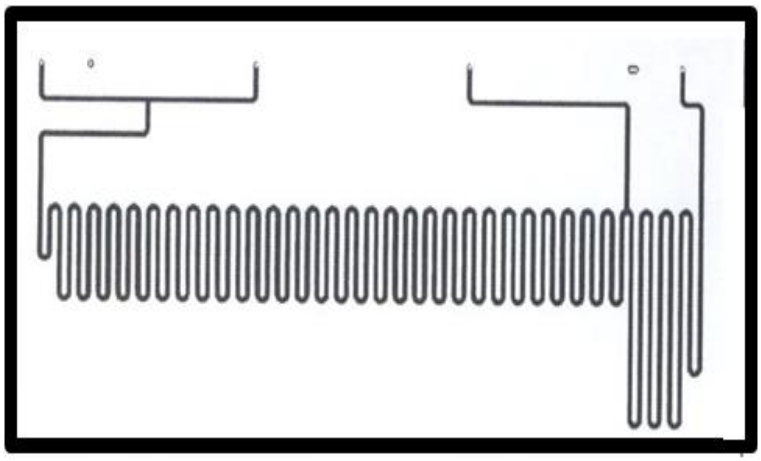

Chip Design 3023 (T-mixer reactor with three inlets and one outlet)

Channel Width = 300 µm

Channel Depth = 60 µm

Reactor Volume = 10.0 µl

Quench Volume = 1.5 µl

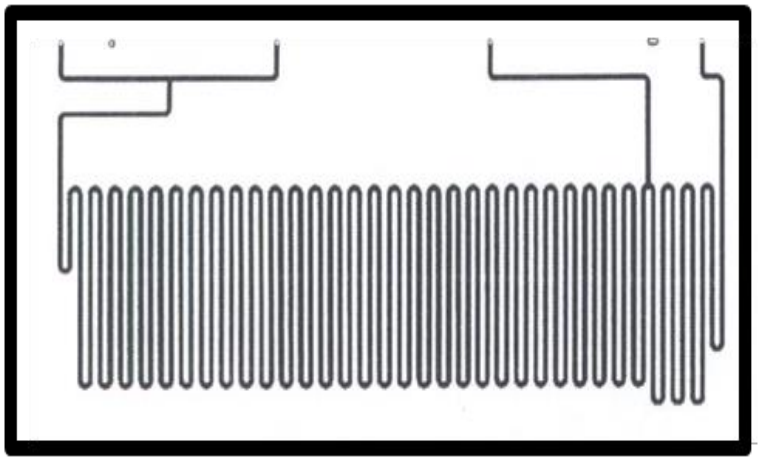

Chip Design 3024

T-mixer reactor with four inlets and one outlet

Channel Width = 300 µm

Channel Depth = 60 µm

Reactor Volume = 10 µl

Quench Volume = 1.5 µl

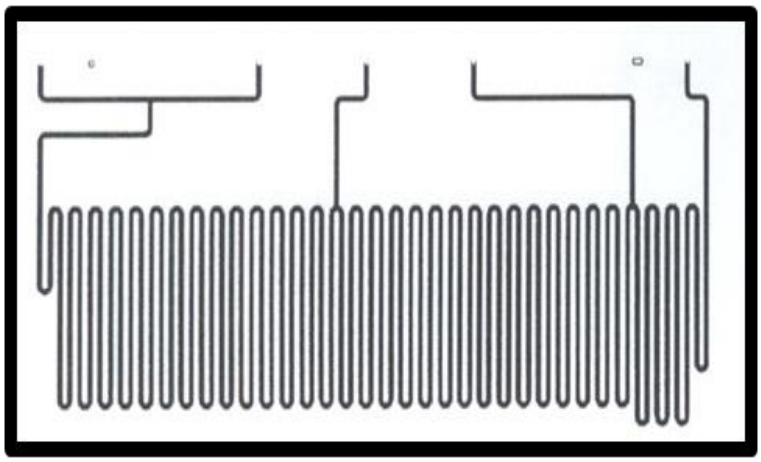

Chip Design 3025

T-mixer reactor with five inlets and one outlet

Channel Width = 300 µm

Channel Depth = 60 µm

Reactor Volume = 10 µl

Quench Volume = 1.5 µl

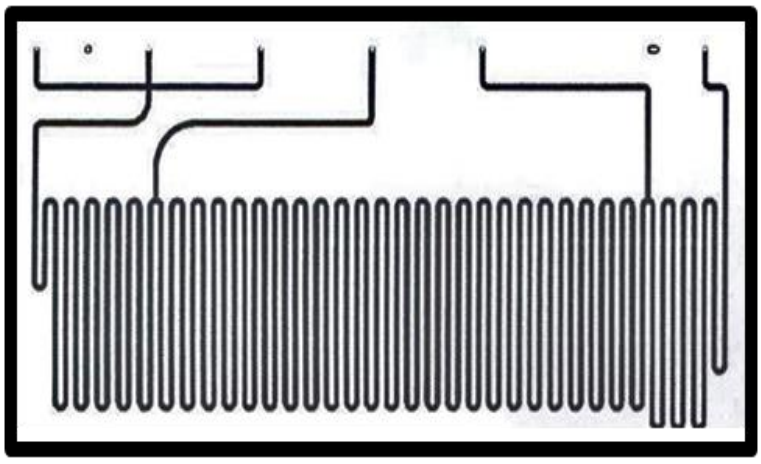

Appendix 2.

TEM images of nanoparticles synthesised under various reaction conditions, included in the critical evaluation of the TEM images presented in **Chapter 4**. Although they are not clear enough to allow for accurate determination of their particle size, the nanoparticles can be seen to be largely spherical nature, although highly agglomerated due to the lack of a surface coating. The nanoparticles were synthesised using different reagent flow rates, temperatures and concentrations, these are detailed in the caption below each set of pictures.

A2.1. Nanoparticles originally produced using the continuous flow focussed technique and in batch.

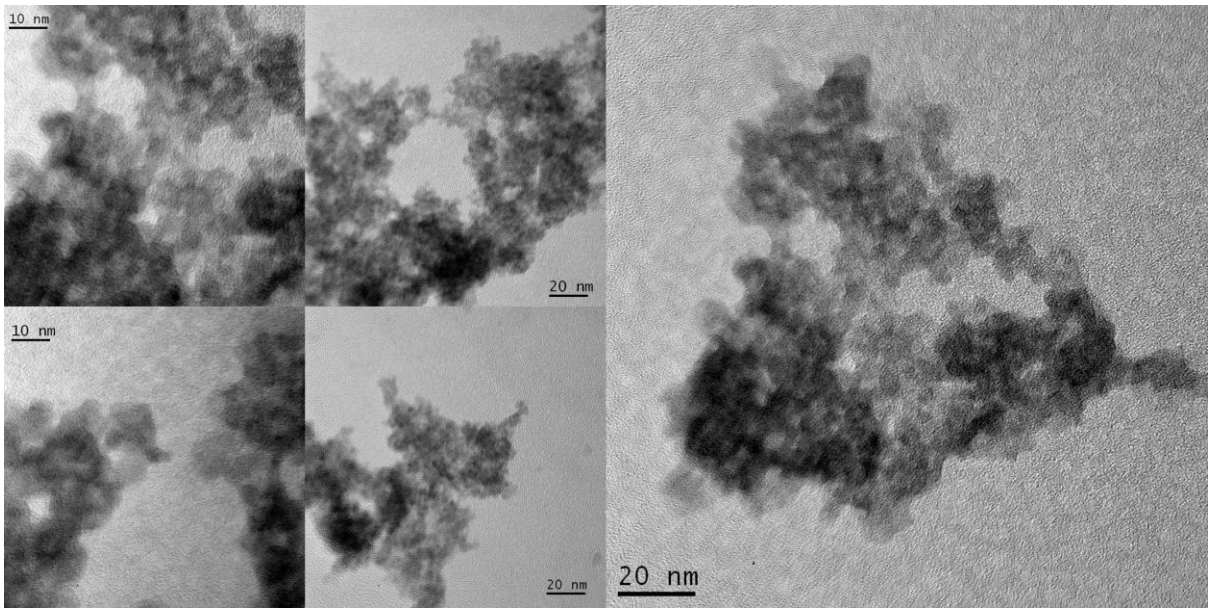

Nanoparticles prepared in the microreactor at flow rates of 1000 ul hr^{-1} from the reaction of an ISPS ($FeCl_2$ = 0.01 M, and $FeCl_3$ = 0.02 M) and base (NaOH = 1.00M), at a temperature of 25.5 °C.

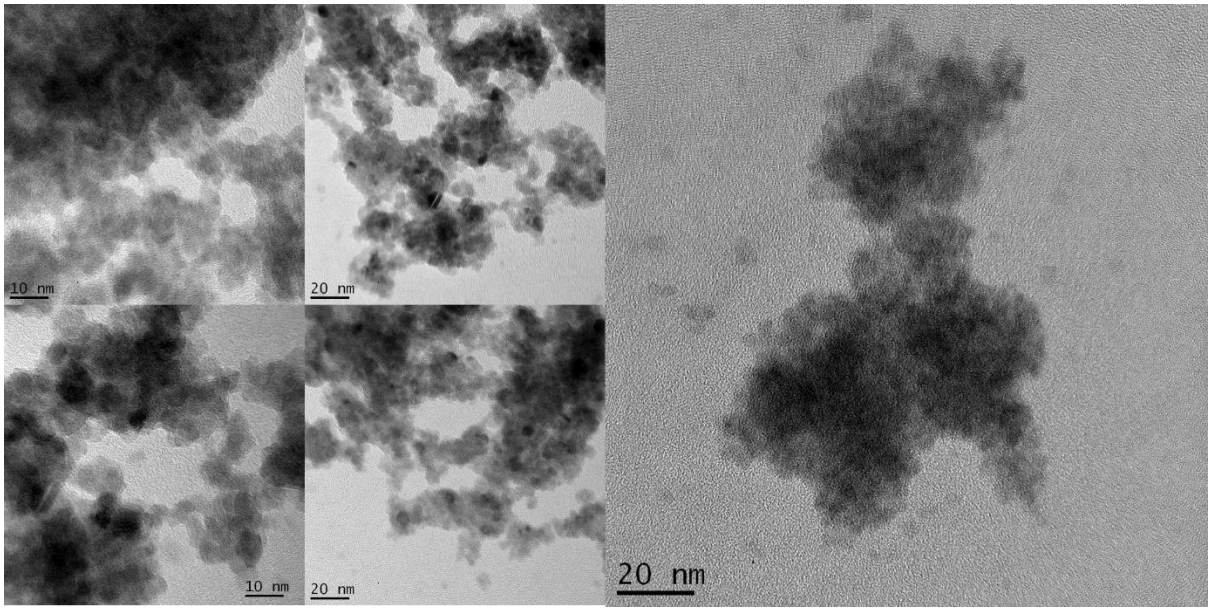

Nanoparticles prepared in the batch from the reaction of an ISPS ($FeCl_2$ = 0.01 M, and $FeCl_3$ = 0.02 M) and base (NaOH = 1.00M), at a temperature of 25.5 °C.

A2.2. IONs Synthesised at Various Flow Rates using the 2D Continuous Flow Focussed

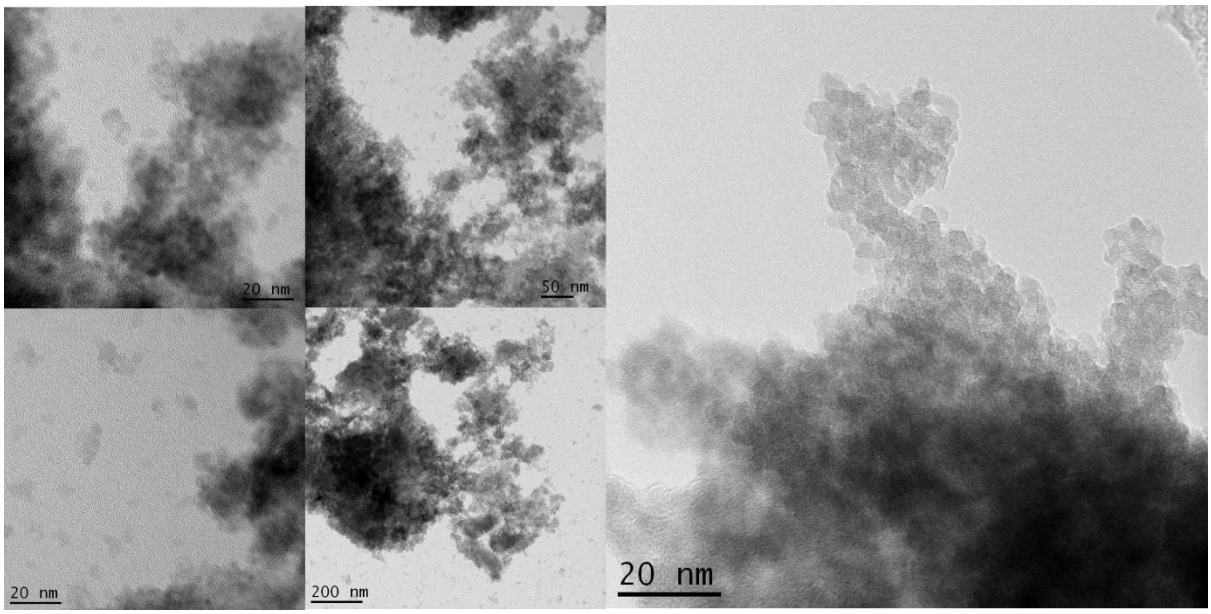

Nanoparticles prepared in the microreactor at flow rates of 750 ul hr^{-1} from the reaction of an ISPS ($FeCl_2$ = 0.01 M, and $FeCl_3$ = 0.02 M) and base (NaOH = 1.00M), at a temperature of 25.5 °C.

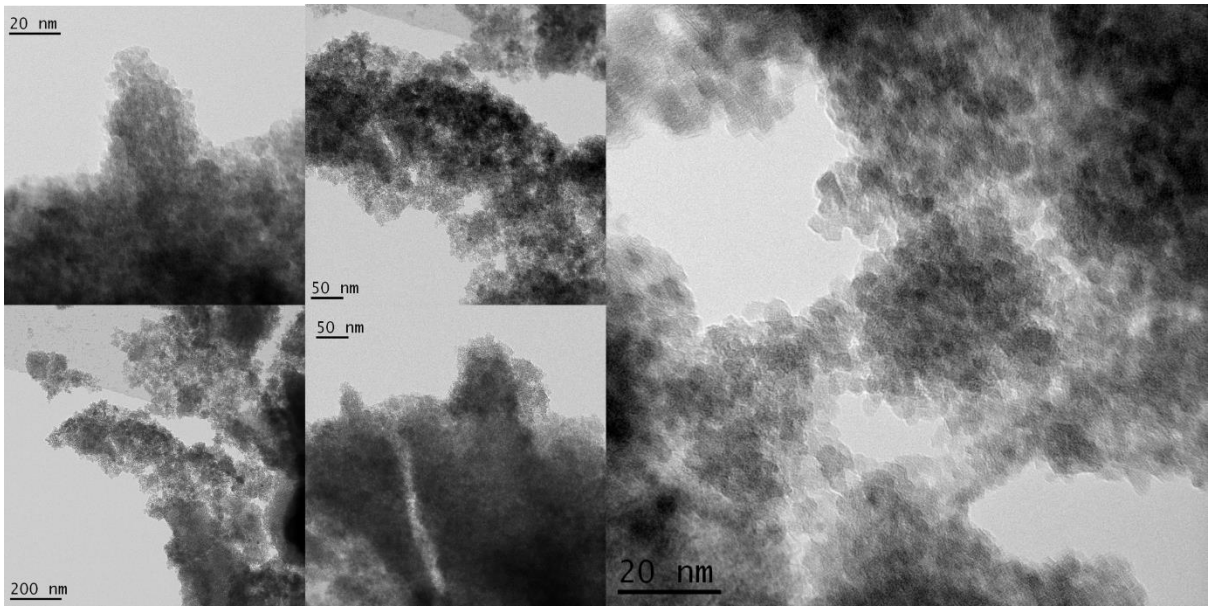

Nanoparticles prepared in the microreactor at flow rates of 1250 ul hr^{-1} from the reaction of an ISPS ($FeCl_2$ = 0.01 M, and $FeCl_3$ = 0.02 M) and base (NaOH = 1.00M), at a temperature of 25.5 °C.

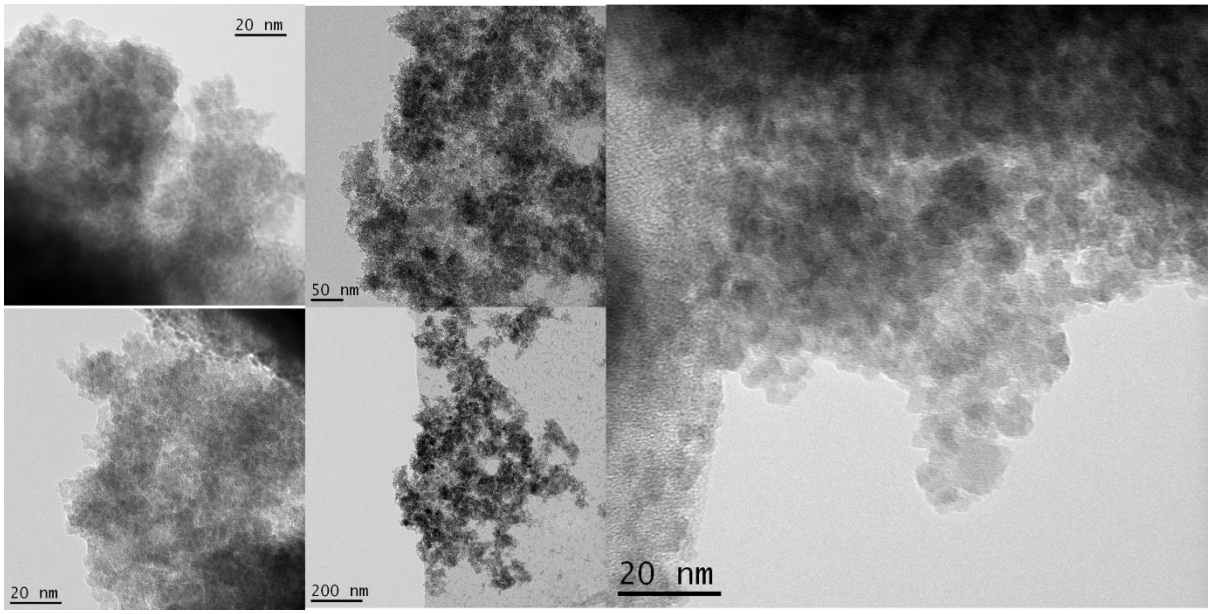

Nanoparticles prepared in the microreactor at flow rates of 1500 ul hr^{-1} from the reaction of an ISPS ($FeCl_2$ = 0.01 M, and $FeCl_3$ = 0.02 M) and base (NaOH = 1.00M), at a temperature of 25.5 °C.

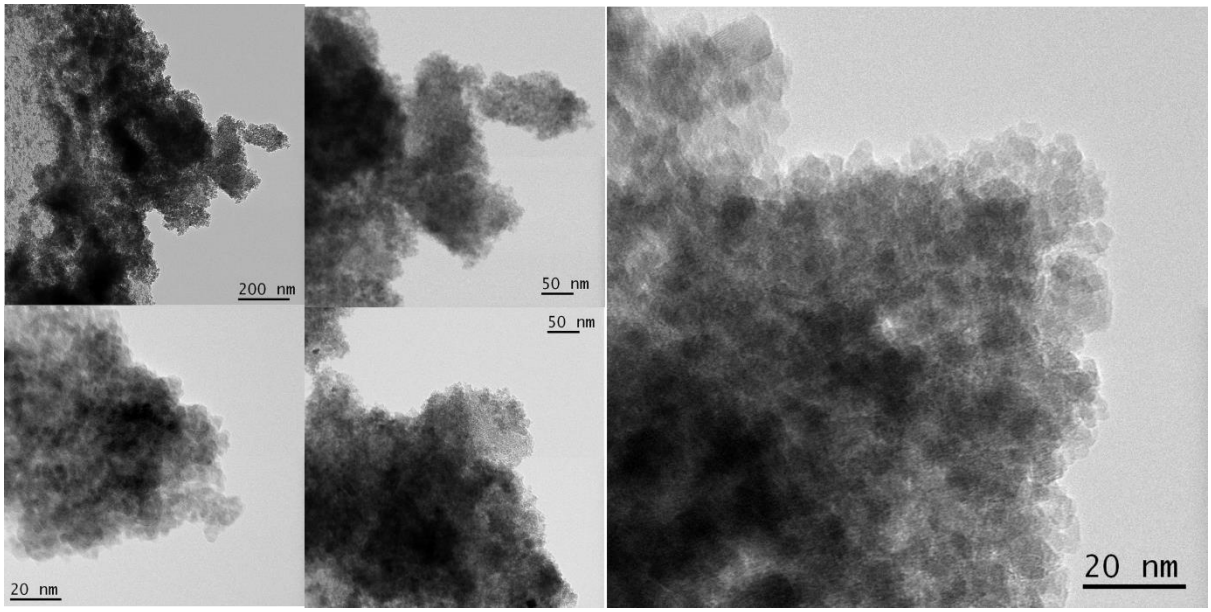

Nanoparticles prepared in the microreactor at flow rates of 2000 ul hr^{-1} from the reaction of an ISPS ($FeCl_2$ = 0.01 M, and $FeCl_3$ = 0.02 M) and base (NaOH = 1.00M), at a temperature of 25.5 °C.

A2.3. IONs Synthesised at Various Temperatures using the 2D Continuous Flow Focussed Technique

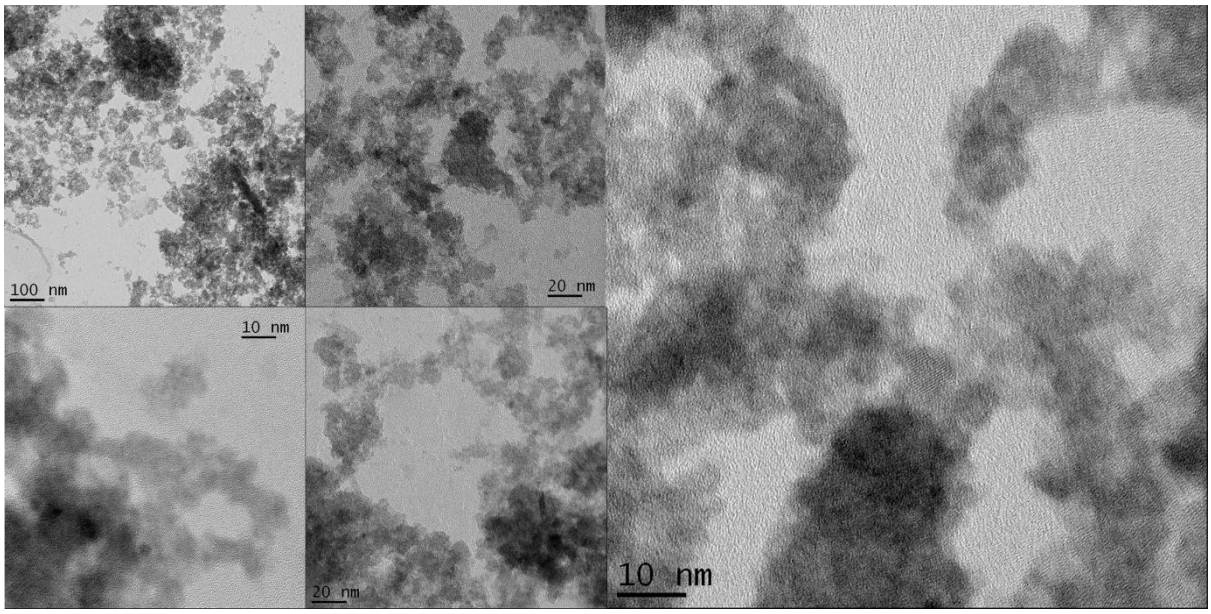

Nanoparticles prepared in the microreactor at flow rates of 2000 ul hr^{-1} from the reaction of an ISPS ($FeCl_2$ = 0.01 M, and $FeCl_3$ = 0.02 M) and base (NaOH = 1.00M), at a temperature of 30.0 °C.

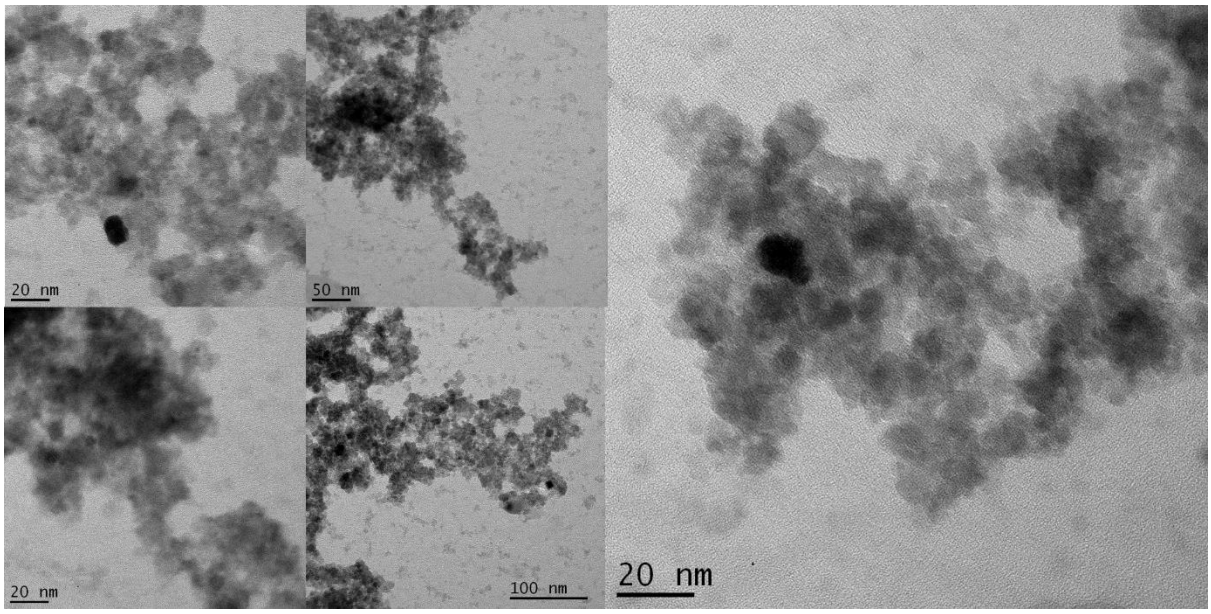

Nanoparticles prepared in the microreactor at flow rates of 2000 ul hr^{-1} from the reaction of an ISPS ($FeCl_2$ = 0.01 M, and $FeCl_3$ = 0.02 M) and base (NaOH = 1.00M), at a temperature of 35.5 °C.

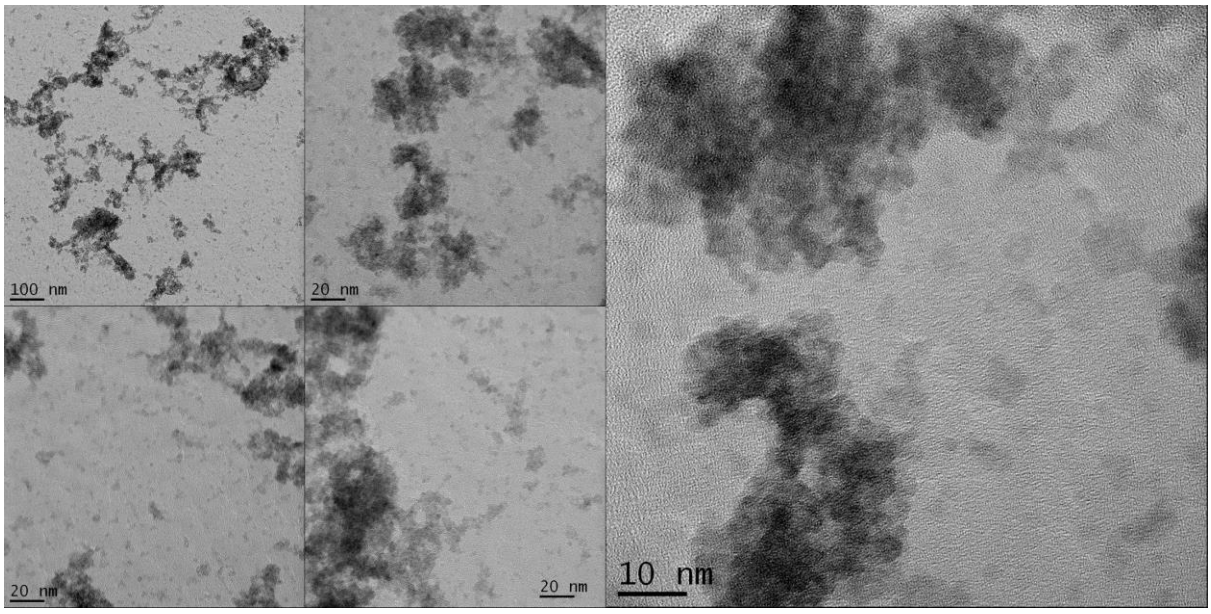

Nanoparticles prepared in the microreactor at flow rates of 2000 ul hr^{-1} from the reaction of an ISPS ($FeCl_2$ = 0.01 M, and $FeCl_3$ = 0.02 M) and base (NaOH = 1.00M), at a temperature of 40.0 °C.

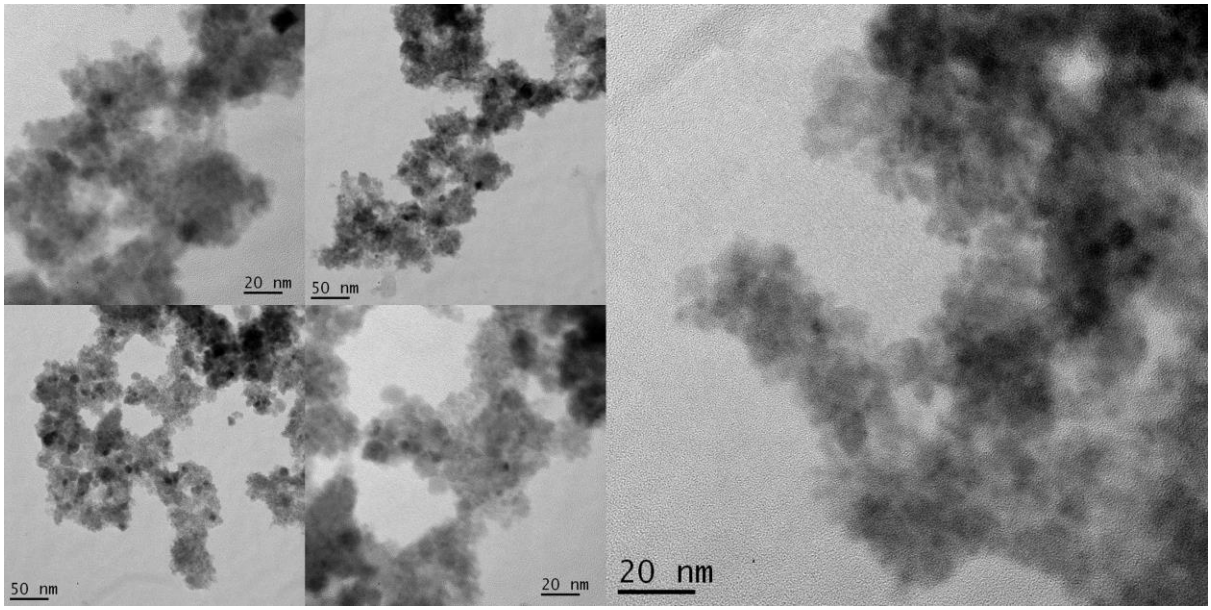

Nanoparticles prepared in the microreactor at flow rates of 2000 ul hr^{-1} from the reaction of an ISPS ($FeCl_2$ = 0.01 M, and $FeCl_3$ = 0.02 M) and base (NaOH = 1.00M), at a temperature of 45.5°C.

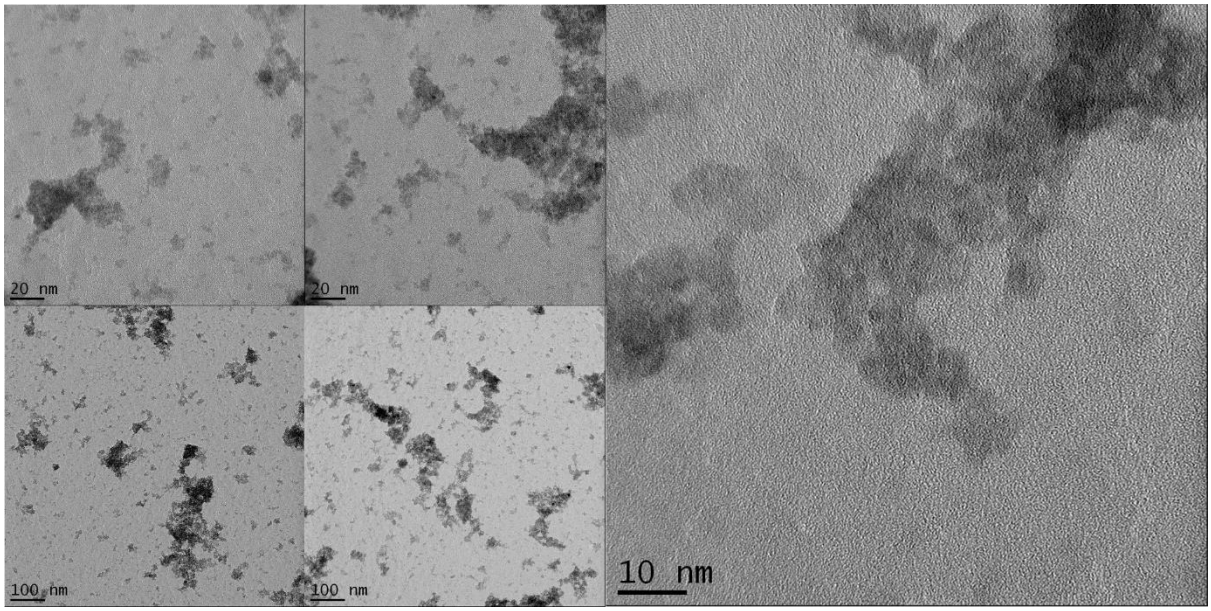

Nanoparticles prepared in the microreactor at flow rates of 2000 ul hr^{-1} from the reaction of an ISPS ($FeCl_2$ = 0.01 M, and $FeCl_3$ = 0.02 M) and base (NaOH = 1.00M), at a temperature of 50.0 °C.

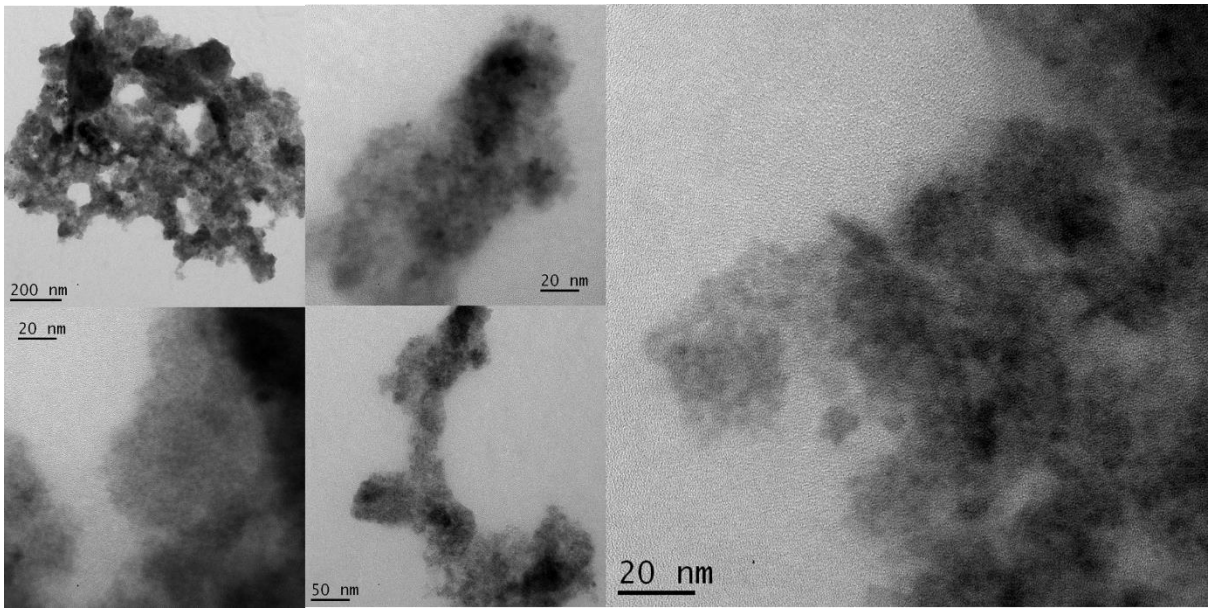

Nanoparticles prepared in the microreactor at flow rates of 2000 ul hr^{-1} from the reaction of an ISPS ($FeCl_2$ = 0.01 M, and $FeCl_3$ = 0.02 M) and base (NaOH = 1.00M), at a temperature of 55.5°C.

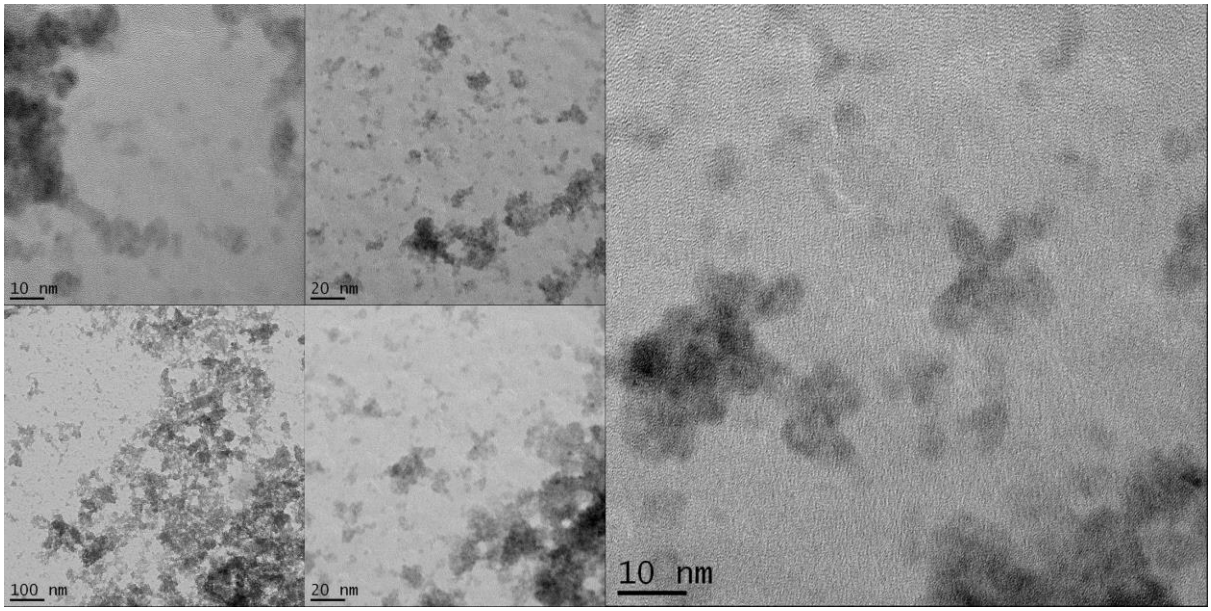

Nanoparticles prepared in the microreactor at flow rates of 2000 ul hr^{-1} from the reaction of an ISPS ($FeCl_2$ = 0.01 M, and $FeCl_3$ = 0.02 M) and base (NaOH = 1.00M), at a temperature of 60 °C.

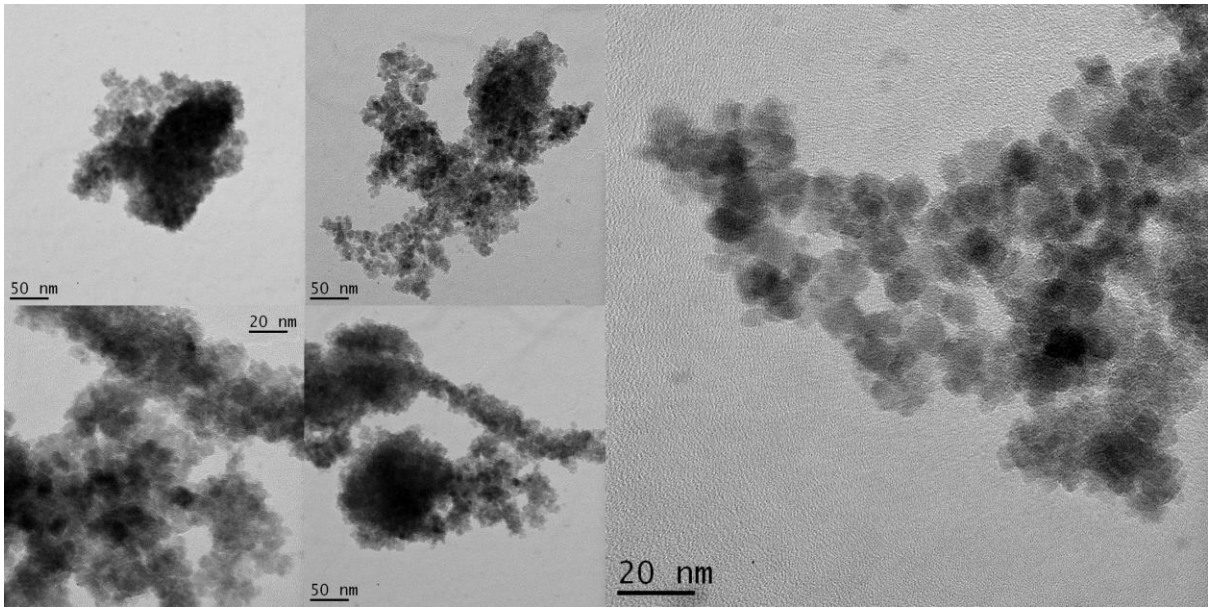

Nanoparticles prepared in the microreactor at flow rates of 2000 ul hr^{-1} from the reaction of an ISPS ($FeCl_2$ = 0.01 M, and $FeCl_3$ = 0.02 M) and base (NaOH = 1.00M), at a temperature of 65.5 °C.

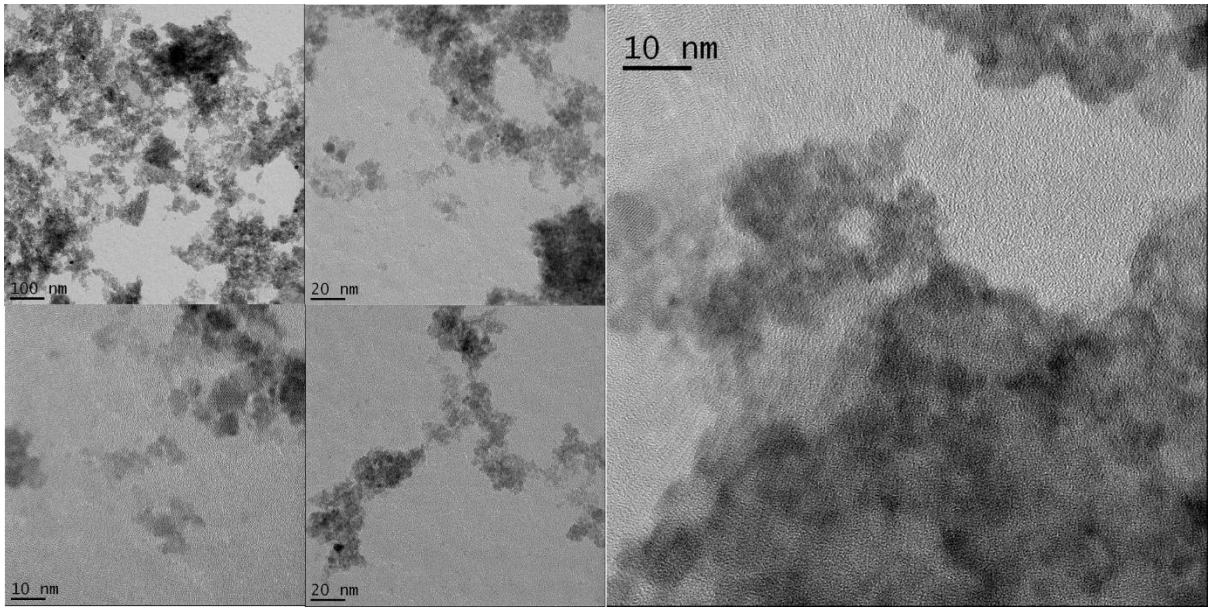

Nanoparticles prepared in the microreactor at flow rates of 2000 ul hr^{-1} from the reaction of an ISPS ($FeCl_2$ = 0.01 M, and $FeCl_3$ = 0.02 M) and base (NaOH = 1.00M), at a temperature of 70 °C.

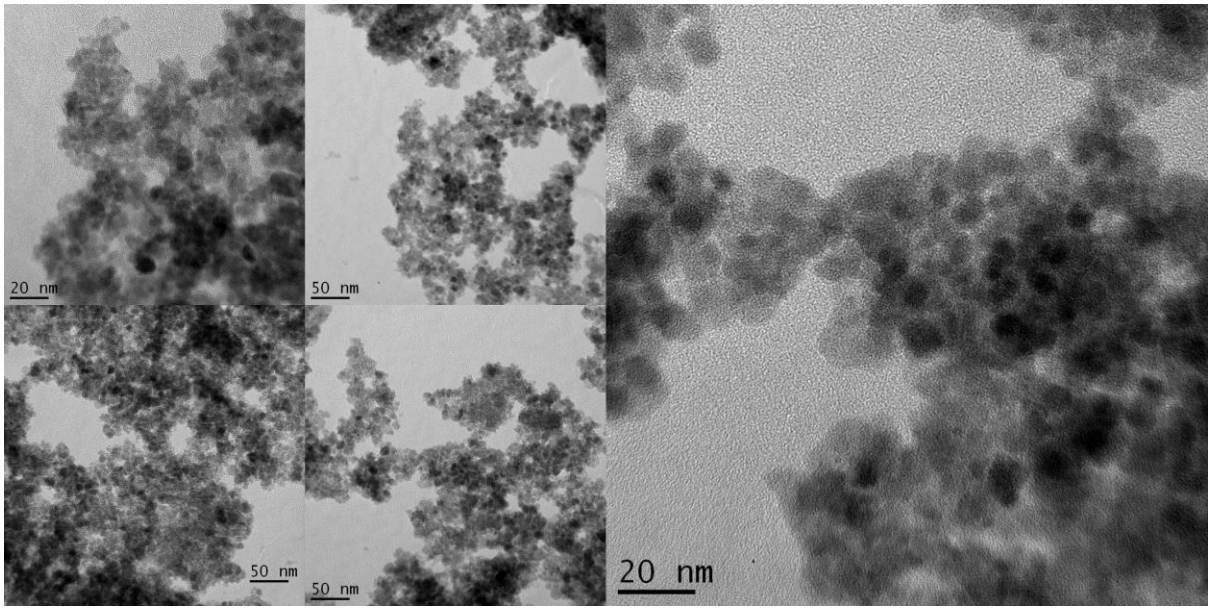

Nanoparticles prepared in the microreactor at flow rates of 2000 ul hr^{-1} from the reaction of an ISPS ($FeCl_2$ = 0.01 M, and $FeCl_3$ = 0.02 M) and base (NaOH = 1.00M), at a temperature of 75.5 °C.

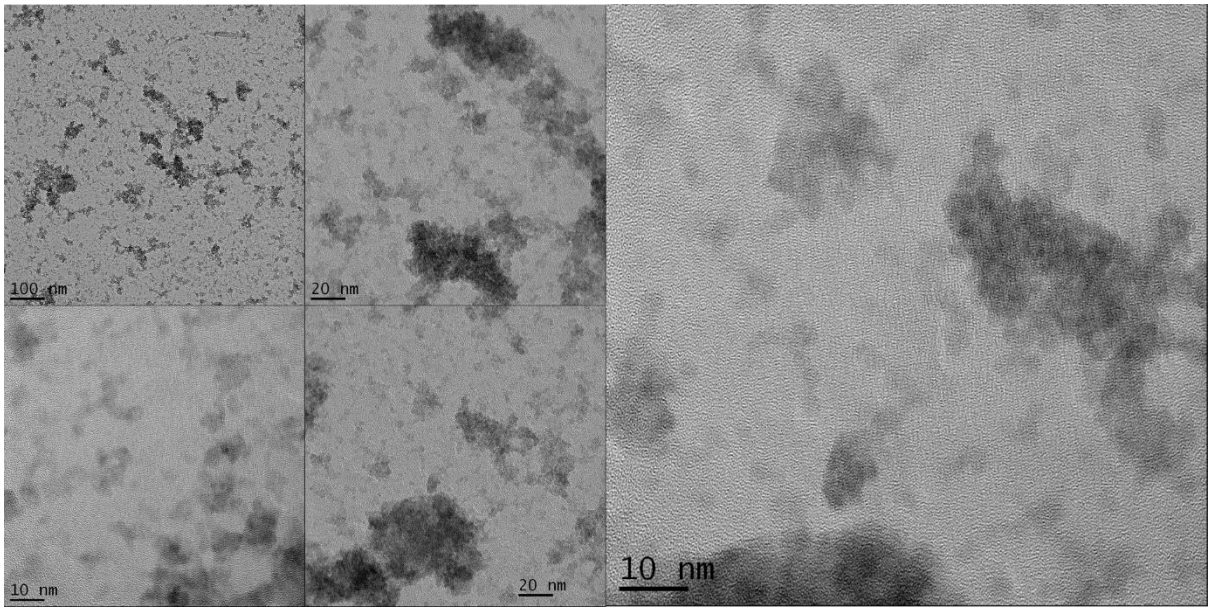

Nanoparticles prepared in the microreactor at flow rates of 2000 ul hr^{-1} from the reaction of an ISPS ($FeCl_2$ = 0.01 M, and $FeCl_3$ = 0.02 M) and base (NaOH = 1.00M), at a temperature of 80.0 °C.

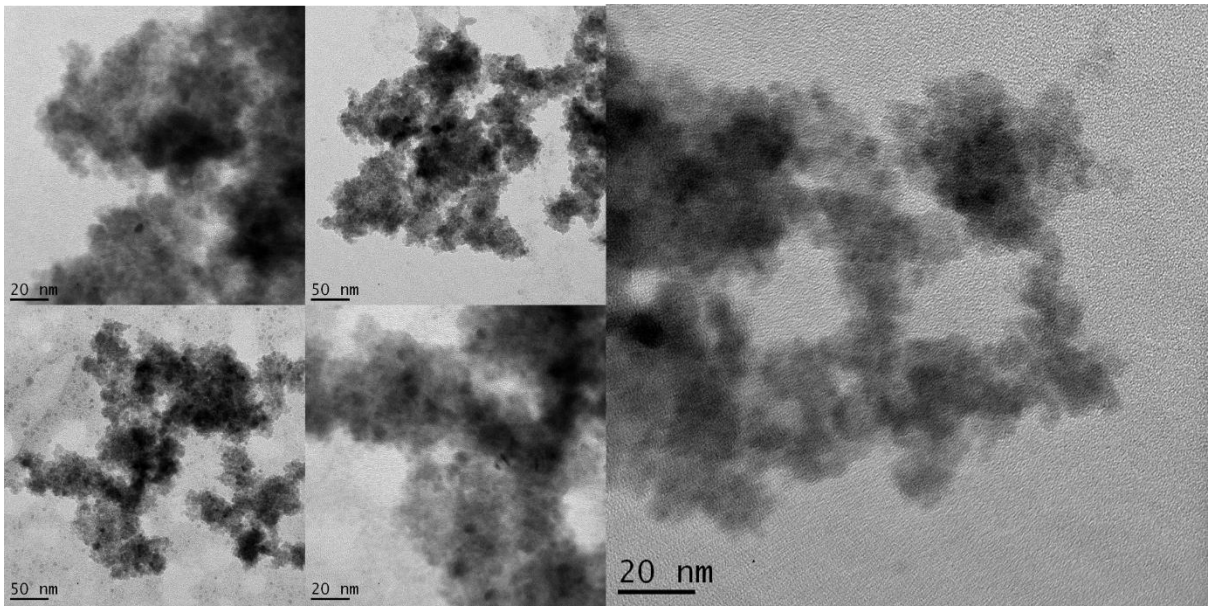

Nanoparticles prepared in the microreactor at flow rates of 2000 ul hr^{-1} from the reaction of an ISPS ($FeCl_2$ = 0.01 M, and $FeCl_3$ = 0.02 M) and base (NaOH = 1.00M), at a temperature of 85.5 °C.

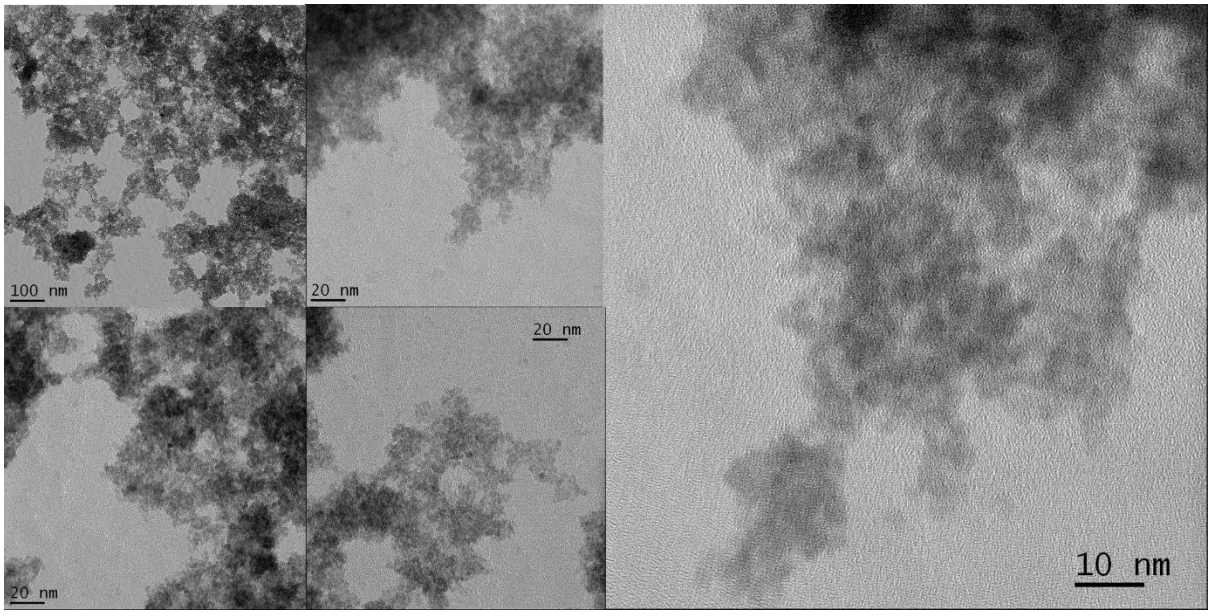

Nanoparticles prepared in the microreactor at flow rates of 2000 ul hr^{-1} from the reaction of an ISPS ($FeCl_2$ = 0.01 M, and $FeCl_3$ = 0.02 M) and base (NaOH = 1.00M), at a temperature of 90 °C.

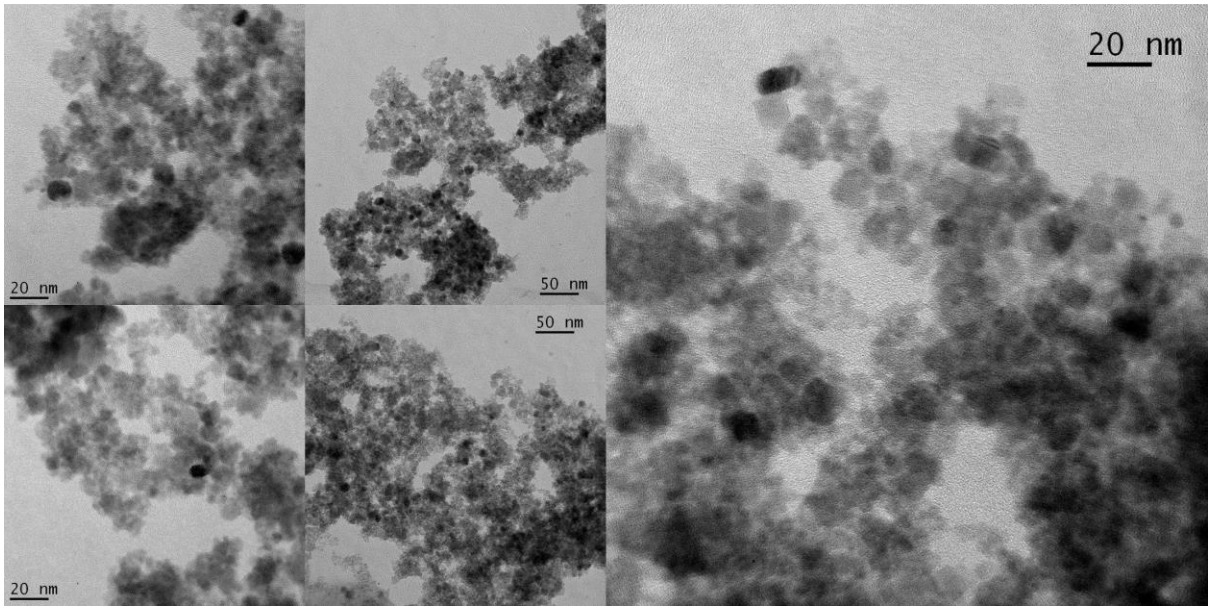

Nanoparticles prepared in the microreactor at flow rates of 2000 ul hr^{-1} from the reaction of an ISPS ($FeCl_2$ = 0.01 M, and $FeCl_3$ = 0.02 M) and base (NaOH = 1.00M), at a temperature of 95.5 °C.

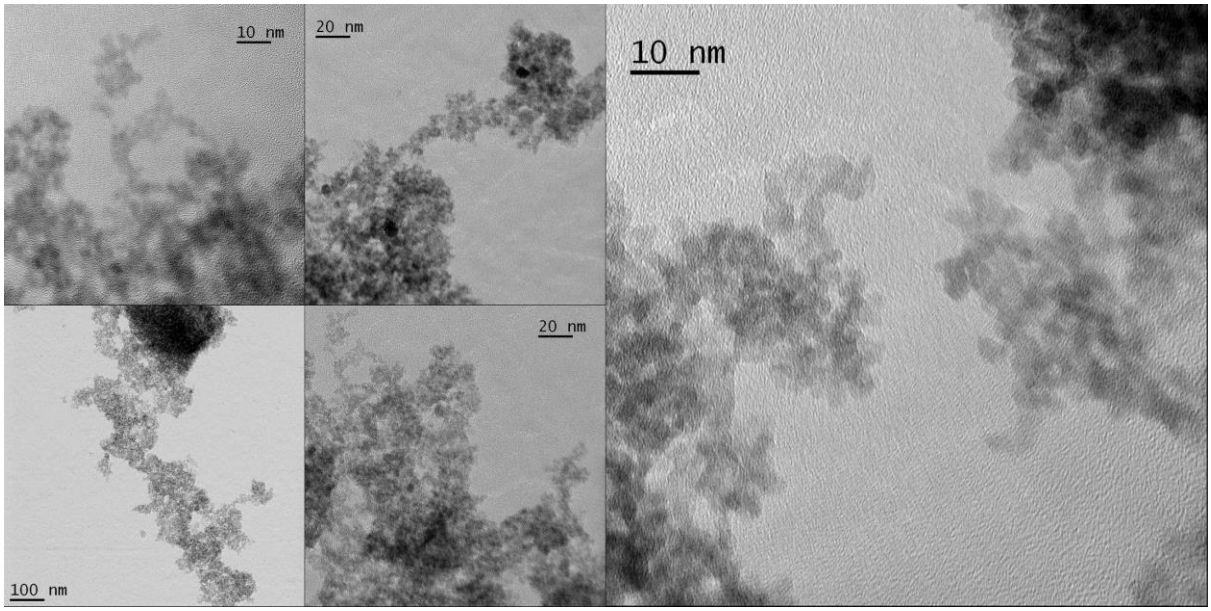

Nanoparticles prepared in the microreactor at flow rates of 2000 ul hr^{-1} from the reaction of an ISPS ($FeCl_2$ = 0.01 M, and $FeCl_3$ = 0.02 M) and base (NaOH = 1.00M), at a temperature of 100 °C.

A2.4. IONs Synthesised at Various Concentrations of Iron Salts within the ISPS using the 2D Continuous Flow Focussed

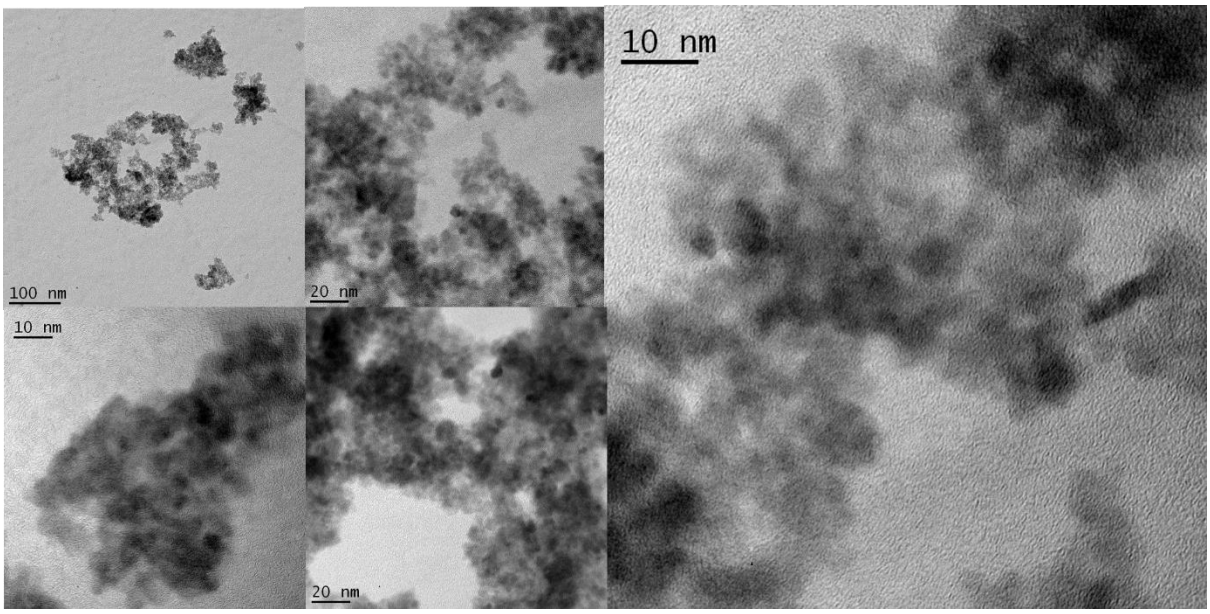

Nanoparticles prepared in the microreactor at flow rates of 2000 ul hr^{-1} from the reaction of an ISPS ($FeCl_2$ = 0.012 M, and $FeCl_3$ = 0.024 M) and base (NaOH = 1.00M), at a temperature of 25.5°C.

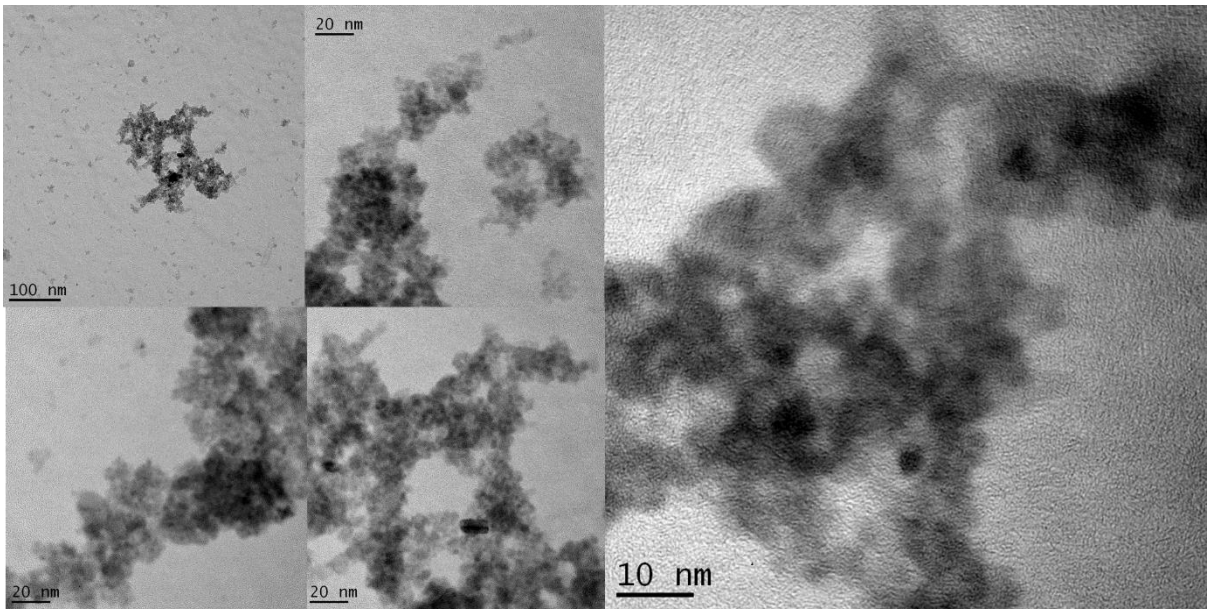

Nanoparticles prepared in the microreactor at flow rates of 2000 ul hr^{-1} from the reaction of an ISPS ($FeCl_2$ = 0.014 M, and $FeCl_3$ = 0.028 M) and base (NaOH = 1.00M), at a temperature of 25.5°C.

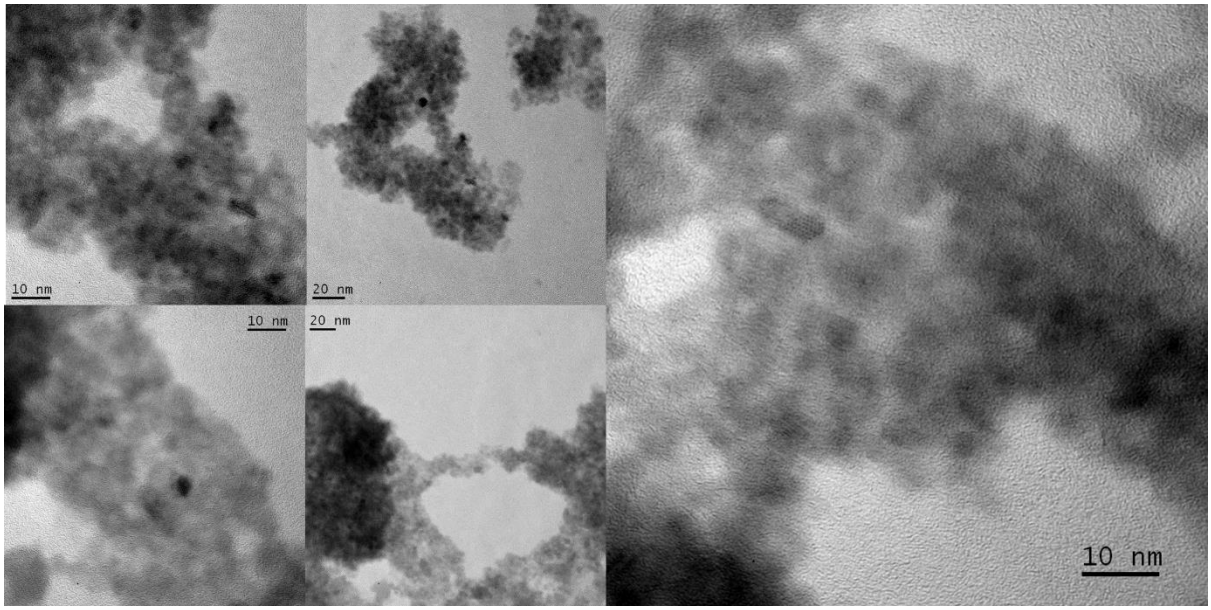

Nanoparticles prepared in the microreactor at flow rates of 2000 ul hr^{-1} from the reaction of an ISPS ($FeCl_2$ = 0.016 M, and $FeCl_3$ = 0.032 M) and base (NaOH = 1.00M), at a temperature of 25.5°C.

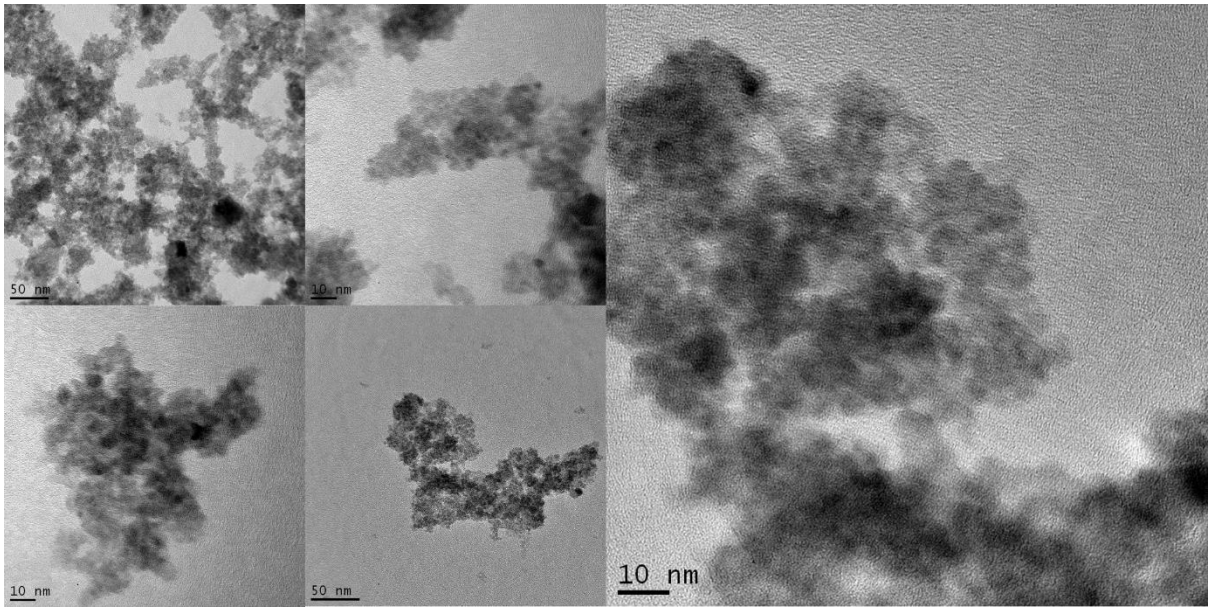

Nanoparticles prepared in the microreactor at flow rates of 2000 ul hr^{-1} from the reaction of an ISPS ($FeCl_2$ = 0.018 M, and $FeCl_3$ = 0.036 M) and base (NaOH = 1.00M), at a temperature of 25.5°C.

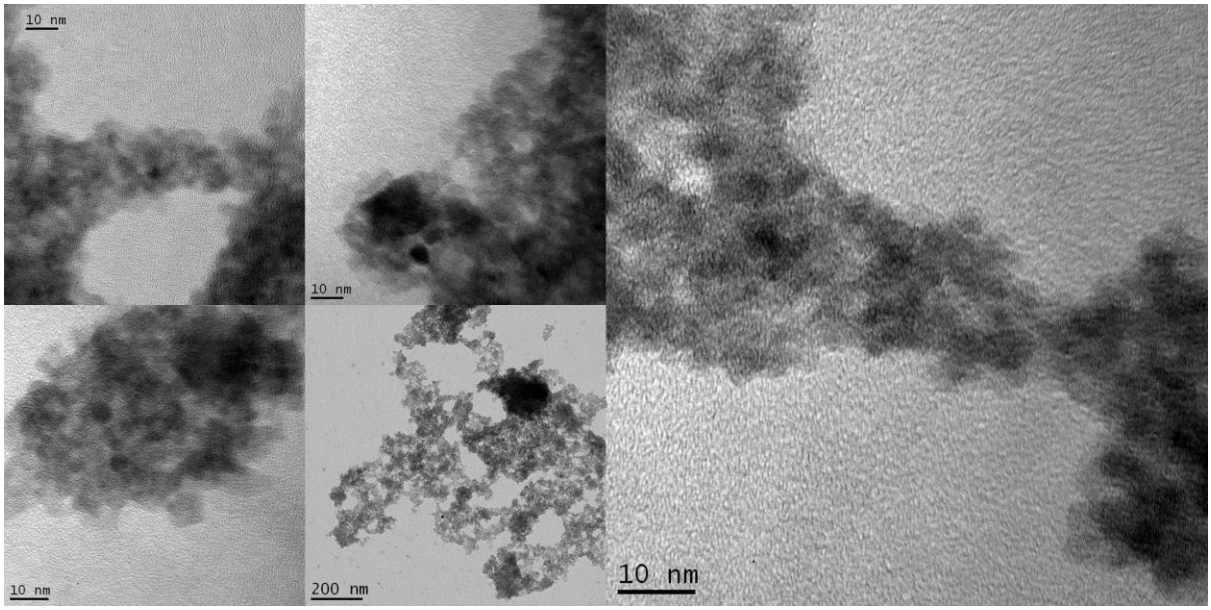

Nanoparticles prepared in the microreactor at flow rates of 2000 ul hr^{-1} from the reaction of an ISPS ($FeCl_2$ = 0.02 M, and $FeCl_3$ = 0.04 M) and base (NaOH = 1.00M), at a temperature of 25.5°C.

Appendix 3.

PXRD patterns of the (440) peaks used to construct the calibration curve used in this work. Both the raw data and the final fitted peaks are shown in each diagram.

Graphs showing the attempted deconvolution of the (440) reflections for calibrants made from specific weight percentages of nanoparticular γ-Fe_2O_3 and bulk Fe_3O_4. In some graphs the deconvolution process can be seen to have worked less well, showing either peaks which have not aligned properly but are of similar intensity. This is particularly obvious for those peaks recorded for calibrants with low weight percentages of γ-Fe_2O_3, and is likely a contributing factor to why such large detection limits are achieved for the technique. The technique can be seen to work far more effectively for calibrants with similar percentages of Fe_3O_4 and γ-Fe_2O_3.

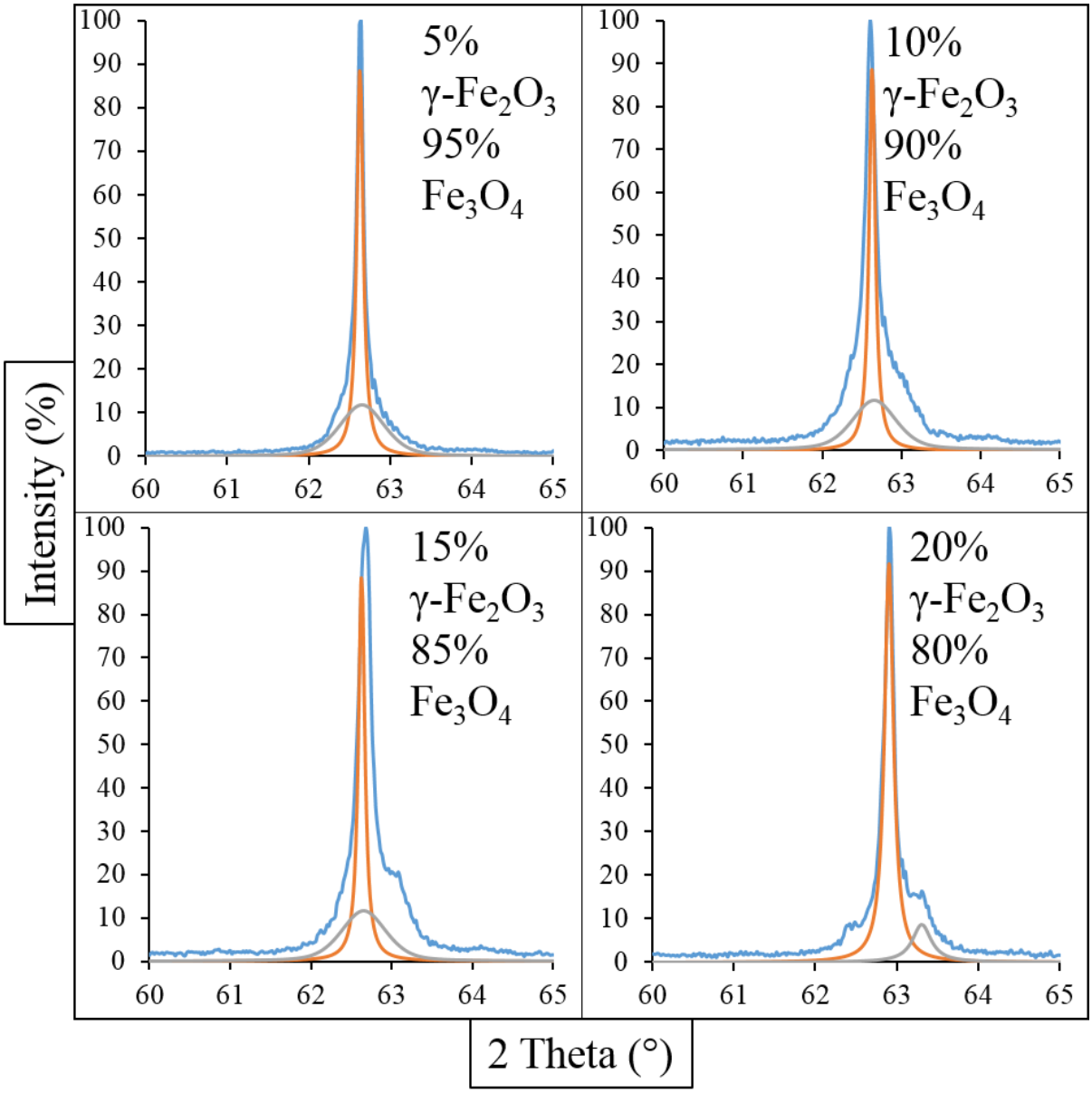

Deconvolution graphs of the (440) peaks taken from the PXRD patterns of the calibrants produced by the intimate grinding of different weight percentages of γ-Fe_2O_3 (5, 10, 15, 20%) and Fe_3O_4 (95, 90,85, 80%). The deconvolution process can be seen to have worked less well for the 5, 10 and 15% γ-Fe_2O_3, the deconvoluted peaks can be seen to be very close in position and the γ-Fe_2O_3 peak (grey) appears to be fitting the peak width rather than the height of any possible second peak. The position of the Fe_3O_4 peak appears to be fitting the height of the peak well at the Fe_3O_4 position, however this appears to be slightly out of position for the 15% γ-Fe_2O_3 85% Fe_3O_4 deconvolution.

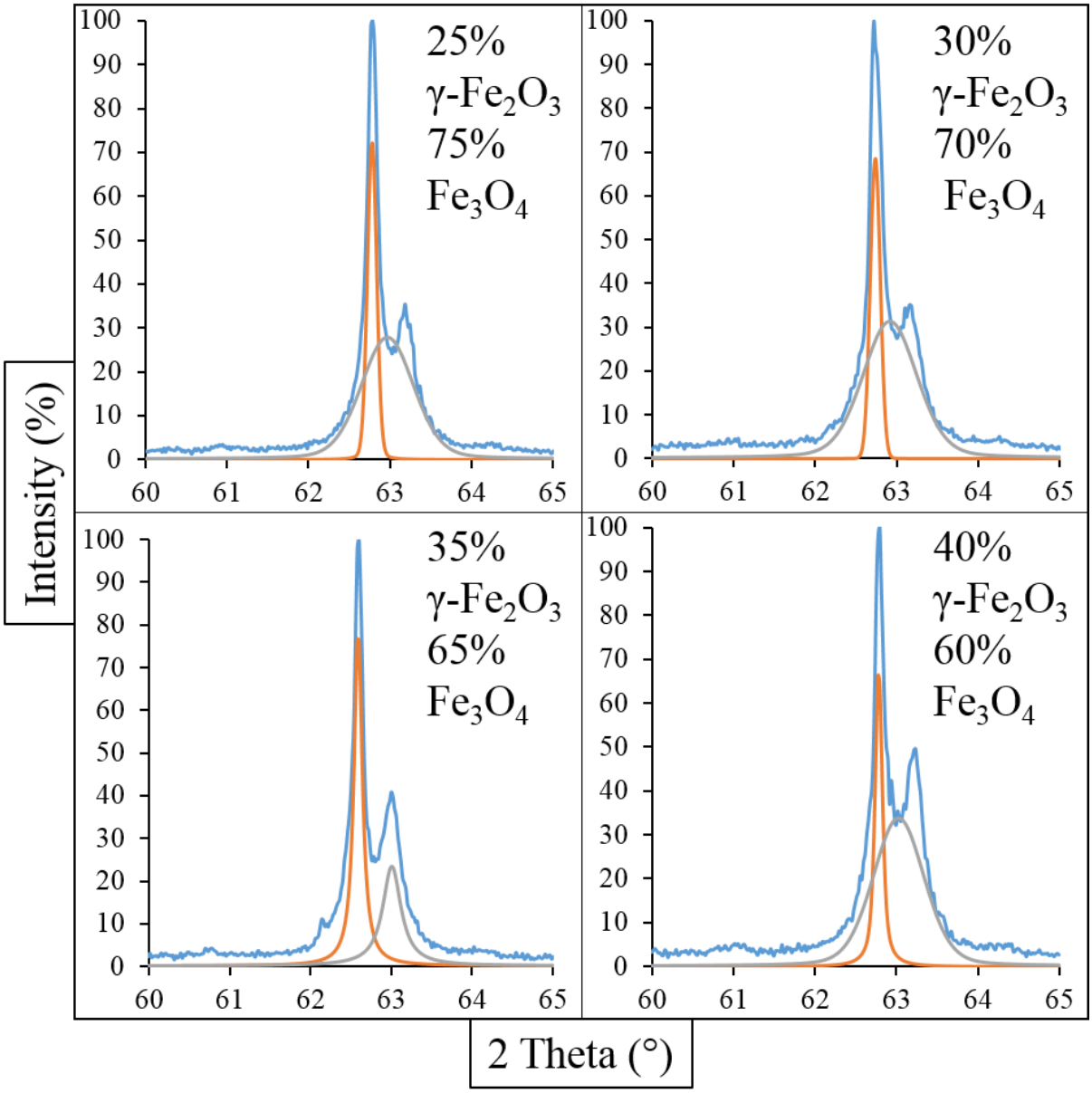

As with the previous deconvolutions the deconvolutions of the calibrants containing γ-Fe_2O_3 (25, 30 and 40%) and Fe_3O_4 (75, 70, and 60%) the γ-Fe_2O_3 peak can be seen to be fitting the width rather than the height of the second peak, however, the heights of the second peaks can also clearly be seen in the PXRD patterns.

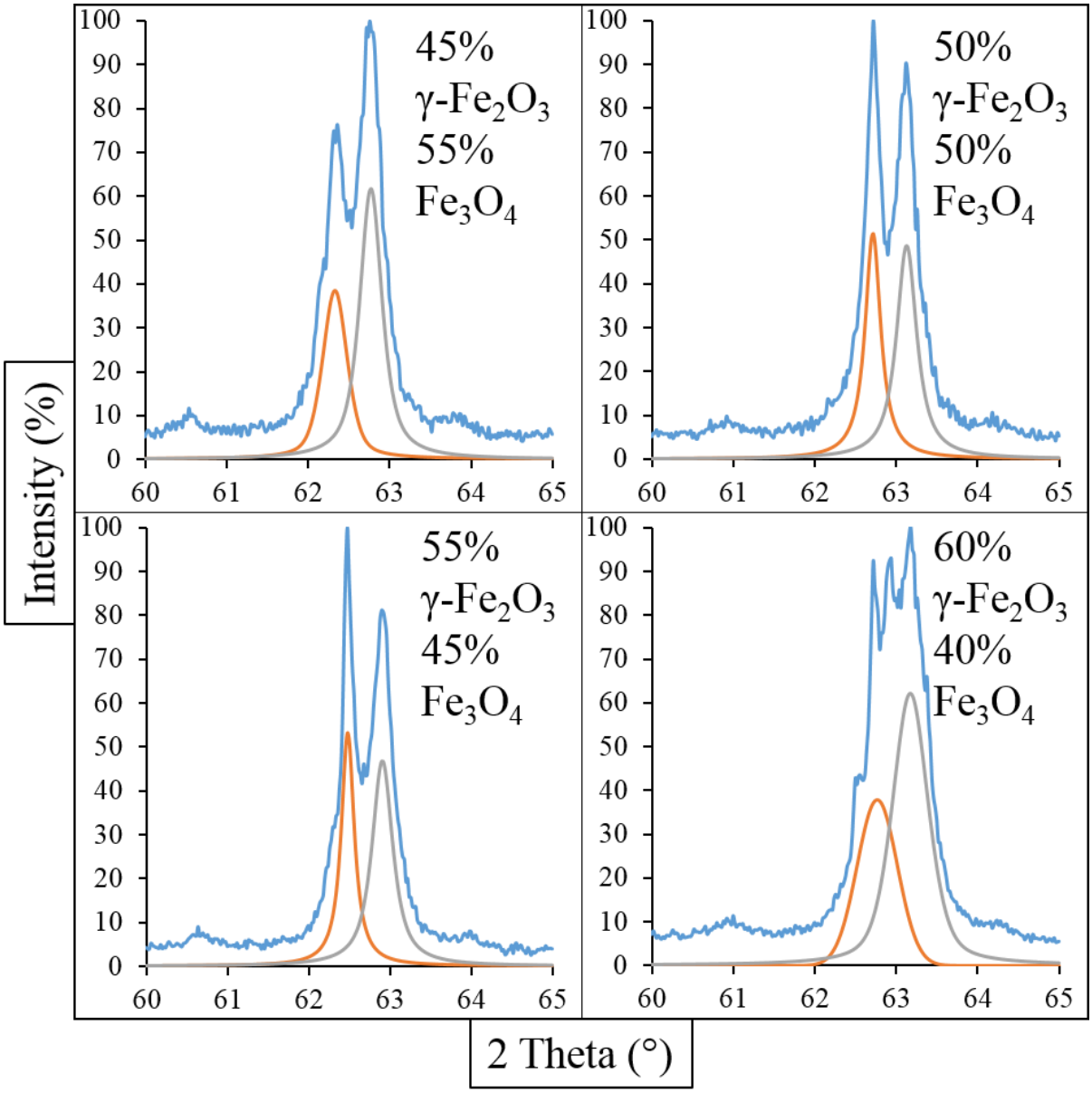

The deconvolutions for the middle of the calibration graph, from the calibrants containing γ-Fe_2O_3 (45, 50, 55, and 60%) and Fe_3O_4 (55, 50, 45, and 40%) can be seen to have deconvoluted much better than those containing lower amounts of γ-Fe_2O_3. This may be due to both peaks being much more prominent and similar in intensity, as well as contributing more evenly to the overall peak width, allowing for XFit to fit the two symmetric peaks belonging to each phase better.

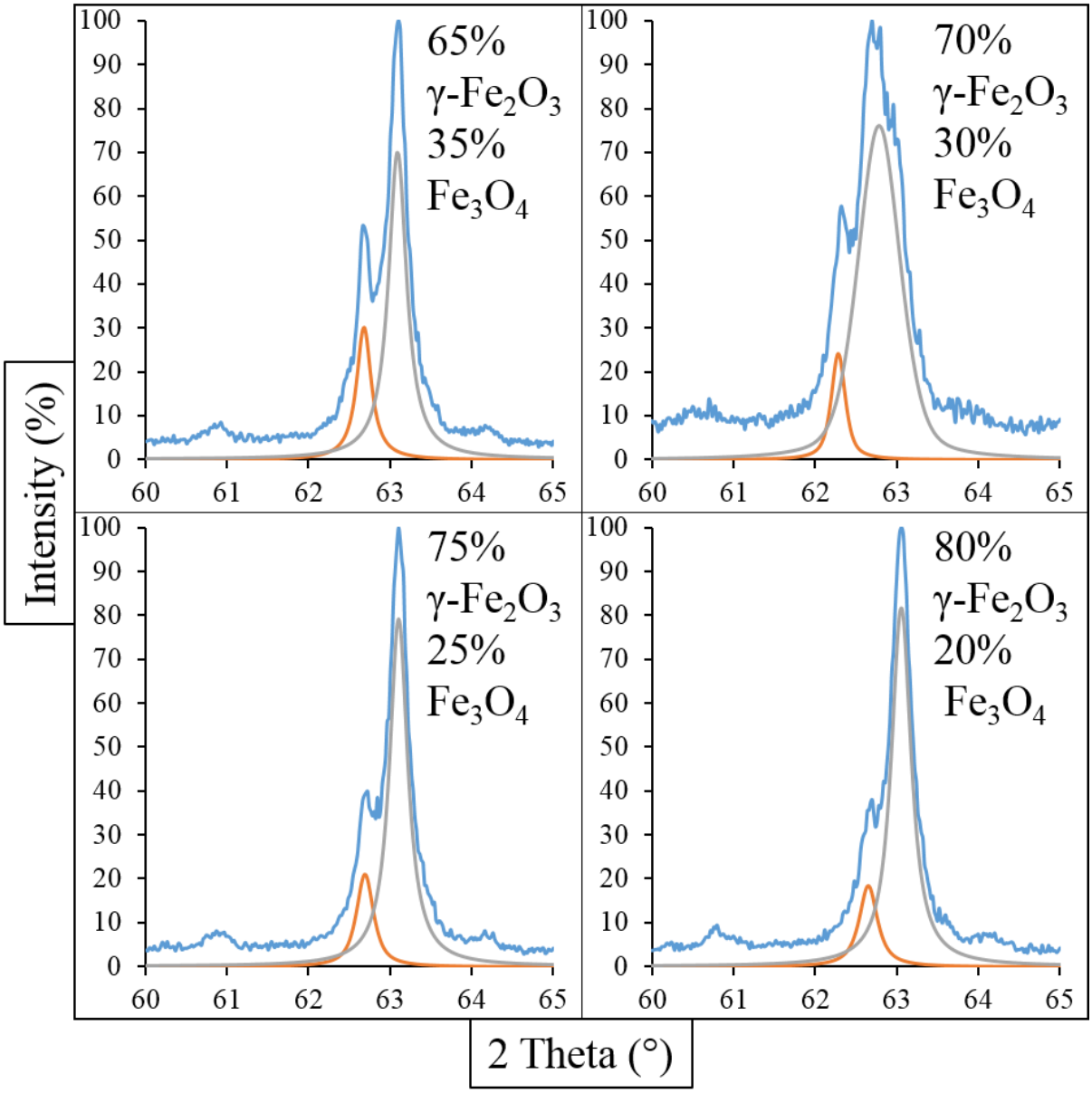

The deconvolution of the peaks of the calibrants containing γ-Fe_2O_3 (65, 70, 75 and 80%) and Fe_3O_4 (35, 30, 25, 20%), have again worked reasonably well as with the previous four calibrants. The deconvolution peaks of these middle calibrants suggest that the amount of γ-Fe_2O_3 may cause the peaks to appear more split and helping in the deconvolution process.

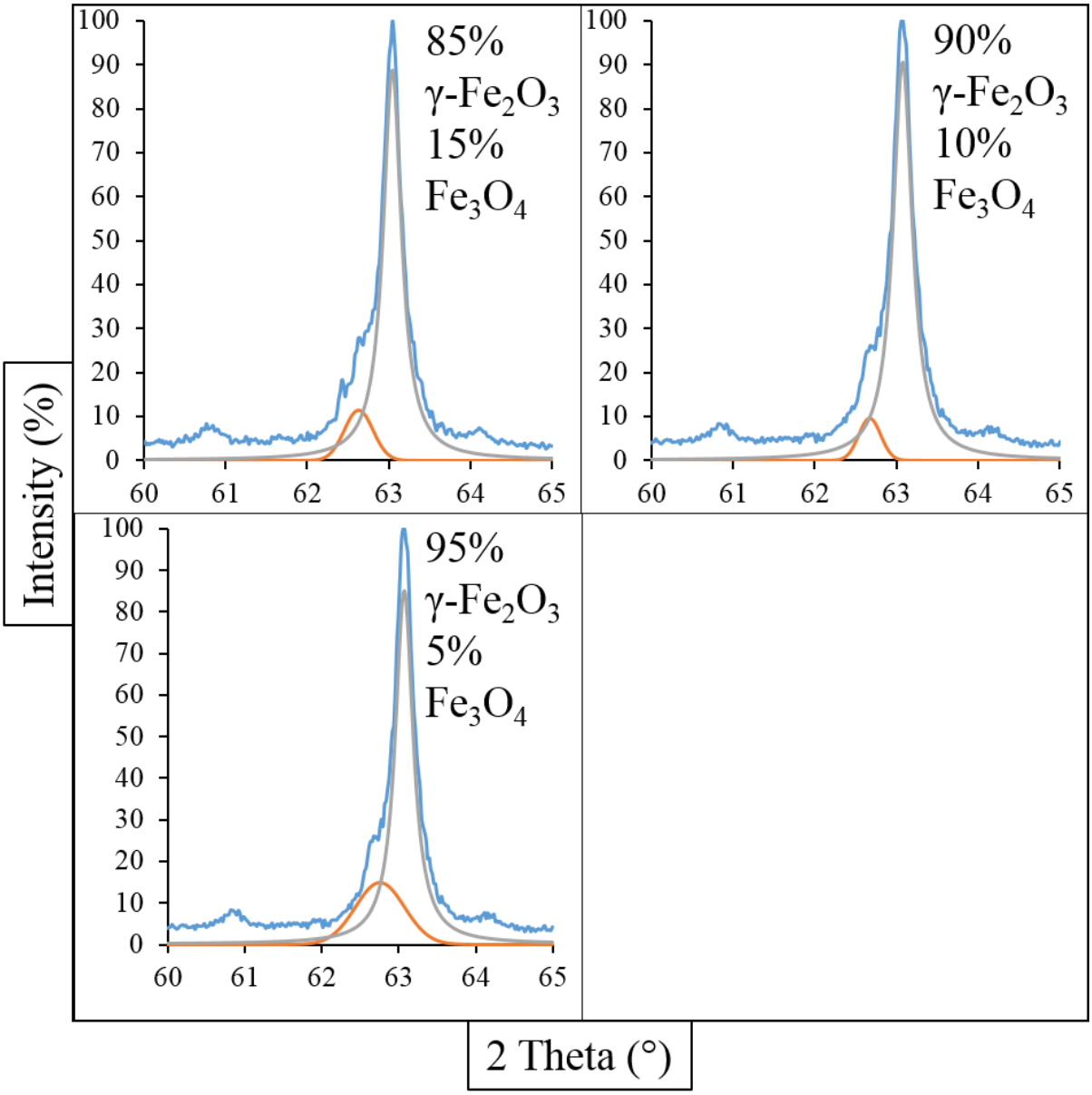

When compared to the deconvolution of the calibrants which contained low percentages of γ-Fe_2O_3 and high percentages of Fe_3O_4, those containing higher percentages of γ-Fe_2O_3 (85, 90 and 95%) and low percentages of Fe_3O_4 (5, 10 and 15%) can be seen to have deconvoluted much better, the exception being that containing 95% γ-Fe_2O_3 and 5% Fe_3O_4 where the Fe_3O_4 peak (orange) can be seen to be modelling the peak width more rather than its height.